

# REPORT DOCUMENTATION PAGE

Form Approved  
OMB No. 0704-0188

The public reporting burden for this collection of information is estimated to average 1 hour per response, including the time for reviewing instructions, searching existing data sources, gathering and maintaining the data needed, and completing and reviewing the collection of information. Send comments regarding this burden estimate or any other aspect of this collection of information, including suggestions for reducing the burden, to Department of Defense, Washington Headquarters Services, Directorate for Information Operations and Reports (0704-0188), 1215 Jefferson Davis Highway, Suite 1204, Arlington, VA 22202-4302. Respondents should be aware that notwithstanding any other provision of law, no person shall be subject to any penalty for failing to comply with a collection of information if it does not display a currently valid OMB control number.

PLEASE DO NOT RETURN YOUR FORM TO THE ABOVE ADDRESS.

1. REPORT DATE (DD-MM-YYYY) 28-05-2009			2. REPORT TYPE Final Technical Report		3. DATES COVERED (From - To) 14-09-2006 to 31-12-2008	
4. TITLE AND SUBTITLE Final Technical Report Hawaii Energy and Environmental Technologies (HEET) Initiative					5a. CONTRACT NUMBER	
					5b. GRANT NUMBER N00014-06-1-1055	
					5c. PROGRAM ELEMENT NUMBER	
6. AUTHOR(S) Rocheleau, Richard E. Bender, Guido Virji, Mahboob Antal, Michael J., Jr. Cooney, Michael J. Liaw, Bor Yann Masutani, Stephen M.					5d. PROJECT NUMBER 08PR07926-00	
					5e. TASK NUMBER	
					5f. WORK UNIT NUMBER	
7. PERFORMING ORGANIZATION NAME(S) AND ADDRESS(ES) University of Hawaii 2530 Dole Street, Sakamaki D200 Honolulu, HI 96822					8. PERFORMING ORGANIZATION REPORT NUMBER	
9. SPONSORING/MONITORING AGENCY NAME(S) AND ADDRESS(ES) Office of Naval Research Regional Office Seattle 1107 NE 45th Street, Suite 350 Seattle WA 98105-4631					10. SPONSOR/MONITOR'S ACRONYM(S) ONR	
					11. SPONSOR/MONITOR'S REPORT NUMBER(S)	
12. DISTRIBUTION/AVAILABILITY STATEMENT Approved for public release; distribution is unlimited.						
13. SUPPLEMENTARY NOTES						
14. ABSTRACT This report covers efforts by the Hawaii Natural Energy Institute of the University of Hawaii under the ONR-funded HEET Initiative that addresses critical technology needs for exploration/utilization of seabed methane hydrates and development/testing of advanced fuel cells and fuel cell systems. Methane hydrates work included: hydrate thermochemistry and kinetics; environmental impacts of methane release from seafloor hydrates; hydrate engineering applications; and international collaborative R&D. In the fuel cell area, accomplishments included: addition of three fuel cell test stands to the Hawaii Fuel Cell Test Facility; modifications to allow stack testing; study of performance impacts of contaminants in anode and cathode feed streams; and upgrading of the dynamic HiL test stand and associated simulation. For the hydrogen production area, efforts were focused on sulfur removal from fuel gas plus reforming activities that included testing with a catalytic autothermal reformer and two different plasma arc reactors. Further work was also carried out with novel fuel cell concepts including biocarbons and bio-fuel cells.						
15. SUBJECT TERMS Fuel Cells, Fuel Cell Testing, MEA Assembly, Hardware-in-Loop Testing, Fuel Processing and Gas Conditioning for Hydrogen Production, Fuels Purity, Methane Hydrates, Biocarbons, Bio-Fuel Cells						
16. SECURITY CLASSIFICATION OF:			17. LIMITATION OF ABSTRACT  UU	18. NUMBER OF PAGES  168	19a. NAME OF RESPONSIBLE PERSON Yaa-Yin Fong, Director of Research Services	
a. REPORT U	b. ABSTRACT U	c. THIS PAGE U			19b. TELEPHONE NUMBER (Include area code) (808) 956-9081	

# **FINAL TECHNICAL REPORT**

## **Hawaii Energy and Environmental Technologies (HEET) Initiative**

**Office of Naval Research**

**Grant Award Number N00014-06-1-1055**

**For the period September 14, 2006 to December 31, 2008**

# **20090611374**

**Hawaii Natural Energy Institute**



**School of Ocean and Earth Science and Technology  
University of Hawaii at Manoa**

**May 2009**



## Table of Contents

<u>Section No.</u>	<u>Section Title</u>	<u>Page</u>
1	Executive Summary	1
2	Introduction	5
3	Fuel Cell Systems	7
3.1	Objectives	7
3.2	PEM Fuel Cell Testing and Component Development	7
3.2.1	Test stands/Infrastructure Upgrades	7
3.2.2	Cell and Component Testing	8
3.2.3	MEA Fabrication Laboratory	14
3.2.4	Papers and Presentations Resulting from Efforts	14
3.3	Fuel Cell Hardware-in-Loop and System Simulation Development	17
3.3.1	Scope of Work and Approach	17
3.3.2	Technical Accomplishments	19
3.3.3	Papers and Presentations Resulting from Efforts	20
3.4	Fuel Processing and Gas Conditioning for Hydrogen Production	23
3.4.1	Sulfur Removal from Fuel Gas at Ambient Temperature	23
3.4.1.1	Absorptive Removal of Tetrahydrothiophene from Synthetic Natural Gas on Modified Activated Carbons	23
3.4.1.1.1	Scope of Work and Approach	23
3.4.1.1.2	Experimental	24
3.4.1.1.3	Technical Accomplishments	28
3.4.1.1.4	References	39
3.4.1.1.5	Paper Resulting from Efforts	40
3.4.1.2	Absorption/Desorption of Dimethylsulfide on Activated Carbon Modified with Iron Chloride	41
3.4.1.2.1	Scope of Work and Approach	41
3.4.1.2.2	Experimental	41
3.4.1.2.3	Technical Accomplishments	44
3.4.1.2.4	References	57
3.4.1.2.5	Paper Resulting from Efforts	58
3.4.2	High Pressure Autothermal Reforming in Low Oxygen Environments	59
3.4.2.1	Scope of Work and Approach	59
3.4.2.2	Experimental	61
3.4.2.3	Technical Accomplishments	64
3.4.2.4	References	79
3.4.2.5	Paper Resulting from Efforts	81
3.4.3	Plasma Reforming of Methane	83
3.4.3.1	Scope of Work and Approach	83
3.4.3.2	Experimental	84
3.4.3.2.1	Gliding Arc Reformer	85
3.4.3.2.2	Reverse Vortex Flow Reformer	86



3.4.3.3	Technical Accomplishments	87
3.4.3.4	References	89
3.5	Novel Fuel Cell and Component Development	91
3.5.1	Biocarbons for Use in Fuel Cells	91
3.5.1.1	Objectives	91
3.5.1.2	Scope of Work and Approach	91
3.5.1.3	Technical Accomplishments	92
3.5.1.4	Papers and Presentations Resulting from Efforts	92
3.5.2	Enzymatic Bio-Fuel Cells	95
3.5.2.1	Objectives	95
3.5.2.2	Scope of Work and Approach	95
3.5.2.3	Technical Accomplishments	96
3.5.2.4	References	102
3.5.2.5	Papers and Presentations Resulting from Efforts	103
4	Methane Hydrates	107
4.1	Objectives	107
4.2	Scope of Work and Approach	108
4.2.1	Hydrate Thermochemistry and Kinetics	108
4.2.2	Environmental Impacts of Methane Release from Seafloor Hydrates	108
4.2.3	Hydrate Engineering Applications	109
4.2.4	International Collaborative R&D	109
4.3	Technical Accomplishments	109
4.3.1	Methane Hydrate Destabilization	109
4.3.2	Subsea Power Generation	125
4.3.3	Environmental Impacts of Methane Release from Seafloor Hydrates	127
4.3.4	Hydrate Engineering Applications	154
4.3.5	International Collaborative R&D	159
4.4	Papers Resulting from Efforts	160
4.5	References	160

**Technical Report for the  
Hawaii Energy and Environmental Technologies (HEET) Initiative  
Grant Award Number N00014-06-1-1055  
(September 14, 2006 to December 31, 2008)**

## **1. Executive Summary**

This report summarizes work conducted under Grant Award Number N00014-06-1-1055, the Hawaii Energy and Environmental Technologies (HEET) Initiative, funded through the Office of Naval Research to the Hawaii Natural Energy Institute (HNEI) of the University of Hawaii. The work reported here continued the focus on critical technology needs associated with the development and testing of advanced fuel cells and fuel cell systems, and the exploration and utilization of seabed methane hydrates, and represents the fourth award of this initiative.

Major accomplishments under the first grant award, Number N00014-01-1-0928, included the planning, design and construction of the Hawaii Fuel Cell Test Facility (HFCTF), which opened in May 2003. In partnership with industry, HNEI established test protocols and initiated a variety of long-term durability studies. The methane hydrates activities under the first agreement initiated studies to characterize hydrate thermochemistry and kinetics, hydrate microbiology and development of international collaborations.

Under the second award (N00014-04-1-0682), HNEI expanded its test capabilities with the addition of three new fuel cell test stands at the HFCTF, including two for fuels purity studies. Tests to characterize the effects of trace amounts of benzene, toluene and carbon monoxide in the hydrogen fuel were initiated. The third stand was designed for high speed dynamic testing for use in Hardware-in-Loop (HiL) work. Testing of a 100 cm<sup>2</sup> single cell via a fuel cell vehicle simulation program was used to validate the test stand capabilities. Modeling and simulation of a fuel cell energy/power system for use in an unmanned underwater vehicle (UUV) was also completed. In addition to the FC testing, HNEI also developed an MEA (membrane electrode assembly) fabrication laboratory to support the existing fuel cell assembly laboratory. Novel fuel cell component research was continued in the areas of using biocarbons in fuel cell bipolar plates and developing enzymatic bio-fuel cells. Alternative fuel research was continued via efforts in fuel processing and gas conditioning for hydrogen production. HNEI's activities in the area of methane hydrates included studies of hydrate destabilization phenomena, with shakedown testing of HNEI's destabilization facility and design and fabrication of a novel fiberoptic probe to identify sample aspects within the calorimeter sample cell using Raman spectroscopy. HNEI sponsored and manned the organizing committee of the 4<sup>th</sup> International Workshop on Methane Hydrates that took place in Victoria, British Columbia, Canada on 9-11 May 2005.

Under the third award (N00014-06-1-0086), the capacity of the HFCTF was again expanded, increasing the total number of test stands to eight. Several of the existing test stands as well as the MEA Fabrication Laboratory were modified for increased performance. The dynamic HiL test stand was also modified to enhance response and to improve operating flexibility, safety, and test stand reliability. Simulation tools for evaluation and screening of fuel cell systems for UUV propulsion systems were developed. In the area of alternative fuel supplies, HNEI continued research on fuel processing and gas conditioning for hydrogen production. This included examination of sulfur removal from fuel gas using activated-carbon-based sorbents, and



reforming seafloor methane for use in underwater fuel cells. Work continued in the development of novel fuel cells and components, specifically in the area of biocarbons for fuel cell use and development of enzymatic bio-fuel cells. HNEI's activities in the area of methane hydrates included an expanded effort in hydrate destabilization. Detailed studies of reagent-induced decomposition of methane hydrates were initiated utilizing a novel instrument that combined spectroscopy and calorimetry. We continued our microbial analysis of sediment samples collected in the Gulf of Mexico and the Hikurangi margin off New Zealand. Model development was pursued to investigate the fate of methane released from the seafloor into the water column, e.g., as a result of inadvertent or purposeful hydrate destabilization. As part of our goal to promote international collaboration, HNEI personnel participated in a multi-national research cruise off New Zealand in June and July 2006.

During the present reporting period (Award N00014-06-1-1055), we continued to expand the capacity and capabilities of the HFCTF and made improvements to the infrastructure to support this expanded capability. Three additional test stands were added to the facility, increasing the total number of test stands to eleven. Several of the existing test stands were modified to allow testing of stacks while monitoring individual cell voltages. The systems are currently used to support Ion Tiger, an ONR-funded UAV project. The existing segmented fuel cell system was expanded by adding spatial resistance and electrochemical impedance spectroscopy (EIS), as well as cyclic and linear-sweep voltammetry (CV and LSV, respectively). Additions of other diagnostic equipment, including frequency response analyzers and galvanostats/potentiostats, and further development and improvement of existing equipment such as the gas analysis system further improved the diagnostic capabilities at the HFCTF. Research activities included studying the performance impact of low-level single and mixed contaminants present in the anode feed stream, the performance impact and poisoning mechanism of low-level sulfur dioxide in the cathode feed stream, the spatial distribution of fuel cell overpotentials along the flow channels, and the feasibility of employing the segmented cell system for the detection of membrane electrode assembly (MEA) defects. Some of these activities were supported in part by US DOE.

HiL development activities focused on upgrading the existing dynamic HiL test stand to accommodate testing of fuel cell stacks up to the 1 kW level. The upgrade included installation of a higher capacity load unit (100 V/150 A/5 kW) and higher-range mass flow controllers, and an update of the software to test stacks in static, dynamic and real-time HiL modes. Simulation tools were modified for evaluation of fuel cell systems for propulsion of an unmanned aerial vehicle.

Activities in the areas of fuel processing and gas conditioning for hydrogen ( $H_2$ ) production focused on identifying and characterizing approaches for sulfur (S) removal from fuel gas and reforming activities. Various modified activated-carbon-based sorbents were evaluated. The sulfur work focused on removal of tetrahydrothiophene (THT) and dimethylsulfide. The best modified sorbent improved S removal by more than 6X compared to the unmodified sorbent. The improved absorption is related to changes in the surface acidity/basicity of the carbon sorbent. Impregnated metals also play important roles.

Regeneration of the used carbon sorbents by thermal desorption was also explored.

Under funding from DARPA, HNEI developed a conceptual design of an ocean floor, fuel-cell based, power generating station fueled by methane from natural gas seeps or from the controlled decomposition of methane hydrates. Building on ongoing activities under HEET, a laboratory-

scale catalytic autothermal reformer capable of operating at pressures of 6 to 50 bar was constructed and tested. The objective of the experimental program was to maximize  $H_2$  production per mole of oxygen ( $O_2$ ) supplied. Tests were conducted using  $O_2$  and hydrogen peroxide ( $H_2O_2$ ) as the oxidizer. The  $H_2$  production per mole of  $O_2$  increased ~14% when using  $H_2O_2$  vs.  $O_2$  as the oxidizer. An equilibrium model was also used to compare experimental and theoretical results. Results of this analysis have been forwarded to NUWC for use in their UUV program.

Plasma reforming activities were initiated, including design, construction, and testing of two plasma arc reactor designs. The first reactor was a planar plasma, gliding arc design and the second was a reverse vortex reactor. Initial tests using methane and air showed the performance of the reverse vortex reactor to be better than the gliding arc one, producing higher levels of hydrogen in the reformat and allowing less methane to pass through the system.

In support of the DARPA-sponsored Direct Carbon Fuel Cell research project at SRI, HNEI prepared biocarbons with various well-specified properties from a wide variety of biomass feedstocks. These biocarbons were shipped to SRI for testing and evaluation. SRI is using its test results to optimize the performance of its carbon fuel cells.

Development of enzymatic bio-fuel cells continues, focused on enzyme immobilization utilizing macroporous chitosan polymer composites that support both mediator-based and direct-electron-transfer mechanisms. Improved *in situ* surface and interface characterization protocols have also been achieved in this work. This approach uses imaging ellipsometry and additional complementary characterization tools to study biocatalytic electrodes and their behavior. A model system that includes polymerized methylene green on electrodes as the electron transfer mediator was studied to elucidate the mediator-based electron-transfer mechanisms.

The methane hydrates activities comprised four subtasks: Hydrate Thermochemistry and Kinetics, Environmental Impacts of Methane Release from Seafloor Hydrates, Hydrate Engineering Applications, and International Collaborative R&D. Subtasks included: laboratory and analytical investigations of hydrate destabilization by chemical reagents; laboratory studies of subsea power system components that utilize seafloor methane; characterization of the microbial community in marine hydrate beds that modulate methane levels in the seafloor sediments and leakage into the water column; development of models to predict the fate of methane released from the seafloor into the water column; preliminary laboratory studies of mixed gas hydrates for gas purification; and the promotion of international R&D partnerships.

Significant progress in understanding hydrate destabilization using thermodynamic inhibitors was gained. We had posited that thermodynamic inhibitors work by tying up liquid water at the hydrate surface and, hence, disrupt the dynamic equilibrium between hydrate decomposition and formation. We tested this hypothesis by conducting a series of experiments with our Raman calorimeter in which three common alcohols and one diol were injected at constant temperature and pressure into a sample cell containing methane hydrate. The calorimeter thermograms of these injections were used to infer the amounts of hydrate decomposed per mole of inhibitor and these data were correlated with the molecular structure of the inhibitor. The results indicated that the effectiveness of an inhibitor to destabilize methane hydrate is related to the number of hydroxyl groups that provide hydrogen bonding sites and the size of the alkyl group, which tends to inhibit this bonding. This is consistent with the experimental observations and supports our hypothesis about the fundamental mechanism of chemical decomposition of hydrates.



The impact of seafloor methane from hydrates on the marine environment was explored via both experiments and modeling. Biological processes (mostly microbial) in the sediment and the water column are believed to play a major role in determining methane levels throughout the marine environment. The underlying metabolic pathways and the factors that affect these processes are not well understood and have been a focus area of the HNEI methane hydrate task. During the present phase of the HEET initiative, we continued our analysis of sediment samples collected from methane hydrate beds in the Hikurangi Margin off New Zealand. The microbiology of these samples included *Bacteria* and *Archaea* communities that were investigated by use of molecular DNA cloning. The clones were DNA sequenced and phylogenetic trees were constructed for each of these communities. The clone results did not indicate the presence of a clearly defined ecology that would be unique to methane hydrate containing sediments.

Similar molecular analyses also were performed on a push-core sample from a hydrate mound in Barkley Canyon in the Gulf of Mexico that was provided by our collaborators at the Naval Research Laboratory (NRL). Results indicate that there is a significant amount of diversity. A species that is known to exist in hydrate-containing sediments was found with high frequency, and another species specifically associated with AOM was detected. A phylogenetic tree using the actual clone sequences currently is being constructed. Work also continues on the development of computer models to investigate the fate of methane released from the seafloor into the water column, e.g., as a result of inadvertent or purposeful hydrate destabilization. As a first step to explore the use of gas hydrates for non-energy related engineering applications, such as gas fractionation or water purification, we conducted experiments with mixed gas hydrates to test the performance of the Raman calorimeter and to confirm our laboratory protocols. The instrument performed well and the protocols we developed appear to be viable. During the next phase of the experiments, the calorimeter gas supply system will be modified to allow extraction and analysis of the gas composition during hydrate formation and decomposition to determine if fractionation is occurring.

Finally, as part of our goal to promote international collaborative R&D on methane hydrates, HNEI supported and helped organize the 6<sup>th</sup> International Workshop on Methane Hydrate R&D that was held in Bergen, Norway in May 2008. The workshop was attended by scientists, engineers, and other stakeholders from 12 countries and a meeting report is available from NRL.



## **2. Introduction**

The Hawaii Energy and Environmental Technologies (HEET) Initiative, funded to the Hawaii Natural Energy Institute (HNEI) of the University of Hawaii through the Office of Naval Research (ONR), was initiated in the summer of 2001 under Grant Award Number N00014-01-1-0928 to address critical technology needs associated with the exploration and utilization of seabed methane hydrates and the development and testing of advanced fuel cells and fuel cell systems. These efforts and a smaller effort in fuels purification were continued under two subsequent agreements (Award No. N00014-04-1-0682: June 15, 2005 to June 30, 2006; and Award No. N00014-06-1-0086: October 17, 2005 to September 30, 2007). Under these programs, the focal point of our activity was development of the Hawaii Fuel Cell Test Facility (HFCTF) which houses dual facilities for fuel cell testing and for the synthesis and characterization of methane hydrates. Research in these areas was described in prior reports.

Our fourth (the current) HEET program (Award No. N00014-06-1-1055), was for the period September 14, 2006 to December 31, 2008. The remaining two sections of this report focus on each of the major areas covered within the HEET initiative. Section 3 is on fuel cell systems, with subsections for each of the associated subtasks for these systems. Section 4 covers methane hydrates, including subsections for the subtasks of this area.



### **3. Fuel Cell Systems**

#### **3.1 Introduction**

This overall task area is organized into four major subtasks: polymer electrolyte membrane (PEM) fuel cell testing and component development; fuel cell Hardware-in-Loop (HiL) and system simulation development; fuels processing and gas conditioning for hydrogen production; and novel fuel cell and component development. Under this Grant, HNEI further expanded the testing and research capabilities of the Hawaii Fuel Cell Test Facility (HFCTF), including additional gas infrastructure to operate the increased amount of test stations, implementation of stack testing for stacks that contain more than four cells, and low-current sensing for improved segmented cell diagnostics. There were new advances in the development of HiL capabilities for evaluating fuel cells under simulated real-world operating conditions, continuing work on fuel processing and gas conditioning research, and the area of novel fuel cells.

Details for the activities conducted under each of these subtasks are given below.

#### **3.2 PEM Fuel Cell Testing and Component Development**

Primary activities in this area included research activities as well as infrastructure and testing capability development. Research activities included studying the performance impact and poisoning mechanism of low-level sulfur dioxide in the cathode feed stream, studying the impact of contaminant mixtures in the anode feed stream, and studying the spatial distribution of fuel cell overpotentials along the flow channels. Testing capabilities were improved by adding test equipment for sub-scale cells, providing existing UTC XT-800 test stations with the option to test small-scale stacks with up to 48 cells, and implementing small-current-sensing capabilities to the segmented cell data acquisition system.

##### **3.2.1 Test Stands/Infrastructure Upgrades**

During the past year, improvements were implemented on the facility infrastructure, several test stands, and diagnostic instruments. With increasing demand for small stack fuel cell testing, we found it valuable to modify one of the UTC XT-800 test stands to allow small stack testing in support of the Ion Tiger unmanned aerial vehicle (UAV) project. This test station now has the capability to run 50 to 600 cm<sup>2</sup> single cells or small stacks (36-cell stacks, < 30 cm<sup>2</sup> per cell). Newly installed Fuel Cell Technologies test stations were modified to allow for H<sub>2</sub>/Helox (mixture of helium and oxygen) operation in support of the segmented cell system.

In anticipation of further impurity work, our gas analysis capability was expanded by splitting our two Varian gas chromatographs (GCs), which effectively doubles our throughput for impurity testing. Previously, both Varian GCs were operated as one unit, sampling off the same port simultaneously. By splitting the systems, we now can measure two sample points independently. The second system is currently setup to study low-level carbon monoxide and carbon dioxide using a Flame Ionization Detector (FID). The original GC system essentially remains unchanged.

With the addition of new test stations and the expansion of existing stations for small stack testing causing an increased demand for high purity water, the original facility small capacity deionized water system was replaced with a Millipore high capacity deionized water system.

The Millipore system consists of a reverse osmosis pre-treatment unit, a 350-liter storage tank and distribution pump, and a high capacity deionized water cartridge system. The new Millipore system increased the supply of deionized water from 1.5 to 12 lpm at 45 psig. Other facility upgrades included the addition of two 3 kW / 4 gpm chiller units providing cooling water to all test stations in the facility.

Cyclic voltammetry (CV) experiments are essential parts of the previously developed protocols for standardized testing and routinely accompany the impurity experiments during beginning of test (BOT) and end of test (EOT) diagnostics. As part of the station and capability upgrades for this award period, 16-channels of the segmented cell data acquisition system were reconfigured for low current sensing to allow CV and single sweep voltammetry experiments with the segmented cell system. The low current configuration of the segmented cell data acquisition increased the sensitivity of the employed Hall sensor devices by a factor of 40, i.e., from a nominal current density of 1.3 A/cm<sup>2</sup> to 0.033 A/cm<sup>2</sup>, thus allowing standard electrochemical diagnostic experiments such as the determination of the electrochemically active surface area of the catalyst via CV or of the hydrogen crossover limiting current via linear sweep voltammetry (LSV). Figure 3.2-1 shows spatial CV experiments performed at all ten segments of the segmented anode electrode simultaneously. The data allowed determining the active Pt catalyst area of each segment area, although a non-segmented anode electrode was assembled in the cell. Similar experiments will be conducted during future contaminant and durability studies.

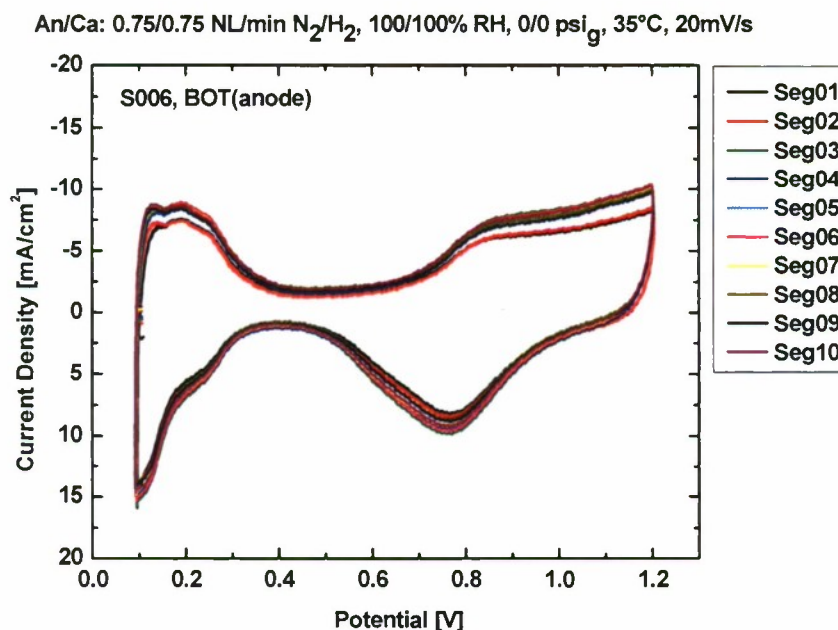


**Figure 3.2-1. Spatial cyclic voltammetry data conducted simultaneously at all segments using the low current setting of the segmented cell data acquisition setup.**

### 3.2.2 Cell and Component Testing

The main focus in this task was to study the effect of fuel and air contaminants on cell performance and durability. For fuel contaminant studies, the previously established gas analysis



system was combined with the existing experimental setup to gain new understanding of the reaction processes related to contaminant exposure. Figure 3.2-2 shows example data for 1 ppm CO exposure at anode/cathode conditions of: 60 °C, 2/2 stoich, 7/7 psi<sub>g</sub>, 100/50% RH, H<sub>2</sub>/Air. The overpotential change of the cell (173 mV), shown in black, was reached at steady state poisoning conditions. Sampling and analyzing the gas at anode and cathode inlet and outlet streams allowed for the successfully closing of the cells molar flow balance for carbon at steady state poisoning conditions to typically within  $\pm 3\%$ . For the data in Figure 3.2-2, the molar flow balance for carbon closed to within  $\pm 0.6\%$  as indicated by the molar flow balance for carbon (green) at steady state poisoning conditions between 80 to 100 hours. Successfully closing the molar flow balance of carbon was essential for calculating the CO coverage of the cell (blue) at any time during the experiment. The residual CO coverage was verified by an independent CV experiment, shown in Figure 3.2-2 as a blue single data point at 160 hours. The data agreed well with the calculated CO coverage and established additional confidence into the developed methodology. Further analysis of the CO coverage vs. the overpotential change resulted in the detection of a hysteresis between the poisoning process and the recovery process. Subsequent modeling analysis showed that this effect may be caused by spatial processes in the cell.

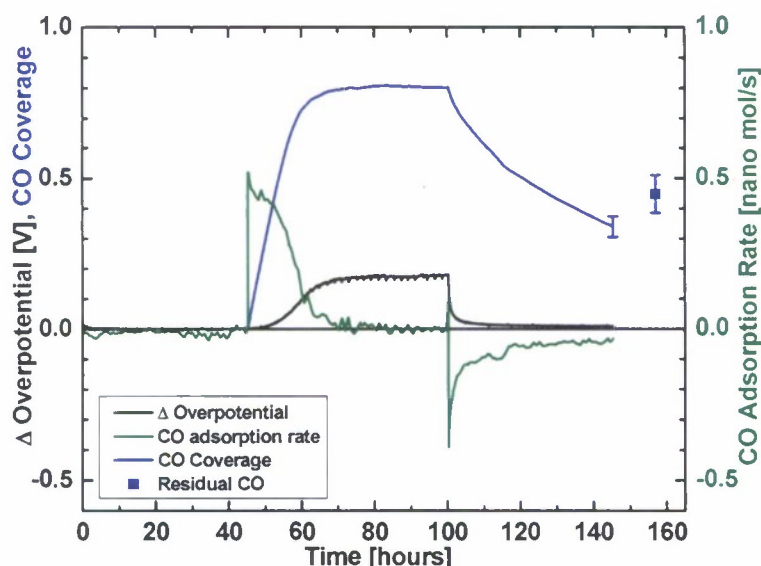


**Figure 3.2-2. Overpotential change, CO coverage, and CO adsorption/removal rates in fuel cell exposed to 1 ppm CO at 1 A/cm<sup>2</sup>, 60°C, 2/2 stoich, 7/7 psi<sub>g</sub>, 100/50% RH, H<sub>2</sub>/Air.**

In addition to single contaminant exposure, mixed contaminant experiments were conducted with CO and toluene (C<sub>7</sub>H<sub>8</sub>). Figure 3.2-3 summarizes the results of three impurity experiments all conducted at the same operating temperature of 60 °C. Two experiments were run with individual impurity injections of i) 2 ppm CO and ii) 20 ppm C<sub>7</sub>H<sub>8</sub>, and the third was run with the mixture of both impurity concentrations. To allow for an easier data comparison, the time scale of each experiment was shifted so that the impurity injections started at exactly 10 hours. In Figure 3.2-3, the overpotentials change with time due to the impurity injections. While the single injection of 20 ppm C<sub>7</sub>H<sub>8</sub> resulted in a very small overpotential change of 8 mV, CO at similar conditions impacted the performance significantly more strongly and caused an



overpotential change of 247 mV. However, cell exposure to the mixture of both impurities resulted in an even greater overpotential change of 345 mV, about 100 mV higher than the sum of the individual overpotential changes of CO and C<sub>7</sub>H<sub>8</sub>. The data indicate that the mixture of impurities can cause an overpotential change that is greater than the sum of the overpotential changes of each single impurity injection.

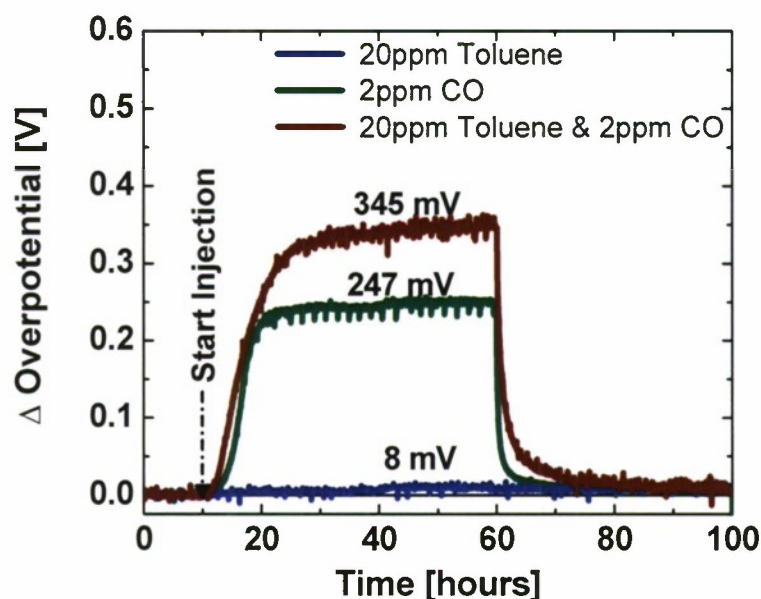


**Figure 3.2-3.** Overpotential change to single exposure to 20 ppm Toluene and 2 ppm CO as well as the mixture of both, at 1 A/cm<sup>2</sup>, 60 °C, 2/2 stoich, 7/7 psi<sub>g</sub>, 100/50% RH, and H<sub>2</sub>/Air.

Figure 3.2-4 shows the overpotential change for the mixed impurity experiment shown in Figure 3.2-3 [top] as well as the molar flow rates at the anode for C<sub>7</sub>H<sub>8</sub> and methylcyclohexane (C<sub>7</sub>H<sub>14</sub>) [middle], and CO and CO<sub>2</sub> [bottom]. Similar to results of single C<sub>7</sub>H<sub>8</sub> injection experiments, a hydrogenation process at the anode was observed that started immediately upon injection of C<sub>7</sub>H<sub>8</sub>. However, in contrast to what was observed during the single impurity injection, the conversion of C<sub>7</sub>H<sub>8</sub> into C<sub>7</sub>H<sub>14</sub> during this experiment decreased significantly over the first 20 hours of the injection and approached a negligible value after approximately 30 hours. The bottom graph of Figure 3.2-4 shows the molar flow rates of CO and CO<sub>2</sub> at the inlet and outlet of the anode over the same period of the experiment. The data confirmed the injection of CO between 10 and 60 hours. With a delay of approximately 7.5 hours with respect to the start of impurity exposure, CO was detected at the outlet of the fuel cell anode. CO values at the anode outlet increased over a 10-hour period to a steady state value, which suggests that adsorption of CO occurred at the fuel cell anode, and that with a progressing saturation of the Pt catalyst layer with CO, the molar flow rates of CO in the anode exhaust increased. However, immediately upon introduction of CO, the molar flow rate of CO<sub>2</sub> at the anode outlet increased over a 20-hour period. The data indicated the conversion of CO to CO<sub>2</sub>, most likely via an electro-oxidation reaction on the platinum catalyst layer.

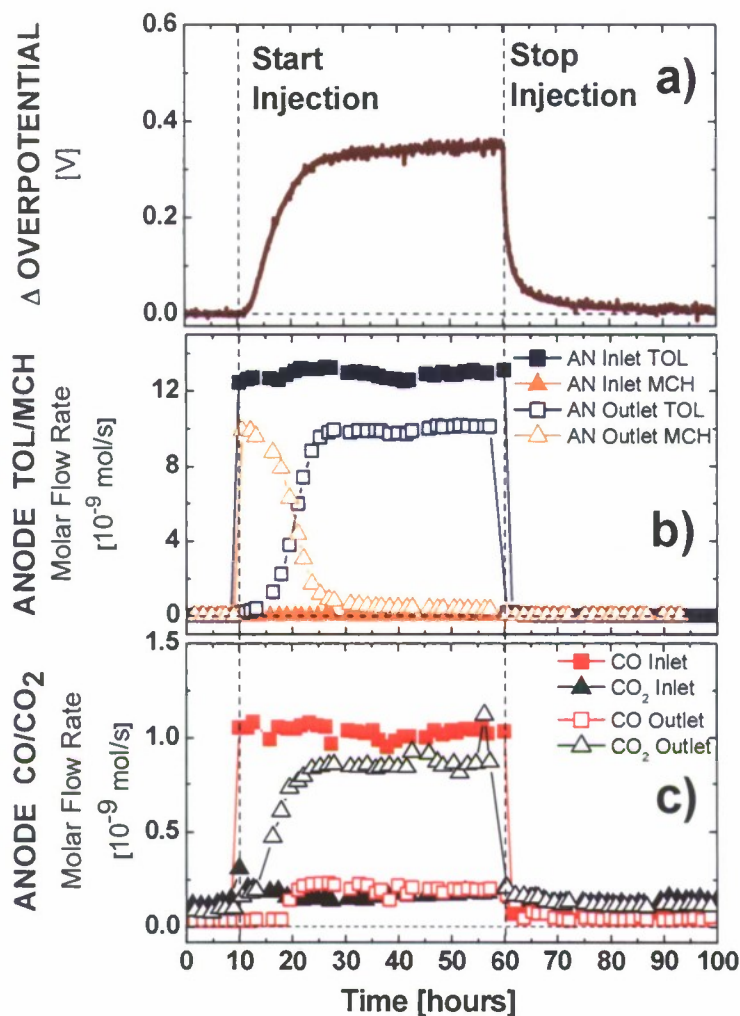


**Figure 3.2-4. Top: Overpotential change to mixed contaminant exposure with 20 ppm Toluene and 2 ppm CO at 1 A/cm<sup>2</sup>, 60 °C, 2/2 stoich, 7/7 psi<sub>g</sub>, 100/50% RH, and H<sub>2</sub>/Air. Middle and Bottom: Gas analysis data at anode inlet and outlets for toluene and methylcyclohexane (MCH), and CO and CO<sub>2</sub>, respectively.**

The data suggest that at the start of the impurity injection, all injected C<sub>7</sub>H<sub>8</sub> entering the cell was at first converted into C<sub>7</sub>H<sub>14</sub>, as observed during the single contaminant exposure. CO, however, was then continuously adsorbed strongly on the Pt catalyst surface and slowly decreased the available reactions sites for the hydrogen oxidation reaction and the hydrogenation of C<sub>7</sub>H<sub>8</sub> over time. With increasing CO coverage, the hydrogen reduction reaction and the hydrogenation of C<sub>7</sub>H<sub>8</sub> competed for the remaining catalyst reaction sites, resulting in greater overpotential than observed for CO alone. The decreasing extent of reaction for the hydrogenation of C<sub>7</sub>H<sub>8</sub> was attributed to a faster reaction rate of the hydrogen oxidation reaction (HOR). However, the competition of the HOR with the C<sub>7</sub>H<sub>8</sub> hydrogenation caused a significantly higher overpotential of 100 mV in the fuel cell.



Air contaminant studies focused on  $\text{SO}_2$ , a critical possible air contaminant for fuel cell applications in a battlefield and naval environment. Experiments have been conducted to study the effects of exposing the cathode to a trace level of  $\text{SO}_2$  during constant current operation at  $0.6 \text{ A/cm}^2$ .  $\text{SO}_2$  exposure with a total dosage of  $0.16 \cdot 10^{-3} \text{ mol SO}_2$  at 1, 2, and 10 ppm concentrations resulted in significant performance degradation. An example experiment conducted with 2 ppm  $\text{SO}_2$  at  $0.6 \text{ A/cm}^2$ ,  $80^\circ\text{C}$ , 2/2 stoich, 7/7 psig, and 100/50% RH is shown in Figure 3.2-5. At all concentrations, steady-state poisoning conditions were reached, and the saturation time and degree of the performance impact increased with contaminant concentration. The cell voltage at steady state during  $\text{SO}_2$  exposure varied up to 53 mV between exposure to 1 and 10 ppm  $\text{SO}_2$ . The poisoning process was identified as a 2-step process, which was indicated by an inflection of the voltage degradation at a cell voltage of 0.65 V. For operation at cell voltages lower than 0.65 V prior to poisoning, no inflection was observed, suggesting that the inflection may be originating from the onset of an  $\text{SO}_2$  reduction process at 0.65 V reported in the literature. Cell recovery by  $\text{H}_2/\text{air}$  operation with pure gases was independent on contaminant concentration and incomplete during all experiments. The resulting cell voltage after recovery was approximately 140 mV lower than the initial cell voltages, which was attributed to sulfur species remaining on the catalyst surface and reducing the electrochemical area (ECA) available at the cathode. Almost complete recovery of the cathode ECA was achieved by CV scanning. An example of a CV scanning experiment is shown in the right graph of Figure 3.2-5. The remaining 16.9% ECA loss may be due to regular electrode degradation of the MEA. However, changes in the CV features of the catalyst developed due to  $\text{SO}_2$  exposure and indicated similarities to Pt/Pt systems in sulfuric acid solution. For further insights and a deeper understanding of the reaction processes, additional studies will be performed.

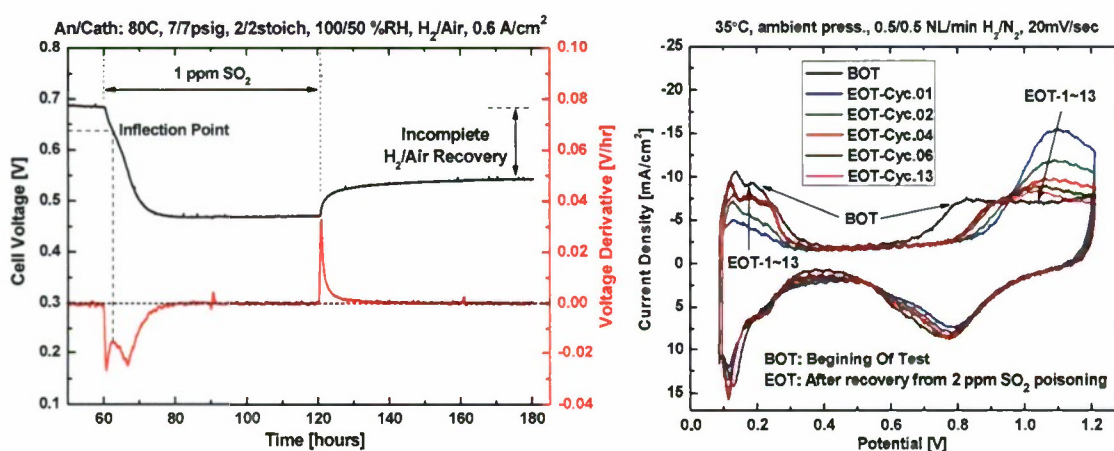


**Figure 3.2-5. Left:** Cell performance impact during contaminant exposure with and recovery from 2 ppm  $\text{SO}_2$  at  $0.6 \text{ A/cm}^2$ ,  $80^\circ\text{C}$ , 2/2 stoich, 7/7 psig, 100/50% RH, and  $\text{H}_2/\text{Air}$ . Cell voltage derivative suggests two reaction mechanisms during  $\text{SO}_2$  exposure. **Right:** Gas analysis data at anode and cathode inlet and outlets for CO,  $\text{CO}_2$ , toluene, and methylcyclohexane.

The overall current density measured in a PEM fuel cell (PEMFC) represents the average of the local reaction rates. Depending on cell design and operating conditions, the spatial variability

may be significant. Four primary loss mechanisms determine the spatial and overall performance of a PEMFC: activation, concentration, ohmic, and mass transfer losses. Activation losses are associated with sluggish reaction kinetics and low catalyst activity. Ohmic losses occur due to limitations of protonic and/or electronic charge transport. Concentration losses are caused by the dilution of the reactant oxygen in air to a concentration of 21%<sub>vol</sub>, and mass transfer losses are associated with the reactant transport resistance to the catalytically-active sites due to bulk diffusion. All four loss mechanisms are functions of the current density and can be spatially dependent.

During this award period, HNEI's segmented cell system was used to characterize the distribution of these various losses in a PEMFC using a six-channel serpentine flow-field. Voltage losses were attributed to each of the mechanisms at each current density by subtracting *iR*-corrected and uncorrected VI curves using three cathode gas compositions: Air, He+O<sub>2</sub>, and O<sub>2</sub>. Activation losses were obtained by subtracting the *iR*-corrected H<sub>2</sub>/O<sub>2</sub> polarization curve from the theoretical open-circuit voltage of 1.23 V. The ohmic overpotential was obtained by subtracting the H<sub>2</sub>/O<sub>2</sub> values from the respective *iR*-corrected values. Subtraction of the H<sub>2</sub>/He+O<sub>2</sub> data from the H<sub>2</sub>/O<sub>2</sub> data yielded the concentration losses, whereas the mass transfer overpotential was obtained by deducting the H<sub>2</sub>/Air values from the H<sub>2</sub>/He+O<sub>2</sub> values.

The resulting spatial overpotential data was analyzed by introducing a homogeneity indicator for each overpotential. This indicator was defined as the slope of the linear fit for the overpotential distribution and was calculated for each current density. An indicator value of zero consequently represents perfectly homogeneous distribution along the flow-field, while positive and negative values represent increasing and decreasing overpotentials along the flow-field, respectively. Figure 3.2-6 shows example data for the homogeneity indicator vs. current density at various humidification configurations. On the left side of Figure 3.2-6, results are shown for the high frequency response (HFR) resistance distribution, and on the right for the concentration overpotential distribution, respectively. The data for the HFR resistance distribution indicate that at all humidification configurations, the homogeneity improved with increasing current densities. Data values were either negative or zero, indicating that the cell resistance either decreased or was constant along the flow-field. For each humidification, a maximum homogeneity was reached at a specific current density, which decreased with increasing cell humidification. The data quantify the contribution of external and internal humidification on the homogeneity of the HFR along the flow-field.

The right side of Figure 3.2-6 shows similar data for the concentration overpotential. The distribution of the concentration overpotential became less homogeneous with current density when operating at drier humidification conditions. Below 0.6 A/cm<sup>2</sup>, however, the humidification of the cell had no impact on the homogeneity of the concentration overpotential. The methodology for separating the fuel cell overpotentials employed, together with HNEI's segmented cell system, allowed studying the dependence of the distribution of overpotentials in a fuel cell with respect to changing operating conditions. This information will be useful for understanding mechanical or electrochemical failure mechanisms of long-term statically or dynamically operated fuel cell systems.



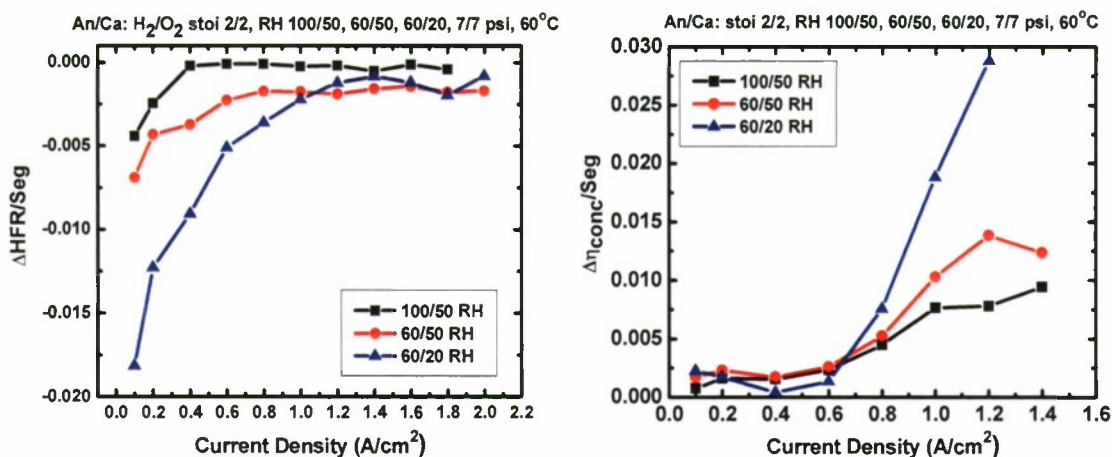


**Figure 3.2-6. Left: Cell resistance homogeneity indicator vs. current density for segmented cell operated at various humidification levels at 60 °C, 2/2 stoich, 7/7 psi<sub>g</sub>, 100/50% RH, and H<sub>2</sub>/O<sub>2</sub>. Right: Concentration overpotential homogeneity indicator vs. current density for segmented cell operated at various humidification levels at 60 °C, 2/2 stoich, 7/7 psi<sub>g</sub>, 100/50% RH, and H<sub>2</sub>/Air.**

### 3.2.3 MEA Fabrication Laboratory

The MEA Fabrication Laboratory is located within the HFCTF. During this grant period, the laboratory was not operated, but it was augmented by the acquisition of a Graphetek plotter for cutting gaskets to be used in the assembly of MEAs. The plotter was received towards the end of the grant period and has not yet been setup. It will be completed and used in future work at the laboratory.

### 3.2.4 Papers and Presentations Resulting from 2008 Efforts

#### PAPERS

G. Bender, M. Angelo, K. Bethune, S. Dorn, and R. Rocheleau, "Method Using Gas Chromatography to Determine the Molar Flow Balance for Proton Exchange Membrane Fuel Cells Exposed to Impurities," submitted to Journal of Power Sources, February 2009.

S. Dorn, G. Bender, K. Bethune, M. Angelo, R. Rocheleau, "The Impact of Trace Carbon Monoxide / Toluene Mixtures on PEMFC Performance," ECS Transactions, 16 (2), 659 (2008).

M. Angelo, S. Dorn, G. Bender, R. Rocheleau, "The Impacts of Repetitive CO Poisoning on MEA Performance and Durability," ECS Transactions, 16 (2), 669 (2008).

Y. Zhai, G. Bender, S. Dorn, M. Angelo, K. Bethune, and R. Rocheleau, "Sulfur Dioxide Contamination in PEMFCs: Degradation and Recovery of Performance," ECS Transactions 16 (2), 873 (2008).

G. Bender, M. Angelo, K. Bethune, S. Dorn, and R. Rocheleau, "Quantitative Analysis of the Performance Impact for Low Level Contaminant Studies on Proton Exchange Membrane Fuel Cells," in preparation for submission to Journal of Power Sources.



G. Bender, M. Angelo, K. Bethune, S. Dorn, and R. Rocheleau, "The Carbon Monoxide Balance Of A Direct Hydrogen Proton Exchange Membrane Fuel Cell During Exposure To Low Level Carbon Monoxide," in preparation for submission to Journal of the Electrochemical Society.

#### PRESENTATIONS

G. Bender, S. Dorn, K. Bethune, M. Angelo, R. Rocheleau, "The Impact of Trace Carbon Monoxide/Toluene Mixtures on Proton Exchange Membrane Fuel Cell Performance," 2nd DOE/ANL Modeling Workshop, National Renewable Energy Laboratory, November 20-21, 2008, Golden, Colorado.

S. Busquet, K. L. Davis, R. M. Moore, G. Bender, R. Rocheleau, "HNEI Simulation Tool for Proton Exchange Membrane Fuel Cells," 2nd DOE/ANL Modeling Workshop, National Renewable Energy Laboratory, November 20-21, 2008, Golden, Colorado.

T. Reshetenko, G. Bender, and R. Rocheleau, "The Voltage Loss Distribution of a PEMFC at Various Operating Conditions," 214th meeting of the Electrochemical Society, Oct. 12-17, 2008, Honolulu, Hawaii.

S. Dorn, G. Bender, K. Bethune, M. Angelo, R. Rocheleau, "The Impact of Trace Carbon Monoxide / Toluene Mixtures on PEMFC Performance," 214th meeting of the Electrochemical Society, Oct. 12-17, 2008, Honolulu, Hawaii.

M. Angelo, S. Dorn, G. Bender, R. Rocheleau, "The Impacts of Repetitive CO Poisoning on MEA Performance and Durability," 214th meeting of the Electrochemical Society, Oct. 12-17, 2008, Honolulu, Hawaii.

G. Bender, M. Angelo, K. Bethune, S. Dorn, and R. Rocheleau, "Impurity Studies at HNEI, University of Hawai'i," ISO/TC197/WG12 Meeting, San Francisco, April 3 2008.

#### POSTER PRESENTATION

"Sulfur Dioxide Contamination in PEMFCs: Degradation and Recovery of Performance," Y. Zhai, G. Bender, S. Dorn, M. Angelo, K. Bethune, and R. Rocheleau, 214th meeting of the Electrochemical Society, Oct. 12-17, 2008, Honolulu, Hawai'i.



### 3.3 Fuel Cell Hardware-in-Loop and System Simulation Development

The objectives of this subtask were divided between two major activities: a) enhancement of existing Hardware-in-Loop (HiL) testing capabilities, and b) development of fuel cell system simulation tools. The HiL capability and simulation tools are intended to contribute towards providing a Rapid Prototyping System (RPS) for naval application of fuel cell systems. Both of these topics will be discussed in the following paragraphs.

#### 3.3.1 Scope of Work and Approach

##### HiL Development

The HNEI fuel cell HiL dynamic test station has been developed and is in operation evaluating PEM fuel cells (PEMFCs) under dynamic application conditions. HiL methodology is well established in the automotive industry, where the technique is applied to develop and debug control algorithms for automotive drive systems. Figure 3.3-1 shows the layout of HNEI's HiL concept.

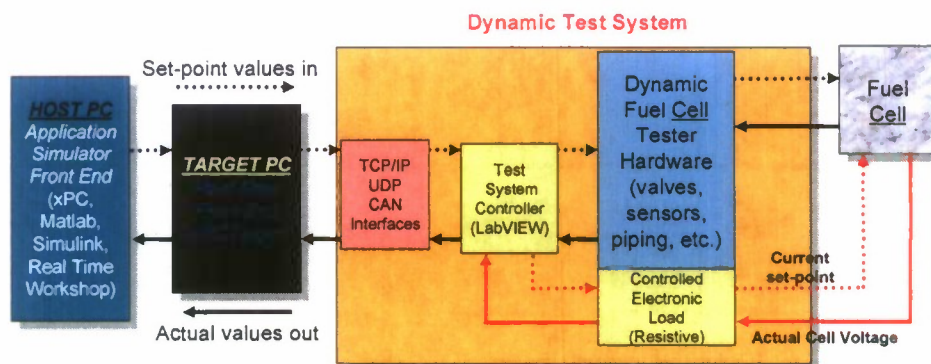


Figure 3.3-1. HNEI fuel cell Hardware-in-Loop concept.

HNEI's fuel cell HiL process is capable of developing optimal control strategies and algorithms for a fuel cell system and its associate components using a real-time simulation for a desired fuel cell application under a dynamic load profile. The de-coupling of parameters, combined with high-end instrumentation, allows distinguishing of the impact and allocation of weak spots, performance degradation, and ageing effects of the cell or stack. The process allows the evaluation of both the performance and durability of a specific fuel cell or stack design (geometry, materials, flow fields, etc.) under dynamic test conditions that mimic the actual conditions that a cell or stack will experience when placed in a realistic environment.

At the beginning of this reporting period, HNEI worked closely with ONR and NRL to identify fuel cell systems that are of near-term U.S. Navy interest which would require testing of the stacks in the HiL mode. The plan during this reporting period was to further upgrade (both hardware and software) our dynamic HiL fuel cell test stand to permit the testing of small fuel cell stacks (e.g., up to the 1 kW level). In order to make this upgrade to stack testing, it was decided to purchase and install a bigger load unit (100 V/150 A/5 kW) and larger-range mass flow controllers (MFCs) for hydrogen (0-20 slpm) and air (0-50 slpm). The idea was to

configure the HiL test stand to have the flexibility of testing a stack or a signal fuel cell by switching between the bigger- and smaller-range load (10 volts/150 amps/1 kW) units. This upgrade to stack-level testing involved a complete restructure of the internal space of the test stand to accommodate the new hardware (load unit and MFCs), development and installation of electronic boards and controller, and redesign of the FPGA (low level programming for safety and alarm system), Real Time and PC software. These hardware and software upgrades were accomplished internally at HNEI. The details of this configuration are discussed in Technical Accomplishments, presented under section 3.3.2 below.

The upgraded HiL stack test system was successfully completed, has a dynamic response time of between 50-100 milliseconds, and is capable of evaluating the fuel cell stack performance and durability within U.S. Navy fuel cell systems. The upgraded dynamic HiL testing will focus on candidate fuel cell stack technology for autonomous applications of interest to the Navy (NRL and NUWC). Furthermore, the upgraded HiL test system now has the diagnostic capability of testing both single cells and stacks in dynamic and real-time HiL modes.

### Simulation Tool Development

Since there is an interest in applying fuel cell stacks to an unmanned aerial vehicle (UAV), our group created a simulation tool called Hybrid Power System (HPSys). Fig 3.3-2 shows the schematic representation of a fuel cell and battery hybrid power system.

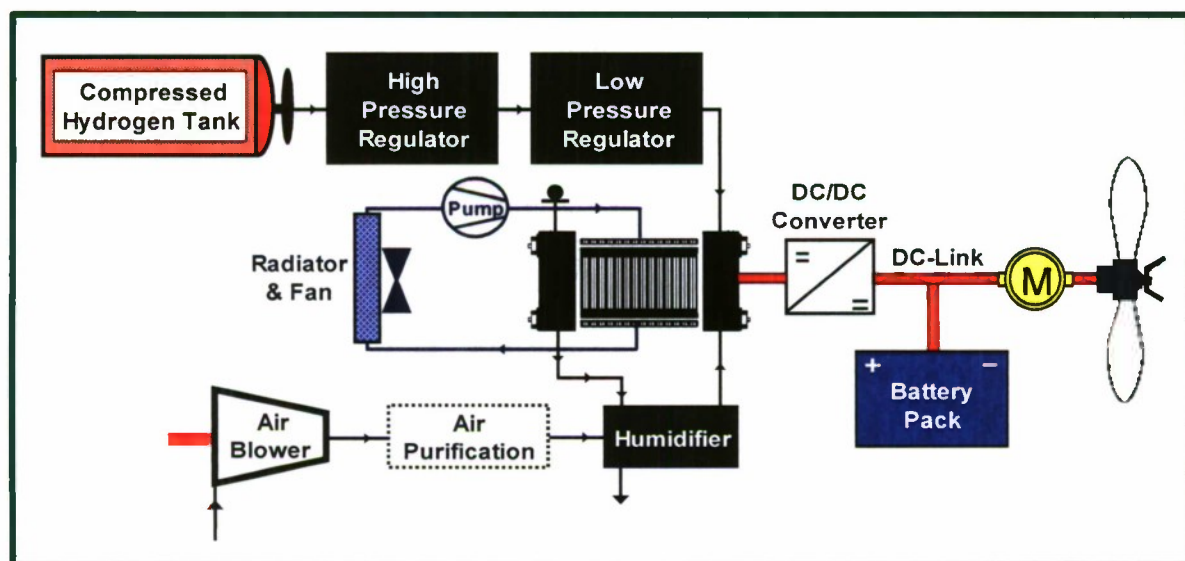


Figure 3.3-2. Schematic representation of a fuel cell and battery hybrid power system.

The HPSys simulation will be used for real-time HiL dynamic testing to evaluate and validate high performance HPSys designs, stacks, balance of plant (BOP) components, and control strategies for naval applications.



### 3.3.2 Technical Accomplishments

#### HiL Development

The HiL project involves the development of a real-time simulation system using a commercially available real-time program and platform (Matlab/Simulink environment and xPC Target Platform). This project consists of running a fuel cell system simulation with a real fuel cell, or stack, using our dynamic-response test stand. During this reporting period, the following main objectives were achieved:

Upgrade of the dynamic HiL fuel cell test stand to permit the testing of small fuel cell stacks. The upgraded HiL fuel cell test stand has the capability of testing both a fuel cell and stack, and achieving dynamic response in the 50-100 millisecond (ms) range. This capability enabled us to test the fuel cell and stacks under realistic dynamic conditions equivalent to what a cell or stack would experience when operated under dynamic transient conditions. A 96-cell monitoring system was also developed and installed. The cell monitoring system supports fast, dynamic HiL real-time testing and features a system of 16-channel modules having up to 240 channels with all channels truly differential and simultaneously sampled. The cell monitoring system will be used to observe the behavior of the individual cell during HiL dynamic simulation test and protect the stack from damage.

The dynamic HiL fuel cell test stand has following specifications:

1. Stack testing up to 5 kW<sub>e</sub> ( EL100 – 100 V/150 A range);
2. Cell testing up to 1 kW<sub>e</sub> ( EL10 – 10 V/220 A range);
3. H<sub>2</sub> MFC with a flowrate range of 0-20 slpm;
4. Air and O<sub>2</sub> MFC with a flowrate range of 0-50 slpm;
5. Low-range O<sub>2</sub> MFC with a flowrate range of 0.01-0.5 slpm;
6. True-Data EIS, impedance spectrum analyzer, for a fuel cell; and
7. Real-time HiL and dynamic testing capability with a response time of 50-100 msec.

The capability of the upgraded HiL fuel cell test stand was demonstrated to visitors during the October 2008 Ion Tiger UAV review meeting held in Honolulu, Hawaii. ONR and NRL personnel were in attendance. The demonstration included the real-time running of an HPSys (Battery and PEMFC) simulator with a Protonex stack and mission power profile provided by NRL.

#### Simulation Tool Development

A fuel cell and battery hybrid power system (HPSys) simulation tool was developed in Matlab/Simulink environment (Figure 3.3-3) during this reporting period. The simulation tool is capable of evaluating fuel cell systems for propulsion of a UAV. The simulation tool is modular in its structure, which allows different components to be added and different fuel cell system configurations to be constructed. The tool has also the flexibility to size up components, apply different operational and control strategies, and test under different load profiles. The simulation tool also has the capability of converting into real time and being used in HiL testing of the simulated fuel cell system with one or many actual hardware components of the system (e.g., a stack by itself or the combination of stack, air blower, and external humidifier).



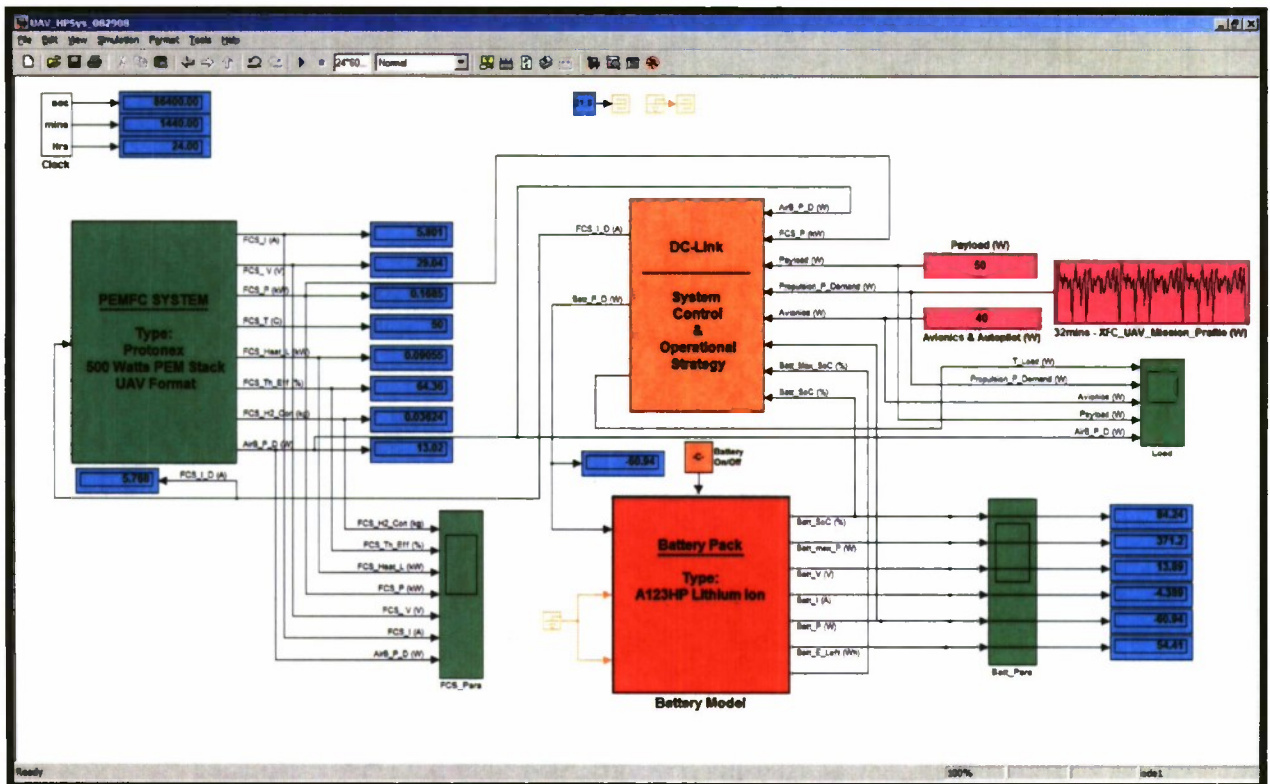


Figure 3.3-3. HPSys simulation in the Matlab/Simulink environment.

### 3.3.3 Papers and Presentations Resulting from Efforts

#### PAPERS

M.B.V. Virji, P.L. Adcock, R.M. Moore, J.B. Lakeman, "Modelling and Simulation of an Indirect Diesel Proton Exchange Membrane Fuel Cell (PEMFC) System for a Marine Application," *Fuel Cell Science and Technology*, Vol. 4, Page 481, November 2007.

R.M. Moore, G. Randolph, M. Virji, and K.-H. Hauer, "Fuel Cell Hardware-in-Loop for PEM Fuel Cell Systems", *Electrochemical Society Transactions – 30<sup>th</sup> Fuel Cell Seminar*, Vol. 5, Issue 1, pp. 309-319, March 2007.

R.M. Moore, K.H. Hauer, G. Randolph, and M. Virji, "Fuel cell evaluation for dynamic applications", *Electrochemical Society Transactions*, v. 3, Issue 1, pp. 923-930, October-November 2006.

R.M. Moore, S. Ramaswamy, J.M. Cunningham, and K.H. Hauer, "A Dynamic Simulation Tool for the Battery-Hybrid Hydrogen Fuel Cell Vehicle," *Fuel Cells—From Fundamentals to Systems*, n. 5, pp. 387-402, October 2006.

R.M. Moore, K.H. Hauer, and S. Ramaswamy, "Energy Utilization and Efficiency Analysis for Hydrogen Fuel Cell Vehicles," *Journal of Power Sources*, Vol. 159, Issue 2, 22 September 2006, pp. 1214-1230.

## PRESENTATIONS

M. Virji, "Fuel Cell Hardware-in-Loop Development and Real Time Fuel Cell Vehicle Simulation," Fuel Cell Seminar, San Antonio, TX, October 15-19, 2007.

R.M. Moore, G. Randolph, M. Virji, K.H. Hauer, "Fuel Cell Based Hardware-in-Loop for PEMFC Systems", 2006 Fuel Cell Seminar, Honolulu, Hawaii, 13-17 November 2006.

R.M. Moore, K.H. Hauer, G. Randolph, M. Virji, "Fuel Cell Evaluation for Dynamic Application," Presentation for the Oral Presentation in Section B (Fuel Cell Systems, Cell Stack and Component Hardware) of the "Proton Exchange Membrane Fuel Cells 6" Seminar at ECS 210, 29 October – 3 November 2006, Cancun, Mexico.





## **3.4 Fuel Processing and Gas Conditioning for Hydrogen Production**

### **Subtask 3.4.1: Sulfur Removal from Fuel Gas at Ambient Temperature**

#### **3.4.1.1 Absorptive Removal of Tetrahydrothiophene (THT) from Synthetic Natural Gas on Modified Activated Carbons**

##### **3.4.1.1.1 Scope of Work and Approach**

Recently, fuel cells have attracted much interest as an environmentally friendly conversion technology in which hydrogen and oxygen are converted into water while producing electricity. One strategy for fuel cell applications is to convert pipelined natural gas to hydrogen using a series of fuel processing steps including fuel reforming, water gas shift reaction, and selective CO oxidation. In this process, sulfur compounds present in the fuel gas can cause severe deactivation of reforming catalysts and fuel cell anodes, even at very low concentration. For example, a gas feed containing 5 ppm of tetrahydrothiophene (THT) would produce reformat containing approximately 1 and 2 ppm of  $\text{H}_2\text{S}$  and this concentration is high enough to adversely affect the performance of proton exchange membrane (PEM) fuel cells [1]. Thus, desulfurization is an essential unit operation in fuel processing for fuel cells applications.

The odorants and the other sulfur compounds present in pipeline gas can be removed by adsorption on activated carbons [2, 3]. Adsorption is regarded as a more effective method for deep desulfurization and can be performed at ambient temperature. In general, the adsorption of sulfur compounds on activated carbons can be classified as either physical adsorption or chemisorption, based on the interaction of the sulfur bearing molecule with the carbon surface.

Physical adsorption is characterized by van der Waals or dispersion forces which are weak intermolecular interactions arising from dipole-dipole or induced dipole attractions. Physical adsorption approaches equilibrium very rapidly and is generally reversible if the vapor pressure of the adsorbate is reduced. Hysteresis may result due to the pore structure of the sorbent. The heat evolved during adsorption is similar to a condensation process, being in the range 4 to 40  $\text{kJ mol}^{-1}$ , and as a result, is assumed to happen very quickly. Due to the long range nature of the attractive forces, physical adsorption may form several layers of adsorbed gas molecules on the solid surface. As the number of layers increases, the adsorption process approaches one of condensation. In activated carbons, adsorptive capacity is affected by pore size and distribution and the number of active sites on the surface [4, 5].

In contrast to physical adsorption, chemisorptive interaction between the solid surface and the adsorbed molecule is much stronger. Chemisorption is mainly responsible for gas-solid reactions and catalysis, and displays chemical specificity, i.e., is particular to the solid and gas species in terms of chemical forces and orientation. These requirements suggest that chemisorption can only occur as a monolayer. The forces involved between participants are of the same order as those in chemical reactions, with the heat of chemisorption being 40 to 600  $\text{kJ mol}^{-1}$ . As a result, chemisorption may be slow and display rate behavior characteristic of processes possessing an activation energy. Gases which have been chemisorbed may be difficult to remove and may leave the surface altered, as in the case of oxygen adsorbed onto solid carbon which is desorbed as CO or  $\text{CO}_2$ . With activated carbons, the surface chemical properties, particularly the presence of different functional groups and metal ions, affect the adsorptive capacity [4, 5].

To increase the adsorptive capacity of activated carbons, surface modification by oxidation [6] or metal impregnation [7, 8] has been investigated. These methods can improve the sulfur capacity of the parent material by creating additional acid groups and adsorption sites on the surface of activated carbons [6, 9, 10]. It was found that  $\text{HNO}_3/\text{H}_2\text{SO}_4$  solutions can form acidic groups on the carbon surface, which interact with thiol groups by hydrogen bonding to enhance their sorption capacity [11]. Impregnation of  $\text{CuCl}_2$  on activated carbon was reported by Kim and Yie [12]. They found that impregnated  $\text{CuCl}_2$  led to a notable decrease in microporosity of the activated carbon, but enhanced the adsorption capacity of methyl mercaptan (MM), indicating that  $\text{CuCl}_2$  may act as adsorption sites for MM. Besides activated carbons, zeolite-based sorbents modified with transition metals have also shown improved adsorption capacity for sulfur compounds. These transition metals, i.e., copper, zinc and silver, were regarded as active materials to adsorb sulfur compounds under ambient conditions [13-15]. This earlier work addresses the adsorption of sulfur compounds at ambient temperatures by surface modification of activated carbons using acid oxidation or metal impregnation. Information on the effect of impregnated metals on the surface features is still lacking. These techniques may influence the mechanism of adsorption of sulfur compounds on the activated carbons, and potentially, the sulfur adsorption capacity.

Tetrahydrothiophene (THT) is a heterocyclic organic compound consisting of a five-membered ring containing four carbon atoms and one sulfur atom. It is a volatile, clear, colorless liquid with a strong unpleasant odor. THT can be used as an odorant in pipeline gas, such as natural gas, city gas or town gas. In Honolulu, synthetic natural gas (SNG) is produced from naphtha and THT is used as an odorant for leak detection. SNG is distributed via pipeline by The Gas Company. Studies on adsorptive removal of gas-phase sulfur compounds have been conducted [16] to utilize the pipeline gas as a reforming feedstock for hydrogen production use in fuel cells.

An objective of this paper is to describe the adsorption of tetrahydrothiophene (THT) present in SNG on activated carbons that have undergone surface modification by oxidation or impregnation to improve adsorption capacity. The purpose is to identify the adsorption mechanism of sulfur compound THT on the modified surface of activated carbons.

#### **3.4.1.1.2 Experimental**

***Synthetic natural gas (SNG) composition.*** Synthetic natural gas (SNG) is produced from petroleum and distributed via pipeline in Honolulu by The Gas Company. SNG is composed of methane ( $\text{CH}_4$ ), hydrogen ( $\text{H}_2$ ), nitrogen ( $\text{N}_2$ ), carbon monoxide ( $\text{CO}$ ), carbon dioxide ( $\text{CO}_2$ ), water vapor ( $\text{H}_2\text{O}$ ), trace amounts of higher hydrocarbons, and sulfur compounds. The detectable sulfur compounds, which are either naturally present or added intentionally as odorants, are hydrogen sulfide ( $\text{H}_2\text{S}$ ), methyl mercaptan (MM), ethyl mercaptan (EM), dimethyl sulfide (DMS), dimethyl disulfide (DMDS), tetrahydrothiophene (THT), ethyl disulfide (EDS), and an additional, as yet unidentified, compound. Among these sulfur compounds, THT is added as an odorant and was present in the highest concentration, contributing roughly 75% in the total sulfur content. The gas composition and sulfur speciation analyses are presented in Tables 3.4.1.1-1 and 3.4.1.1-2, respectively.



**Table 3.4.1.1-1. Pipeline gas composition.**

Component	Quantity
Methane	79-84%
Hydrogen	9-10%
Carbon dioxide	3-5%
Carbon monoxide	0.25-0.4%
Water *	0.24-0.32 g/m <sup>3</sup>
Ethane *	0-0.01%
Propylene *	0%
Propane *	0.03-0.5%
n-Butane *	1.5-4%
i-Butane *	1.5-3%
n-Pentane *	0.25-0.75%
i-Pentane *	0.5-1%
neo-Pentane *	0-0.05%
C6+ *	0-0.1%
Tetrahydrothiophene **	0.004%
C2+ **	3.78-9.41%

\*From The Gas Company Analysis Report of January 2000

\*\*From The Gas Company Data Sheet of November 1998

**Table 3.4.1.1-2. Sulfur speciation analysis in the pipeline gas.**

Component	Quantity, ppm
H <sub>2</sub> S	0.06-0.15
Methyl mercaptan	0.05-0.13
Ethyl mercaptan	0.1-0.4
Dimethyl sulfide	0.06-0.22
Dimethyl disulfide	0.07-0.23
Tetrahydrothiophene	4.2-7.8
Ethyl disulfide	0.13-0.18
Unknown species	0.3-1.0

**Sorbent evaluation and sulfur compounds analysis.** A sorbent column was constructed from a stainless steel pipe 45.7 cm in length and 2.43 cm in inner diameter. All of the components including the sorbent column and gas delivery lines were treated with a Sulfinert<sup>®</sup> coating or were made from Teflon<sup>®</sup> to prevent sulfur compounds from being adsorbed on the working surfaces of the system. A Teflon<sup>®</sup> insert with an inner diameter of 1.2 cm was packed with carbon and placed in the column.

A 4.0 gram mass of sorbent was tested in all cases. The sorbent bed was about 8 cm long with the major axis oriented vertically. To distribute the flow evenly, 3 mm layers of 3 mm diameter



glass beads were packed into the column below and above the sorbent. SNG was supplied to the carbon column from a laboratory gas service valve at a flow rate of 4.0 - 4.5 l/min using a pump. After the SNG passed through the carbon column it was analyzed with a gas chromatograph (GC).

The concentrations of sulfur species were measured with a Shimadzu 2041 GC equipped with a capillary column (Rtx-1, 60m-0.53-7 $\mu$ m, Restek Corporation) and sulfur chemiluminescent detector (SCD) (Sievers Model 355). Helium (He) served as carrier gas and a six-port sampling valve was used to make automatic injections. A permeation tube device (Model 355, Kin-Tek Laboratories) loaded with a THT permeation tube was used to calibrate.

In each analysis the column temperature was held for 1 min at 50°C, ramped to 125 °C at 20 °C/min, ramped again to 180 °C at 10 °C/min, held at 180 °C for 1 min and finally cooled to 50 °C at 100 °C/min. Thus, effluent gas was sampled and analyzed with a cycle time of 13 min. In addition, sulfur compounds present in SNG were analyzed from a by-pass path before and after the sorption test, to verify stable operation of the system. Tests typically lasted 10 hours.

The sulfur adsorption capacity of carbon sorbents was determined by breakthrough testing. The breakthrough point is defined as the first detection of THT at a concentration  $\geq 0.2$  ppm. The sulfur capacity was calculated by using the following equation:

$$S_{cap} (mg / g) = \frac{Q(l / min) \times t(min) \times S_{conc} (ppm) \times 32000 (mg / mol)}{22.4(l / mol) \times m_{sorb} (g) \times 10^6} \quad (1)$$

where,  $S_{cap} (mg/g)$ : the sulfur capacity in milligram elemental sulfur per gram sorbent;  $Q(l/min)$ : SNG flow rate;  $t(min)$ : breakthrough time;  $S_{conc} (ppm)$ : total sulfur concentration in SNG for all sulfur compounds;  $m_{sorb} (g)$ : mass of sorbent tested; and 32000 (mg / mol), 22.4(l / mol), and  $10^6$  are sulfur molar weight, molar volume of ideal gas, and unit conversion from ppm to molar concentration, respectively.

**Modification of activated carbons.** A coconut shell activated carbon (OLC Plus 12x30, Calgon Carbon Corporation) was used as the parent material for all samples modified by oxidation and impregnation.

In the oxidation, carbon was prepared by mixing 40 g of the virgin activated carbon (AC) with 70 ml of 68-70% HNO<sub>3</sub> or 100 ml of 50% H<sub>2</sub>O<sub>2</sub> at room temperature until there was no further gas evolution. The sample was washed with distilled water until no further change in pH was detected (around pH = 5), and then dried overnight in an oven at 115 °C.

Virgin carbon was impregnated by immersing 40 gram in a 0.1N solution of the selected metal at 70-80 °C for 6 hours. The modified carbon was then dried at 115 °C overnight. The selected metal impurities were from the Zn group (Zn(NO<sub>3</sub>)<sub>2</sub> and ZnAc<sub>2</sub>), Cu group (Cu(NO<sub>3</sub>)<sub>2</sub> and CuSO<sub>4</sub>), Fe group (FeCl<sub>3</sub>), K group (AC-KMnO<sub>4</sub>, KCl, KOH and K<sub>2</sub>CO<sub>3</sub>), and Na group (NaOH and Na<sub>2</sub>CO<sub>3</sub>). The loaded amount was around 0.40 mmol metal per gram virgin activated carbon except as noted. A composite sorbent was prepared based on carbon oxidized by HNO<sub>3</sub> (AC-HNO<sub>3</sub>) with FeCl<sub>3</sub> loading at varied contents, which was denoted as AC/HNO<sub>3</sub>-FeCl<sub>3</sub>. The names and preparation conditions for these carbon sorbents are in Table 3.4.1.1-3.

**Table 3.4.1.1-3. Carbons name and preparation conditions.**

<b>Carbons name</b>	<b>Solution / Concentration / Volume, ml</b>	<b>Ions loaded, mmol / g, AC</b>
<b>Treated with oxidizer</b>		
AC-HNO <sub>3</sub>	HNO <sub>3</sub> / 50% / 100	-
AC-H <sub>2</sub> O <sub>2</sub>	H <sub>2</sub> O <sub>2</sub> / 70% / 70	-
AC-KMnO <sub>4</sub>	KMnO <sub>4</sub> / 0.155 M / 40	-
<b>Impregnated with Cu</b>		
AC-CuSO <sub>4</sub>	CuSO <sub>4</sub> / 0.101N / 150	0.38
AC-Cu(NO <sub>3</sub> ) <sub>2</sub> -38	Cu(NO <sub>3</sub> ) <sub>2</sub> / 0.142N / 106	0.38
AC-Cu(NO <sub>3</sub> ) <sub>2</sub> -53	Cu(NO <sub>3</sub> ) <sub>2</sub> / 0.142N / 150	0.53
<b>Impregnated with Zn</b>		
AC-ZnAc <sub>2</sub> <sup>#</sup>	ZnAc <sub>2</sub> / 0.099N / 150	0.37
AC-Zn(NO <sub>3</sub> ) <sub>2</sub>	Zn(NO <sub>3</sub> ) <sub>2</sub> / 0.106N / 150	0.40
<b>Impregnated with Fe</b>		
AC-FeCl <sub>3</sub>	FeCl <sub>3</sub> / 0.099N / 150	0.37
<b>Impregnated with Na</b>		
AC-NaOH	NaOH / 1.006N / 15	0.38
AC-Na <sub>2</sub> CO <sub>3</sub>	Na <sub>2</sub> CO <sub>3</sub> / 0.753N / 19.9	0.37
<b>Impregnated with K</b>		
AC-KOH	KOH / 0.099N / 150	0.37
AC-K <sub>2</sub> CO <sub>3</sub>	K <sub>2</sub> CO <sub>3</sub> / 0.101N / 150	0.38
AC-KCl	KCl / 0.099N / 150	0.37
<b>Treated with oxidizer/ Impregnated with Fe</b>		
AC/HNO <sub>3</sub> -FeCl <sub>3</sub> -37	HNO <sub>3</sub> / 50% / 100, FeCl <sub>3</sub> / 0.099N / 150	0.37
AC/HNO <sub>3</sub> -FeCl <sub>3</sub> -70*	HNO <sub>3</sub> / 50% / 100, FeCl <sub>3</sub> / 0.099N / 140	0.70
AC/HNO <sub>3</sub> -FeCl <sub>3</sub> -105*	HNO <sub>3</sub> / 50% / 100, FeCl <sub>3</sub> / 0.099N / 210	1.05

<sup>#</sup>: ZnAc<sub>2</sub> is denoted as zinc acetate

\*: The modification was based on 20 gram of virgin activated carbon.

**Characteristics of carbon sorbents.** Nitrogen (liquid N<sub>2</sub>) adsorption/desorption isotherms for the samples were measured at 77 K (Autosorb<sup>®</sup>-1, Quantachrome Instruments, Boynton Beach, FL). Before the experiments the samples were first heated and degassed at 110 °C for 2 hours under a vacuum of 10<sup>-5</sup> torr (1.33×10<sup>-7</sup> Pa). Specific surface area (S<sub>BET</sub>) was calculated by using the multipoint BET method in the relative pressure (P/P<sub>0</sub>) range of 0.01-0.1; the total pore volume (V<sub>0</sub>) and the average pore diameter (D<sub>ave</sub>) were calculated from the amount of gas adsorbed at



related pressure of 0.995-0.999. In addition, density functional theory (DFT) was used to analyze the pore structure parameters, such as micropore volume ( $V_{\text{micro}}$ , pore width less than 2 nm), total pore volume ( $V_{\text{total}}$ , pore width less than 36 nm), and mode pore width ( $D_w$ ). The DFT calculation method is provided from the instrument data process software, and assumes that the activated carbon contains slit-shaped pores.

The surface morphology and elemental mapping of the carbons was conducted using a scanning electron micrograph (Zeiss DSM926, Germany) equipped with energy dispersive x-ray spectroscopy detector (Oxford 6533) at an accelerating voltage of 20 kV.

Carbon suspension provides useful information about the overall surface functional properties. The value indicates the average acidity/basicity of carbon sample. In this study, a 0.4 g sample of carbon was placed in 20 ml distilled water and equilibrated overnight and the pH of the suspension was measured by pH detector (Orion, Model 290A) [10].

#### 3.4.1.1.3 Technical Accomplishments

**Evaluation of carbon sorbents by adsorption capacity of THT.** The performance of each carbon sorbent was evaluated by breakthrough testing using SNG from the utility gas service available in the laboratory. Figure 3.4.1.1-1 presents the breakthrough curves for each carbon sorbent included in the study. Note that the volume of SNG has been normalized by the mass of activated carbon sorbent in the test sample to provide a common basis for comparison. For simplification, Figure 3.4.1.1-1(a) presents the breakthrough curves for carbons modified by oxidizers and Figure 3.4.1.1-1(b) presents similar data for carbons modified by impregnation.

Apparently, the modification method strongly influenced the adsorption capacity of THT on the carbons. Long-term monitoring of THT indicates that the laboratory SNG supply is not constant, varying between 4.2-7.8 ppm as listed in Table 3.4.1.1-3. Thus it is not possible to use Figure 3.4.1.1-1 as a quantitative evaluation for carbon sorbent performance. To eliminate the effects of varied experimental conditions, such as SNG flow rate, THT concentration during the test period, and sample size, Equation 1 was used to calculate the THT capacity of virgin and modified activated carbons and results are presented in Figure 3.4.1.1-2 on the basis of elemental S (mg) adsorbed per gram of sorbent.

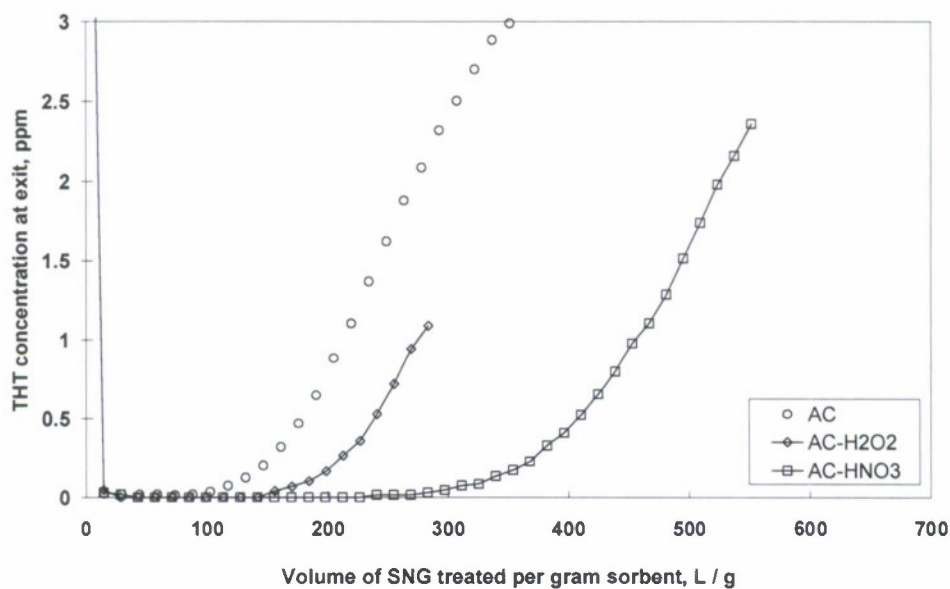
Virgin carbon (AC) had an uptake capacity of 0.91 mg S/g of sample, AC-FeCl<sub>3</sub>, AC-HNO<sub>3</sub> and their composite AC/HNO<sub>3</sub>-FeCl<sub>3</sub> had the highest THT capacity with 2.4 mg/g, 3.43 mg/g and 4.24 mg/g, respectively. Three carbons, AC-ZnAc<sub>2</sub>, AC-K<sub>2</sub>CO<sub>3</sub> and AC-KCl, had a THT capacity less than that of AC. All other carbons had increased capacities; however, some only marginally so. In general, activated carbons treated with oxidizers had increased THT capacity and were ranked according to increasing performance in the following order: H<sub>2</sub>O<sub>2</sub> and HNO<sub>3</sub>. Metal impregnated carbons did not display a clear performance enhancement trend. By comparing with the THT capacity of modified samples with virgin carbon AC, the modified carbons can be classified into the following three categories: Group 1, 0.6-1.5 mg S per gram sample; Group 2, 1.5-2.5 mg S per gram sample; and Group 3, more than 2.5 mg S per gram sample.

Group 1: Negative or minor effect carbons, AC-ZnAc<sub>2</sub>, AC-K<sub>2</sub>CO<sub>3</sub>, AC-KCl, AC-KOH and AC-NaOH;

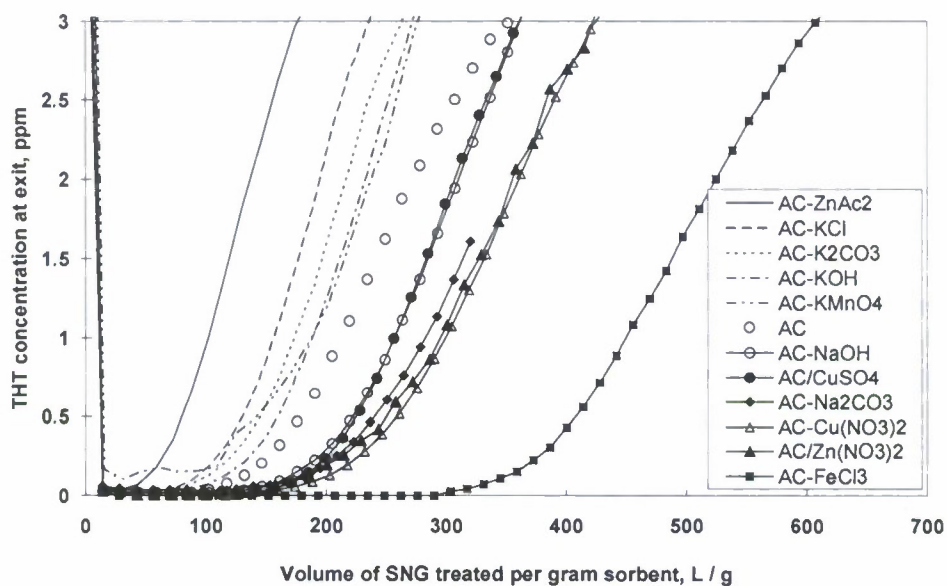
Group 2: Effective carbons, AC-KMnO<sub>4</sub>, AC-CuSO<sub>4</sub>, AC-Na<sub>2</sub>CO<sub>3</sub>, AC-Cu(NO<sub>3</sub>)<sub>2</sub>, AC-H<sub>2</sub>O<sub>2</sub>, and AC-Zn(NO<sub>3</sub>)<sub>2</sub>; and



Group 3: Major effective carbons, AC-FeCl<sub>3</sub>, AC-HNO<sub>3</sub> and AC/HNO<sub>3</sub>-FeCl<sub>3</sub>.



(a)



(b)

Figure 3.4.1.1-1. Breakthrough curves of THT for modified activated carbons; (a) oxidized activated carbons; (b) impregnated activated carbons with equal metal loadings.

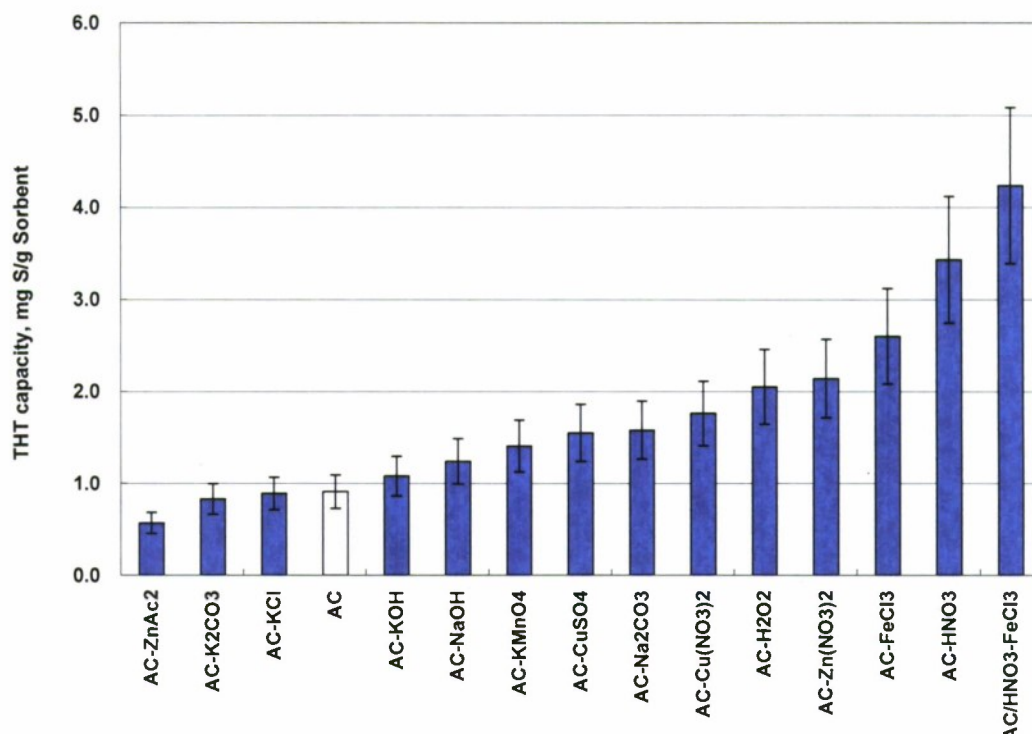
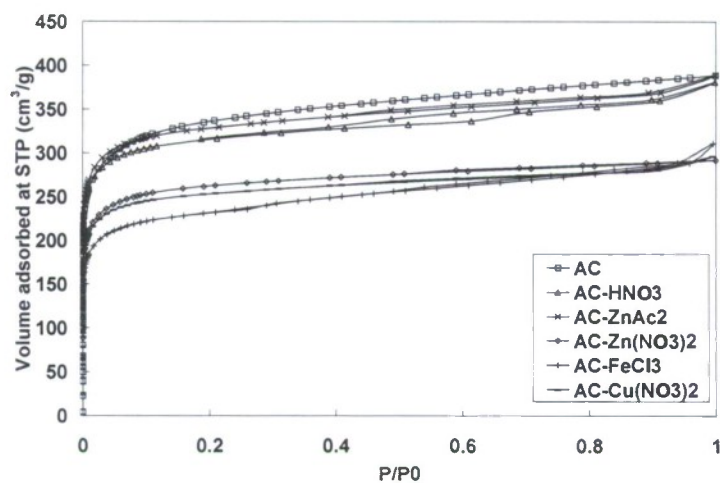


Figure 3.4.1.1-2. THT adsorptive capacities of virgin and modified activated carbons (note that metal loadings are equal for all samples).

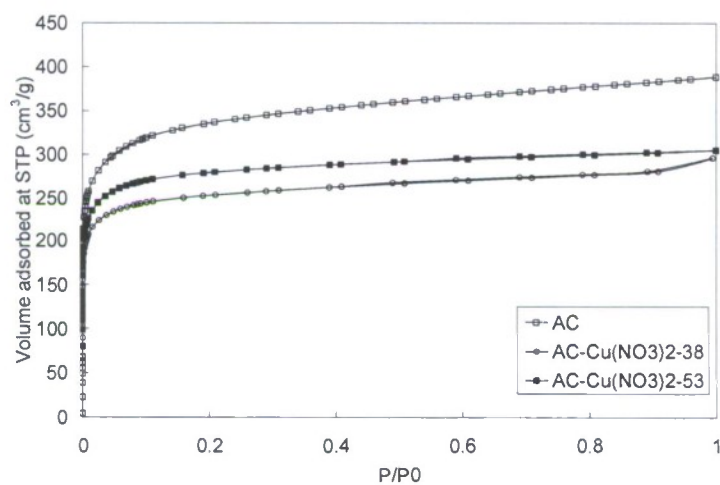
**Effect of modification on the physical characteristics of carbons surface.** The effects of the modification on the physical surface characteristics the Group 2 carbon sorbents were investigated. Information on the pore structure of activated carbon includes characterizations of the surface area, pore volume, pore size and distribution. Figures 3.4.1.1-3 and 3.4.1.1-4 show the isotherms and pore size distribution obtained for the virgin and selected modified activated carbons.

Figure 3.4.1.1-3(a) presents the effect of loaded metal types on the isotherms. The selected modified carbon sorbents are AC-Zn(NO<sub>3</sub>)<sub>2</sub>, AC-ZnAc<sub>2</sub>, AC-Cu(NO<sub>3</sub>)<sub>2</sub>, AC-HNO<sub>3</sub> and AC-FeCl<sub>3</sub>, which are in Group 2 and 3 except for AC-ZnAc<sub>2</sub>. Figures 3.4.1.1-3(b) and (c) illustrate the effect that varied amounts of metal loaded on the activated carbon has on the isotherms for the sorbents AC-Cu(NO<sub>3</sub>)<sub>2</sub> and AC/HNO<sub>3</sub>-FeCl<sub>3</sub>, respectively. All of the adsorption isotherms are shown be similar and close to type I of the IUPAC classification, which is typical of microporous activated carbons. Moreover, the N<sub>2</sub> isotherms of these carbons also show the H4 type hysteresis loop indicating the presence of slit-shaped pores with narrow pore size distribution. Based on these isotherms, the pore size distributions were calculated using the DFT equilibrium model and are shown in Figure 3.4.1.1-4.

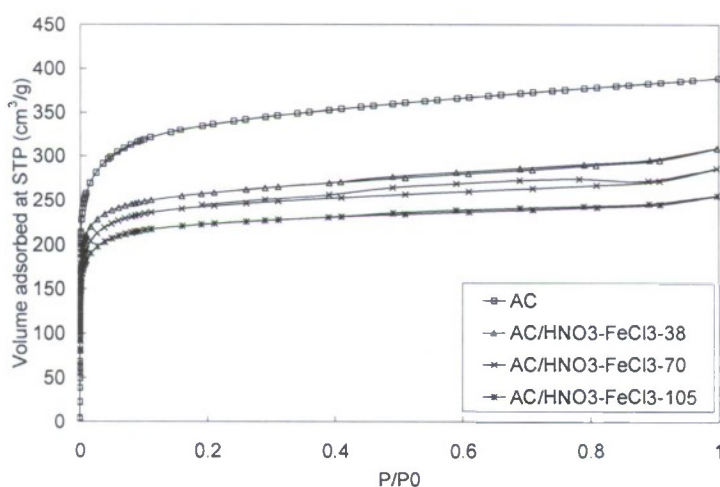
It was found that the metal loading and oxidation did not change either the N<sub>2</sub> adsorption isotherms (Figure 3.4.1.1-3) or the pore size distribution (Figure 3.4.1.1-4) to a great extent. All samples possess primarily micropores, which according to the IUPAC classification have widths below 20 Å (2 nm).



(a)



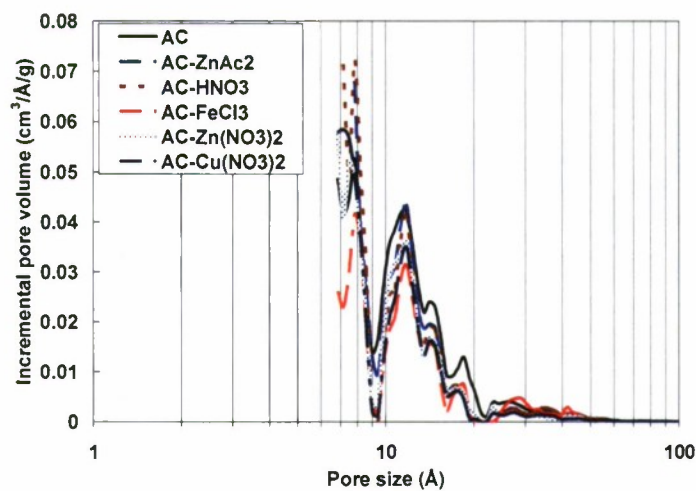
(b)



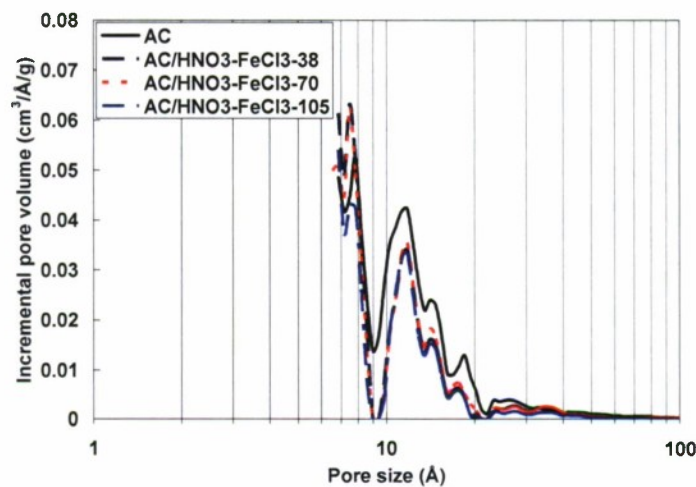
(c)

Figure 3.4.1.1-3. Nitrogen adsorption isotherms for the virgin and modified activated carbons.

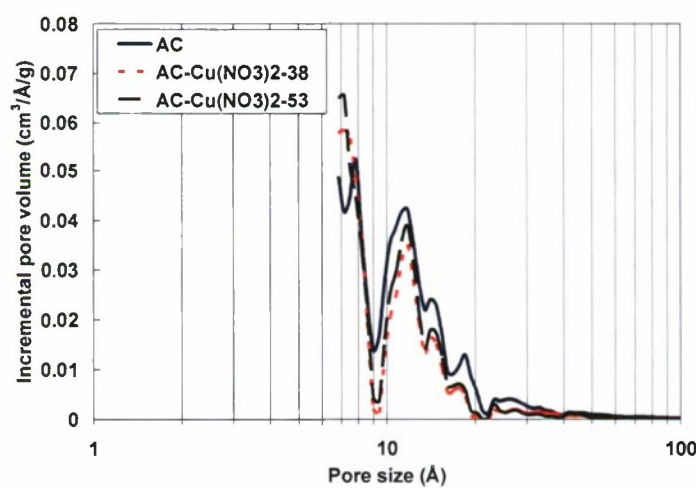




(a)



(b)



(c)

**Figure 3.4.1.1-4. DFT micropore size distribution for virgin and modified activated carbons.**

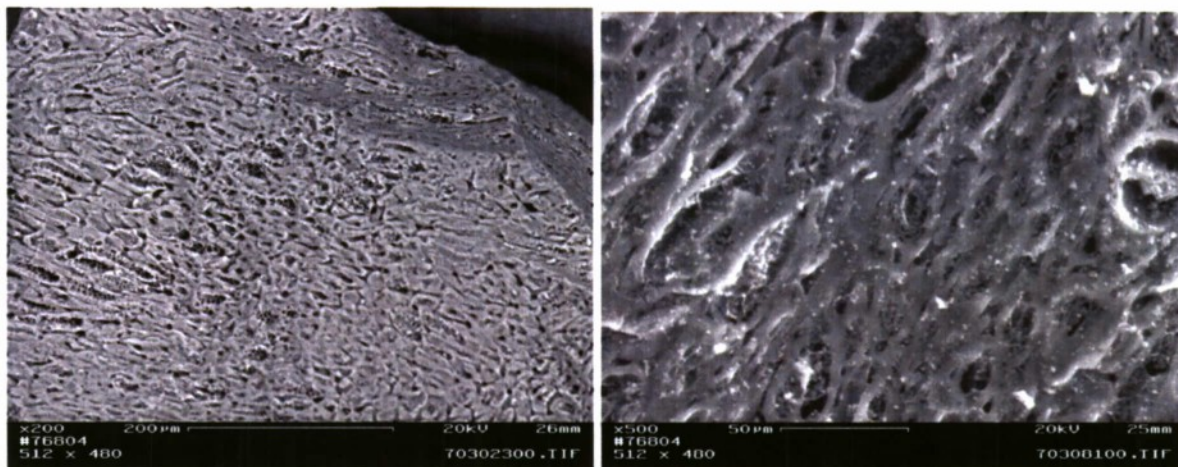
Parameters calculated from adsorption isotherms for test carbons are shown in Table 3.4.1.1-4. It was expected that impregnated carbons would have reduced surface area and pore volume, but the pore structure parameters varied widely for different impregnation metals. Pore structure parameters for AC-ZnAc<sub>2</sub> show 15% reductions in  $S_{\text{BET}}$  and  $V_0$  values compared to virgin carbon, indicating that ZnAc<sub>2</sub> impregnated on the carbon had a minimal effect on pore characteristics. This may be due to poor dispersion of ZnAc<sub>2</sub> on the carbon surface. The other impregnated carbons, such as AC-Zn(NO<sub>3</sub>)<sub>2</sub>, AC-Cu(NO<sub>3</sub>)<sub>2</sub>, AC-FeCl<sub>3</sub> and AC/HNO<sub>3</sub>-FeCl<sub>3</sub>, exhibited 20-30% reductions in surface area ( $S_{\text{BET}}$ ) and total pore volume ( $V_0$ ) and a 75-80% reduction in average pore diameter ( $D_{\text{ave}}$ ). DFT micro pore volume ( $V_{\text{micro}}$ ) and total volume ( $V_{\text{total}}$ ) of these samples were reduced 15-20% compared to the parent activated carbon (AC). The data indicate that the carbon surfaces were covered by loaded metals. Greater metal loading resulted in reduced pore volume and surface area for the three samples derived from AC/HNO<sub>3</sub> loaded with varied amounts of FeCl<sub>3</sub> [Figure 3.4.1.1-3(b) & 3.4.1.1-4(b)], but this trend was not observed for the AC-Cu(NO<sub>3</sub>)<sub>2</sub> samples [Figure 3.4.1.1-3(c) & 3.4.1.1-4(c)]. An interpretation of these results is non-uniformity in the samples or the dispersion of the metals on the samples.

Comparison of the pore structure of the parent material (AC) with the activated carbon oxidized by HNO<sub>3</sub> (AC-HNO<sub>3</sub>) shows little difference. This does not support the assertion by Figueiredo [6] that the carbon porous structure could be destroyed by strong oxidative effects such as those produced by HNO<sub>3</sub>.

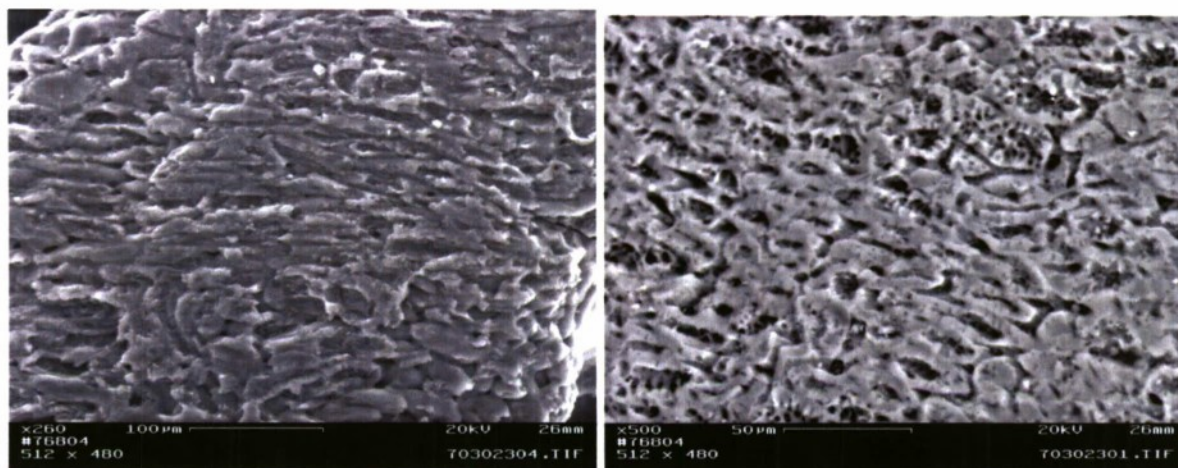
The surface morphologies of the virgin and modified carbons were investigated by SEM and photos of the sample surfaces are shown in Figure 3.4.1.1-5. In comparison to virgin carbon AC [Figure 3.4.1.1-5(a)], AC-HNO<sub>3</sub> [Figure 3.4.1.1-5(b)] has a smoother surface without visible presence of small surface particles, due to the acid treatment and water rinse. Small particles are distributed across the surface of impregnated carbons, with particle shapes varying with the type of metal loaded on the sample [Figure 3.4.1.1-5(c) to 3.4.1.1-5(f)]. For the AC-Zn(NO<sub>3</sub>)<sub>2</sub> sample [Figure 3.4.1.1-5(c)], almost all particles are rectangular in shape and roughly 1  $\mu\text{m}$  in size. These particles are of uniform size and are evenly dispersed on the carbon surface. In comparison, AC-ZnAc<sub>2</sub> [Figure 3.4.1.1-5(d)] is less uniformly distributed and with a variety of particle shapes and the appearance of irregularly shaped agglomerates. These kinds of particle could be the result of poor dispersion on the carbon surface and could be easily removed from the surface. This could be a contributing factor for the observed weak effect that ZnAc<sub>2</sub> impregnation had on the pore structure parameters of activated carbon. The particles deposited on the surface of AC-Cu(NO<sub>3</sub>)<sub>2</sub> [Figure 3.4.1.1-5(e)] have needle shapes of uniform size and are well dispersed. The AC-FeCl<sub>3</sub> sample [Figure 3.4.1.1-5(f)] is characterized by well dispersed deposited particles with irregular shape. The impregnation technique used this study resulted in varied dispersion of the selected metals on the carbon surface and this contributed to the observed differences in pore structure for the modified activated carbons.

***Relationship between the surface characteristics and THT adsorption capacity.*** THT is a saturated molecule that is less reactive, more polar, and more basic than thiophenes, in which neither of the sulfur lone electron pairs is engaged in aromatic  $\pi$ -electron system [17]. Therefore, THT molecule can adhere to the surface through van der Waals force or weak hydrogen bonds between THT and functional groups. Thus it is normally expected that the activated carbons have a higher adsorption capacity when greater numbers of acidic functional groups are available on the carbon surfaces.

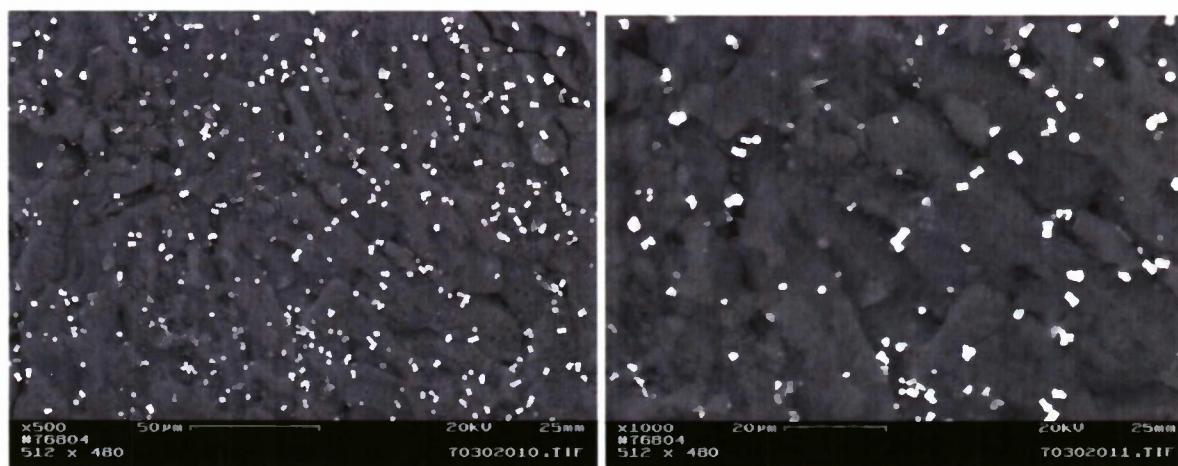




a. AC



b. AC-HNO<sub>3</sub>



c. AC-Zn(NO<sub>3</sub>)<sub>2</sub>

Figure 3.4.1.1-5. SEM pictures for virgin carbon and modified carbons.



PCL XL error

Subsystem: USERSTREAM

Error: MissingData

Operator: Text

Position: 120152

# **FINAL TECHNICAL REPORT**

## **Hawaii Energy and Environmental Technologies (HEET) Initiative**

**Office of Naval Research**

**Grant Award Number N00014-06-1-1055**

**For the period September 14, 2006 to December 31, 2008**

**Hawaii Natural Energy Institute**



**School of Ocean and Earth Science and Technology  
University of Hawaii at Manoa**

**May 2009**





## Table of Contents

<u>Section No.</u>	<u>Section Title</u>	<u>Page</u>
1	Executive Summary	1
2	Introduction	5
3	Fuel Cell Systems	7
3.1	Objectives	7
3.2	PEM Fuel Cell Testing and Component Development	7
3.2.1	Test stands/Infrastructure Upgrades	7
3.2.2	Cell and Component Testing	8
3.2.3	MEA Fabrication Laboratory	14
3.2.4	Papers and Presentations Resulting from Efforts	14
3.3	Fuel Cell Hardware-in-Loop and System Simulation Development	17
3.3.1	Scope of Work and Approach	17
3.3.2	Technical Accomplishments	19
3.3.3	Papers and Presentations Resulting from Efforts	20
3.4	Fuel Processing and Gas Conditioning for Hydrogen Production	23
3.4.1	Sulfur Removal from Fuel Gas at Ambient Temperature	23
3.4.1.1	Absorptive Removal of Tetrahydrothiophene from Synthetic Natural Gas on Modified Activated Carbons	23
3.4.1.1.1	Scope of Work and Approach	23
3.4.1.1.2	Experimental	24
3.4.1.1.3	Technical Accomplishments	28
3.4.1.1.4	References	39
3.4.1.1.5	Paper Resulting from Efforts	40
3.4.1.2	Absorption/Desorption of Dimethylsulfide on Activated Carbon Modified with Iron Chloride	41
3.4.1.2.1	Scope of Work and Approach	41
3.4.1.2.2	Experimental	41
3.4.1.2.3	Technical Accomplishments	44
3.4.1.2.4	References	57
3.4.1.2.5	Paper Resulting from Efforts	58
3.4.2	High Pressure Autothermal Reforming in Low Oxygen Environments	59
3.4.2.1	Scope of Work and Approach	59
3.4.2.2	Experimental	61
3.4.2.3	Technical Accomplishments	64
3.4.2.4	References	79
3.4.2.5	Paper Resulting from Efforts	81
3.4.3	Plasma Reforming of Methane	83
3.4.3.1	Scope of Work and Approach	83
3.4.3.2	Experimental	84
3.4.3.2.1	Gliding Arc Reformer	85
3.4.3.2.2	Reverse Vortex Flow Reformer	86

3.4.3.3	Technical Accomplishments	87
3.4.3.4	References	89
3.5	Novel Fuel Cell and Component Development	91
3.5.1	Biocarbons for Use in Fuel Cells	91
3.5.1.1	Objectives	91
3.5.1.2	Scope of Work and Approach	91
3.5.1.3	Technical Accomplishments	92
3.5.1.4	Papers and Presentations Resulting from Efforts	92
3.5.2	Enzymatic Bio-Fuel Cells	95
3.5.2.1	Objectives	95
3.5.2.2	Scope of Work and Approach	95
3.5.2.3	Technical Accomplishments	96
3.5.2.4	References	102
3.5.2.5	Papers and Presentations Resulting from Efforts	103
4	Methane Hydrates	107
4.1	Objectives	107
4.2	Scope of Work and Approach	108
4.2.1	Hydrate Thermochemistry and Kinetics	108
4.2.2	Environmental Impacts of Methane Release from Seafloor Hydrates	108
4.2.3	Hydrate Engineering Applications	109
4.2.4	International Collaborative R&D	109
4.3	Technical Accomplishments	109
4.3.1	Methane Hydrate Destabilization	109
4.3.2	Subsea Power Generation	125
4.3.3	Environmental Impacts of Methane Release from Seafloor Hydrates	127
4.3.4	Hydrate Engineering Applications	154
4.3.5	International Collaborative R&D	159
4.4	Papers Resulting from Efforts	160
4.5	References	160

**Technical Report for the  
Hawaii Energy and Environmental Technologies (HEET) Initiative  
Grant Award Number N00014-06-1-1055  
(September 14, 2006 to December 31, 2008)**

## **1. Executive Summary**

This report summarizes work conducted under Grant Award Number N00014-06-1-1055, the Hawaii Energy and Environmental Technologies (HEET) Initiative, funded through the Office of Naval Research to the Hawaii Natural Energy Institute (HNEI) of the University of Hawaii. The work reported here continued the focus on critical technology needs associated with the development and testing of advanced fuel cells and fuel cell systems, and the exploration and utilization of seabed methane hydrates, and represents the fourth award of this initiative.

Major accomplishments under the first grant award, Number N00014-01-1-0928, included the planning, design and construction of the Hawaii Fuel Cell Test Facility (HFCTF), which opened in May 2003. In partnership with industry, HNEI established test protocols and initiated a variety of long-term durability studies. The methane hydrates activities under the first agreement initiated studies to characterize hydrate thermochemistry and kinetics, hydrate microbiology and development of international collaborations.

Under the second award (N00014-04-1-0682), HNEI expanded its test capabilities with the addition of three new fuel cell test stands at the HFCTF, including two for fuels purity studies. Tests to characterize the effects of trace amounts of benzene, toluene and carbon monoxide in the hydrogen fuel were initiated. The third stand was designed for high speed dynamic testing for use in Hardware-in-Loop (HiL) work. Testing of a 100 cm<sup>2</sup> single cell via a fuel cell vehicle simulation program was used to validate the test stand capabilities. Modeling and simulation of a fuel cell energy/power system for use in an unmanned underwater vehicle (UUV) was also completed. In addition to the FC testing, HNEI also developed an MEA (membrane electrode assembly) fabrication laboratory to support the existing fuel cell assembly laboratory. Novel fuel cell component research was continued in the areas of using biocarbons in fuel cell bipolar plates and developing enzymatic bio-fuel cells. Alternative fuel research was continued via efforts in fuel processing and gas conditioning for hydrogen production. HNEI's activities in the area of methane hydrates included studies of hydrate destabilization phenomena, with shakedown testing of HNEI's destabilization facility and design and fabrication of a novel fiberoptic probe to identify sample aspects within the calorimeter sample cell using Raman spectroscopy. HNEI sponsored and manned the organizing committee of the 4<sup>th</sup> International Workshop on Methane Hydrates that took place in Victoria, British Columbia, Canada on 9-11 May 2005.

Under the third award (N00014-06-1-0086), the capacity of the HFCTF was again expanded, increasing the total number of test stands to eight. Several of the existing test stands as well as the MEA Fabrication Laboratory were modified for increased performance. The dynamic HiL test stand was also modified to enhance response and to improve operating flexibility, safety, and test stand reliability. Simulation tools for evaluation and screening of fuel cell systems for UUV propulsion systems were developed. In the area of alternative fuel supplies, HNEI continued research on fuel processing and gas conditioning for hydrogen production. This included examination of sulfur removal from fuel gas using activated-carbon-based sorbents, and



reforming seafloor methane for use in underwater fuel cells. Work continued in the development of novel fuel cells and components, specifically in the area of biocarbons for fuel cell use and development of enzymatic bio-fuel cells. HNEI's activities in the area of methane hydrates included an expanded effort in hydrate destabilization. Detailed studies of reagent-induced decomposition of methane hydrates were initiated utilizing a novel instrument that combined spectroscopy and calorimetry. We continued our microbial analysis of sediment samples collected in the Gulf of Mexico and the Hikurangi margin off New Zealand. Model development was pursued to investigate the fate of methane released from the seafloor into the water column, e.g., as a result of inadvertent or purposeful hydrate destabilization. As part of our goal to promote international collaboration, HNEI personnel participated in a multi-national research cruise off New Zealand in June and July 2006.

During the present reporting period (Award N00014-06-1-1055), we continued to expand the capacity and capabilities of the HFCTF and made improvements to the infrastructure to support this expanded capability. Three additional test stands were added to the facility, increasing the total number of test stands to eleven. Several of the existing test stands were modified to allow testing of stacks while monitoring individual cell voltages. The systems are currently used to support Ion Tiger, an ONR-funded UAV project. The existing segmented fuel cell system was expanded by adding spatial resistance and electrochemical impedance spectroscopy (EIS), as well as cyclic and linear-sweep voltammetry (CV and LSV, respectively). Additions of other diagnostic equipment, including frequency response analyzers and galvanostats/potentiostats, and further development and improvement of existing equipment such as the gas analysis system further improved the diagnostic capabilities at the HFCTF. Research activities included studying the performance impact of low-level single and mixed contaminants present in the anode feed stream, the performance impact and poisoning mechanism of low-level sulfur dioxide in the cathode feed stream, the spatial distribution of fuel cell overpotentials along the flow channels, and the feasibility of employing the segmented cell system for the detection of membrane electrode assembly (MEA) defects. Some of these activities were supported in part by US DOE.

HiL development activities focused on upgrading the existing dynamic HiL test stand to accommodate testing of fuel cell stacks up to the 1 kW level. The upgrade included installation of a higher capacity load unit (100 V/150 A/5 kW) and higher-range mass flow controllers, and an update of the software to test stacks in static, dynamic and real-time HiL modes. Simulation tools were modified for evaluation of fuel cell systems for propulsion of an unmanned aerial vehicle.

Activities in the areas of fuel processing and gas conditioning for hydrogen ( $H_2$ ) production focused on identifying and characterizing approaches for sulfur (S) removal from fuel gas and reforming activities. Various modified activated-carbon-based sorbents were evaluated. The sulfur work focused on removal of tetrahydrothiophene (THT) and dimethylsulfide. The best modified sorbent improved S removal by more than 6X compared to the unmodified sorbent. The improved absorption is related to changes in the surface acidity/basicity of the carbon sorbent. Impregnated metals also play important roles.

Regeneration of the used carbon sorbents by thermal desorption was also explored.

Under funding from DARPA, HNEI developed a conceptual design of an ocean floor, fuel-cell based, power generating station fueled by methane from natural gas seeps or from the controlled decomposition of methane hydrates. Building on ongoing activities under HEET, a laboratory-

scale catalytic autothermal reformer capable of operating at pressures of 6 to 50 bar was constructed and tested. The objective of the experimental program was to maximize H<sub>2</sub> production per mole of oxygen (O<sub>2</sub>) supplied. Tests were conducted using O<sub>2</sub> and hydrogen peroxide (H<sub>2</sub>O<sub>2</sub>) as the oxidizer. The H<sub>2</sub> production per mole of O<sub>2</sub> increased ~14% when using H<sub>2</sub>O<sub>2</sub> vs. O<sub>2</sub> as the oxidizer. An equilibrium model was also used to compare experimental and theoretical results. Results of this analysis have been forwarded to NUWC for use in their UUV program.

Plasma reforming activities were initiated, including design, construction, and testing of two plasma arc reactor designs. The first reactor was a planar plasma, gliding arc design and the second was a reverse vortex reactor. Initial tests using methane and air showed the performance of the reverse vortex reactor to be better than the gliding arc one, producing higher levels of hydrogen in the reformat and allowing less methane to pass through the system.

In support of the DARPA-sponsored Direct Carbon Fuel Cell research project at SRI, HNEI prepared biocarbons with various well-specified properties from a wide variety of biomass feedstocks. These biocarbons were shipped to SRI for testing and evaluation. SRI is using its test results to optimize the performance of its carbon fuel cells.

Development of enzymatic bio-fuel cells continues, focused on enzyme immobilization utilizing macroporous chitosan polymer composites that support both mediator-based and direct-electron-transfer mechanisms. Improved *in situ* surface and interface characterization protocols have also been achieved in this work. This approach uses imaging ellipsometry and additional complementary characterization tools to study biocatalytic electrodes and their behavior. A model system that includes polymerized methylene green on electrodes as the electron transfer mediator was studied to elucidate the mediator-based electron-transfer mechanisms.

The methane hydrates activities comprised four subtasks: Hydrate Thermochemistry and Kinetics, Environmental Impacts of Methane Release from Seafloor Hydrates, Hydrate Engineering Applications, and International Collaborative R&D. Subtasks included: laboratory and analytical investigations of hydrate destabilization by chemical reagents; laboratory studies of subsea power system components that utilize seafloor methane; characterization of the microbial community in marine hydrate beds that modulate methane levels in the seafloor sediments and leakage into the water column; development of models to predict the fate of methane released from the seafloor into the water column; preliminary laboratory studies of mixed gas hydrates for gas purification; and the promotion of international R&D partnerships.

Significant progress in understanding hydrate destabilization using thermodynamic inhibitors was gained. We had posited that thermodynamic inhibitors work by tying up liquid water at the hydrate surface and, hence, disrupt the dynamic equilibrium between hydrate decomposition and formation. We tested this hypothesis by conducting a series of experiments with our Raman calorimeter in which three common alcohols and one diol were injected at constant temperature and pressure into a sample cell containing methane hydrate. The calorimeter thermograms of these injections were used to infer the amounts of hydrate decomposed per mole of inhibitor and these data were correlated with the molecular structure of the inhibitor. The results indicated that the effectiveness of an inhibitor to destabilize methane hydrate is related to the number of hydroxyl groups that provide hydrogen bonding sites and the size of the alkyl group, which tends to inhibit this bonding. This is consistent with the experimental observations and supports our hypothesis about the fundamental mechanism of chemical decomposition of hydrates.



The impact of seafloor methane from hydrates on the marine environment was explored via both experiments and modeling. Biological processes (mostly microbial) in the sediment and the water column are believed to play a major role in determining methane levels throughout the marine environment. The underlying metabolic pathways and the factors that affect these processes are not well understood and have been a focus area of the HNEI methane hydrate task. During the present phase of the HEET initiative, we continued our analysis of sediment samples collected from methane hydrate beds in the Hikurangi Margin off New Zealand. The microbiology of these samples included *Bacteria* and *Archaea* communities that were investigated by use of molecular DNA cloning. The clones were DNA sequenced and phylogenetic trees were constructed for each of these communities. The clone results did not indicate the presence of a clearly defined ecology that would be unique to methane hydrate containing sediments.

Similar molecular analyses also were performed on a push-core sample from a hydrate mound in Barkley Canyon in the Gulf of Mexico that was provided by our collaborators at the Naval Research Laboratory (NRL). Results indicate that there is a significant amount of diversity. A species that is known to exist in hydrate-containing sediments was found with high frequency, and another species specifically associated with AOM was detected. A phylogenetic tree using the actual clone sequences currently is being constructed. Work also continues on the development of computer models to investigate the fate of methane released from the seafloor into the water column, e.g., as a result of inadvertent or purposeful hydrate destabilization. As a first step to explore the use of gas hydrates for non-energy related engineering applications, such as gas fractionation or water purification, we conducted experiments with mixed gas hydrates to test the performance of the Raman calorimeter and to confirm our laboratory protocols. The instrument performed well and the protocols we developed appear to be viable. During the next phase of the experiments, the calorimeter gas supply system will be modified to allow extraction and analysis of the gas composition during hydrate formation and decomposition to determine if fractionation is occurring.

Finally, as part of our goal to promote international collaborative R&D on methane hydrates, HNEI supported and helped organize the 6<sup>th</sup> International Workshop on Methane Hydrate R&D that was held in Bergen, Norway in May 2008. The workshop was attended by scientists, engineers, and other stakeholders from 12 countries and a meeting report is available from NRL.



## **2. Introduction**

The Hawaii Energy and Environmental Technologies (HEET) Initiative, funded to the Hawaii Natural Energy Institute (HNEI) of the University of Hawaii through the Office of Naval Research (ONR), was initiated in the summer of 2001 under Grant Award Number N00014-01-1-0928 to address critical technology needs associated with the exploration and utilization of seabed methane hydrates and the development and testing of advanced fuel cells and fuel cell systems. These efforts and a smaller effort in fuels purification were continued under two subsequent agreements (Award No. N00014-04-1-0682: June 15, 2005 to June 30, 2006; and Award No. N00014-06-1-0086: October 17, 2005 to September 30, 2007). Under these programs, the focal point of our activity was development of the Hawaii Fuel Cell Test Facility (HFCTF) which houses dual facilities for fuel cell testing and for the synthesis and characterization of methane hydrates. Research in these areas was described in prior reports.

Our fourth (the current) HEET program (Award No. N00014-06-1-1055), was for the period September 14, 2006 to December 31, 2008. The remaining two sections of this report focus on each of the major areas covered within the HEET initiative. Section 3 is on fuel cell systems, with subsections for each of the associated subtasks for these systems. Section 4 covers methane hydrates, including subsections for the subtasks of this area.



### **3. Fuel Cell Systems**

#### **3.1 Introduction**

This overall task area is organized into four major subtasks: polymer electrolyte membrane (PEM) fuel cell testing and component development; fuel cell Hardware-in-Loop (HiL) and system simulation development; fuels processing and gas conditioning for hydrogen production; and novel fuel cell and component development. Under this Grant, HNEI further expanded the testing and research capabilities of the Hawaii Fuel Cell Test Facility (HFCTF), including additional gas infrastructure to operate the increased amount of test stations, implementation of stack testing for stacks that contain more than four cells, and low-current sensing for improved segmented cell diagnostics. There were new advances in the development of HiL capabilities for evaluating fuel cells under simulated real-world operating conditions, continuing work on fuel processing and gas conditioning research, and the area of novel fuel cells.

Details for the activities conducted under each of these subtasks are given below.

#### **3.2 PEM Fuel Cell Testing and Component Development**

Primary activities in this area included research activities as well as infrastructure and testing capability development. Research activities included studying the performance impact and poisoning mechanism of low-level sulfur dioxide in the cathode feed stream, studying the impact of contaminant mixtures in the anode feed stream, and studying the spatial distribution of fuel cell overpotentials along the flow channels. Testing capabilities were improved by adding test equipment for sub-scale cells, providing existing UTC XT-800 test stations with the option to test small-scale stacks with up to 48 cells, and implementing small-current-sensing capabilities to the segmented cell data acquisition system.

##### **3.2.1 Test Stands/Infrastructure Upgrades**

During the past year, improvements were implemented on the facility infrastructure, several test stands, and diagnostic instruments. With increasing demand for small stack fuel cell testing, we found it valuable to modify one of the UTC XT-800 test stands to allow small stack testing in support of the Ion Tiger unmanned aerial vehicle (UAV) project. This test station now has the capability to run 50 to 600 cm<sup>2</sup> single cells or small stacks (36-cell stacks, < 30 cm<sup>2</sup> per cell). Newly installed Fuel Cell Technologies test stations were modified to allow for H<sub>2</sub>/Helox (mixture of helium and oxygen) operation in support of the segmented cell system.

In anticipation of further impurity work, our gas analysis capability was expanded by splitting our two Varian gas chromatographs (GCs), which effectively doubles our throughput for impurity testing. Previously, both Varian GCs were operated as one unit, sampling off the same port simultaneously. By splitting the systems, we now can measure two sample points independently. The second system is currently setup to study low-level carbon monoxide and carbon dioxide using a Flame Ionization Detector (FID). The original GC system essentially remains unchanged.

With the addition of new test stations and the expansion of existing stations for small stack testing causing an increased demand for high purity water, the original facility small capacity deionized water system was replaced with a Millipore high capacity deionized water system.



The Millipore system consists of a reverse osmosis pre-treatment unit, a 350-liter storage tank and distribution pump, and a high capacity deionized water cartridge system. The new Millipore system increased the supply of deionized water from 1.5 to 12 lpm at 45 psig. Other facility upgrades included the addition of two 3 kW / 4 gpm chiller units providing cooling water to all test stations in the facility.

Cyclic voltammetry (CV) experiments are essential parts of the previously developed protocols for standardized testing and routinely accompany the impurity experiments during beginning of test (BOT) and end of test (EOT) diagnostics. As part of the station and capability upgrades for this award period, 16-channels of the segmented cell data acquisition system were reconfigured for low current sensing to allow CV and single sweep voltammetry experiments with the segmented cell system. The low current configuration of the segmented cell data acquisition increased the sensitivity of the employed Hall sensor devices by a factor of 40, i.e., from a nominal current density of 1.3 A/cm<sup>2</sup> to 0.033 A/cm<sup>2</sup>, thus allowing standard electrochemical diagnostic experiments such as the determination of the electrochemically active surface area of the catalyst via CV or of the hydrogen crossover limiting current via linear sweep voltammetry (LSV). Figure 3.2-1 shows spatial CV experiments performed at all ten segments of the segmented anode electrode simultaneously. The data allowed determining the active Pt catalyst area of each segment area, although a non-segmented anode electrode was assembled in the cell. Similar experiments will be conducted during future contaminant and durability studies.

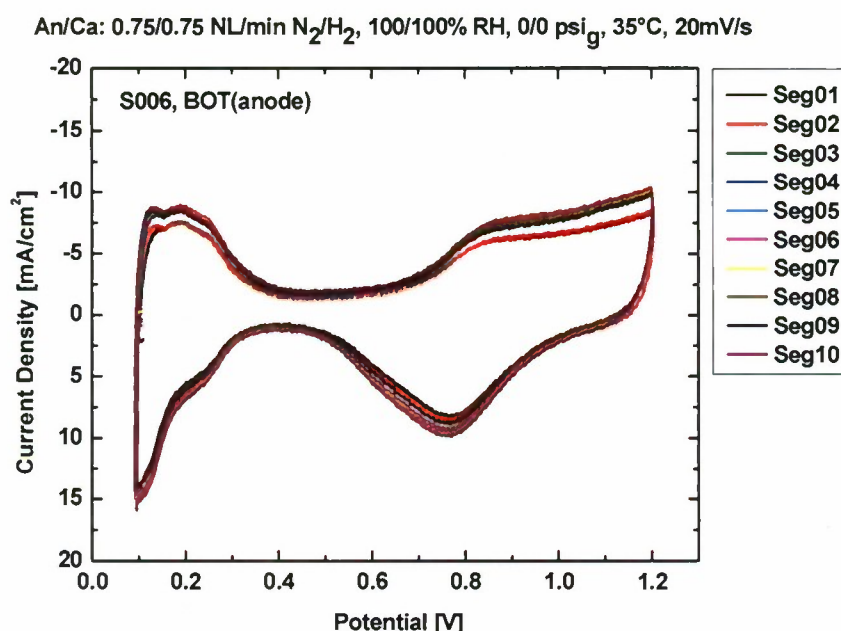


**Figure 3.2-1. Spatial cyclic voltammetry data conducted simultaneously at all segments using the low current setting of the segmented cell data acquisition setup.**

### 3.2.2 Cell and Component Testing

The main focus in this task was to study the effect of fuel and air contaminants on cell performance and durability. For fuel contaminant studies, the previously established gas analysis

system was combined with the existing experimental setup to gain new understanding of the reaction processes related to contaminant exposure. Figure 3.2-2 shows example data for 1 ppm CO exposure at anode/cathode conditions of: 60 °C, 2/2 stoich, 7/7 psi<sub>g</sub>, 100/50% RH, H<sub>2</sub>/Air. The overpotential change of the cell (173 mV), shown in black, was reached at steady state poisoning conditions. Sampling and analyzing the gas at anode and cathode inlet and outlet streams allowed for the successfully closing of the cells molar flow balance for carbon at steady state poisoning conditions to typically within  $\pm 3\%$ . For the data in Figure 3.2-2, the molar flow balance for carbon closed to within  $\pm 0.6\%$  as indicated by the molar flow balance for carbon (green) at steady state poisoning conditions between 80 to 100 hours. Successfully closing the molar flow balance of carbon was essential for calculating the CO coverage of the cell (blue) at any time during the experiment. The residual CO coverage was verified by an independent CV experiment, shown in Figure 3.2-2 as a blue single data point at 160 hours. The data agreed well with the calculated CO coverage and established additional confidence into the developed methodology. Further analysis of the CO coverage vs. the overpotential change resulted in the detection of a hysteresis between the poisoning process and the recovery process. Subsequent modeling analysis showed that this effect may be caused by spatial processes in the cell.

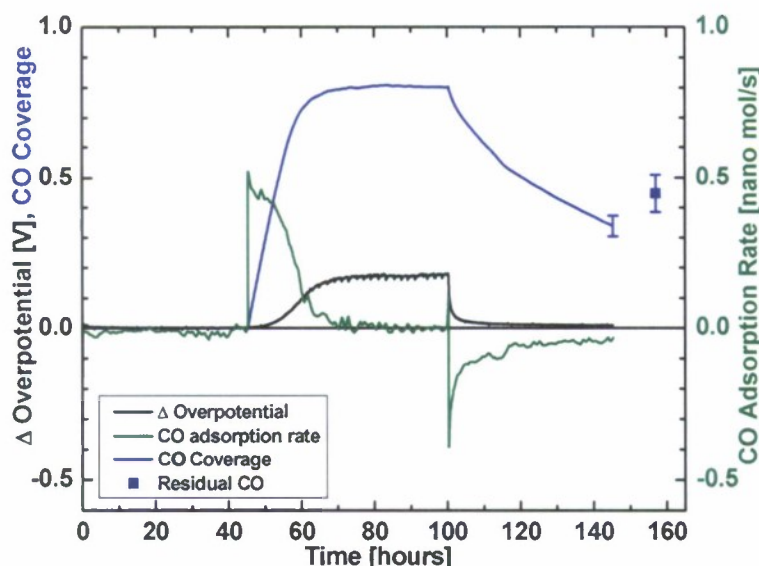


**Figure 3.2-2. Overpotential change, CO coverage, and CO adsorption/removal rates in fuel cell exposed to 1 ppm CO at 1 A/cm<sup>2</sup>, 60°C, 2/2 stoich, 7/7 psi<sub>g</sub>, 100/50% RH, H<sub>2</sub>/Air.**

In addition to single contaminant exposure, mixed contaminant experiments were conducted with CO and toluene (C<sub>7</sub>H<sub>8</sub>). Figure 3.2-3 summarizes the results of three impurity experiments all conducted at the same operating temperature of 60 °C. Two experiments were run with individual impurity injections of i) 2 ppm CO and ii) 20 ppm C<sub>7</sub>H<sub>8</sub>, and the third was run with the mixture of both impurity concentrations. To allow for an easier data comparison, the time scale of each experiment was shifted so that the impurity injections started at exactly 10 hours. In Figure 3.2-3, the overpotentials change with time due to the impurity injections. While the single injection of 20 ppm C<sub>7</sub>H<sub>8</sub> resulted in a very small overpotential change of 8 mV, CO at similar conditions impacted the performance significantly more strongly and caused an



overpotential change of 247 mV. However, cell exposure to the mixture of both impurities resulted in an even greater overpotential change of 345 mV, about 100 mV higher than the sum of the individual overpotential changes of CO and C<sub>7</sub>H<sub>8</sub>. The data indicate that the mixture of impurities can cause an overpotential change that is greater than the sum of the overpotential changes of each single impurity injection.

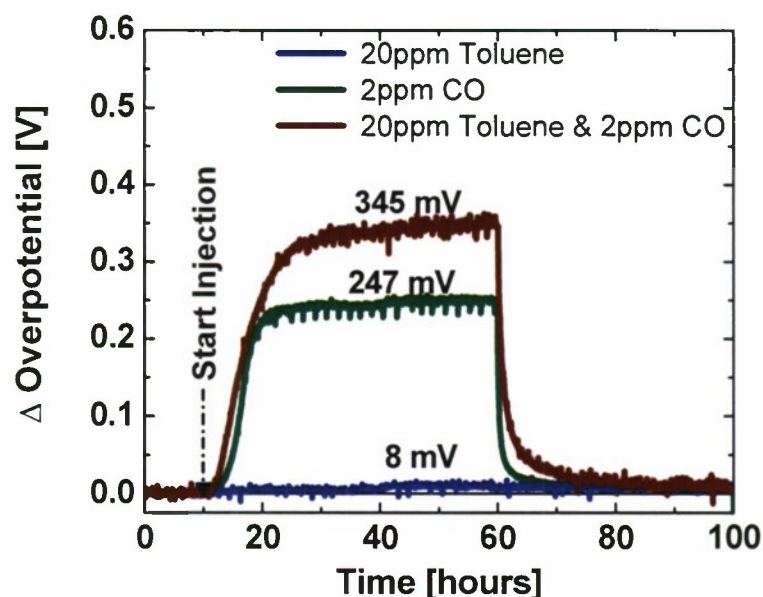


**Figure 3.2-3. Overpotential change to single exposure to 20 ppm Toluene and 2 ppm CO as well as the mixture of both, at 1 A/cm<sup>2</sup>, 60 °C, 2/2 stoich, 7/7 psi<sub>g</sub>, 100/50% RH, and H<sub>2</sub>/Air.**

Figure 3.2-4 shows the overpotential change for the mixed impurity experiment shown in Figure 3.2-3 [top] as well as the molar flow rates at the anode for C<sub>7</sub>H<sub>8</sub> and methylcyclohexane (C<sub>7</sub>H<sub>14</sub>) [middle], and CO and CO<sub>2</sub> [bottom]. Similar to results of single C<sub>7</sub>H<sub>8</sub> injection experiments, a hydrogenation process at the anode was observed that started immediately upon injection of C<sub>7</sub>H<sub>8</sub>. However, in contrast to what was observed during the single impurity injection, the conversion of C<sub>7</sub>H<sub>8</sub> into C<sub>7</sub>H<sub>14</sub> during this experiment decreased significantly over the first 20 hours of the injection and approached a negligible value after approximately 30 hours. The bottom graph of Figure 3.2-4 shows the molar flow rates of CO and CO<sub>2</sub> at the inlet and outlet of the anode over the same period of the experiment. The data confirmed the injection of CO between 10 and 60 hours. With a delay of approximately 7.5 hours with respect to the start of impurity exposure, CO was detected at the outlet of the fuel cell anode. CO values at the anode outlet increased over a 10-hour period to a steady state value, which suggests that adsorption of CO occurred at the fuel cell anode, and that with a progressing saturation of the Pt catalyst layer with CO, the molar flow rates of CO in the anode exhaust increased. However, immediately upon introduction of CO, the molar flow rate of CO<sub>2</sub> at the anode outlet increased over a 20-hour period. The data indicated the conversion of CO to CO<sub>2</sub>, most likely via an electro-oxidation reaction on the platinum catalyst layer.



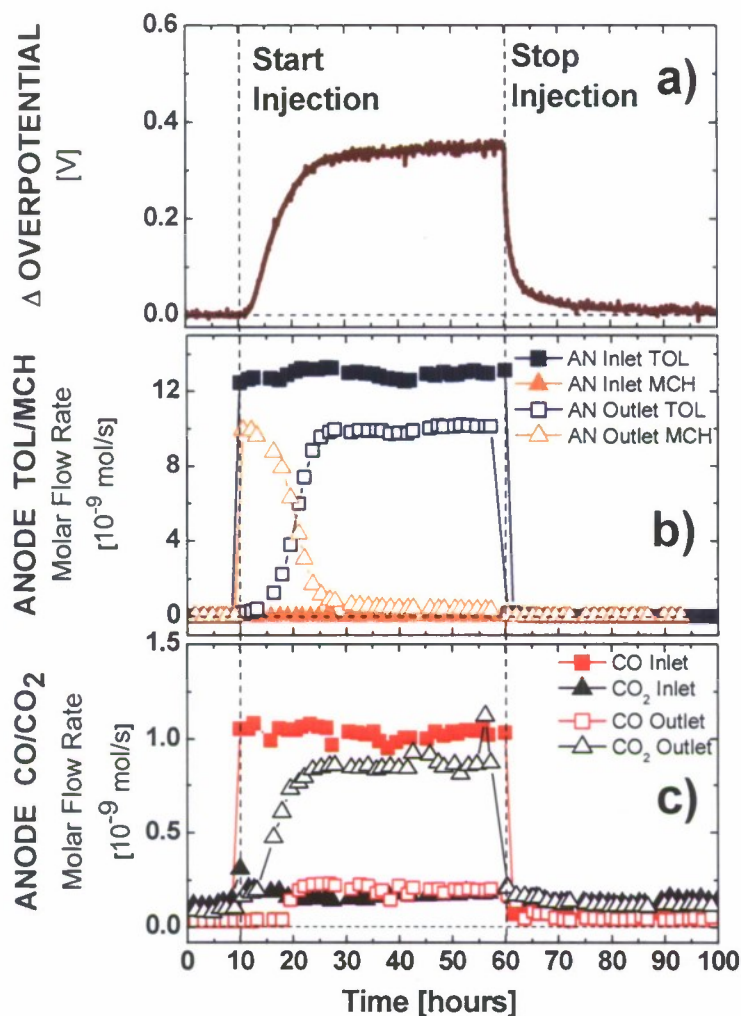


**Figure 3.2-4. Top: Overpotential change to mixed contaminant exposure with 20 ppm Toluene and 2 ppm CO at 1 A/cm<sup>2</sup>, 60 °C, 2/2 stoich, 7/7 psi<sub>g</sub>, 100/50% RH, and H<sub>2</sub>/Air. Middle and Bottom: Gas analysis data at anode inlet and outlets for toluene and methylcyclohexane (MCH), and CO and CO<sub>2</sub>, respectively.**

The data suggest that at the start of the impurity injection, all injected C<sub>7</sub>H<sub>8</sub> entering the cell was at first converted into C<sub>7</sub>H<sub>14</sub>, as observed during the single contaminant exposure. CO, however, was then continuously adsorbed strongly on the Pt catalyst surface and slowly decreased the available reactions sites for the hydrogen oxidation reaction and the hydrogenation of C<sub>7</sub>H<sub>8</sub> over time. With increasing CO coverage, the hydrogen reduction reaction and the hydrogenation of C<sub>7</sub>H<sub>8</sub> competed for the remaining catalyst reaction sites, resulting in greater overpotential than observed for CO alone. The decreasing extent of reaction for the hydrogenation of C<sub>7</sub>H<sub>8</sub> was attributed to a faster reaction rate of the hydrogen oxidation reaction (HOR). However, the competition of the HOR with the C<sub>7</sub>H<sub>8</sub> hydrogenation caused a significantly higher overpotential of 100 mV in the fuel cell.

Air contaminant studies focused on  $\text{SO}_2$ , a critical possible air contaminant for fuel cell applications in a battlefield and naval environment. Experiments have been conducted to study the effects of exposing the cathode to a trace level of  $\text{SO}_2$  during constant current operation at  $0.6 \text{ A/cm}^2$ .  $\text{SO}_2$  exposure with a total dosage of  $0.16 \cdot 10^{-3} \text{ mol SO}_2$  at 1, 2, and 10 ppm concentrations resulted in significant performance degradation. An example experiment conducted with 2 ppm  $\text{SO}_2$  at  $0.6 \text{ A/cm}^2$ ,  $80^\circ \text{C}$ , 2/2 stoich, 7/7 psig, and 100/50% RH is shown in Figure 3.2-5. At all concentrations, steady-state poisoning conditions were reached, and the saturation time and degree of the performance impact increased with contaminant concentration. The cell voltage at steady state during  $\text{SO}_2$  exposure varied up to 53 mV between exposure to 1 and 10 ppm  $\text{SO}_2$ . The poisoning process was identified as a 2-step process, which was indicated by an inflection of the voltage degradation at a cell voltage of 0.65 V. For operation at cell voltages lower than 0.65 V prior to poisoning, no inflection was observed, suggesting that the inflection may be originating from the onset of an  $\text{SO}_2$  reduction process at 0.65 V reported in the literature. Cell recovery by  $\text{H}_2/\text{air}$  operation with pure gases was independent on contaminant concentration and incomplete during all experiments. The resulting cell voltage after recovery was approximately 140 mV lower than the initial cell voltages, which was attributed to sulfur species remaining on the catalyst surface and reducing the electrochemical area (ECA) available at the cathode. Almost complete recovery of the cathode ECA was achieved by CV scanning. An example of a CV scanning experiment is shown in the right graph of Figure 3.2-5. The remaining 16.9% ECA loss may be due to regular electrode degradation of the MEA. However, changes in the CV features of the catalyst developed due to  $\text{SO}_2$  exposure and indicated similarities to Pt/Pt systems in sulfuric acid solution. For further insights and a deeper understanding of the reaction processes, additional studies will be performed.

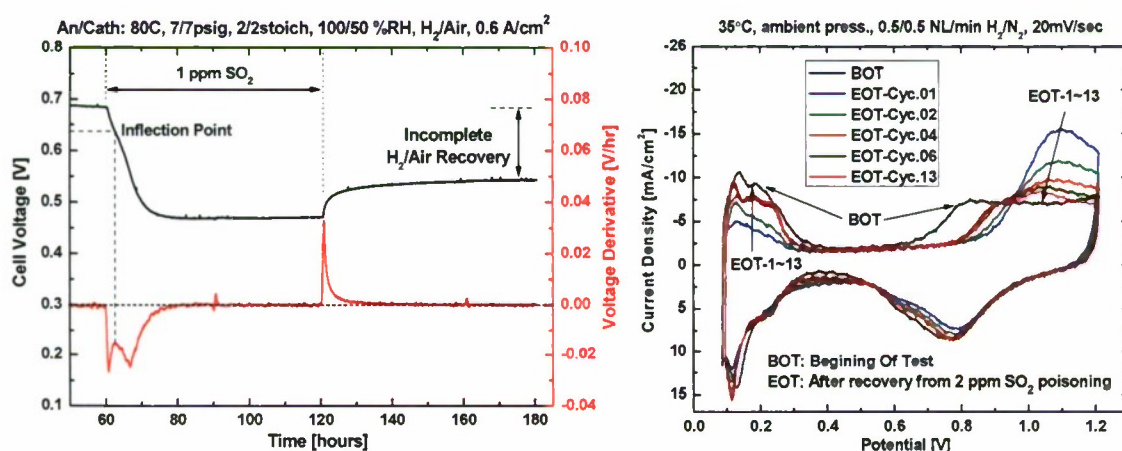


**Figure 3.2-5. Left: Cell performance impact during contaminant exposure with and recovery from 2 ppm  $\text{SO}_2$  at  $0.6 \text{ A/cm}^2$ ,  $80^\circ \text{C}$ , 2/2 stoich, 7/7 psig, 100/50% RH, and  $\text{H}_2/\text{Air}$ . Cell voltage derivative suggests two reaction mechanisms during  $\text{SO}_2$  exposure. Right: Gas analysis data at anode and cathode inlet and outlets for CO,  $\text{CO}_2$ , toluene, and methylcyclohexane.**

The overall current density measured in a PEM fuel cell (PEMFC) represents the average of the local reaction rates. Depending on cell design and operating conditions, the spatial variability



may be significant. Four primary loss mechanisms determine the spatial and overall performance of a PEMFC: activation, concentration, ohmic, and mass transfer losses. Activation losses are associated with sluggish reaction kinetics and low catalyst activity. Ohmic losses occur due to limitations of protonic and/or electronic charge transport. Concentration losses are caused by the dilution of the reactant oxygen in air to a concentration of 21%<sub>vol</sub>, and mass transfer losses are associated with the reactant transport resistance to the catalytically-active sites due to bulk diffusion. All four loss mechanisms are functions of the current density and can be spatially dependent.

During this award period, HNEI's segmented cell system was used to characterize the distribution of these various losses in a PEMFC using a six-channel serpentine flow-field. Voltage losses were attributed to each of the mechanisms at each current density by subtracting iR-corrected and uncorrected VI curves using three cathode gas compositions: Air, He+O<sub>2</sub>, and O<sub>2</sub>. Activation losses were obtained by subtracting the iR-corrected H<sub>2</sub>/O<sub>2</sub> polarization curve from the theoretical open-circuit voltage of 1.23 V. The ohmic overpotential was obtained by subtracting the H<sub>2</sub>/O<sub>2</sub> values from the respective iR-corrected values. Subtraction of the H<sub>2</sub>/He+O<sub>2</sub> data from the H<sub>2</sub>/O<sub>2</sub> data yielded the concentration losses, whereas the mass transfer overpotential was obtained by deducting the H<sub>2</sub>/Air values from the H<sub>2</sub>/He+O<sub>2</sub> values.

The resulting spatial overpotential data was analyzed by introducing a homogeneity indicator for each overpotential. This indicator was defined as the slope of the linear fit for the overpotential distribution and was calculated for each current density. An indicator value of zero consequently represents perfectly homogeneous distribution along the flow-field, while positive and negative values represent increasing and decreasing overpotentials along the flow-field, respectively. Figure 3.2-6 shows example data for the homogeneity indicator vs. current density at various humidification configurations. On the left side of Figure 3.2-6, results are shown for the high frequency response (HFR) resistance distribution, and on the right for the concentration overpotential distribution, respectively. The data for the HFR resistance distribution indicate that at all humidification configurations, the homogeneity improved with increasing current densities. Data values were either negative or zero, indicating that the cell resistance either decreased or was constant along the flow-field. For each humidification, a maximum homogeneity was reached at a specific current density, which decreased with increasing cell humidification. The data quantify the contribution of external and internal humidification on the homogeneity of the HFR along the flow-field.

The right side of Figure 3.2-6 shows similar data for the concentration overpotential. The distribution of the concentration overpotential became less homogeneous with current density when operating at drier humidification conditions. Below 0.6 A/cm<sup>2</sup>, however, the humidification of the cell had no impact on the homogeneity of the concentration overpotential. The methodology for separating the fuel cell overpotentials employed, together with HNEI's segmented cell system, allowed studying the dependence of the distribution of overpotentials in a fuel cell with respect to changing operating conditions. This information will be useful for understanding mechanical or electrochemical failure mechanisms of long-term statically or dynamically operated fuel cell systems.



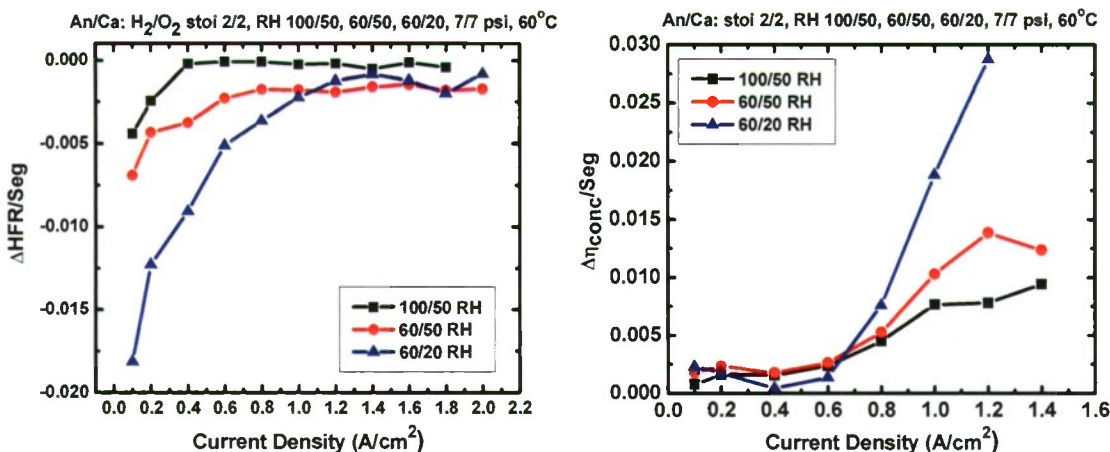


**Figure 3.2-6. Left: Cell resistance homogeneity indicator vs. current density for segmented cell operated at various humidification levels at 60 °C, 2/2 stoich, 7/7 psi<sub>g</sub>, 100/50% RH, and H<sub>2</sub>/O<sub>2</sub>. Right: Concentration overpotential homogeneity indicator vs. current density for segmented cell operated at various humidification levels at 60 °C, 2/2 stoich, 7/7 psi<sub>g</sub>, 100/50% RH, and H<sub>2</sub>/Air.**

### 3.2.3 MEA Fabrication Laboratory

The MEA Fabrication Laboratory is located within the HFCTF. During this grant period, the laboratory was not operated, but it was augmented by the acquisition of a Graphetek plotter for cutting gaskets to be used in the assembly of MEAs. The plotter was received towards the end of the grant period and has not yet been setup. It will be completed and used in future work at the laboratory.

### 3.2.4 Papers and Presentations Resulting from 2008 Efforts

#### PAPERS

G. Bender, M. Angelo, K. Bethune, S. Dorn, and R. Rocheleau, "Method Using Gas Chromatography to Determine the Molar Flow Balance for Proton Exchange Membrane Fuel Cells Exposed to Impurities," submitted to Journal of Power Sources, February 2009.

S. Dorn, G. Bender, K. Bethune, M. Angelo, R. Rocheleau, "The Impact of Trace Carbon Monoxide / Toluene Mixtures on PEMFC Performance," ECS Transactions, 16 (2), 659 (2008).

M. Angelo, S. Dorn, G. Bender, R. Rocheleau, "The Impacts of Repetitive CO Poisoning on MEA Performance and Durability," ECS Transactions, 16 (2), 669 (2008).

Y. Zhai, G. Bender, S. Dorn, M. Angelo, K. Bethune, and R. Rocheleau, "Sulfur Dioxide Contamination in PEMFCs: Degradation and Recovery of Performance," ECS Transactions 16 (2), 873 (2008).

G. Bender, M. Angelo, K. Bethune, S. Dorn, and R. Rocheleau, "Quantitative Analysis of the Performance Impact for Low Level Contaminant Studies on Proton Exchange Membrane Fuel Cells," in preparation for submission to Journal of Power Sources.

G. Bender, M. Angelo, K. Bethune, S. Dorn, and R. Rocheleau, "The Carbon Monoxide Balance Of A Direct Hydrogen Proton Exchange Membrane Fuel Cell During Exposure To Low Level Carbon Monoxide," in preparation for submission to Journal of the Electrochemical Society.

#### PRESENTATIONS

G. Bender, S. Dorn, K. Bethune, M. Angelo, R. Rocheleau, "The Impact of Trace Carbon Monoxide/Toluene Mixtures on Proton Exchange Membrane Fuel Cell Performance," 2nd DOE/ANL Modeling Workshop, National Renewable Energy Laboratory, November 20-21, 2008, Golden, Colorado.

S. Busquet, K. L. Davis, R. M. Moore, G. Bender, R. Rocheleau, "HNEI Simulation Tool for Proton Exchange Membrane Fuel Cells," 2nd DOE/ANL Modeling Workshop, National Renewable Energy Laboratory, November 20-21, 2008, Golden, Colorado.

T. Reshetenko, G. Bender, and R. Rocheleau, "The Voltage Loss Distribution of a PEMFC at Various Operating Conditions," 214th meeting of the Electrochemical Society, Oct. 12-17, 2008, Honolulu, Hawaii.

S. Dorn, G. Bender, K. Bethune, M. Angelo, R. Rocheleau, "The Impact of Trace Carbon Monoxide / Toluene Mixtures on PEMFC Performance," 214th meeting of the Electrochemical Society, Oct. 12-17, 2008, Honolulu, Hawaii.

M. Angelo, S. Dorn, G. Bender, R. Rocheleau, "The Impacts of Repetitive CO Poisoning on MEA Performance and Durability," 214th meeting of the Electrochemical Society, Oct. 12-17, 2008, Honolulu, Hawaii.

G. Bender, M. Angelo, K. Bethune, S. Dorn, and R. Rocheleau, "Impurity Studies at HNEI, University of Hawai'i," ISO/TC197/WG12 Meeting, San Francisco, April 3 2008.

#### POSTER PRESENTATION

"Sulfur Dioxide Contamination in PEMFCs: Degradation and Recovery of Performance," Y. Zhai, G. Bender, S. Dorn, M. Angelo, K. Bethune, and R. Rocheleau, 214th meeting of the Electrochemical Society, Oct. 12-17, 2008, Honolulu, Hawai'i.





### 3.3 Fuel Cell Hardware-in-Loop and System Simulation Development

The objectives of this subtask were divided between two major activities: a) enhancement of existing Hardware-in-Loop (HiL) testing capabilities, and b) development of fuel cell system simulation tools. The HiL capability and simulation tools are intended to contribute towards providing a Rapid Prototyping System (RPS) for naval application of fuel cell systems. Both of these topics will be discussed in the following paragraphs.

#### 3.3.1 Scope of Work and Approach

##### HiL Development

The HNEI fuel cell HiL dynamic test station has been developed and is in operation evaluating PEM fuel cells (PEMFCs) under dynamic application conditions. HiL methodology is well established in the automotive industry, where the technique is applied to develop and debug control algorithms for automotive drive systems. Figure 3.3-1 shows the layout of HNEI's HiL concept.

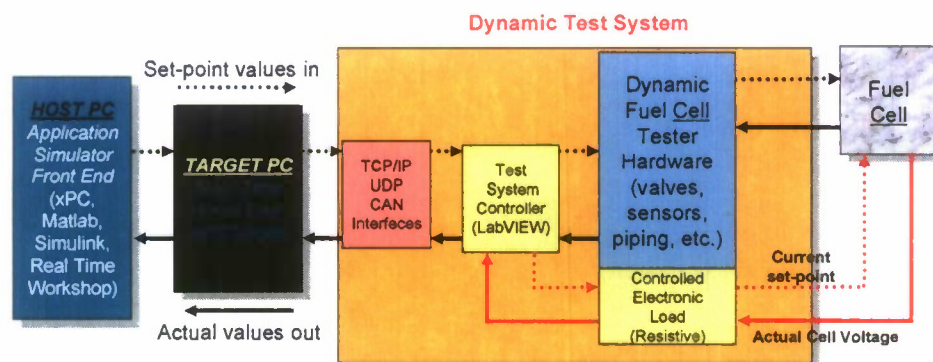


Figure 3.3-1. HNEI fuel cell Hardware-in-Loop concept.

HNEI's fuel cell HiL process is capable of developing optimal control strategies and algorithms for a fuel cell system and its associate components using a real-time simulation for a desired fuel cell application under a dynamic load profile. The de-coupling of parameters, combined with high-end instrumentation, allows distinguishing of the impact and allocation of weak spots, performance degradation, and ageing effects of the cell or stack. The process allows the evaluation of both the performance and durability of a specific fuel cell or stack design (geometry, materials, flow fields, etc.) under dynamic test conditions that mimic the actual conditions that a cell or stack will experience when placed in a realistic environment.

At the beginning of this reporting period, HNEI worked closely with ONR and NRL to identify fuel cell systems that are of near-term U.S. Navy interest which would require testing of the stacks in the HiL mode. The plan during this reporting period was to further upgrade (both hardware and software) our dynamic HiL fuel cell test stand to permit the testing of small fuel cell stacks (e.g., up to the 1 kW level). In order to make this upgrade to stack testing, it was decided to purchase and install a bigger load unit (100 V/150 A/5 kW) and larger-range mass flow controllers (MFCs) for hydrogen (0-20 slpm) and air (0-50 slpm). The idea was to

configure the HiL test stand to have the flexibility of testing a stack or a signal fuel cell by switching between the bigger- and smaller-range load (10 volts/150 amps/1 kW) units. This upgrade to stack-level testing involved a complete restructure of the internal space of the test stand to accommodate the new hardware (load unit and MFCs), development and installation of electronic boards and controller, and redesign of the FPGA (low level programming for safety and alarm system), Real Time and PC software. These hardware and software upgrades were accomplished internally at HNEI. The details of this configuration are discussed in Technical Accomplishments, presented under section 3.3.2 below.

The upgraded HiL stack test system was successfully completed, has a dynamic response time of between 50-100 milliseconds, and is capable of evaluating the fuel cell stack performance and durability within U.S. Navy fuel cell systems. The upgraded dynamic HiL testing will focus on candidate fuel cell stack technology for autonomous applications of interest to the Navy (NRL and NUWC). Furthermore, the upgraded HiL test system now has the diagnostic capability of testing both single cells and stacks in dynamic and real-time HiL modes.

### Simulation Tool Development

Since there is an interest in applying fuel cell stacks to an unmanned aerial vehicle (UAV), our group created a simulation tool called Hybrid Power System (HPSys). Fig 3.3-2 shows the schematic representation of a fuel cell and battery hybrid power system.

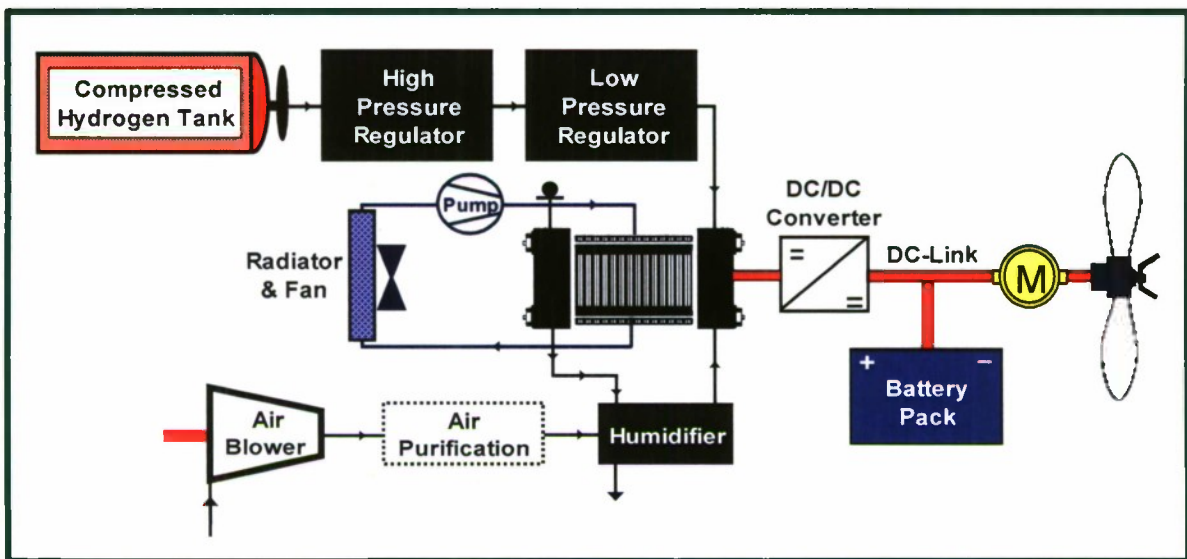


Figure 3.3-2. Schematic representation of a fuel cell and battery hybrid power system.

The HPSys simulation will be used for real-time HiL dynamic testing to evaluate and validate high performance HPSys designs, stacks, balance of plant (BOP) components, and control strategies for naval applications.



### 3.3.2 Technical Accomplishments

#### HiL Development

The HiL project involves the development of a real-time simulation system using a commercially available real-time program and platform (Matlab/Simulink environment and xPC Target Platform). This project consists of running a fuel cell system simulation with a real fuel cell, or stack, using our dynamic-response test stand. During this reporting period, the following main objectives were achieved:

Upgrade of the dynamic HiL fuel cell test stand to permit the testing of small fuel cell stacks. The upgraded HiL fuel cell test stand has the capability of testing both a fuel cell and stack, and achieving dynamic response in the 50-100 millisecond (ms) range. This capability enabled us to test the fuel cell and stacks under realistic dynamic conditions equivalent to what a cell or stack would experience when operated under dynamic transient conditions. A 96-cell monitoring system was also developed and installed. The cell monitoring system supports fast, dynamic HiL real-time testing and features a system of 16-channel modules having up to 240 channels with all channels truly differential and simultaneously sampled. The cell monitoring system will be used to observe the behavior of the individual cell during HiL dynamic simulation test and protect the stack from damage.

The dynamic HiL fuel cell test stand has following specifications:

1. Stack testing up to 5 kW<sub>e</sub> ( EL100 – 100 V/150 A range);
2. Cell testing up to 1 kW<sub>e</sub> ( EL10 – 10 V/220 A range);
3. H<sub>2</sub> MFC with a flowrate range of 0-20 slpm;
4. Air and O<sub>2</sub> MFC with a flowrate range of 0-50 slpm;
5. Low-range O<sub>2</sub> MFC with a flowrate range of 0.01-0.5 slpm;
6. True-Data EIS, impedance spectrum analyzer, for a fuel cell; and
7. Real-time HiL and dynamic testing capability with a response time of 50-100 msec.

The capability of the upgraded HiL fuel cell test stand was demonstrated to visitors during the October 2008 Ion Tiger UAV review meeting held in Honolulu, Hawaii. ONR and NRL personnel were in attendance. The demonstration included the real-time running of an HPSys (Battery and PEMFC) simulator with a Protonex stack and mission power profile provided by NRL.

#### Simulation Tool Development

A fuel cell and battery hybrid power system (HPSys) simulation tool was developed in Matlab/Simulink environment (Figure 3.3-3) during this reporting period. The simulation tool is capable of evaluating fuel cell systems for propulsion of a UAV. The simulation tool is modular in its structure, which allows different components to be added and different fuel cell system configurations to be constructed. The tool has also the flexibility to size up components, apply different operational and control strategies, and test under different load profiles. The simulation tool also has the capability of converting into real time and being used in HiL testing of the simulated fuel cell system with one or many actual hardware components of the system (e.g., a stack by itself or the combination of stack, air blower, and external humidifier).



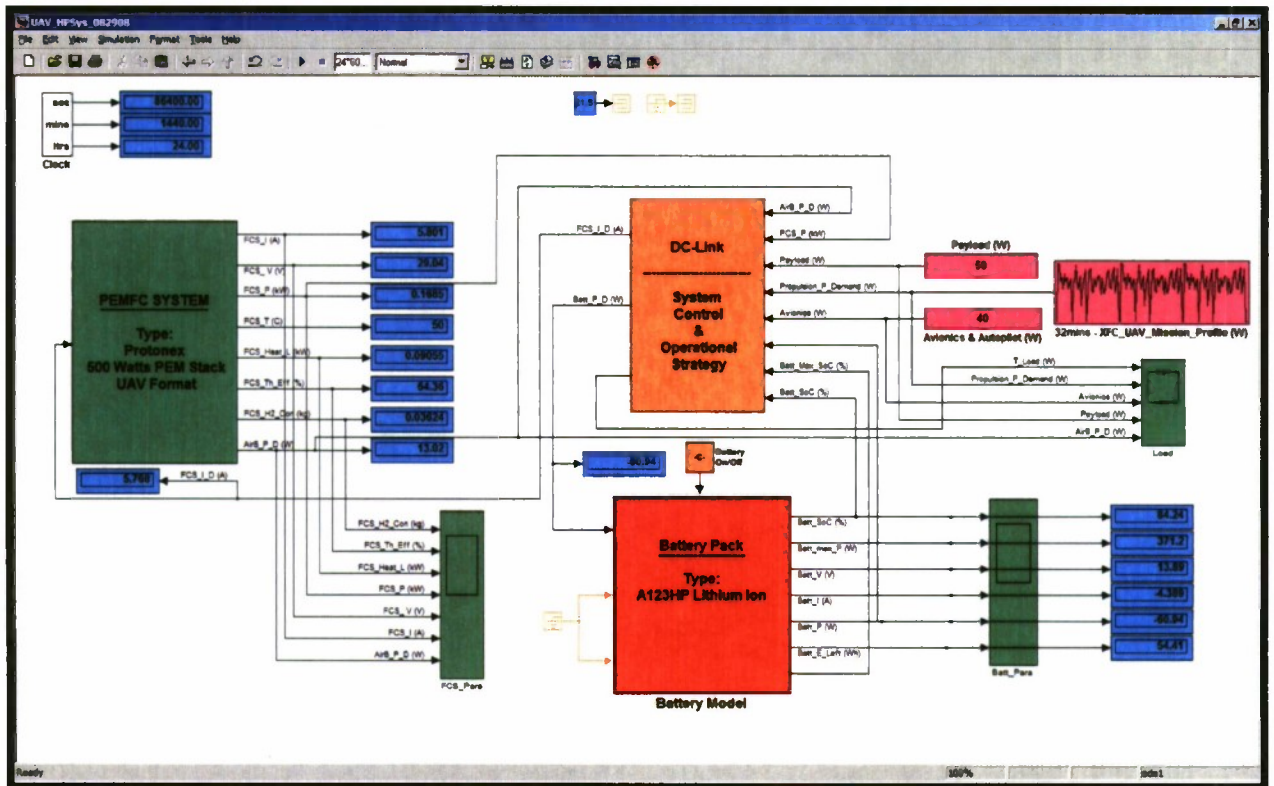


**Figure 3.3-3. HPSys simulation in the Matlab/Simulink environment.**

### 3.3.3 Papers and Presentations Resulting from Efforts

## PAPERS

M.B.V. Virji, P.L. Adcock, R.M. Moore, J.B. Lakeman, "Modelling and Simulation of an Indirect Diesel Proton Exchange Membrane Fuel Cell (PEMFC) System for a Marine Application," *Fuel Cell Science and Technology*, Vol. 4, Page 481, November 2007.

R.M. Moore, G. Randolph, M. Virji, and K.-H. Hauer, "Fuel Cell Hardware-in-Loop for PEM Fuel Cell Systems", Electrochemical Society Transactions – 30<sup>th</sup> Fuel Cell Seminar, Vol. 5, Issue 1, pp. 309-319, March 2007.

R.M. Moore, K.H. Hauer, G. Randolph, and M. Virji, "Fuel cell evaluation for dynamic applications", Electrochemical Society Transactions, v. 3, Issue 1, pp. 923-930, October-November 2006.

R.M. Moore, S. Ramaswamy, J.M. Cunningham, and K.H. Hauer, "A Dynamic Simulation Tool for the Battery-Hybrid Hydrogen Fuel Cell Vehicle," Fuel Cells—From Fundamentals to Systems, n. 5, pp. 387-402, October 2006.

R.M. Moore, K.H. Hauer, and S. Ramaswamy, "Energy Utilization and Efficiency Analysis for Hydrogen Fuel Cell Vehicles," Journal of Power Sources, Vol. 159, Issue 2, 22 September 2006, pp. 1214-1230.

## PRESENTATIONS

M. Virji, "Fuel Cell Hardware-in-Loop Development and Real Time Fuel Cell Vehicle Simulation," Fuel Cell Seminar, San Antonio, TX, October 15-19, 2007.

R.M. Moore, G. Randolph, M. Virji, K.H. Hauer, "Fuel Cell Based Hardware-in-Loop for PEMFC Systems", 2006 Fuel Cell Seminar, Honolulu, Hawaii, 13-17 November 2006.

R.M. Moore, K.H. Hauer, G. Randolph, M. Virji, "Fuel Cell Evaluation for Dynamic Application," Presentation for the Oral Presentation in Section B (Fuel Cell Systems, Cell Stack and Component Hardware) of the "Proton Exchange Membrane Fuel Cells 6" Seminar at ECS 210, 29 October – 3 November 2006, Cancun, Mexico.





## 3.4 Fuel Processing and Gas Conditioning for Hydrogen Production

### Subtask 3.4.1: Sulfur Removal from Fuel Gas at Ambient Temperature

#### 3.4.1.1 Absorptive Removal of Tetrahydrothiophene (THT) from Synthetic Natural Gas on Modified Activated Carbons

##### 3.4.1.1.1 Scope of Work and Approach

Recently, fuel cells have attracted much interest as an environmentally friendly conversion technology in which hydrogen and oxygen are converted into water while producing electricity. One strategy for fuel cell applications is to convert pipelined natural gas to hydrogen using a series of fuel processing steps including fuel reforming, water gas shift reaction, and selective CO oxidation. In this process, sulfur compounds present in the fuel gas can cause severe deactivation of reforming catalysts and fuel cell anodes, even at very low concentration. For example, a gas feed containing 5 ppm of tetrahydrothiophene (THT) would produce reformat containing approximately 1 and 2 ppm of  $H_2S$  and this concentration is high enough to adversely affect the performance of proton exchange membrane (PEM) fuel cells [1]. Thus, desulfurization is an essential unit operation in fuel processing for fuel cells applications.

The odorants and the other sulfur compounds present in pipeline gas can be removed by adsorption on activated carbons [2, 3]. Adsorption is regarded as a more effective method for deep desulfurization and can be performed at ambient temperature. In general, the adsorption of sulfur compounds on activated carbons can be classified as either physical adsorption or chemisorption, based on the interaction of the sulfur bearing molecule with the carbon surface.

Physical adsorption is characterized by van der Waals or dispersion forces which are weak intermolecular interactions arising from dipole-dipole or induced dipole attractions. Physical adsorption approaches equilibrium very rapidly and is generally reversible if the vapor pressure of the adsorbate is reduced. Hysteresis may result due to the pore structure of the sorbent. The heat evolved during adsorption is similar to a condensation process, being in the range 4 to 40  $kJ\ mol^{-1}$ , and as a result, is assumed to happen very quickly. Due to the long range nature of the attractive forces, physical adsorption may form several layers of adsorbed gas molecules on the solid surface. As the number of layers increases, the adsorption process approaches one of condensation. In activated carbons, adsorptive capacity is affected by pore size and distribution and the number of active sites on the surface [4, 5].

In contrast to physical adsorption, chemisorptive interaction between the solid surface and the adsorbed molecule is much stronger. Chemisorption is mainly responsible for gas-solid reactions and catalysis, and displays chemical specificity, i.e., is particular to the solid and gas species in terms of chemical forces and orientation. These requirements suggest that chemisorption can only occur as a monolayer. The forces involved between participants are of the same order as those in chemical reactions, with the heat of chemisorption being 40 to 600  $kJ\ mol^{-1}$ . As a result, chemisorption may be slow and display rate behavior characteristic of processes possessing an activation energy. Gases which have been chemisorbed may be difficult to remove and may leave the surface altered, as in the case of oxygen adsorbed onto solid carbon which is desorbed as CO or  $CO_2$ . With activated carbons, the surface chemical properties, particularly the presence of different functional groups and metal ions, affect the adsorptive capacity [4, 5].

To increase the adsorptive capacity of activated carbons, surface modification by oxidation [6] or metal impregnation [7, 8] has been investigated. These methods can improve the sulfur capacity of the parent material by creating additional acid groups and adsorption sites on the surface of activated carbons [6, 9, 10]. It was found that  $\text{HNO}_3/\text{H}_2\text{SO}_4$  solutions can form acidic groups on the carbon surface, which interact with thiol groups by hydrogen bonding to enhance their sorption capacity [11]. Impregnation of  $\text{CuCl}_2$  on activated carbon was reported by Kim and Yie [12]. They found that impregnated  $\text{CuCl}_2$  led to a notable decrease in microporosity of the activated carbon, but enhanced the adsorption capacity of methyl mercaptan (MM), indicating that  $\text{CuCl}_2$  may act as adsorption sites for MM. Besides activated carbons, zeolite-based sorbents modified with transition metals have also shown improved adsorption capacity for sulfur compounds. These transition metals, i.e., copper, zinc and silver, were regarded as active materials to adsorb sulfur compounds under ambient conditions [13-15]. This earlier work addresses the adsorption of sulfur compounds at ambient temperatures by surface modification of activated carbons using acid oxidation or metal impregnation. Information on the effect of impregnated metals on the surface features is still lacking. These techniques may influence the mechanism of adsorption of sulfur compounds on the activated carbons, and potentially, the sulfur adsorption capacity.

Tetrahydrothiophene (THT) is a heterocyclic organic compound consisting of a five-membered ring containing four carbon atoms and one sulfur atom. It is a volatile, clear, colorless liquid with a strong unpleasant odor. THT can be used as an odorant in pipeline gas, such as natural gas, city gas or town gas. In Honolulu, synthetic natural gas (SNG) is produced from naphtha and THT is used as an odorant for leak detection. SNG is distributed via pipeline by The Gas Company. Studies on adsorptive removal of gas-phase sulfur compounds have been conducted [16] to utilize the pipeline gas as a reforming feedstock for hydrogen production use in fuel cells.

An objective of this paper is to describe the adsorption of tetrahydrothiophene (THT) present in SNG on activated carbons that have undergone surface modification by oxidation or impregnation to improve adsorption capacity. The purpose is to identify the adsorption mechanism of sulfur compound THT on the modified surface of activated carbons.

#### **3.4.1.1.2 Experimental**

**Synthetic natural gas (SNG) composition.** Synthetic natural gas (SNG) is produced from petroleum and distributed via pipeline in Honolulu by The Gas Company. SNG is composed of methane ( $\text{CH}_4$ ), hydrogen ( $\text{H}_2$ ), nitrogen ( $\text{N}_2$ ), carbon monoxide ( $\text{CO}$ ), carbon dioxide ( $\text{CO}_2$ ), water vapor ( $\text{H}_2\text{O}$ ), trace amounts of higher hydrocarbons, and sulfur compounds. The detectable sulfur compounds, which are either naturally present or added intentionally as odorants, are hydrogen sulfide ( $\text{H}_2\text{S}$ ), methyl mercaptan (MM), ethyl mercaptan (EM), dimethyl sulfide (DMS), dimethyl disulfide (DMDS), tetrahydrothiophene (THT), ethyl disulfide (EDS), and an additional, as yet unidentified, compound. Among these sulfur compounds, THT is added as an odorant and was present in the highest concentration, contributing roughly 75% in the total sulfur content. The gas composition and sulfur speciation analyses are presented in Tables 3.4.1.1-1 and 3.4.1.1-2, respectively.



**Table 3.4.1.1-1. Pipeline gas composition.**

Component	Quantity
Methane	79-84%
Hydrogen	9-10%
Carbon dioxide	3-5%
Carbon monoxide	0.25-0.4%
Water*	0.24-0.32 g/m <sup>3</sup>
Ethane*	0-0.01%
Propylene*	0%
Propane*	0.03-0.5%
n-Butane*	1.5-4%
i-Butane*	1.5-3%
n-Pentane*	0.25-0.75%
i-Pentane*	0.5-1%
neo-Pentane*	0-0.05%
C6+*	0-0.1%
Tetrahydrothiophene**	0.004%
C2+**	3.78-9.41%

\*From The Gas Company Analysis Report of January 2000

\*\*From The Gas Company Data Sheet of November 1998

**Table 3.4.1.1-2. Sulfur speciation analysis in the pipeline gas.**

Component	Quantity, ppm
H <sub>2</sub> S	0.06-0.15
Methyl mercaptan	0.05-0.13
Ethyl mercaptan	0.1-0.4
Dimethyl sulfide	0.06-0.22
Dimethyl disulfide	0.07-0.23
Tetrahydrothiophene	4.2-7.8
Ethyl disulfide	0.13-0.18
Unknown species	0.3-1.0

**Sorbent evaluation and sulfur compounds analysis.** A sorbent column was constructed from a stainless steel pipe 45.7 cm in length and 2.43 cm in inner diameter. All of the components including the sorbent column and gas delivery lines were treated with a Sulfinert<sup>®</sup> coating or were made from Teflon<sup>®</sup> to prevent sulfur compounds from being adsorbed on the working surfaces of the system. A Teflon<sup>®</sup> insert with an inner diameter of 1.2 cm was packed with carbon and placed in the column.

A 4.0 gram mass of sorbent was tested in all cases. The sorbent bed was about 8 cm long with the major axis oriented vertically. To distribute the flow evenly, 3 mm layers of 3 mm diameter



glass beads were packed into the column below and above the sorbent. SNG was supplied to the carbon column from a laboratory gas service valve at a flow rate of 4.0 - 4.5 l/min using a pump. After the SNG passed through the carbon column it was analyzed with a gas chromatograph (GC).

The concentrations of sulfur species were measured with a Shimadzu 2041 GC equipped with a capillary column (Rtx-1, 60m-0.53-7um, Restek Corporation) and sulfur chemiluminescent detector (SCD) (Sievers Model 355). Helium (He) served as carrier gas and a six-port sampling valve was used to make automatic injections. A permeation tube device (Model 355, Kin-Tek Laboratories) loaded with a THT permeation tube was used to calibrate.

In each analysis the column temperature was held for 1 min at 50°C, ramped to 125 °C at 20 °C/min, ramped again to 180 °C at 10 °C/min, held at 180 °C for 1 min and finally cooled to 50 °C at 100 °C/min. Thus, effluent gas was sampled and analyzed with a cycle time of 13 min. In addition, sulfur compounds present in SNG were analyzed from a by-pass path before and after the sorption test, to verify stable operation of the system. Tests typically lasted 10 hours.

The sulfur adsorption capacity of carbon sorbents was determined by breakthrough testing. The breakthrough point is defined as the first detection of THT at a concentration  $\geq 0.2$  ppm. The sulfur capacity was calculated by using the following equation:

$$S_{cap} (mg / g) = \frac{Q(l / min) \times t(min) \times S_{conc} (ppm) \times 32000 (mg / mol)}{22.4(l / mol) \times m_{sorb} (g) \times 10^6} \quad (1)$$

where,  $S_{cap} (mg / g)$ : the sulfur capacity in milligram elemental sulfur per gram sorbent;  $Q(l / min)$ : SNG flow rate;  $t(min)$ : breakthrough time;  $S_{conc} (ppm)$ : total sulfur concentration in SNG for all sulfur compounds;  $m_{sorb} (g)$ : mass of sorbent tested; and  $32000 (mg / mol)$ ,  $22.4(l / mol)$ , and  $10^6$  are sulfur molar weight, molar volume of ideal gas, and unit conversion from ppm to molar concentration, respectively.

**Modification of activated carbons.** A coconut shell activated carbon (OLC Plus 12x30, Calgon Carbon Corporation) was used as the parent material for all samples modified by oxidation and impregnation.

In the oxidation, carbon was prepared by mixing 40 g of the virgin activated carbon (AC) with 70 ml of 68-70%  $HNO_3$  or 100 ml of 50%  $H_2O_2$  at room temperature until there was no further gas evolution. The sample was washed with distilled water until no further change in pH was detected (around pH = 5), and then dried overnight in an oven at 115 °C.

Virgin carbon was impregnated by immersing 40 gram in a 0.1N solution of the selected metal at 70-80 °C for 6 hours. The modified carbon was then dried at 115 °C overnight. The selected metal impurities were from the Zn group ( $Zn(NO_3)_2$  and  $ZnAc_2$ ), Cu group ( $Cu(NO_3)_2$  and  $CuSO_4$ ), Fe group ( $FeCl_3$ ), K group ( $AC-KMnO_4$ ,  $KCl$ ,  $KOH$  and  $K_2CO_3$ ), and Na group ( $NaOH$  and  $Na_2CO_3$ ). The loaded amount was around 0.40 mmol metal per gram virgin activated carbon except as noted. A composite sorbent was prepared based on carbon oxidized by  $HNO_3$  ( $AC-HNO_3$ ) with  $FeCl_3$  loading at varied contents, which was denoted as  $AC/HNO_3-FeCl_3$ . The names and preparation conditions for these carbon sorbents are in Table 3.4.1.1-3.

**Table 3.4.1.1-3. Carbons name and preparation conditions.**

<b>Carbons name</b>	<b>Solution / Concentration / Volume, ml</b>	<b>Ions loaded, mmol / g. AC</b>
<b>Treated with oxidizer</b>		
AC-HNO <sub>3</sub>	HNO <sub>3</sub> / 50% / 100	-
AC-H <sub>2</sub> O <sub>2</sub>	H <sub>2</sub> O <sub>2</sub> / 70% / 70	-
AC-KMnO <sub>4</sub>	KMnO <sub>4</sub> / 0.155 M / 40	-
<b>Impregnated with Cu</b>		
AC-CuSO <sub>4</sub>	CuSO <sub>4</sub> / 0.101N / 150	0.38
AC-Cu(NO <sub>3</sub> ) <sub>2</sub> -38	Cu(NO <sub>3</sub> ) <sub>2</sub> / 0.142N / 106	0.38
AC-Cu(NO <sub>3</sub> ) <sub>2</sub> -53	Cu(NO <sub>3</sub> ) <sub>2</sub> / 0.142N / 150	0.53
<b>Impregnated with Zn</b>		
AC-ZnAc <sub>2</sub> <sup>#</sup>	ZnAc <sub>2</sub> / 0.099N / 150	0.37
AC-Zn(NO <sub>3</sub> ) <sub>2</sub>	Zn(NO <sub>3</sub> ) <sub>2</sub> / 0.106N / 150	0.40
<b>Impregnated with Fe</b>		
AC-FeCl <sub>3</sub>	FeCl <sub>3</sub> / 0.099N / 150	0.37
<b>Impregnated with Na</b>		
AC-NaOH	NaOH / 1.006N / 15	0.38
AC-Na <sub>2</sub> CO <sub>3</sub>	Na <sub>2</sub> CO <sub>3</sub> / 0.753N / 19.9	0.37
<b>Impregnated with K</b>		
AC-KOH	KOH / 0.099N / 150	0.37
AC-K <sub>2</sub> CO <sub>3</sub>	K <sub>2</sub> CO <sub>3</sub> / 0.101N / 150	0.38
AC-KCl	KCl / 0.099N / 150	0.37
<b>Treated with oxidizer/ Impregnated with Fe</b>		
AC/HNO <sub>3</sub> -FeCl <sub>3</sub> -37	HNO <sub>3</sub> / 50% / 100, FeCl <sub>3</sub> / 0.099N / 150	0.37
AC/HNO <sub>3</sub> -FeCl <sub>3</sub> -70*	HNO <sub>3</sub> / 50% / 100, FeCl <sub>3</sub> / 0.099N / 140	0.70
AC/HNO <sub>3</sub> -FeCl <sub>3</sub> -105*	HNO <sub>3</sub> / 50% / 100, FeCl <sub>3</sub> / 0.099N / 210	1.05

#: ZnAc<sub>2</sub> is denoted as zinc acetate

\*: The modification was based on 20 gram of virgin activated carbon.

**Characteristics of carbon sorbents.** Nitrogen (liquid N<sub>2</sub>) adsorption/desorption isotherms for the samples were measured at 77 K (Autosorb<sup>®</sup>-1, Quantachrome Instruments, Boynton Beach, FL). Before the experiments the samples were first heated and degassed at 110 °C for 2 hours under a vacuum of 10<sup>-5</sup> torr (1.33×10<sup>-7</sup> Pa). Specific surface area (S<sub>BET</sub>) was calculated by using the multipoint BET method in the relative pressure (P/P<sub>0</sub>) range of 0.01-0.1; the total pore volume (V<sub>0</sub>) and the average pore diameter (D<sub>ave</sub>) were calculated from the amount of gas adsorbed at



related pressure of 0.995-0.999. In addition, density functional theory (DFT) was used to analyze the pore structure parameters, such as micropore volume ( $V_{\text{micro}}$ , pore width less than 2 nm), total pore volume ( $V_{\text{total}}$ , pore width less than 36 nm), and mode pore width ( $D_w$ ). The DFT calculation method is provided from the instrument data process software, and assumes that the activated carbon contains slit-shaped pores.

The surface morphology and elemental mapping of the carbons was conducted using a scanning electron micrograph (Zeiss DSM926, Germany) equipped with energy dispersive x-ray spectroscopy detector (Oxford 6533) at an accelerating voltage of 20 kV.

Carbon suspension provides useful information about the overall surface functional properties. The value indicates the average acidity/basicity of carbon sample. In this study, a 0.4 g sample of carbon was placed in 20 ml distilled water and equilibrated overnight and the pH of the suspension was measured by pH detector (Orion, Model 290A) [10].

#### 3.4.1.1.3 Technical Accomplishments

**Evaluation of carbon sorbents by adsorption capacity of THT.** The performance of each carbon sorbent was evaluated by breakthrough testing using SNG from the utility gas service available in the laboratory. Figure 3.4.1.1-1 presents the breakthrough curves for each carbon sorbent included in the study. Note that the volume of SNG has been normalized by the mass of activated carbon sorbent in the test sample to provide a common basis for comparison. For simplification, Figure 3.4.1.1-1(a) presents the breakthrough curves for carbons modified by oxidizers and Figure 3.4.1.1-1(b) presents similar data for carbons modified by impregnation.

Apparently, the modification method strongly influenced the adsorption capacity of THT on the carbons. Long-term monitoring of THT indicates that the laboratory SNG supply is not constant, varying between 4.2-7.8 ppm as listed in Table 3.4.1.1-3. Thus it is not possible to use Figure 3.4.1.1-1 as a quantitative evaluation for carbon sorbent performance. To eliminate the effects of varied experimental conditions, such as SNG flow rate, THT concentration during the test period, and sample size, Equation 1 was used to calculate the THT capacity of virgin and modified activated carbons and results are presented in Figure 3.4.1.1-2 on the basis of elemental S (mg) adsorbed per gram of sorbent.

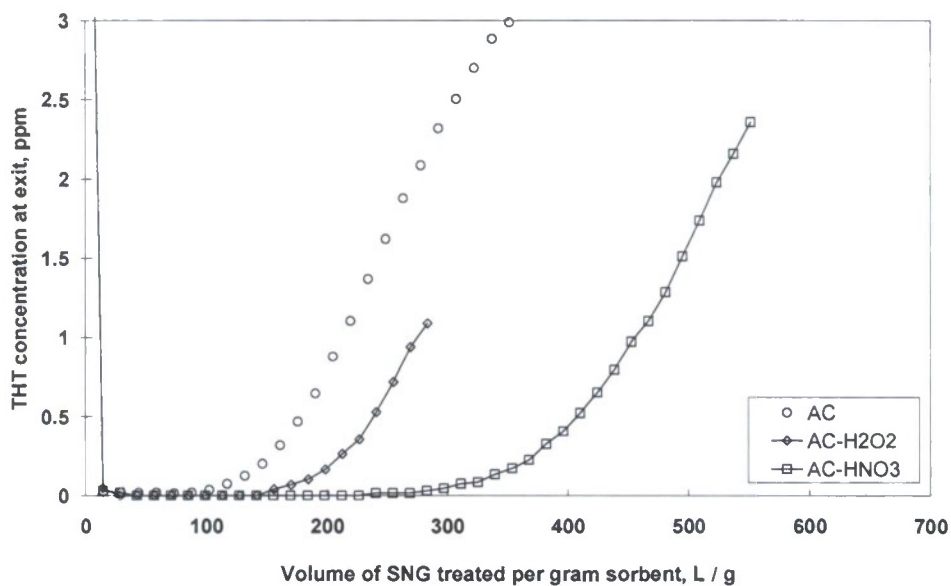
Virgin carbon (AC) had an uptake capacity of 0.91 mg S/g of sample, AC-FeCl<sub>3</sub>, AC-HNO<sub>3</sub> and their composite AC/HNO<sub>3</sub>-FeCl<sub>3</sub> had the highest THT capacity with 2.4 mg/g, 3.43 mg/g and 4.24 mg/g, respectively. Three carbons, AC-ZnAc<sub>2</sub>, AC-K<sub>2</sub>CO<sub>3</sub> and AC-KCl, had a THT capacity less than that of AC. All other carbons had increased capacities; however, some only marginally so. In general, activated carbons treated with oxidizers had increased THT capacity and were ranked according to increasing performance in the following order: H<sub>2</sub>O<sub>2</sub> and HNO<sub>3</sub>. Metal impregnated carbons did not display a clear performance enhancement trend. By comparing with the THT capacity of modified samples with virgin carbon AC, the modified carbons can be classified into the following three categories: Group 1, 0.6-1.5 mg S per gram sample; Group 2, 1.5-2.5 mg S per gram sample; and Group 3, more than 2.5 mg S per gram sample.

Group 1: Negative or minor effect carbons, AC-ZnAc<sub>2</sub>, AC-K<sub>2</sub>CO<sub>3</sub>, AC-KCl, AC-KOH and AC-NaOH;

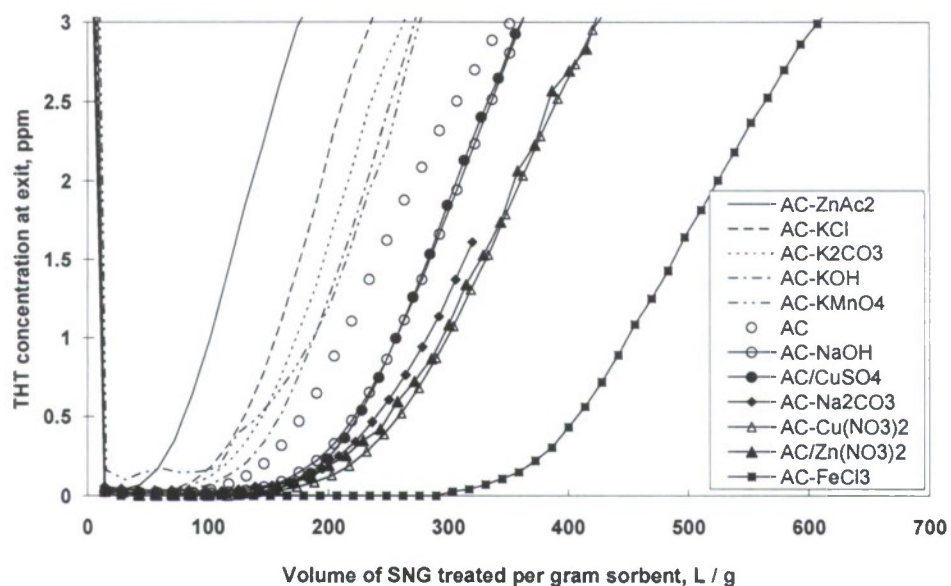
Group 2: Effective carbons, AC-KMnO<sub>4</sub>, AC-CuSO<sub>4</sub>, AC-Na<sub>2</sub>CO<sub>3</sub>, AC-Cu(NO<sub>3</sub>)<sub>2</sub>, AC-H<sub>2</sub>O<sub>2</sub>, and AC-Zn(NO<sub>3</sub>)<sub>2</sub>; and



Group 3: Major effective carbons, AC-FeCl<sub>3</sub>, AC-HNO<sub>3</sub> and AC/HNO<sub>3</sub>-FeCl<sub>3</sub>.



(a)



(b)

Figure 3.4.1.1-1. Breakthrough curves of THT for modified activated carbons; (a) oxidized activated carbons; (b) impregnated activated carbons with equal metal loadings.

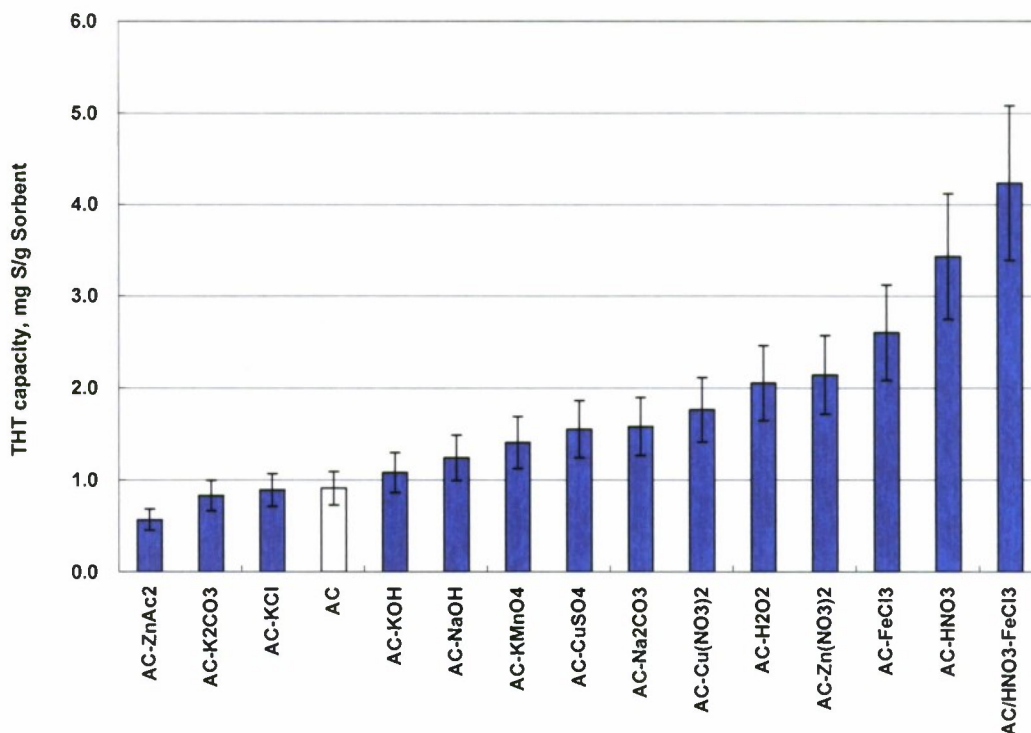
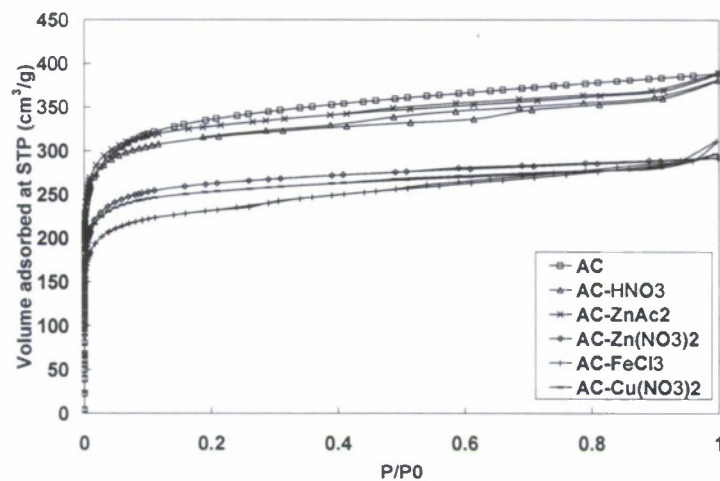


**Figure 3.4.1.1-2. THT adsorptive capacities of virgin and modified activated carbons (note that metal loadings are equal for all samples).**

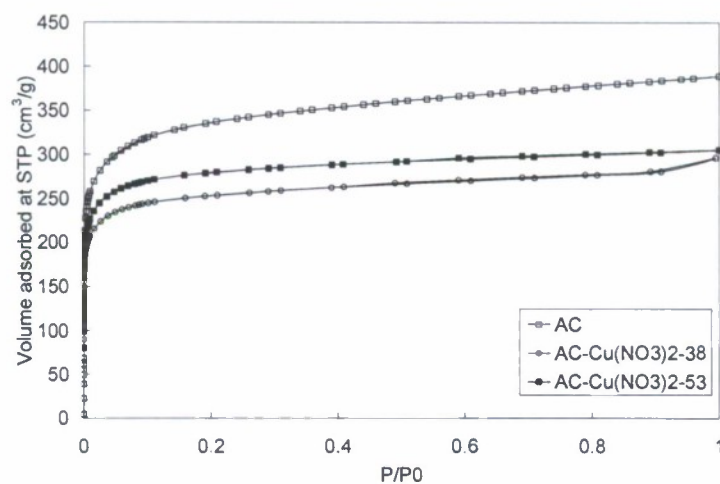
***Effect of modification on the physical characteristics of carbons surface.*** The effects of the modification on the physical surface characteristics the Group 2 carbon sorbents were investigated. Information on the pore structure of activated carbon includes characterizations of the surface area, pore volume, pore size and distribution. Figures 3.4.1.1-3 and 3.4.1.1-4 show the isotherms and pore size distribution obtained for the virgin and selected modified activated carbons.

Figure 3.4.1.1-3(a) presents the effect of loaded metal types on the isotherms. The selected modified carbon sorbents are AC-Zn(NO<sub>3</sub>)<sub>2</sub>, AC-ZnAc<sub>2</sub>, AC-Cu(NO<sub>3</sub>)<sub>2</sub>, AC-HNO<sub>3</sub> and AC-FeCl<sub>3</sub>, which are in Group 2 and 3 except for AC-ZnAc<sub>2</sub>. Figures 3.4.1.1-3(b) and (c) illustrate the effect that varied amounts of metal loaded on the activated carbon has on the isotherms for the sorbents AC-Cu(NO<sub>3</sub>)<sub>2</sub> and AC/HNO<sub>3</sub>-FeCl<sub>3</sub>, respectively. All of the adsorption isotherms are shown be similar and close to type I of the IUPAC classification, which is typical of microporous activated carbons. Moreover, the N<sub>2</sub> isotherms of these carbons also show the H4 type hysteresis loop indicating the presence of slit-shaped pores with narrow pore size distribution. Based on these isotherms, the pore size distributions were calculated using the DFT equilibrium model and are shown in Figure 3.4.1.1-4.

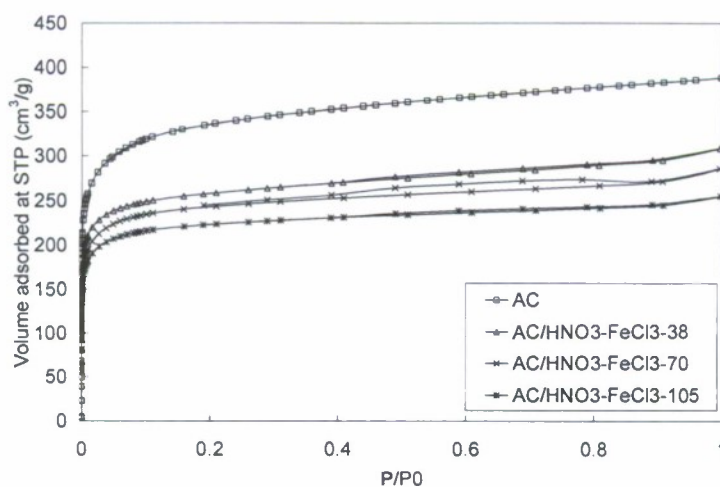
It was found that the metal loading and oxidation did not change either the N<sub>2</sub> adsorption isotherms (Figure 3.4.1.1-3) or the pore size distribution (Figure 3.4.1.1-4) to a great extent. All samples possess primarily micropores, which according to the IUPAC classification have widths below 20 Å (2 nm).



(a)



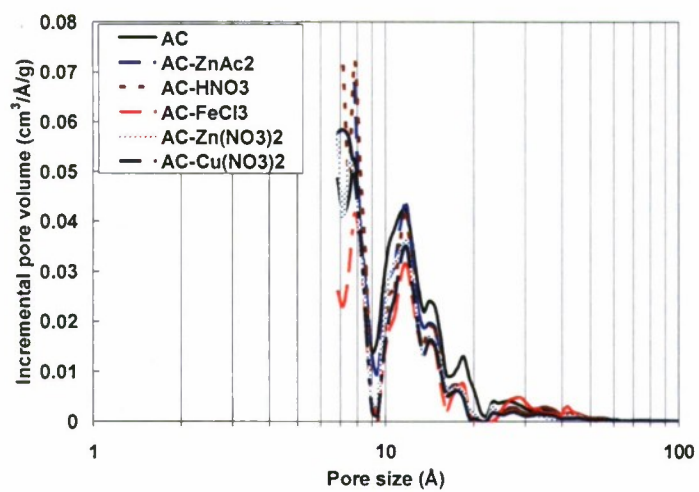
(b)



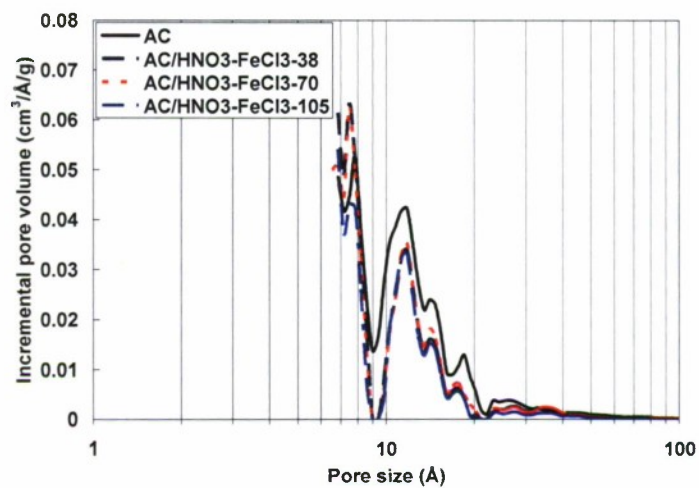
(c)

**Figure 3.4.1.1-3. Nitrogen adsorption isotherms for the virgin and modified activated carbons.**

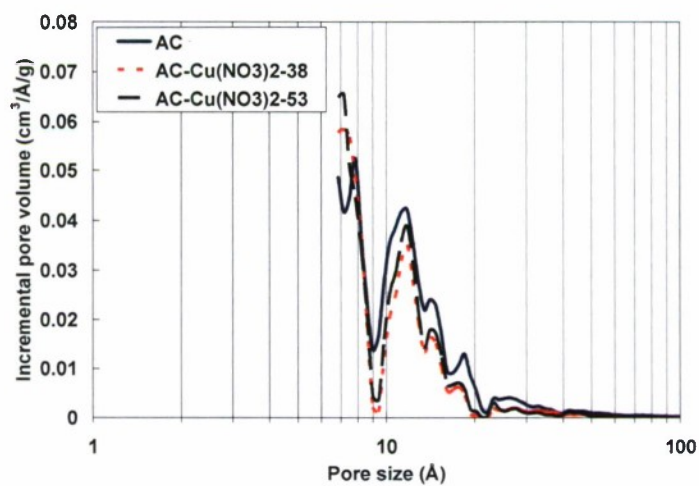




(a)



(b)



(c)

Figure 3.4.1.1-4. DFT micropore size distribution for virgin and modified activated carbons.

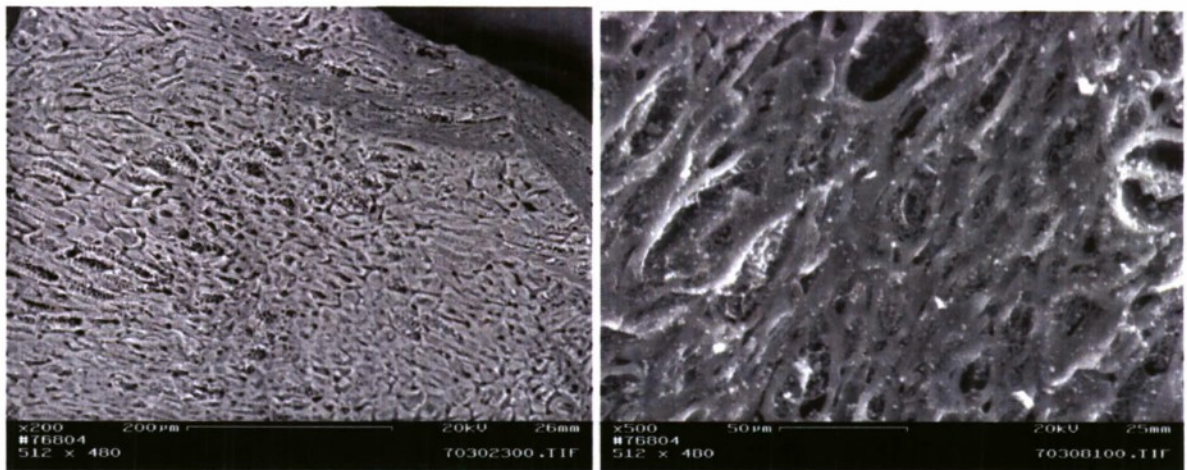
Parameters calculated from adsorption isotherms for test carbons are shown in Table 3.4.1.1-4. It was expected that impregnated carbons would have reduced surface area and pore volume, but the pore structure parameters varied widely for different impregnation metals. Pore structure parameters for AC-ZnAc<sub>2</sub> show 15% reductions in  $S_{\text{BET}}$  and  $V_0$  values compared to virgin carbon, indicating that ZnAc<sub>2</sub> impregnated on the carbon had a minimal effect on pore characteristics. This may be due to poor dispersion of ZnAc<sub>2</sub> on the carbon surface. The other impregnated carbons, such as AC-Zn(NO<sub>3</sub>)<sub>2</sub>, AC-Cu(NO<sub>3</sub>)<sub>2</sub>, AC-FeCl<sub>3</sub> and AC/HNO<sub>3</sub>-FeCl<sub>3</sub>, exhibited 20-30% reductions in surface area ( $S_{\text{BET}}$ ) and total pore volume ( $V_0$ ) and a 75-80% reduction in average pore diameter ( $D_{\text{ave}}$ ). DFT micro pore volume ( $V_{\text{micro}}$ ) and total volume ( $V_{\text{total}}$ ) of these samples were reduced 15-20% compared to the parent activated carbon (AC). The data indicate that the carbon surfaces were covered by loaded metals. Greater metal loading resulted in reduced pore volume and surface area for the three samples derived from AC/HNO<sub>3</sub> loaded with varied amounts of FeCl<sub>3</sub> [Figure 3.4.1.1-3(b) & 3.4.1.1-4(b)], but this trend was not observed for the AC-Cu(NO<sub>3</sub>)<sub>2</sub> samples [Figure 3.4.1.1-3(c) & 3.4.1.1-4(c)]. An interpretation of these results is non-uniformity in the samples or the dispersion of the metals on the samples.

Comparison of the pore structure of the parent material (AC) with the activated carbon oxidized by HNO<sub>3</sub> (AC-HNO<sub>3</sub>) shows little difference. This does not support the assertion by Figueiredo [6] that the carbon porous structure could be destroyed by strong oxidative effects such as those produced by HNO<sub>3</sub>.

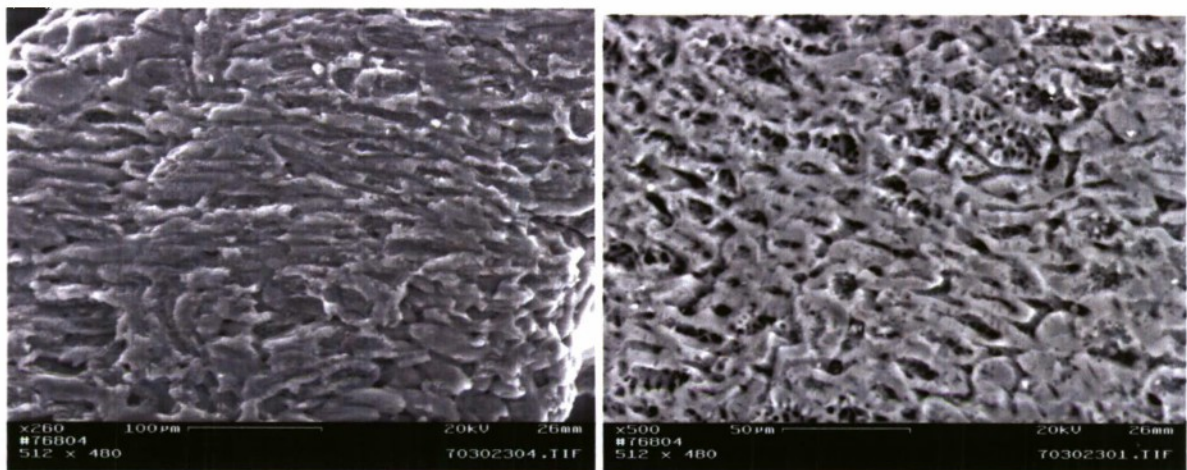
The surface morphologies of the virgin and modified carbons were investigated by SEM and photos of the sample surfaces are shown in Figure 3.4.1.1-5. In comparison to virgin carbon AC [Figure 3.4.1.1-5(a)], AC-HNO<sub>3</sub> [Figure 3.4.1.1-5(b)] has a smoother surface without visible presence of small surface particles, due to the acid treatment and water rinse. Small particles are distributed across the surface of impregnated carbons, with particle shapes varying with the type of metal loaded on the sample [Figure 3.4.1.1-5(c) to 3.4.1.1-5(f)]. For the AC-Zn(NO<sub>3</sub>)<sub>2</sub> sample [Figure 3.4.1.1-5(c)], almost all particles are rectangular in shape and roughly 1  $\mu\text{m}$  in size. These particles are of uniform size and are evenly dispersed on the carbon surface. In comparison, AC-ZnAc<sub>2</sub> [Figure 3.4.1.1-5(d)] is less uniformly distributed and with a variety of particle shapes and the appearance of irregularly shaped agglomerates. These kinds of particle could be the result of poor dispersion on the carbon surface and could be easily removed from the surface. This could be a contributing factor for the observed weak effect that ZnAc<sub>2</sub> impregnation had on the pore structure parameters of activated carbon. The particles deposited on the surface of AC-Cu(NO<sub>3</sub>)<sub>2</sub> [Figure 3.4.1.1-5(e)] have needle shapes of uniform size and are well dispersed. The AC-FeCl<sub>3</sub> sample [Figure 3.4.1.1-5(f)] is characterized by well dispersed deposited particles with irregular shape. The impregnation technique used this study resulted in varied dispersion of the selected metals on the carbon surface and this contributed to the observed differences in pore structure for the modified activated carbons.

***Relationship between the surface characteristics and THT adsorption capacity.*** THT is a saturated molecule that is less reactive, more polar, and more basic than thiophenes, in which neither of the sulfur lone electron pairs is engaged in aromatic  $\pi$ -electron system [17]. Therefore, THT molecule can adhere to the surface through van der Waals force or weak hydrogen bonds between THT and functional groups. Thus it is normally expected that the activated carbons have a higher adsorption capacity when greater numbers of acidic functional groups are available on the carbon surfaces.

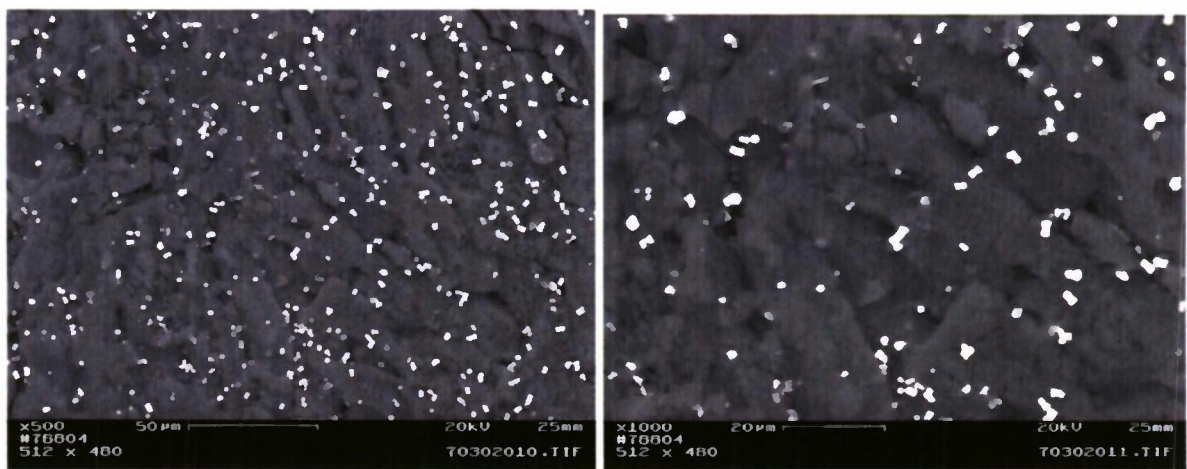




a. AC



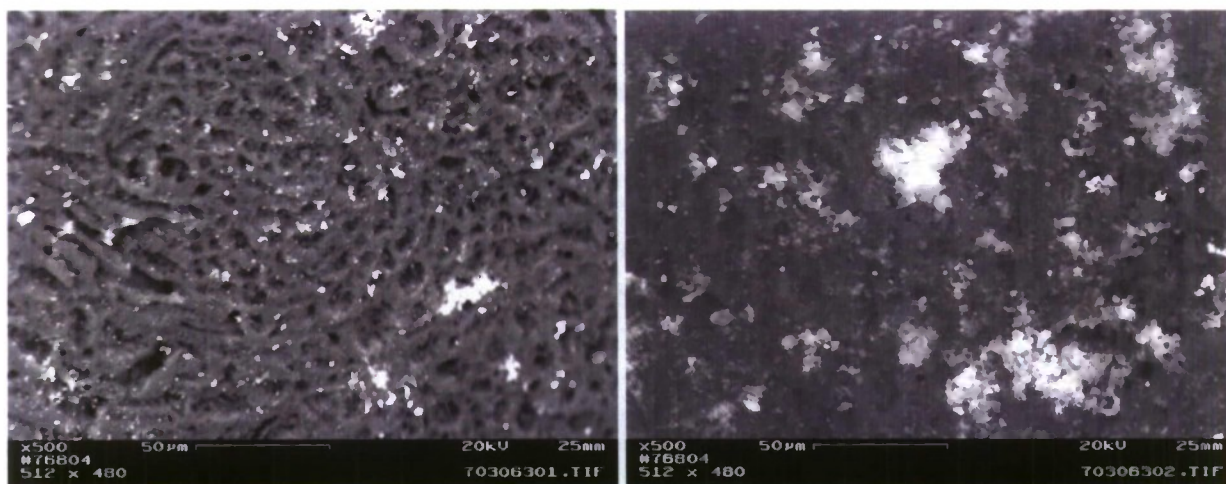
b. AC-HNO<sub>3</sub>



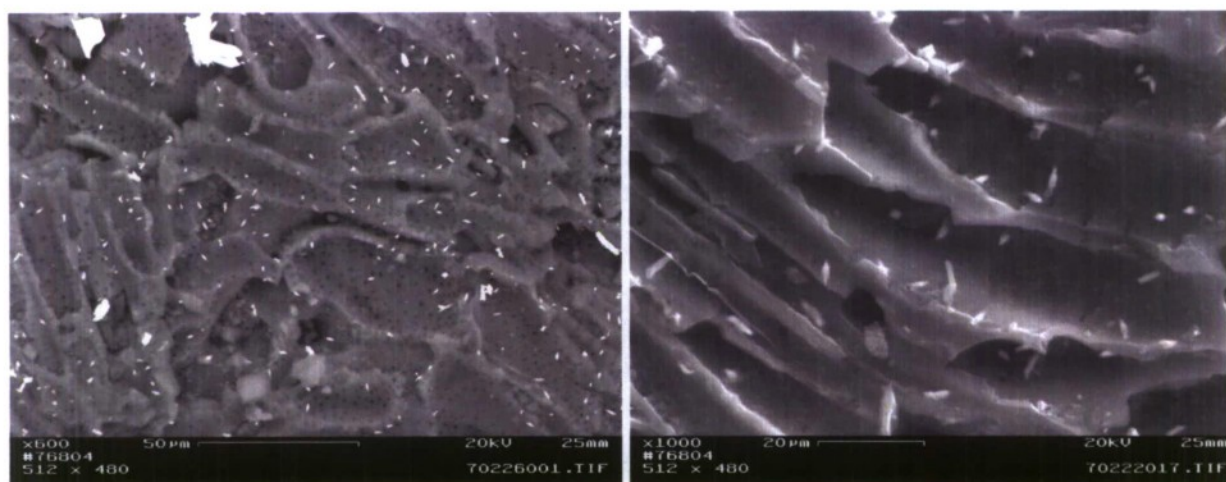
c. AC-Zn(NO<sub>3</sub>)<sub>2</sub>

Figure 3.4.1.1-5. SEM pictures for virgin carbon and modified carbons.

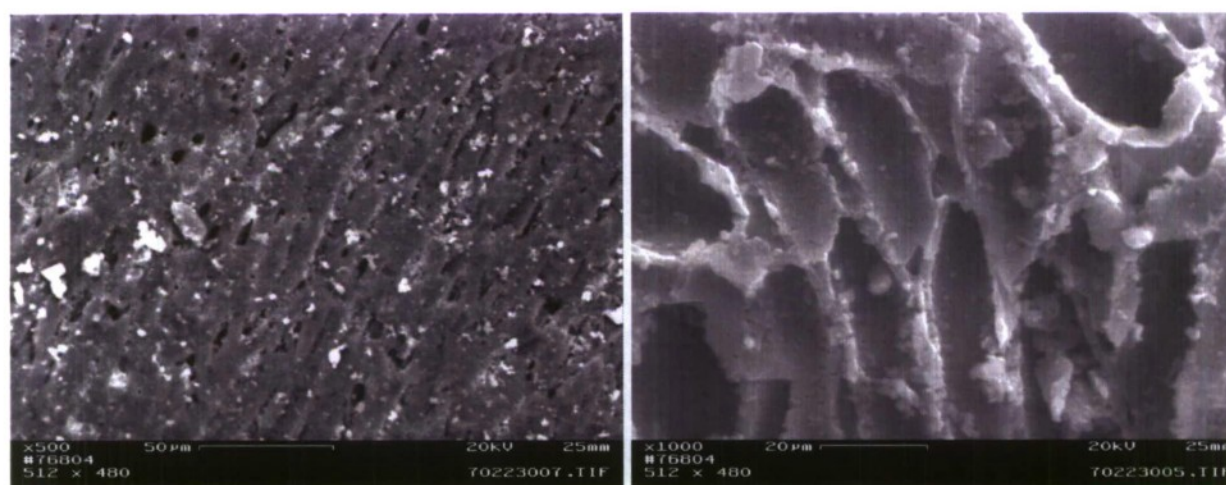




d. AC-ZnAc<sub>2</sub>



e. AC-Cu(NO<sub>3</sub>)<sub>2</sub>



f. AC-FeCl<sub>3</sub>

Figure 3.4.1.1-5 (cont'd). SEM pictures for virgin carbon and modified carbons.

The pore size distributions (Figure 3.4.1.1-4) and the calculated parameters in Table 3.4.1.1-4 of virgin carbon (AC) and oxidized carbon (AC-HNO<sub>3</sub>) were very similar and had higher values of volume and surface area than any of the impregnated metal samples included in Table 3.4.1.1-4. All of these modified carbons had increased THT adsorption capacities compared to the virgin carbon. From this it can be inferred that the primary reason of improvement is due to the surface chemical properties rather than the physical properties summarized in Table 3.4.1.1-4.

It has been demonstrated that modification by oxidation can create acidic functional groups on carbon surfaces, [18] and that these are present largely as carboxylic acid groups with smaller amounts of phenolic hydroxyl groups. The amount of acidic groups depends on the oxidizer and treatment conditions. For example, HNO<sub>3</sub> oxidation can produce a large amount of acid surface groups including carboxylic acid, anhydrides, lactones and phenol groups [6, 9]. H<sub>2</sub>O<sub>2</sub> oxidation, however, generates fewer acidic groups than the HNO<sub>3</sub> treatment [19]. The effect of metal impregnation on the acidity/basicity of carbon surfaces is still not as clear. It is commonly thought that inorganic metals can be ionized on the carbon surface and present the properties of acidity or basicity, depending on the kind of impregnated materials. Hereafter, acidic carbons are defined as those carbons that show acidic behavior and adsorb appreciable amounts of bases but very little of acids; the converse is true for basic carbons. These acidic/basic groups form active sites where sulfur compounds may attach to the carbon surface. For THT adsorption, therefore, the key point of the modification is to increase the acidic density on the carbon surface to accommodate the basicity of the THT molecule.

**Table 3.4.1.1-4. Pore structure parameters of virgin carbon and modified carbons.**

Sample name	$S_{\text{BET}}, \text{m}^2/\text{g}$ ( $P/P_0=0.01-0.1$ )	$V_G, \text{cm}^3/\text{g}$ ( $P/P_0=0.995-0.999$ )	$D_{\text{ave}}, \text{nm}$	Pore structure parameter by DFT calculation			
				$V_{\text{micro}}, \text{cm}^3$ (less than 2nm)	$V_{\text{total}}, \text{cm}^3$ (less than 36nm)	than	$D_w \text{ (mode)}, \text{nm}$
AC	1252.9	0.601	0.960	0.450	0.538		0.600
AC-HNO <sub>3</sub>	1282.6	0.628	0.980	0.434	0.528		0.785
AC-ZnAc <sub>2</sub>	1066.8	0.513	0.962	0.451	0.538		0.785
AC-FeCl <sub>3</sub>	864.4	0.481	0.223	0.306	0.422		0.786
AC-Zn(NO <sub>3</sub> ) <sub>2</sub>	1003.9	0.453	0.181	0.363	0.408		0.686
AC-Cu(NO <sub>3</sub> ) <sub>2</sub> -38	970.7	0.459	0.189	0.350	0.411		0.718
AC-Cu(NO <sub>3</sub> ) <sub>2</sub> -53	998.1	0.473	0.190	0.389	0.426		0.718
AC/HNO <sub>3</sub> -FeCl <sub>3</sub> -38	929.6	0.479	0.206	0.352	0.430		0.751
AC/HNO <sub>3</sub> -FeCl <sub>3</sub> -70	931.0	0.444	0.191	0.334	0.401		0.841
AC/HNO <sub>3</sub> -FeCl <sub>3</sub> -105	855.5	0.396	0.185	0.310	0.355		0.686



Since the acidic functional groups and metals are able to ionize in water and to behave like acids or bases, the acidity/basicity of carbon surface can be determined by measuring the pH of a suspension of carbon particles<sup>10</sup> which is directly related to the number and strength of acidic/basic groups present on the surface. The relationship between the pH values and THT adsorption capacities is presented in Figure 3.4.1.1-6. The data indicate that AC/HNO<sub>3</sub>-FeCl<sub>3</sub> was most acidic with pH ranged from 2.33 to 2.03, whereas those carbons loaded with Na, K metals were more basic. More acidic carbons had greater THT adsorption capacity and this can be used to explain the current results, i.e., the poor adsorption capacity of Group I and the enhanced capacity of Group 3.

The THT adsorption capacities of carbons loaded with varied amounts of AC-Cu(NO<sub>3</sub>)<sub>2</sub> and AC/HNO<sub>3</sub>-FeCl<sub>3</sub> are shown in Figure 3.4.1.1-7. The THT capacity increases linearly with increasing metal loading, indicating that the metals play a role in creating additional adsorption sites. In addition, the pH values of these carbon samples also decrease with increasing metal loading, indicating that more acidic functional groups were created. Thus, increased metal loadings result in increased acidic functional groups and a concomitant increase in THT capacity.

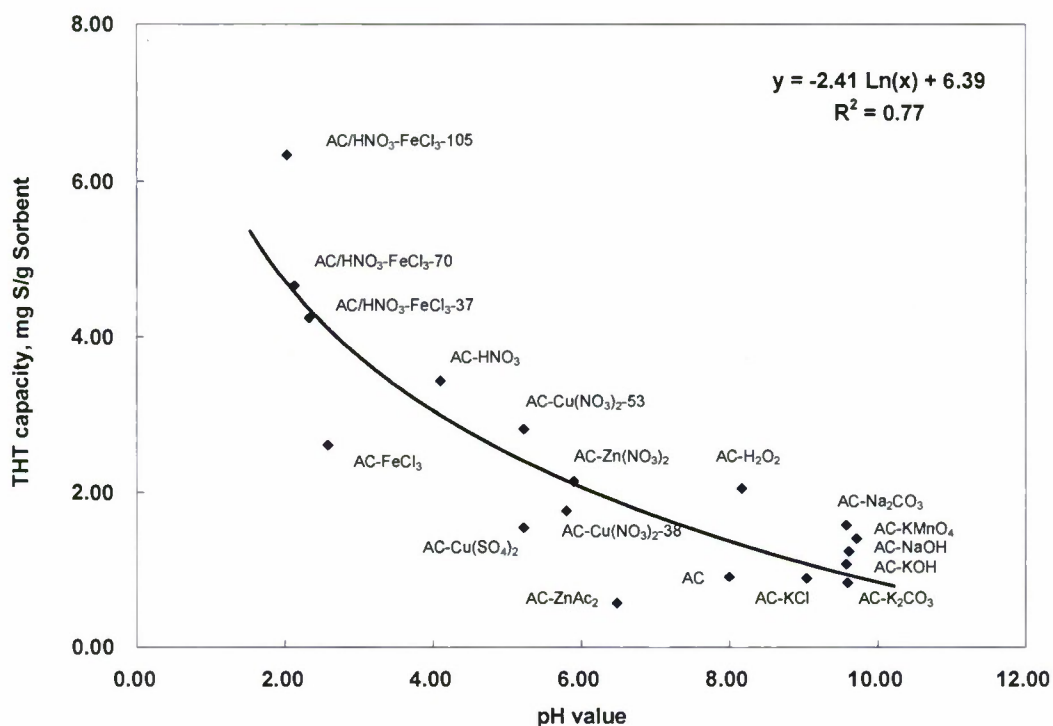


Figure 3.4.1.1-6. The relationship between pH values and THT capacity of carbons.

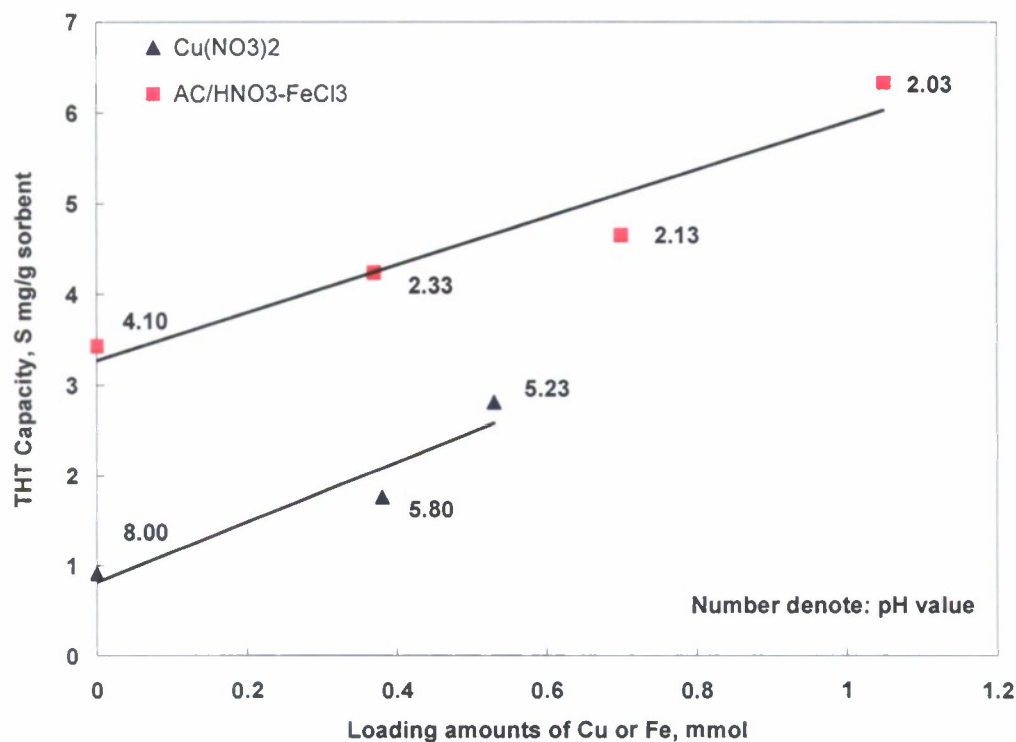


Figure 3.4.1.1-7. Effect of metals loading amounts on the THT capacity of activated carbons.

#### 3.4.1.1.4 References

1. de Wild, P. J.; Nyqvist, R. G.; de Bruijn, F. A.; Stobbe, E. R. *J. Power Sources* **2006**, *159*, 995-1004.
2. Bagreev, A.; Bashkova, S.; Bandosz, T. J. *Langmuir*. **2002**, *18*, 8553-8559.
3. Bandosz, T.; Askew, S.; Kelly, W. R.; Bagreev, A.; Adib, F.; Turk, A. *Water Sci. Technol.* **2000**, *42*, 399-401.
4. Szekely, J., J. W. Evans, and H.Y. Sohn, *Gas-Solid Reactions*. Academic Press: San Francisco, USA, 1976.
5. Adamson, A. W., *Physical Chemistry of Surfaces*. John Wiley and Sons, Inc: New York, USA, 1990.
6. Figueiredo, J. L.; Pereira, M. F. R.; Freitas, M. M. A.; Orfao, J. J. M. *Carbon* **1999**, *37*, 1379-1389.
7. Chiang, H.-L.; Tsai, J.-H.; Chang, D.-H.; Jeng, F.-T. *Chemosphere* **2000**, *41*, 1227-1232.
8. Hagio, H.; Fukagawa, Y. *J. Jpn. Petrol. Inst.* **2006**, *49*, 98-101.
9. Otake, Y.; Jenkins, R. G. *Carbon* **1993**, *31*, 109-21.
10. Bashkova, S.; Bagreev, A.; Bandosz, T. J. *Catal. Today* **2005**, *99*, 323-328.
11. Tamai, H.; Nagoya, H.; Shiono, T. *J. Colloid Interf. Sci.* **2006**, *300*, 814-817.
12. Kim Dae, J.; Yie Jae, E. *J. Colloid Interf. Sci.* **2005**, *283*, 311-315.
13. Yang, R. T.; Hernandez-Maldonado, A. J.; Yang, F. H. *Science* **2003**, *301*, 79-81.
14. Satokawa, S.; Kobayashi, Y.; Fujiki, H. *Appl. Catal. B-Environ.* **2005**, *56*, 51-56.
15. Kim, H.-T.; Jun, K.-W.; Potdar, H. S.; Yoon, Y.-S.; Kim, M.-J. *Energ. Fuel.* **2007**, *21*, 327-332.

16. Cui, H.; Reese, M. A.; Turn, S. Q., Removal of sulfur compounds from synthetic natural gas using modified activated carbon. *Abstracts of Papers, 234th ACS National Meeting, Boston, MA, United States, August 19-23, 2007* **2007**, FUEL-221.
17. Bezverkhyy, I.; Bouguessa, K.; Geantet, C.; Vrinat, M. *Appl. Catal. B-Environ.* **2006**, *62*, 299-305.
18. Chingombe, P.; Saha, B.; Wakeman, R. J. *Carbon* **2005**, *43*, 3132-3143.
19. Moreno-Castilla, C.; Lopez-Ramon, M. V.; Carrasco-Marin, F. *Carbon* **2000**, *38*, 1995-2001.

#### **3.4.1.1.5 Paper Resulting from this Effort**

Cui, H., S.Q. Turn, and M.A. Reese. 2008. Adsorptive removal of tetrahydrothiophene (THT) from synthetic natural gas on modified activated carbons. *Energy & Fuels*. 22(4) pp. 2550-2558.



### 3.4.1.2 Absorption/Desorption of Dimethylsulfide on Activated Carbon Modified with Iron Chloride

#### 3.4.1.2.1 Scope of Work and Approach

Dimethylsulfide (DMS) is a non-polar, stable, organic, reduced sulfur compound present in the natural environment. It is the dominant sulfur compound in seawater [1, 2] and is also produced in industrial processes. DMS can be used as an ingredient in odorants for pipeline gas due to its stable chemical characteristics even when exposed to black iron pipes and tanks [1]. Sulfur odorants are added to pipeline gas as a safety precaution but must be completely removed if the pipeline gas is to be used as a feedstock for  $H_2$  production to supply fuel cells. Thus sulfur removal is an important step in fuel processing.

One method for sulfur odorant removal from pipeline gas is adsorption using activated carbon [1, 3-16]. Modification of carbon surfaces by using either oxidation or impregnation has been explored as a method to improve sulfur adsorption capacity and consequently reduce the sorbent consumption. Greater sulfur capacity results from the creation of more functional groups or active adsorption sites on the carbon surface. Adsorptive sites may oxidize reduced sulfur molecules, creating bigger molecules which are more easily adsorbed in the micropores of activated carbon. An example of this is the improvement of methyl mercaptan (MM) adsorptive capacity by carbon surface modification. Oxygen functional groups facilitate the oxidation of MM to form dimethyl disulfide (DMDS) [8, 13]. DMDS is a larger molecule with a higher boiling point and is more easily adsorbed in the carbon micropores.

Similar efforts have been attempted to remove DMS, which is regarded as the most difficult sulfur compound [5, 12, 17, 18] to remove from pipeline gas by adsorption. Oxidation/adsorption is one applicable path for DMS occupancy on the carbon surface and the activated carbon surface can be modified to enhance its sulfur capacity. In a previous investigation using pipelined synthetic natural gas (SNG) [17, 18], activated carbon modified with iron chloride ( $FeCl_3$ ) solution had a slightly greater DMS adsorptive capacity ( $0.03 \text{ mg S g}^{-1}$  carbon) compared with the 12 other virgin and modified carbons that displayed almost zero capacity. The role of  $FeCl_3$  on oxidation/adsorption has been pointed out in the case of MM [19], which was assumed to be oxidized to DMDS by the catalytic participation of iron on the carbon surface. For DMS adsorption, however, no such investigations were found in the literature. Efforts to improve the adsorptive capacity of activated carbon for DMS by means of surface modification would benefit from a better understanding of the adsorption behavior and mechanism.

An objective of this work is to investigate the adsorption behavior and mechanism of DMS on activated carbon sorbent that was modified with  $FeCl_3$ . This effort was based on the analysis of sulfur species removed from sorbent loaded with DMS using mild extraction with solvent and temperature programmed desorption (TPD). As a reference, similar tests were conducted to investigate MM adsorption/desorption behaviors using the same carbon sorbents. Experimental results could verify if the oxidation/adsorption mechanism can be applied on the MM and DMS adsorption on the modified carbons.

#### 3.4.1.2.2 Experimental

**Sorbents preparation and properties.** A coconut activated carbon (OLC Plus 12x30, Calgon Carbon Corporation) was used as the parent carbon in this study.  $FeCl_3$  was loaded using an

impregnation method to produce a concentration of 0.4 mmol metal ( $\text{Fe}^{3+}$ ) per gram carbon. Details of the impregnation process can be found elsewhere [18, 20].

The basic pore properties for the original and modified carbon sorbents are presented in Table 3.4.1.2-1. Nitrogen (liquid  $\text{N}_2$ ) adsorption/desorption isotherms for the samples were measured at 77 K (Autosorb<sup>®</sup>-1, Quantachrome Instruments, Boynton Beach, FL). Before the measurements, samples were heated and degassed at 110 °C for 2 hours under a vacuum of  $10^{-5}$  torr ( $1.33 \times 10^{-7}$  Pa). Specific surface area ( $S_{\text{BET}}$ ) was calculated by using the multipoint BET method in the relative pressure ( $P/P_0$ ) range of 0.01-0.1. The total pore volume ( $V_0$ ) and the average pore diameter ( $D_{\text{ave}}$ ) were calculated from the amount of gas adsorbed at the related pressure of 0.995-0.999. In addition, density functional theory (DFT) was used to analyze the pore structure parameters, including micropore volume ( $V_{\text{micro}}$  – pore width less than 2 nm), total pore volume ( $V_{\text{total}}$  – pore width less than 36 nm), and mode pore width ( $D_w$ ). The DFT calculation method is provided from the Autosorb<sup>®</sup>-1 data processing software and assumes that the activated carbon contains slit-shaped pores.

**Experimental apparatus and analysis process.** The laboratory scale apparatus, consisting of a sulfur gas generator, sorbent column, and sulfur detector, is shown in Figure 3.4.1.2-1. The trace gas generator (Model CO395, Kin-Tek Laboratories, La Marque, TX,) was loaded with a DMS permeation tube (KIN-TEK Part No. HRT-006.50-1006/40) as a sulfur source. Permeation tubes provide a calibrated mass emission rate at constant temperature under an inert purge flow. A DMS emission rate of  $1268 \text{ ng min}^{-1}$  at 40 °C was combined with an  $\text{N}_2$  carrier gas flow to provide a gas with regulated DMS concentration. A permeation tube (KIN-TEK Part No. SRT-2-010.00-1004/50) with an emission rate of  $1015 \text{ ng MM min}^{-1}$  at 50 °C was used for the MM tests.

**Table 3.4.1.2-1. Properties of activated carbon sorbents.**

Sample name	$S_{\text{BET}}$ , $\text{m}^2/\text{g}$ ( $P/P_0=0.01-0.1$ )	$V_0$ , $\text{cm}^3/\text{g}$ ( $P/P_0=0.995-0.999$ )	$D_{\text{ave}}$ , nm	Pore structure parameter by DFT calculation		
				$V_{\text{micro}}$ , $\text{cm}^3$ (less than 2nm)	$V_{\text{total}}$ , $\text{cm}^3$ (less than 36nm)	$D_w$ (mode), nm
AC	1252.9	0.601	0.960	0.450	0.538	0.600
AC- $\text{FeCl}_3$	864.4	0.481	0.223	0.306	0.422	0.786

$S_{\text{BET}}$  – specific surface area;  $V_0$  – total pore volume;  $D_{\text{ave}}$  – average pore diameter;  $V_{\text{micro}}$  – pore width less than 2 nm;  $V_{\text{total}}$  – pore width less than 36 nm;  $D_w$  – mode pore width; DFT – density functional theory.



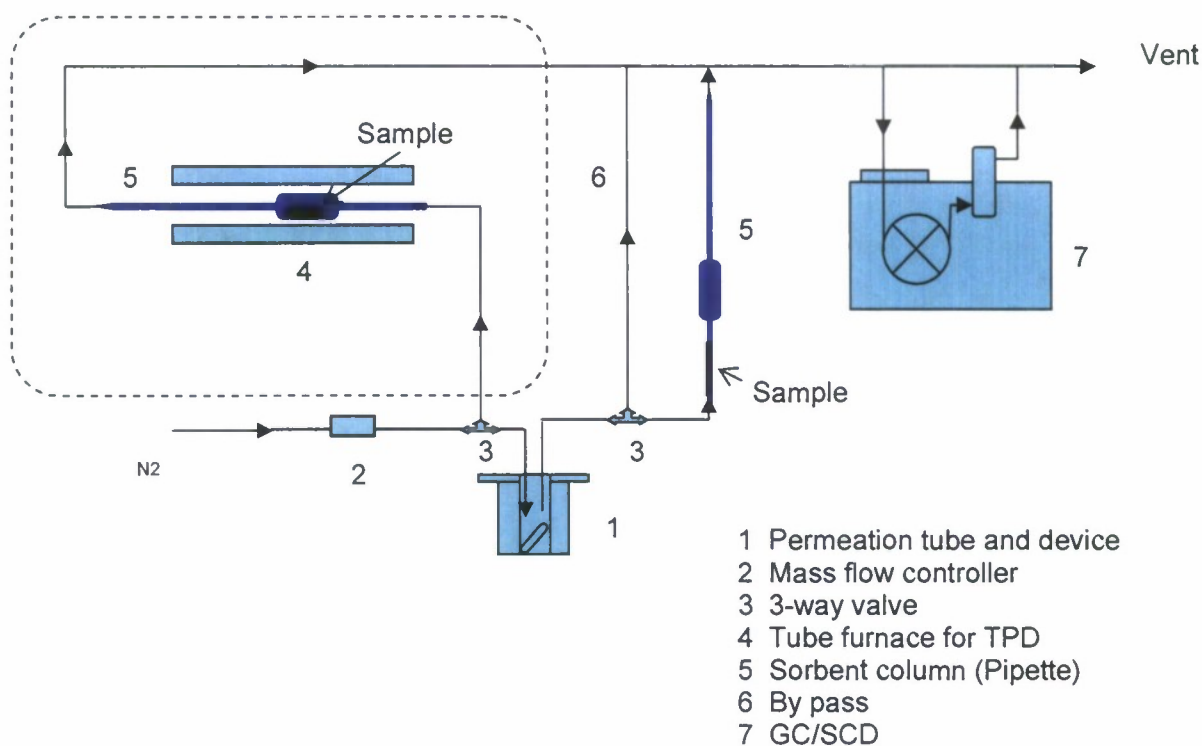


**Figure 3.4.1.2-1. Experimental setup for carbon sorbents adsorption and desorption.**

A 35 ml glass pipette was used as a sorbent column. The column was oriented vertically for adsorption and extraction tests, and was placed in a tube furnace horizontally for TPD tests. Two types of adsorption tests were performed. The first type included breakthrough and TPD tests, using 0.2 g sorbent samples. The sulfur capacity (milligram S per gram activated carbon) was also determined from these tests. The second type was quantitative adsorption tests, in which 1.5 g carbon sorbent was subjected to adsorption of DMS for 15 to 16 hours without experiencing break through. The resulting samples contained a known mass of S and were used in subsequent extraction and TPD tests to allow S mass balances to be performed. During both types of adsorption tests, the DMS permeation tube device was used to generate a N<sub>2</sub> stream containing 1.40 ppm DMS at a flow rate of  $326 \pm 2 \text{ ml min}^{-1}$ . Both types of adsorption tests were conducted at ambient conditions (typically 26 °C and 0.1 MPa).

After the adsorption tests were completed, sorbents loaded with DMS were extracted with n-octane. A 0.2-g sorbent sample loaded with DMS from the quantitative adsorption tests was packed into a vertically-positioned pipette. Each sample was leached three times with 10 ml of n-octane. The resulting 30 ml solvent volume was analyzed for sulfur compounds. This was a mild extraction process that was not expected to extract all adsorbed compounds from the sorbents and the solid sample in the pipette was subsequently subjected to TPD testing. In addition, 0.2-g samples of non-extracted sorbents from the same quantitative adsorption tests were subjected to TPD testing. The sample temperature was ramped from 25 °C to 300 °C at  $1^\circ\text{C min}^{-1}$  using a programmable tube furnace. N<sub>2</sub> was used as a sweep gas at a flow of  $326 \pm 2 \text{ ml min}^{-1}$  and the exit gas was analyzed for sulfur compounds.



Gaseous samples were analyzed for sulfur using a Shimadzu 2014 gas chromatograph (GC) equipped with a capillary column (Rtx-1, 60m-0.53-7um, Restek Corporation) and sulfur chemiluminescence detector (SCD) (Sievers Model 355, GE Analytical Instruments, Boulder, CO). Helium served as the carrier gas and a six-port sampling valve equipped with a 125  $\mu$ l sample loop was used to make automatic injections. In each analysis the column temperature was held for 1 min at 50 °C, ramped to 125 °C at 20 °C min<sup>-1</sup>, ramped a second time to 180 °C at 10 °C min<sup>-1</sup>, held at 180 °C for 1 min, and finally cooled to 50 °C at 100 °C min<sup>-1</sup>. Thus, effluent gas was able to be sampled and analyzed with a cycle time of 15 min. In addition, DMS was analyzed from a bypass path before and after the adsorption and desorption tests, to make calibrations and to confirm that the system was operating stably.

Sulfur analyses of the liquid samples were performed by manual injection on the same GC using an injection volume of 2  $\mu$ l. Because the sulfur SCD produces an equimolar response to sulfur, independent of the host sulfur compound, 25 ppm ( $\pm 0.5\%$ ) H<sub>2</sub>S calibration gas (Scotty® 58, Scott Specialty Gases) was used in the sulfur analysis for the liquid samples. Other analytical parameters were the same used for the gas samples.

The test procedures outlined above for DMS were used for the MM tests as well.

#### 3.4.1.2.3 Technical Accomplishments

**Breakthrough curves.** The adsorption of DMS (1.40 ppm) in an N<sub>2</sub> carrier gas on activated carbon sorbents were carried out to estimate sulfur capacities and evaluate sulfur capture capabilities. Figure 3.4.1.2-2 shows the breakthrough curves of virgin carbon (AC) and carbon loaded with FeCl<sub>3</sub> (AC-FeCl<sub>3</sub>). The adsorptive capacities of the two carbon sorbents are also shown in this figure; 3.32 mg S g<sup>-1</sup> sorbent for AC-FeCl<sub>3</sub> and 2.23 mg S g<sup>-1</sup> sorbent for AC. The adsorption capacity was calculated by integrating the area under the DMS breakthrough curve and subtracting it from the total sulfur input up to the point of breakthrough. The breakthrough time is defined as the point at which the DMS concentration in the effluent gas reached 0.2 ppm. Obviously, the impregnation of FeCl<sub>3</sub> leads to increases in the breakthrough time and in the amount of DMS adsorbed by the carbon, despite a notable decrease in the surface area, micropore area, and volume (data shown in Table 3.4.1.2-1). Both samples primarily possess micropores that are less than 2 nm in width and the impregnation of FeCl<sub>3</sub> did not change the pore size distribution to a great extent. Complete analysis of sample pore size distributions have been report elsewhere [20]. From this it can be inferred that the significant factor in the improvement of DMS capacity results from the new chemical properties produced by the addition of FeCl<sub>3</sub>, rather than changes in the physical properties such as pore surface area and pore structure of carbon phase.

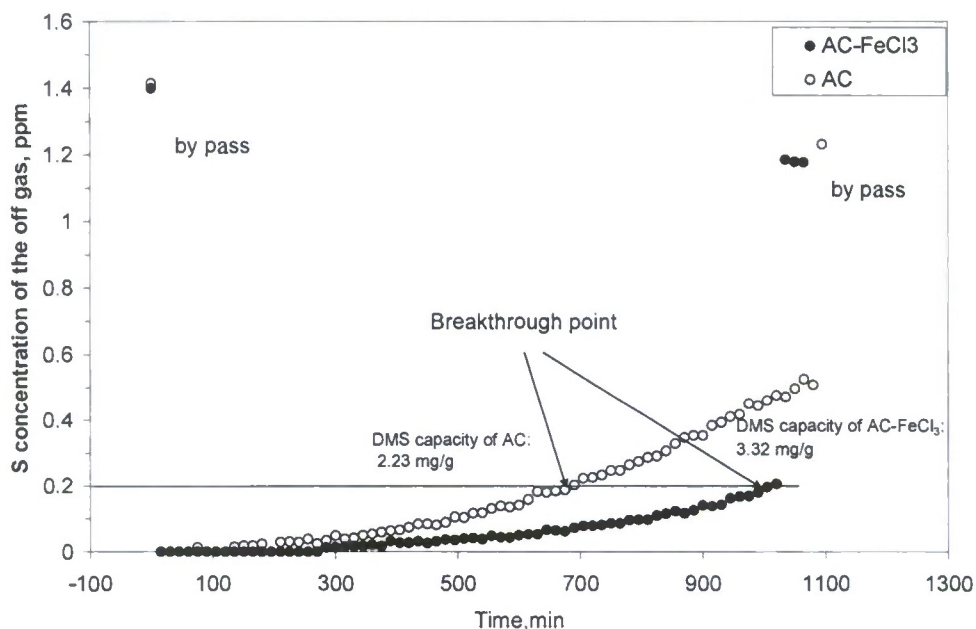


**Figure 3.4.1.2-2. DMS breakthrough curves for activated carbon (AC) and activated carbon impregnated with  $\text{FeCl}_3$  (AC- $\text{FeCl}_3$ ).**

Adsorption of MM (1.43ppm in  $\text{N}_2$ ) on AC and AC- $\text{FeCl}_3$  was also carried out. Breakthrough was not observed for either of the sorbents during the test time up to 20 hours, indicating that MM is more easily captured by the carbon sorbents than DMS.

**Extraction analysis.** If the oxidation/adsorption reaction occurs on the carbon surface, then it would be expected that the oxidation products could be dissolved and recovered by solvent extraction and that sulfur compounds could be identified by analysis of the solvent. The properties of possible oxidation products with their precursor are listed in Table 3.4.1.2-2.

**Table 3.4.1.2-2. Basic properties of dimethylsulfide (DMS).**

Chemical name	MM	DMDS	DMS	DMSO	DMSO2
Molecular formula	$\text{H}_3\text{C-SH}$	$\text{H}_3\text{C-S-S-CH}_3$	$\text{H}_3\text{C-S-CH}_3$	$\begin{array}{c} \text{O} \\    \\ \text{H}_3\text{C-S-CH}_3 \end{array}$	$\begin{array}{c} \text{O} \\    \\ \text{H}_3\text{C-S-CH}_3 \\    \\ \text{O} \end{array}$
Molar mass (g/mol)	48.11	94.19	62.13	78.13	94.13
Density, (g/cm <sup>3</sup> )	-	1.06	0.840	1.100	-
Melting point (°C)	-123	-85	-98	18.5	109
Boiling point (°C)	5.95	109	37	189	238

The MM adsorption and oxidation to DMDS is described by three global reactions steps: equations (1) to (3). MM is adsorbed onto the activated carbon surface and then oxidized by the oxidation functional groups or adsorbed oxygen. The product DMDS is adsorbed more strongly than MM due to its larger size and higher boiling point. Metal impurities (such as FeCl<sub>3</sub>) could play important roles in catalytic oxidation, since metal impurities can transfer oxygen to the adsorbed MM. A more detailed discussion of MM adsorption mechanism can be found elsewhere. [21]

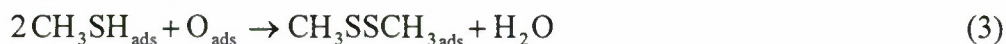
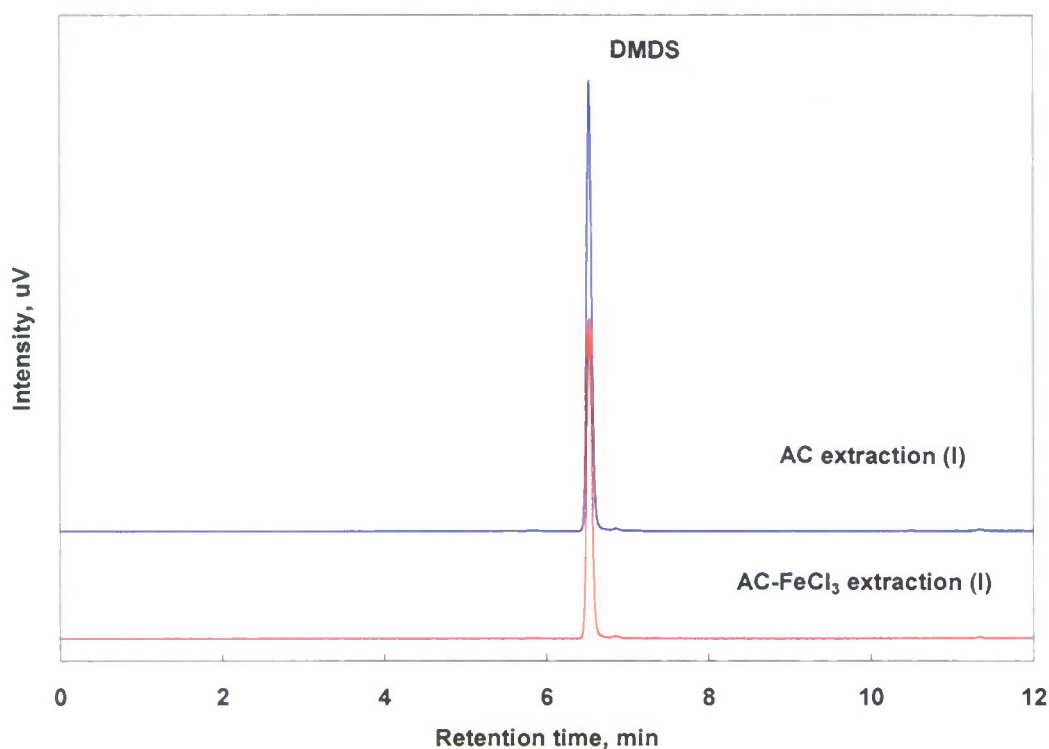


Figure 3.4.1.2-3 shows the sulfur speciation results by GC/SCD analysis of the extract samples resulting from n-octane leaching of AC and AC-FeCl<sub>3</sub> quantitatively loaded with MM. DMDS was detected as the single peak in the chromatogram indicating that DMDS was formed on the carbon surface during MM adsorption process. AC and AC-FeCl<sub>3</sub> were equally capable of converting MM to DMDS at these test conditions, as no other sulfur compounds were observed in the extracts. Recall that MM breakthrough was not obtained for AC or AC-FeCl<sub>3</sub> over a 20-hour test period. Likewise the current data does not reveal distinct difference between the two sorbents and does not illuminate the role of impregnated FeCl<sub>3</sub> on the MM oxidation/adsorption process. It is reasonable to believe, however, that FeCl<sub>3</sub> is an oxidant that can provide or create more active sites for sulfur compounds on the carbon surface. These adsorption sites perhaps are functional groups containing oxygen, metal anions (Fe<sup>3+</sup>), or chlorine with negatively-charged ions (Cl<sup>-</sup>).





**Figure 3.4.1.2-3. Chromatograms of sulfur species in n-octane-extract of AC and AC-FeCl<sub>3</sub> adsorbed with MM.**

It is noted that the molecular structure of DMS is different with that of MM. DMS molecule does not have the polar group (-SH) that MM does and it includes two pairs of lone electrons around the S atom. This gives a higher nucleophilicity that could be attacked by an electrophile. The possible oxidation products would be dimethyl sulfoxide (DMSO) by the attack of one oxygen atom, or dimethyl sulfone (DMSO<sub>2</sub>) by the attack of two oxygen atoms. These oxidation products have bigger molecular sizes and considerably higher boiling points as shown in Table 3.4.1.2-2 and could be easier to adsorb in micropores of activated carbons. A possible path for the oxidation/adsorption process is shown in equation (4).

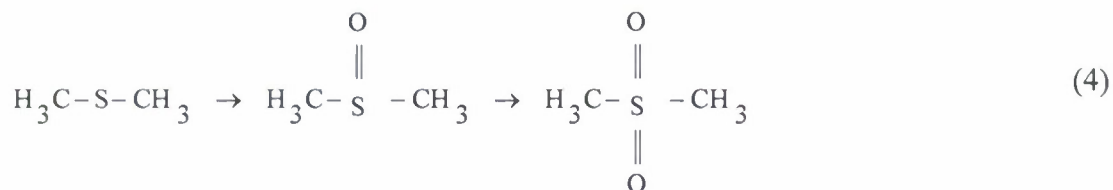
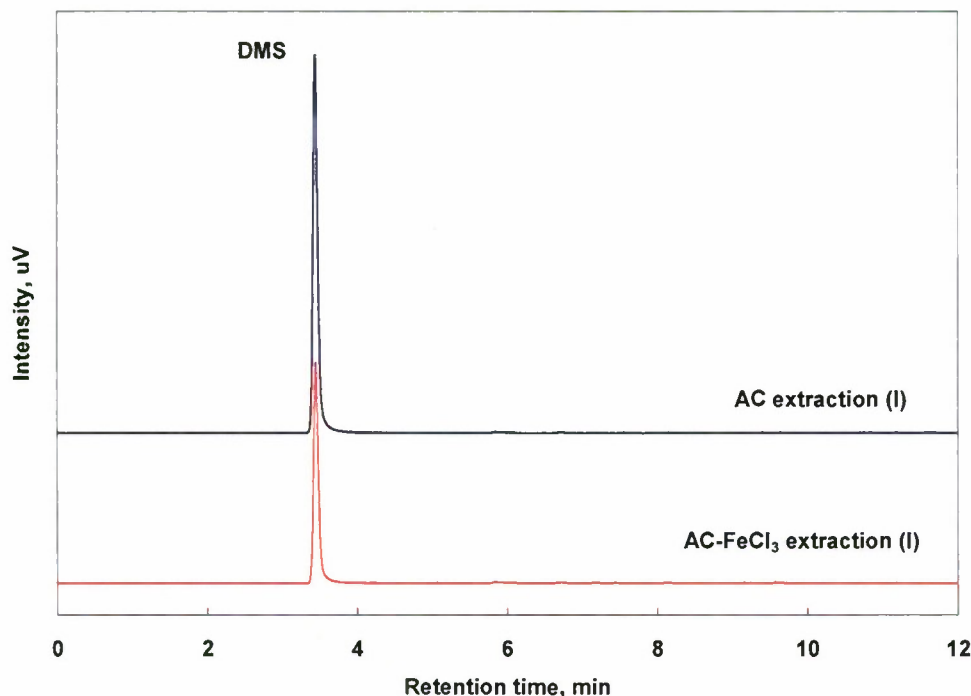


Figure 3.4.1.2-4 shows the sulfur speciation results by GC/SCD analysis of the extract samples resulting from n-octane leaching of AC and AC-FeCl<sub>3</sub> quantitatively loaded with DMS. DMS was detected as the single peak in the GC profiles, and no other sulfur compounds were observed in either of the extracts. This indicates that DMS is the only extractable compound occupying the carbon surfaces of both AC and AC-FeCl<sub>3</sub>. It also suggests that adsorption plays an important role in the increased DMS capacity displayed by AC-FeCl<sub>3</sub> (Figure 3.4.1.2-1) rather

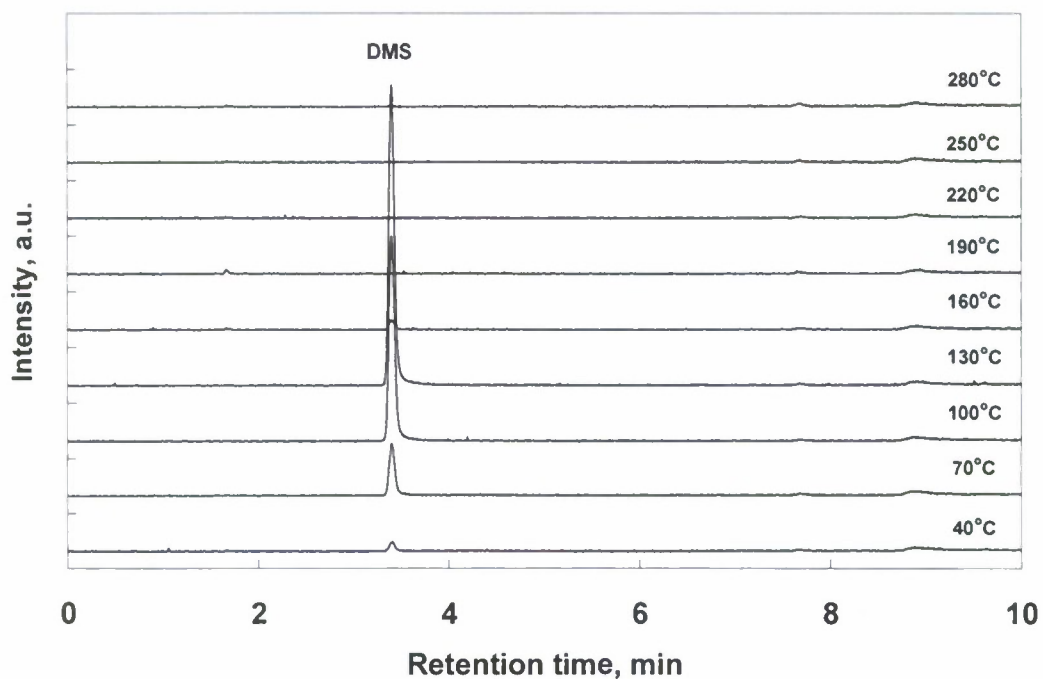
than adsorption/oxidation of DMS on the carbon surface. Unlike methyl mercaptan (MM) that has both polar (-SH) and non-polar (-CH<sub>3</sub>) functional groups, DMS lacks the polar group (-SH) that would result in strong affinity towards other polar functional groups on the carbon surface.



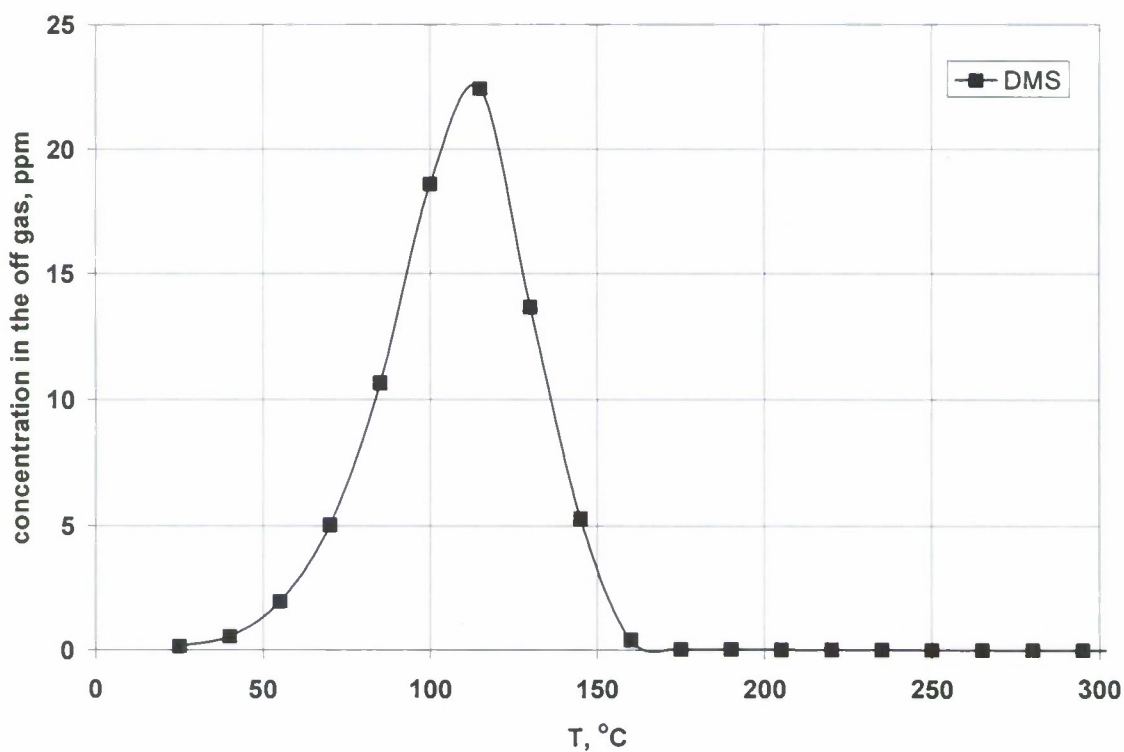
**Figure 3.4.1.2-4. Chromatograms of sulfur species in n-octane-extract of AC and AC-FeCl<sub>3</sub> adsorbed with DMS.**

**Temperature programmed desorption (TPD).** Adsorption/oxidation mechanism cannot explain the increased DMS capacity of AC-FeCl<sub>3</sub>, since no sulfur compounds but DMS were detected in the extract samples. TPD was used to gain insight into the role of FeCl<sub>3</sub> in the improvement of DMS capacity and the possible adsorption mechanism for DMS on the carbon surface.

Figures 3.4.1.2-5(a) and 3.4.1.2-6(a) show GC SCD chromatograms from analyses of the N<sub>2</sub> sweep gas at the exit of the apparatus for TPD tests of sorbents AC and AC-FeCl<sub>3</sub>, respectively, that had previously used in DMS adsorption tests. The relationships of sulfur compound concentrations in the off gas to desorption temperatures are presented in Figures 3.4.1.2-5(b) and 3.4.1.2-6(b).



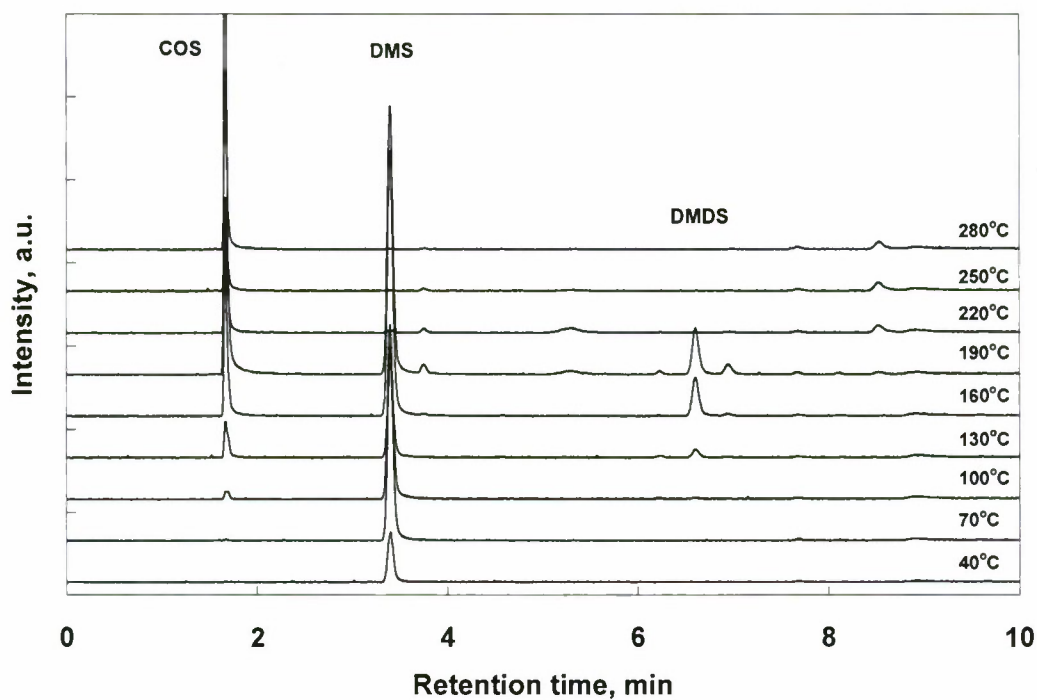
(a)



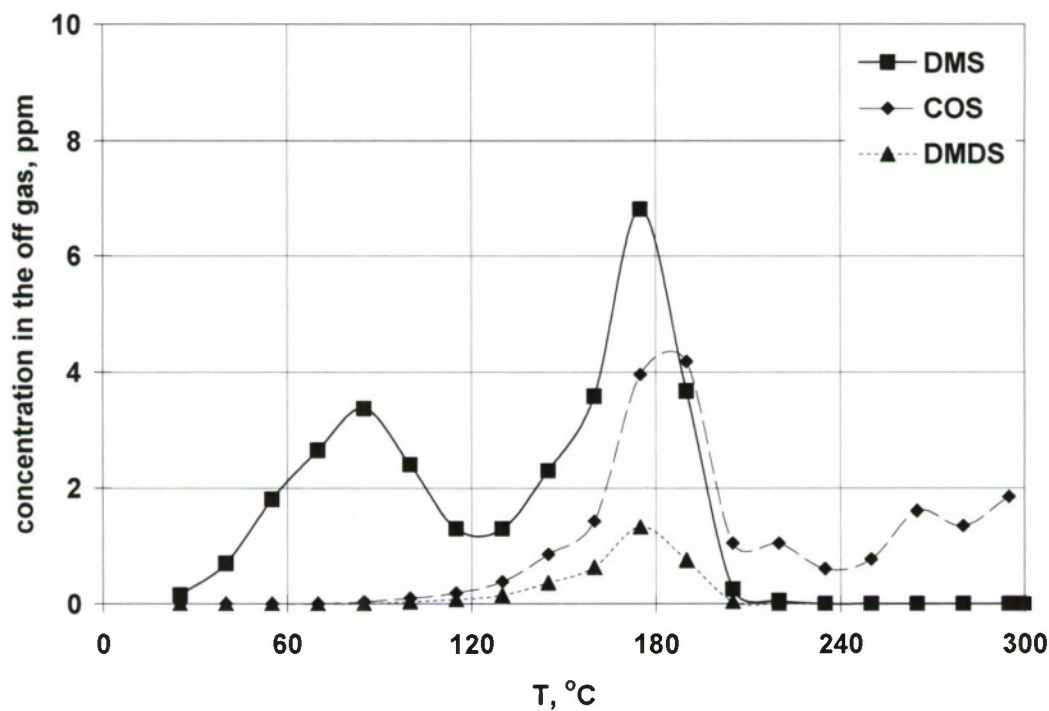
(b)

Figure 3.4.1.2-5. GC SCD chromatograms (a) and associated TPD profiles (b) from analyses of the  $N_2$  sweep gas at the exit of the test apparatus during thermal desorption of the AC samples with DMS adsorbed.





(a)



(b)

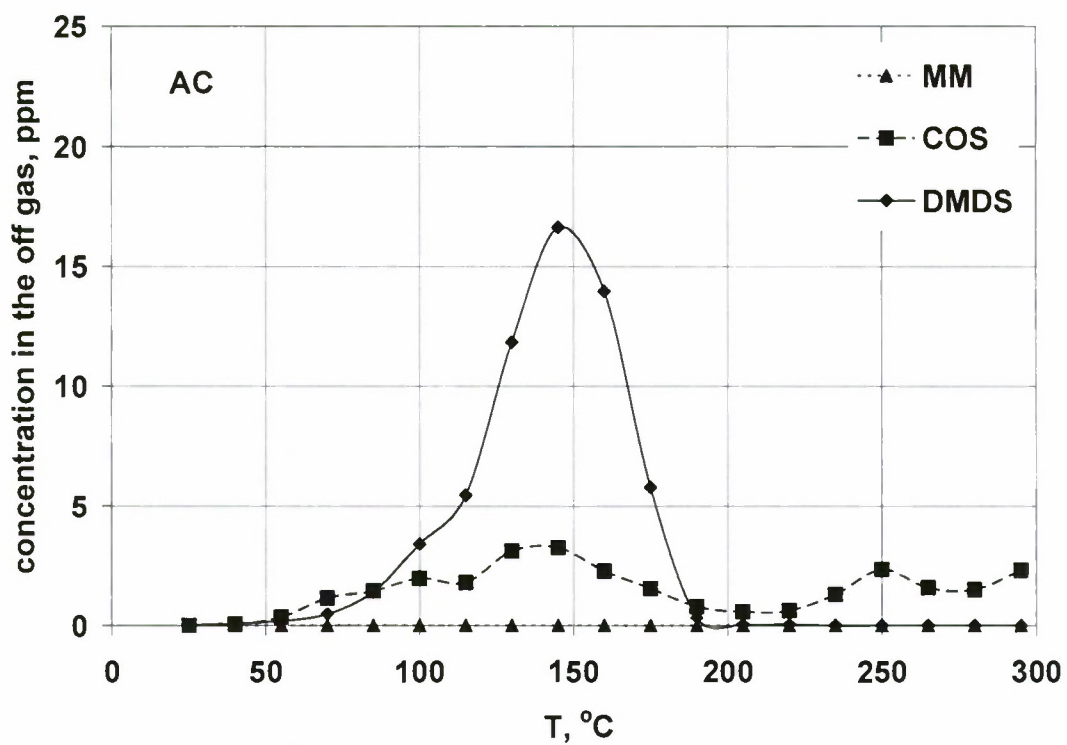
Figure 3.4.1.2-6. GC SCD chromatograms (a) and associated TPD profiles (b) from analyses of the  $N_2$  sweep gas at the exit of the test apparatus during thermal desorption of the  $AC-FeCl_3$  samples with DMS adsorbed.

As shown in Figure 3.4.1.2-5, only DMS was found to be released in the TPD test of sorbent AC. DMS was first detected at room temperature (25 °C), reached a maximum at ~115 °C, and completed desorption at ~160 °C. DMS, COS, and DMDS were detected in the effluent gas generated from AC-FeCl<sub>3</sub> during the TPD process as shown in Figure 3.4.1.2-6. The desorption of DMS has a bimodal relationship to temperature with maxima at 85 °C and 175 °C. At temperatures above 120 °C, COS and DMDS were also detected in the effluent gas, accompanying DMS.

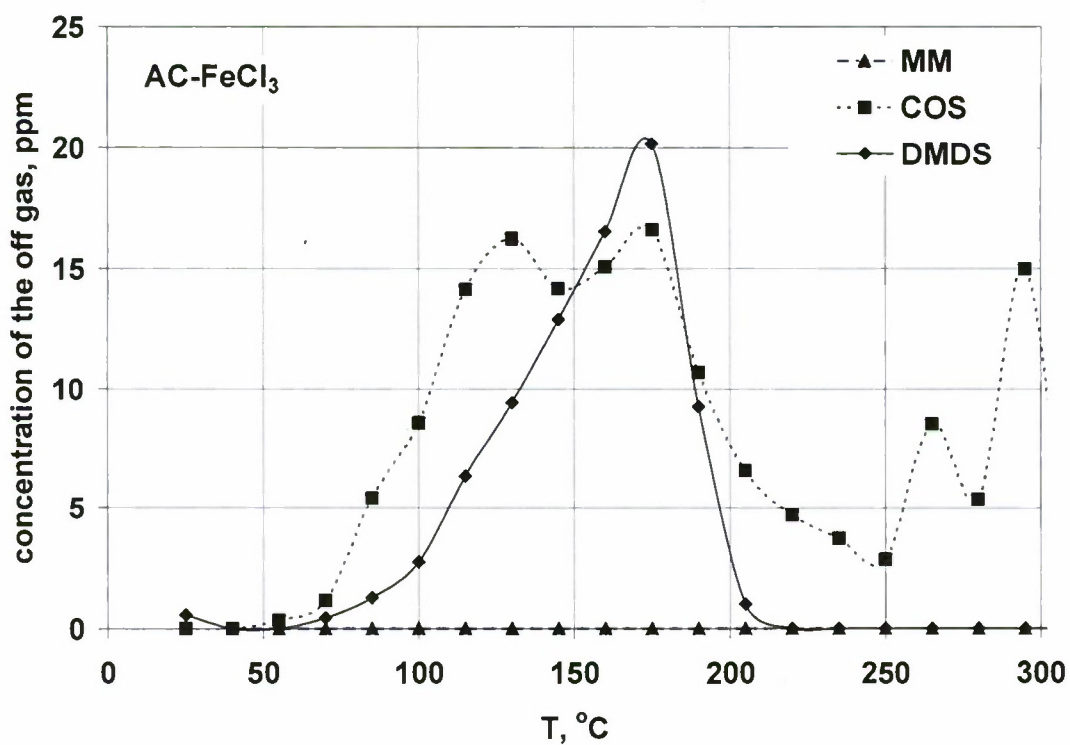
Comparing Figures 3.4.1.2-5(b) and 3.4.1.2-6(b) shows that the first DMS release peak for AC-FeCl<sub>3</sub> has the same temperature range observed for AC. This peak reflects a weak interaction of DMS with the carbon phase. The second DMS peak appeared at higher temperature and was only observed for AC-FeCl<sub>3</sub> indicating that FeCl<sub>3</sub> provides new adsorption sites on the modified carbon surface. The higher release temperature reflects a stronger interaction between the DMS molecules and these new adsorption sites.

The bimodal desorption peaks are not found in the TPD profiles shown in Figures 3.4.1.2-7(a) and 3.4.1.2-7(b) for sorbents AC and AC-FeCl<sub>3</sub> with MM adsorbed. DMDS was a primary sulfur compound detected at the exit of TPD processes for both AC and AC-FeCl<sub>3</sub> and no MM was detected. This verifies that adsorption/oxidization of MM occurs on the carbon surface and the resulting oxidization product is DMDS. Moreover, a single TPD peak of DMDS indicates that FeCl<sub>3</sub> does not provide another adsorptive position for DMDS on the carbon surface. If it did, multiple peaks indicating different adsorption paths would be detected.

It should be noted that DMDS and COS were also found in the TPD processes for AC-FeCl<sub>3</sub> loaded with DMS, but not found in its extract sample, as shown in Figures 3.4.1.2-4 and 3.4.1.2-6. These sulfur compounds are regarded as the interaction products of DMS and surface C-O complexes generated during TPD at elevated temperatures with the catalysis of FeCl<sub>3</sub>. Similarly, COS is also found in the TPD process gas produced from AC and AC-FeCl<sub>3</sub> adsorbed with MM. Greater amounts of COS were released from the AC-FeCl<sub>3</sub> test, indicating that FeCl<sub>3</sub> may serve as a catalyst in the decomposition reaction. The detailed reaction path needs to be explored further.



(a)



(b)

Figure 3.4.1.2-7. TPD profiles during thermal desorption of AC (a) and AC-FeCl<sub>3</sub>(b) with MM adsorption.

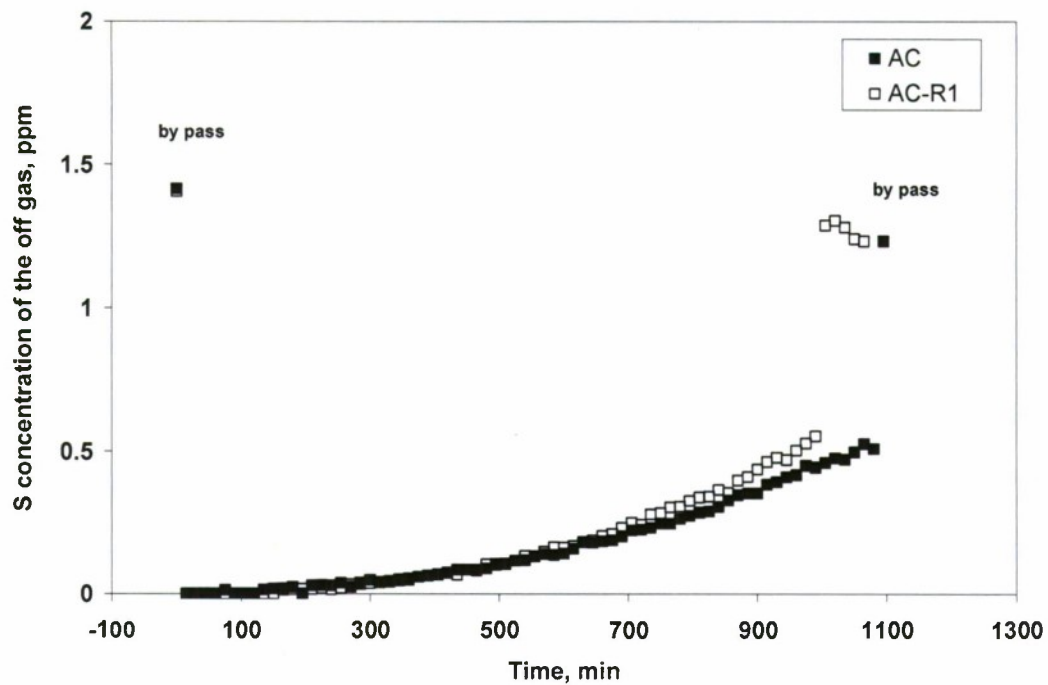


**Thermal regeneration and mass balance.** Thermal desorption was considered as an option for spent sorbent regeneration. Figure 3.4.1.2-8(a) shows the DMS breakthrough behavior for virgin AC sorbent and for AC sorbent that had been used in a DMS breakthrough test with subsequent TPD regeneration (sample identified as AC-R1). After the breakthrough test of Figure 3.4.1.2-8(a), samples AC and AC-R1 was subjected to TPD regeneration and the results are compared in Figure 3.4.1.2-8(b). Similarly, the adsorption and TPD behaviors of sorbent AC-FeCl<sub>3</sub> and the regenerated samples (AC-FeCl<sub>3</sub>-R1, R2 and R3) are shown in Figure 3.4.1.2-9.

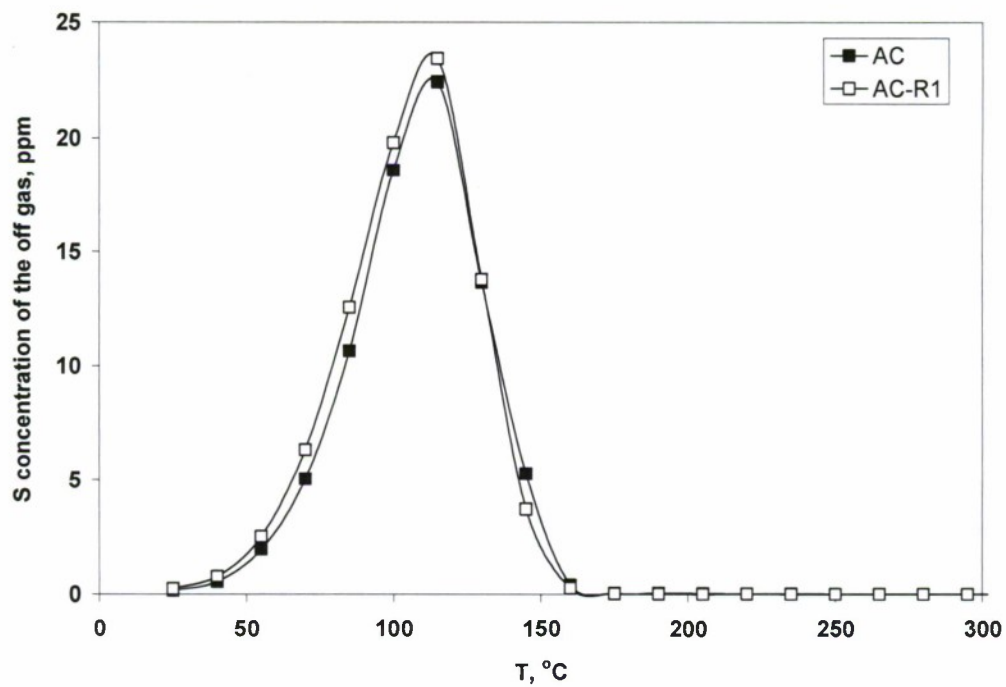
Compared with original AC, the adsorption/desorption behaviors of spent sorbent (AC-R1) are very similar. This indicates that heating to 300 °C in an inert atmosphere had no impact on the AC's adsorptive ability and the spent AC could be regenerated by thermal desorption without capacity loss. This is not the case for AC-FeCl<sub>3</sub> where the spent samples display a shorter breakthrough time than the original AC-FeCl<sub>3</sub>. The regenerated samples displayed similar adsorption and TPD trends through three adsorption-desorption cycles and were similar to that of the virgin carbon sample, AC. This shows that the new adsorption sites created by FeCl<sub>3</sub> modification on the carbon surface are not thermally stable and could not be regenerated by thermal desorption.

The AC and AC-FeCl<sub>3</sub> samples that were extracted by n-octane were also subjected to TPD tests. The TPD profiles of DMS release are shown in Figure 3.4.1.2-10. Compared with the TPD patterns of samples that were not extracted (Figures 3.4.1.2-5 and 3.4.1.2-6), the DMS release peaks shift to lower temperatures for both AC and AC-FeCl<sub>3</sub>. It was also found that DMS was released over only one temperature interval centered at ~150 °C during the TPD process for sample AC-FeCl<sub>3</sub>. This indicates that DMS that was desorbed at lower temperature in Figure 3.4.1.2-6 was related to weak adsorption on the carbon phase and was almost been completely extracted by n-octane. In addition to DMS, DMDS and COS were also detected in the effluent gas from the thermal desorption of the AC-FeCl<sub>3</sub> sample that had been extracted, as shown in Figure 3.4.1.2-11. This validates the findings of the TPD performed with the non-extracted samples and indicates that FeCl<sub>3</sub> plays a catalytic role in the formation of DMDS and COS during the thermal desorption.

Quantitative adsorption tests were intentionally conducted with similar sulfur mass loading. In the ideal case, all sulfur loaded on the samples during an adsorption test is expected to be recovered by solvent extraction or thermal desorption. Due to the small sorbent sample sizes, it was not possible to quantitatively analyze the sulfur content of the solid phase, (i.e., sulfur that was not desorbed) after extraction and desorption to fully calculate a sulfur balance. Table 3.4.1.2-3 summarizes the distribution of sulfur recovered from the solid samples by n-octane extraction and thermal desorption. The total recovered as a percentage of the S loaded as DMS was 113% for virgin carbon AC and 95% for AC-FeCl<sub>3</sub>. The sulfur distribution is almost the same for both sorbents, with nearly half extracted by n-octane and the other half released during TPD.

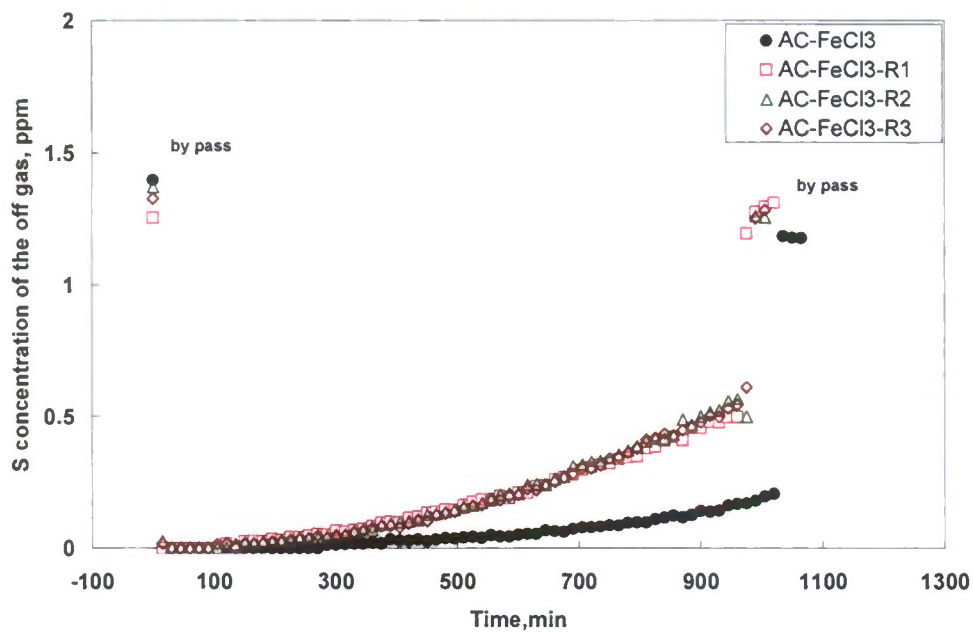


(a)

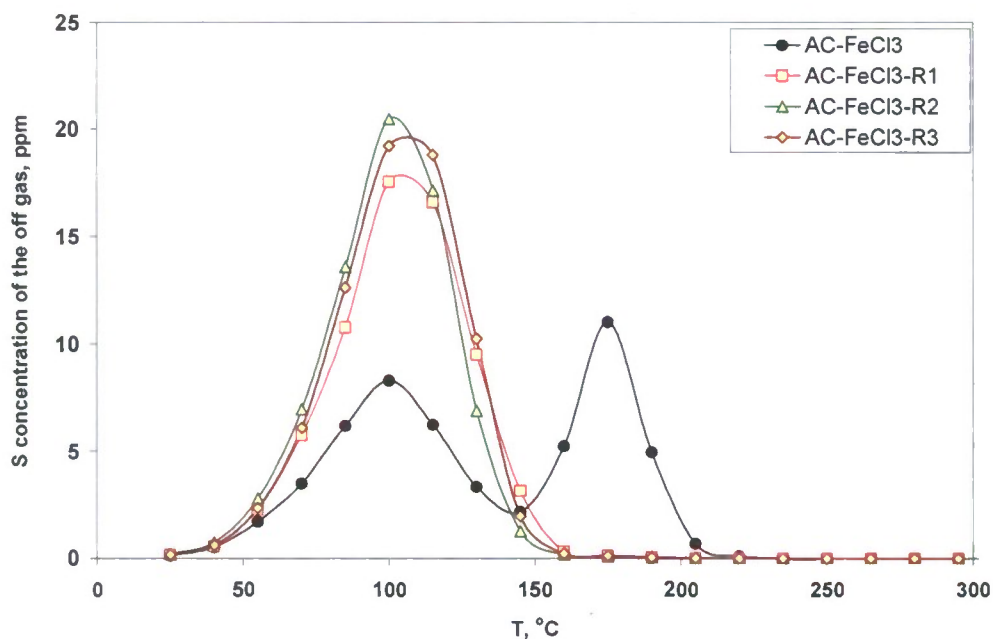


(b)

**Figure 3.4.1.2-8. Adsorption and desorption of sorbent AC and AC-R1. Sample AC-R1 had been used in a DMS breakthrough test with subsequent TPD regeneration prior to the current test.**



(a) Adsorption



(b) Desorption

**Figure 3.4.1.2-9. Adsorption and desorption of fresh and regenerated AC-FeCl<sub>3</sub> sorbent samples. Regenerated samples are identified as AC-FeCl<sub>3</sub>-R# where # indicates the number of times the sample has been regenerated.**



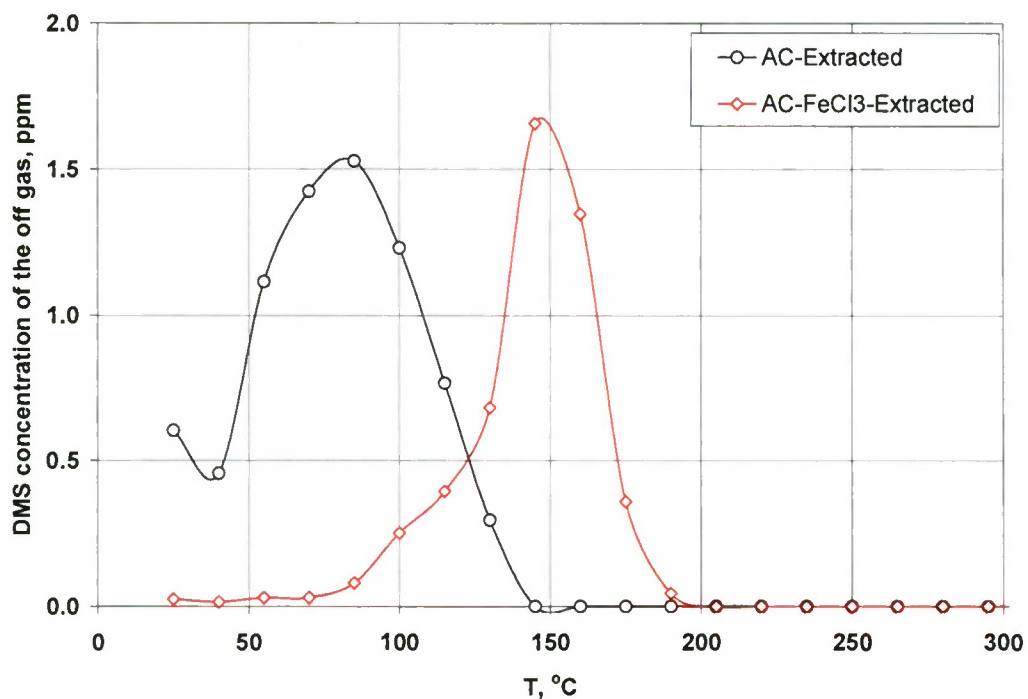


Figure 3.4.1.2-10. Comparison of TPD curves of AC and AC-FeCl<sub>3</sub> samples that had been subjected to quantitative adsorption tests with DMS and then extracted with n-octane.

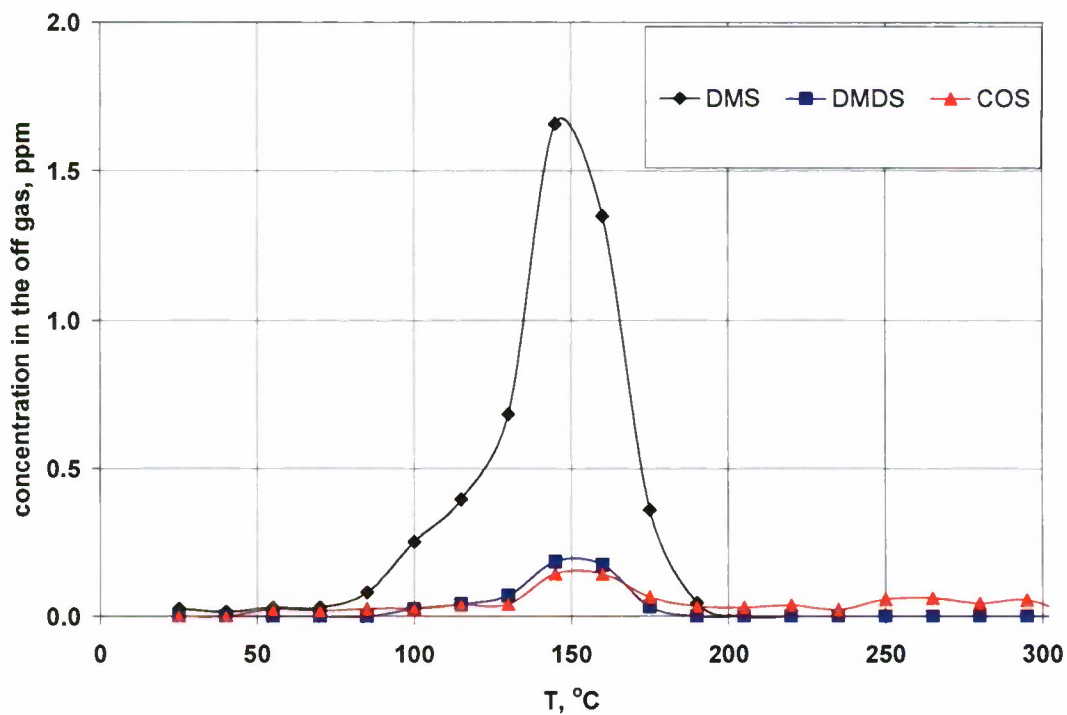


Figure 3.4.1.2-11. TPD profiles of AC-FeCl<sub>3</sub> that had been subjected to a quantitative adsorption test with DMS and then extracted with n-octane.

**Table 3.4.1.2-3. Sulfur recovery balance for AC and AC-FeCl<sub>3</sub> sorbents.**

Sulfur distribution	AC	AC-FeCl <sub>3</sub>
DMS loaded by adsorption mg S per g sorbent	0.389	0.412
DMS in n-octane extraction samples (liquid) mg S per g sorbent	0.213	0.161
weight %	54.8	39.2
(DMS+COS+DMDS) recovered by TPD after extraction mg S per g sorbent	0.230	0.229
weight %	57.8	55.7
Total S recovered as percentage of S loaded weight %	112.6	94.9

### 3.4.1.2.4 References

1. Dimethyl sulfide overview. In Gaylord Chemical Corporation: June 2007.
2. Iliuta, M. C.; Larachi, F., Solubility of Total Reduced Sulfurs (Hydrogen Sulfide, Methyl Mercaptan, Dimethyl Sulfide, and Dimethyl Disulfide) in Liquids. *Journal of Chemical & Engineering Data* **2007**, 52, (1), 2-19.
3. Satokawa, S.; Kobayashi, Y.; Fujiki, H., Adsorptive removal of dimethylsulfide and t-butylmercaptan from pipeline natural gas fuel on Ag zeolites under ambient conditions. *Applied Catalysis, B: Environmental* **2005**, 56, (1-2), 51-56.
4. Takatsu, K.; Takegoshi, G.; Katsuno, H.; Kawashima, Y.; Matsumoto, H., Room temperature sulfur removal from LPG with adsorbent for fuel cell application-adsorption behavior of sulfur compounds. *Journal of the Japan Petroleum Institute* **2007**, 50, (4), 200-207.
5. Alptekin, G.; DeVoss, S.; Dubovik, M.; Monroe, J.; Amalfitano, R.; Israelson, G., Regenerable sorbent for natural gas desulfurization. *Journal of Materials Engineering and Performance* **2006**, 15, (4), 433-438.
6. Bagreev, A.; Menendez, J. A.; Dukhno, I.; Tarasenko, Y.; Bandosz, T. J., Oxidative adsorption of methyl mercaptan on nitrogen-enriched bituminous coal-based activated carbon. *Carbon* **2004**, 43, (1), 208-210.
7. Bandosz, T. J., On the Adsorption/Oxidation of Hydrogen Sulfide on Activated Carbons at Ambient Temperatures. *Journal of Colloid and Interface Science* **2002**, 246, (1), 1-20.
8. Bashkova, S.; Bagreev, A.; Bandosz, T. J., Adsorption of Methyl Mercaptan on Activated Carbons. *Environmental Science and Technology* **2002**, 36, (12), 2777-2782.
9. Bezverkhyy, I.; Bouguessa, K.; Geantet, C.; Vrinat, M., Adsorption of tetrahydrothiophene on faujasite type zeolites: Breakthrough curves and FTIR spectroscopy study. *Applied Catalysis, B: Environmental* **2006**, 62, (3-4), 299-305.
10. Guo, J.; Luo, Y.; Lua, A. C.; Chi, R.-a.; Chen, Y.-l.; Bao, X.-t.; Xiang, S.-x., Adsorption of hydrogen sulphide (H<sub>2</sub>S) by activated carbons derived from oil-palm shell. *Carbon* **2007**, 45, (2), 330-336.

11. Hagio, H.; Fukagawa, Y., Development of desulfurization unit for LPG use in fuel cells. *Journal of the Japan Petroleum Institute* **2006**, 49, (2), 98-101.
12. Israelson, G., Results of testing various natural gas desulfurization adsorbents. *Journal of Materials Engineering and Performance* **2004**, 13, (3), 282-286.
13. Kim Dae, J.; Yie Jae, E., Role of copper chloride on the surface of activated carbon in adsorption of methyl mercaptan. *Journal of colloid and interface science* **2005**, 283, (2), 311-5.
14. Tamai, H.; Nagoya, H.; Shiono, T., Adsorption of methyl mercaptan on surface modified activated carbon. *Journal of Colloid and Interface Science* **2006**, 300, (2), 814-817.
15. Yan, R.; Chin, T.; Ng, Y. L.; Duan, H.; Liang, D. T.; Tay, J. H., Influence of Surface Properties on the Mechanism of H<sub>2</sub>S Removal by Alkaline Activated Carbons. *Environmental Science and Technology* **2004**, 38, (1), 316-323.
16. Yang, R. T.; Hernandez-Maldonado, A. J.; Yang, F. H., Desulfurization of Transportation Fuels with Zeolites Under Ambient Conditions. *Science (Washington, DC, United States)* **2003**, 301, (5629), 79-81.
17. Cui, H.; Reese, M. A.; Turn, S. Q., Removal of sulfur compounds from synthetic natural gas using modified activated carbon. *Abstracts of Papers, 234th ACS National Meeting, Boston, MA, United States, August 19-23, 2007* **2007**, FUEL-221.
18. Cui, H.; Turn, S. Q.; Reese, M. A., Removal of sulfur compounds from utility pipelined synthetic natural gas using modified activated carbons. *Catalysis Today* **2008**, doi:10.1016/j.cattod.2008.03.024.
19. Bashkova, S.; Bagreev, A.; Bandosz, T. J., Catalytic properties of activated carbon surface in the process of adsorption/oxidation of methyl mercaptan. *Catalysis Today* **2005**, 99, (3-4), 323-328.
20. Cui, H.; Turn, S. Q.; Reese, M. A., Adsorptive Removal of Tetrahydrothiophene (THT) from Synthetic Natural Gas on Modified Activated Carbons. *Energy & Fuels* **2008**, 22, (4), 2550-2558.
21. Bagreev, A.; Bashkova, S.; Bandosz, T. J., Dual Role of Water in the Process of Methyl Mercaptan Adsorption on Activated Carbons. *Langmuir* **2002**, 18, (22), 8553-8559.

#### **3.4.1.2.5 Paper Resulting from this Effort**

Cui, H., and S.Q. Turn. 2009. Adsorption/desorption of dimethylsulfide on activated carbon modified with iron chloride. *Catalysis B: Environmental*. doi:10.1016/j.apcatb.2008.09.025.



## **Subtask 3.4.2: High Pressure Autothermal Reforming in Low Oxygen Environments**

### **3.4.2.1 Scope of Work and Approach**

The development of fuel cells and fuel cell powered vehicles has been a topic of great interest in recent years [1]. Fuel cells offer potential for higher efficiency and lower pollutant emissions when compared to traditional combustion based power systems [2]. The proton exchange membrane fuel cell (PEMFC) is currently considered the most viable fuel cell technology for the near future [3-5]. As with almost all types of fuel cells, oxygen and hydrogen are supplied to a PEMFC in order to generate electrical power. Air, which is made up of ~21 % oxygen, is most often used as the oxygen source [6]. Therefore, as long as the fuel cell operates in aerobic environments, a pump can provide a continuous air supply. Low oxygen environments however, encountered by sub-sea or space applications, pose the challenge of oxidant supply [7]. Additionally, hydrogen, while abundant, is not freely present in nature as molecular hydrogen and must be produced from another source such as water, hydrocarbons, or biomass. While it is likely that in the future, hydrogen will be produced by electrolysis using photovoltaic or wind power, currently the most economic way to produce hydrogen is by catalytic thermochemical reforming of hydrocarbons. Reforming technology has been a heavily researched topic and has been implemented in industry for some time.

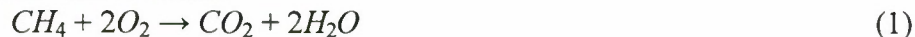
In light of the current research and development of fuel cells and fuel processing techniques, there has been recent interest in constructing small scale, underwater, power generating stations. In concept, these remote units, using onboard fuel cells to generate power, would be deployed on the ocean floor where natural gas seeps or methane hydrates are present. Methane from these sources would be collected and purified to remove catalyst-poisoning  $H_2S$ . After purification the gas stream would be reformed to produce a hydrogen rich gas for the fuel cell. While methane would be available in abundance, a major limitation for operating a reformer and fuel cell on the seafloor is having oxygen available at sufficiently high concentrations. Additionally, since the unit would be deployed on the ocean floor and operate at ambient pressure, design of components would need to accommodate the effects of elevated pressure on the physical system and reformer and fuel cell chemistry. An alternative to operating the reformer at ambient pressure would be to operate the reformer in a submerged pressure hull that would allow the system to operate at a lower pressure. The latter system would require that methane at the ambient pressure of the ocean floor be decompressed and that unwanted byproducts be recompressed for removal from the pressure hull. Operating the reformer at ambient pressure was selected over this alternative.

Applications include powering underwater sensory equipment and recharging unmanned submersibles. Currently, unmanned, untethered, vehicles (UUVs) are predominately powered by batteries and therefore have a limited range. The mission range and duration of battery powered UUV could be extended indefinitely if recharging could be completed underwater. It would also be beneficial if the vehicle did not have to surface in order to recharge, so as to avoid detection.

**Fuel reforming.** A fuel processor generally produces hydrogen from a hydrocarbon feedstock by one of three techniques: steam reforming (SR), partial oxidation reforming (POX), or autothermal reforming (ATR) [8, 9]. SR and ATR reactors typically employ catalysts.

ATR combines thermal effects from both SR and POX reforming so that the heat required to support the endothermic steam reforming reaction is provided by oxidation reactions, resulting in a lower overall temperature [10]. ATR can be described by a reaction scheme based on the following four reactions:

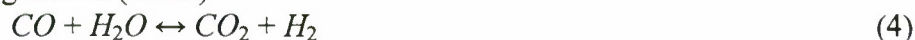
Combustion of methane:



Steam reforming reactions:



Water gas shift (WGS):



By varying the reactant ratios of  $O_2$  and  $H_2O$  with respect to the fuel, the set of reactions can be net endothermic, net exothermic, or thermally neutral. Also since ATR generates heat *in situ*, it does not require an external burner or heat exchangers like SR. When using methane as feedstock, Takeguchi *et al.* stated that while the equilibrium hydrogen production of ATR is slightly less than SR, the process consumes slightly more than half the heat [11]. ATR has been selected as the most promising reforming technique for the current application due to its simple design and efficiency for small scale systems.

**Methane Resource.** The hydrocarbon feedstock for this specialized reforming application will come from two sources: marine natural gas seeps and methane hydrates. It has been estimated that 6 to 85 Tg of methane pass through the seabed of the continental shelves annually [12]. One of the most intense known seeps in the world, the Shane Seep (depth: 22-67 m), is located along the continental shelf just off shore from Santa Barbara, CA [13, 14]. Other studied seeps include Coquille Bank located off shore from Cape Blanca, OR, (depth: 132 m), Bluff Seep located off shore from Eel River, CA (depth: 43 m), and Hecta Bank Seep located off shore from Florence, OR (depth: 83 m) [15]. Analysis of gas samples from the Shane Seep taken over a period of several months showed a composition averaging 83.4%  $CH_4$ , 11.7%  $CO_2$ , 1.8%  $N_2$ , and 0.28%  $O_2$ , with the balance being classified as non methane hydrocarbons [16]. These seeps provide a largely untapped supply of relatively pure methane that could be potentially harvested.

The second fuel source, methane hydrates, are ice-like crystalline structures with methane molecules held within the lattice of water molecules [17]. In 1999, Kvenvolden estimated the total global resource to be greater than  $10^{15} \text{ m}^3$  but less than  $10^{17} \text{ m}^3$  [18]. When appropriate expansion factors are applied,  $1 \text{ m}^3$  of pure methane hydrate expands to approximately  $164 \text{ m}^3$  of methane and  $0.8 \text{ m}^3$  of water at standard pressure and temperature [19]. Methane hydrates thus provide an extremely dense source of methane which, after dissociation, could be collected in the gas phase at ambient pressures and used as a feedstock for reforming. Gas hydrates in the marine environment occur in the gas hydrate stability zone (GHSZ). The stability zone is dependent on temperature and pressure and, with favorable conditions, can begin at depths as shallow as 300 m below sea level [20].

**Oxygen Resource.** Oxygen concentration in natural gas seeps and the dissolved oxygen concentration in sea water are very low. The highest recorded molar  $O_2$  concentration in natural gas seeps in the literature reviewed was 0.3 % [16] and the average molar  $O_2$  concentration in sea water at depths where seeps are located is less than 0.0005 % [21]. Given the low oxygen



environment, oxygen storage will be required on board the remote power unit to feed both the fuel reformer and the fuel cell.

One source of oxygen is the decomposition of hydrogen peroxide described by the following equation:



The decomposition of hydrogen peroxide can thus provide  $O_2$ ,  $H_2O$ , and heat, all of which could be utilized to operate a reformer and fuel cell on the seafloor. Moreover, since  $H_2O_2$  is a liquid, the oxygen available per unit volume is high. This is desirable from the perspective of minimizing the size of storage tanks used to transport oxidizer from the surface to the seafloor. Pure  $H_2O_2$  has a molarity of  $\sim 42 \text{ mol l}^{-1}$  at 1 bar and 25 °C. Since the decomposition of 1 mole of  $H_2O_2$  yields 0.5 mole of  $O_2$ , the oxidizer density is about 21 mol  $O_2 \text{ l}^{-1} H_2O_2$ . In comparison, pure  $O_2$  gas would have to be stored at 485 bar and 5 °C to attain a density of 21 mol/liter. Additionally,  $H_2O_2$  has a specific gravity of 1.4, which is double that of  $O_2$  stored in the gas phase at 485 bar. This increase in density is beneficial as it provides negative buoyancy. Therefore, due to its favorable traits,  $H_2O_2$  was selected as a candidate oxidizer for the system.

Purchasing  $H_2O_2$  in a solution at a concentration greater than 50% by weight can be difficult and no effort was made to exceed this limit for safety reasons.  $H_2O_2$  at 67% (weight) or greater can be dangerous as the heat of decomposition is sufficient to vaporize the water present in the solution and can lead to spontaneous decomposition. Therefore, while the heat of decomposition of high concentration  $H_2O_2$  may lead to hazardous conditions, the heat of decomposition from lower concentration  $H_2O_2$  solutions (<50% weight) is beneficial to the reforming process.

Hydrogen peroxide is common in the literature; often in papers dealing with propellants and very rarely in papers dealing with reforming. Patents [22] exist on the topic of using  $H_2O_2$  for ATR reforming of methanol, ethanol, and other hydrocarbons. The basic concept in both patents is to decompose  $H_2O_2$  to release steam,  $O_2$ , and heat to support ATR reactions. To date, outside of the patents, no papers have appeared which deal with the use of  $H_2O_2$  as an oxidant for use in methane fuel reforming.

**Objectives.** The objective of this study was to determine optimal ATR operating conditions at 6, 28 and 50 bar and to conduct performance comparisons using  $H_2O_2$  as both the steam and oxygen source. The range of pressures selected corresponds to operation at various natural gas seep depths as well as shallow methane hydrate formations. For this fuel rich, oxygen limited, reforming application it is of particular interest to maximize moles of  $H_2$  produced per mole of  $O_2$  supplied.

### 3.4.2.2 Experimental

**Experimental test facility.** The schematic layout of the test facility is shown in Figure 3.4.2-1.



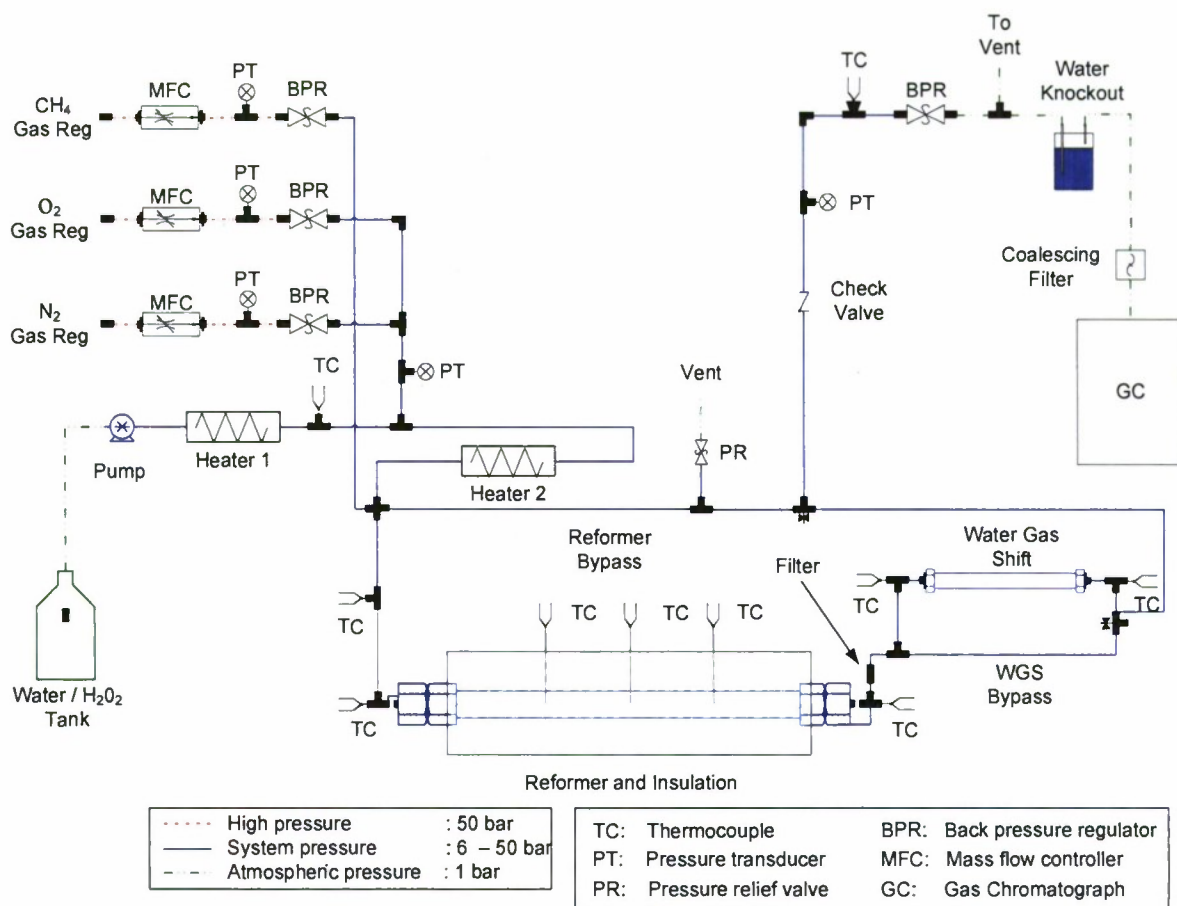


**Figure 3.4.2-1. Schematic layout of 50 bar reforming system.**

Methane (Grade 5.0), oxygen, and nitrogen from gas bottles were metered to the reactor using mass flow controllers (MFC) (Brooks 5850 Series E). Water or hydrogen peroxide solution was supplied to the reactor by a high pressure piston metering pump. Resistance element heat tracing was applied to the transfer lines between the reservoir and the reactor to preheat the liquid. Pressure in the reactor was set and controlled with a back pressure regulator. Flow rates were controlled and recorded along with temperatures and pressures using LabVIEW<sup>®</sup> (National Instruments, Austin, TX) running on a laptop computer. Temperatures of reactor inlet and outlet flows and three locations on the outside wall of the reactor were measured with thermocouples. To operate in autothermal mode, the reactor (61 cm long, XXS, 316 stainless steel pipe) was insulated with high temperature insulation (Thermcraft Inc., Winston-Salem, NC). To bring the reactor up to initial operating temperature, two spiral wound, resistance heating wire elements were inset in the insulation on either side of the reactor. Downstream of the reactor, the reformatte passed through a condenser and coalescing filter (Balston, Model 31G) in series. The dry, effluent, gas was analyzed with a gas chromatograph (GC) (Shimadzu 14A, Columbia, MD) equipped with a Carboxen<sup>™</sup> 1000 column (45/60, SUPELCO) and thermal conductivity detector (TCD).

**Experimental design.** A sub-sea power generating station located on the ocean floor would be operated at a fixed depth with an associated operating pressure. The focus of this study was to find optimal operating conditions at 6, 28, and 50 bar representing depths of 60, 280 and 500 m below sea level. In addition to pressure, other independent variables were the molar steam to carbon (S/C) and oxygen to carbon (O<sub>2</sub>/C) ratios defined by the inlet flows of fuel, oxidizer, and water. Temperature and gas composition and yield were dependent variables.

Typically, parametric studies are used to observe the response of a dependent variable while each independent variable is incrementally changed over a specified range. For this study however, a 2<sup>2</sup> factorial design approach was used [23]. Utilizing surface response methodology (SRM), a two-level factorial design allows both independent variables (S/C; O<sub>2</sub>/C) to be changed simultaneously.

A sample of the 2<sup>2</sup> factorial design for this study is shown in Table 3.4.2-1. The first column "Order" refers to the randomized sequence of the experimental runs. Each "Run", generally comprised 5 or 6 gas samples and was conducted with the S/C and O<sub>2</sub>/C ratios set to a high (+1) or low (-1) value as shown in columns 3 and 4. Using data from the literature [24], previous tests, and equilibrium calculations, the initial high and low values for both variables were selected as shown in Table 3.4.2-2. The fifth column in Table 3.4.2-1 refers to two-level interactions of the two independent variables and is used later as an estimate of experimental error [23].

**Table 3.4.2-1. Variable levels for factorial experimental design.**

Order	Run	S/C	O <sub>2</sub> /C	S/C x O <sub>2</sub> /C interaction
2	1	-1	-1	1
4	2	1	-1	-1
3	3	-1	1	-1
1	4	1	1	1

**Table 3.4.2-2. Initial operating conditions for low pressure (6 bar) experiments.**

#	Variable		Value		CH <sub>4</sub> Flow l min <sup>-1</sup>
	Name	Unit	+	-	
1	S/C	/	3.75	2.25	2.50
2	O <sub>2</sub> /C	/	0.58	0.46	2.50

The following is an overview of how the experimental design was conducted. After the initial factorial (4 runs) was completed, the results were analyzed to calculate the path of steepest ascent. This is the direction which caused the response variable to increase the greatest rate. New test conditions were then conducted along the path of steepest ascent until a maximum response was found. Around this new found maximum, another factorial was conducted to confirm that the maximum had been found or to reveal a new path of steepest ascent that would identify a new maximum.

**Operating procedure.** Standard operating procedures were followed each time an experiment was run. At the start of each new set of experiments (new pressure level), approximately 33 grams of fresh, sulfide nickel catalyst on a gamma alumina support (Catalyst Ni-0309S, Engelhard, Newark NJ) was loaded into the reactor. Under normal circumstances the same catalyst was generally left in the reformer for several days of testing. After the system integrity was verified by conducting a pressure test, calibration procedures were carried out for the GC and MFCs using certified standard gases and a bubble flow meter (mini-BUCK Calibrator M-30, A.P. BUCK, Orlando, FL), respectively.

After completing the calibration procedure the N<sub>2</sub> flow was set to 0.5 lpm, and the backpressure regulator on the system was turned to the open position. The reactor heating elements were energized until the catalyst bed rose above light off temperature. Typically the catalyst bed would reach about 650 °C in less than half an hour. At that temperature O<sub>2</sub> was metered into the reformer at the appropriate flow rate for the selected test and the CH<sub>4</sub> flow rate was set to 2.5 lpm (for all tests). Almost immediately a temperature increase in the reactor was detected due to the partial oxidation of CH<sub>4</sub>. When the temperature increase was observed, the reactor heating element was turned off, the water pump and the water heating element were turned on, and the system pressure was set by adjusting the back pressure regulator. Within 45 minutes of turning on the water flow, the system temperatures and reformat gas composition were typically stabilized. The reformat gas was sampled every 10 minutes after temperatures and gas compositions stabilized. After several GC analyses were recorded for a given condition the S/C and O<sub>2</sub>/C set points were changed and a new stable condition was generally acquired in 30 minutes or less. When the experimental run was completed, the CH<sub>4</sub> flow was turned off and the system was purged with O<sub>2</sub>, N<sub>2</sub>, and steam for several minutes

**Modeling.** Thermochemical equilibrium conditions for reforming over a wide range of S/C and O<sub>2</sub>/C ratios at 6, 28 and 50 bar were calculated using FACTSage<sup>TM</sup> 5.1 (Thermfact/CRCT, Montreal, Canada). The initial reactant gas species, reactant molar ratios, temperature, and pressure were specified for each run. Equilibrium results were calculated using final state points of system pressure and enthalpy equal to reactant conditions. The results served as a general comparative benchmark for experimental results.

### 3.4.2.3 Technical Accomplishments

**Methane reforming results at 6 bar pressure.** Eighteen ATR runs were conducted at 6 bar using both bottled O<sub>2</sub> and liquid H<sub>2</sub>O<sub>2</sub> solution as oxidizer. The results for all 6 bar tests are presented in Table 3.4.2-3 while Table 3.4.2-4 shows the individual effects of the S/C and O<sub>2</sub>/C ratio on the molar ratio of H<sub>2(out)</sub>/O<sub>2(in)</sub> for the first factorial. Table 3.4.2-4 also shows the two-factor interaction effect, in this case the S/C and O<sub>2</sub>/C ratios, which, according to Box *et al.* [23], provides a reasonable approximation of variance and an estimate of experimental error.



Table 3.4.2-3. Summary of autothermal reforming test results at 6 bar.

Variables				Moles per mole of CH <sub>4</sub> (in)										Total		
Run	S/C	O <sub>2</sub> /C	Trials <sup>a</sup>	H <sub>2</sub> /O <sub>2</sub>	σ %	[H <sub>2</sub> ] %	σ %	H <sub>2</sub>	σ %	CO	σ %	CH <sub>4</sub>	σ %	CO <sub>2</sub>	σ %	I min <sup>-1</sup>
1	3.00	0.52	6	4.06	0.6	68.75	0.1	2.12	0.5	0.20	0.4	0.19	0.9	0.61	0.4	8.25
2	2.25	0.58	8	3.83	2.5	69.79	1.0	2.23	3.3	0.31	8.0	0.11	9.0	0.58	5.2	8.53
3	3.75	0.58	6	3.99	0.4	70.70	0.1	2.33	0.2	0.20	1.3	0.12	0.8	0.68	0.2	8.77
4	3.75	0.46	6	4.10	0.5	66.05	0.1	1.90	0.4	0.11	1.4	0.29	0.7	0.60	0.2	7.67
5	2.25	0.46	5	4.12	0.8	65.65	1.9	1.90	1.0	0.18	5.7	0.27	1.5	0.55	1.6	7.70
6	3.35	0.44	5	4.14	1.1	64.86	1.9	1.84	1.4	0.12	24.4	0.29	8.2	0.56	3.0	7.50
7	3.50	0.40	BT <sup>b</sup>	4.08	0.0	62.66	0.4	1.63	1.8	0.08	4.8	0.37	0.7	0.52	3.2	6.93
8	3.00	0.52	4	4.07	1.6	68.40	0.7	2.07	1.4	0.19	0.6	0.18	0.7	0.60	0.8	8.08
9	3.00	0.52	5	3.88	0.7	66.95	1.8	2.01	0.4	0.27	1.3	0.19	1.2	0.51	0.6	7.96
10	3.35	0.44	3	3.98	0.5	64.40	0.1	1.74	0.8	0.09	1.2	0.33	0.5	0.55	0.8	7.27
11	2.60	0.48	4	3.99	1.0	66.48	0.4	1.90	1.1	0.16	1.9	0.26	2.2	0.55	1.2	7.67
12	4.10	0.48	BT <sup>b</sup>													
13	2.60	0.40	BT <sup>b</sup>	3.96	1.1	62.08	0.5	1.60	1.4	0.12	8.0	0.38	0.5	0.48	2.4	6.94
14	4.10	0.40	BT <sup>b</sup>													
15	3.35	0.44	3	4.02	0.5	64.57	0.1	1.76	1.1	0.10	1.5	0.33	0.5	0.55	0.9	7.32
16	3.35	0.44	6	3.95	0.6	64.54	0.3	1.75	0.8	0.09	1.9	0.33	0.8	0.55	0.3	7.30
17	3.35	0.44	5 <sup>c</sup>	4.38	2.4	66.80	2.4	1.95	2.8	0.12	2.9	0.25	3.6	0.59	3.0	7.76
18	3.75	0.46	4 <sup>c</sup>	4.47	1.6	68.29	0.3	2.04	1.6	0.11	3.1	0.23	2.8	0.63	1.7	8.03

<sup>a</sup>trials are the number of repetitions at each run condition

<sup>b</sup>indicates break through of high temperature reaction zone

<sup>c</sup>indicates H<sub>2</sub>O<sub>2</sub> was used

**Table 3.4.2-4. Results of 2<sup>2</sup> factorial experiment showing the effect of changing S/C and O<sub>2</sub>/C ratio one step on the H<sub>2(out)</sub>/O<sub>2(in)</sub> yield.**

Main effects	H <sub>2(out)</sub> /O <sub>2(in)</sub>	Error
S/C	0.037	±0.045
O <sub>2</sub> /C	-0.102	±0.045
<b>Interaction effect</b>		
S/C x O <sub>2</sub> /C	0.045	

Based on the initial factorial (runs #2 to #5), a path of steepest ascent was calculated to identify operating conditions that would increase the moles of H<sub>2(out)</sub>/O<sub>2(in)</sub>. The path is shown in Figure 3.4.2-2 by a dashed line which passes through the center point of the first factorial. Two runs were completed along this path; run #6 produced a slight increase in yield while run #7 resulted in a yield decrease before the high temperature reaction zone blew out of the backend of the reformer. The center point, first factorial, and the path of steepest ascent (runs #1 to #8) made up test group 1. The first test point along the path of steepest ascent (S/C = 3.35 and an O<sub>2</sub>/C = 0.44) was the test condition with the highest yield and was used as the center point for a second factorial.

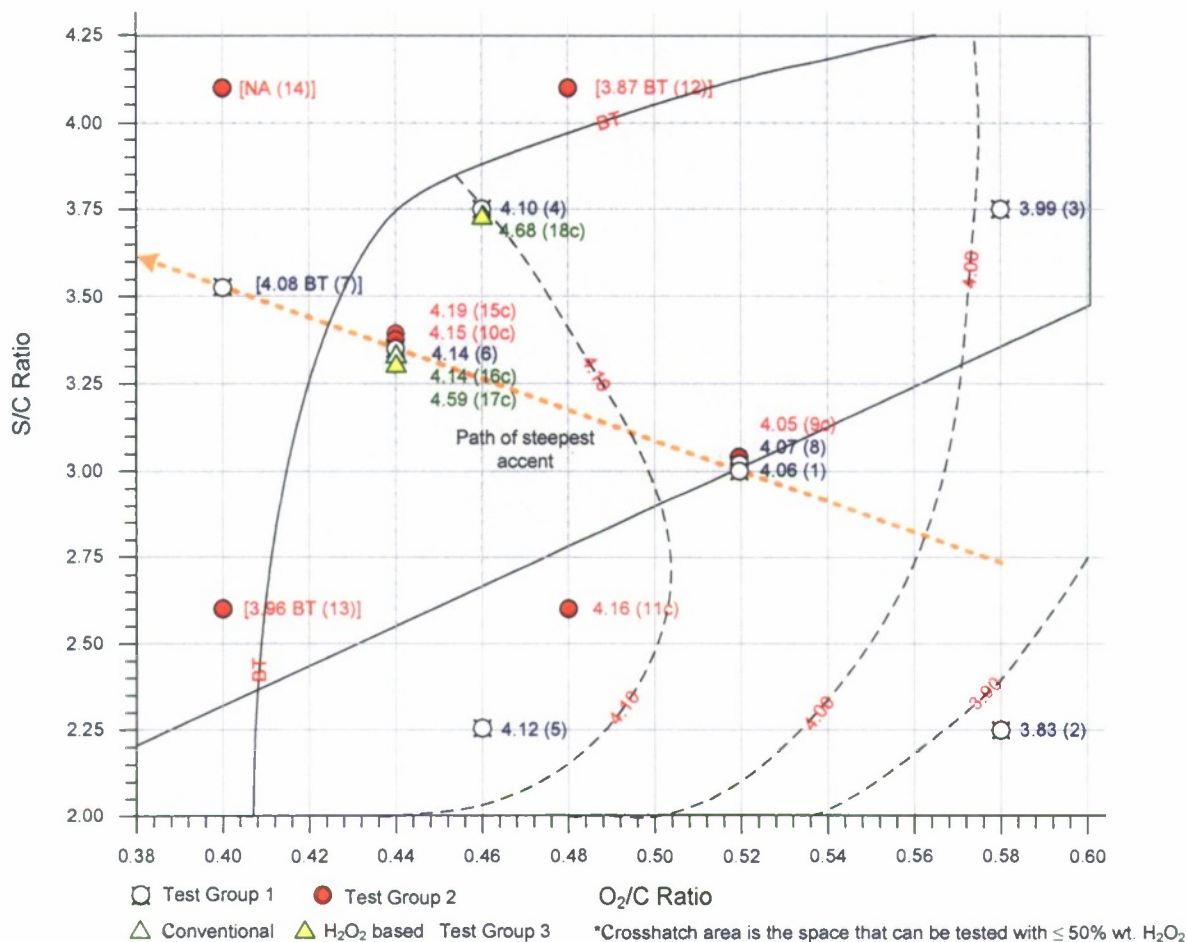


**Figure 3.4.2-2. Yield (moles H<sub>2</sub> per mole O<sub>2</sub>) surface response of autothermal reforming as a function of S/C and O<sub>2</sub>/C ratios based on corrected results at 6 bar operating pressure.**

Runs #9 to #15 made up test group 2 and were conducted four days after the first 8 runs were completed. These runs included replicating old conditions (for comparison) as well as running the second factorial. A correction factor of 4.25 %, the average decrease in yield from replicated runs, was later used to correct all group 2 test results. The same catalyst was reused in test group 2 as was used in test group 1.

When attempting to run the second factorial it was only possible to attain steady-state operation for one of the four conditions. Run #12 and #13 were attempted, but in both cases the high temperature reaction zone blew out of the backend of the reactor. This was due to the high S/C ratio in run #12 and the low O<sub>2</sub>/C ratio in run #13. Run #14 wasn't attempted.

Finally, two performance comparisons using H<sub>2</sub>O<sub>2</sub> as oxidizer were conducted, making up test group 3. Again to compensate for day to day differences, the results for test group 3 were multiplied by a correction factor of 4.8%, the percentage difference between run #6 and run #16: a run replicated from test group 1 and 3, respectively.

In Figure 3.4.2-2 the type of data point marker used to depict the run conditions also shows test grouping. The number to the right of the marker is the moles of H<sub>2(out)</sub>/O<sub>2(in)</sub> and the number in



brackets following the yield is the run number as identified in Table 3.4.2-3. "BT" refers to conditions where the high temperature reaction zone blew through the backend of reactor. If a number is listed before the BT label, it refers to the yield before the high temperature reaction zone blew through. Estimated contour lines have been added to the figure to show the  $H_{2(out)}/O_{2(in)}$  yield based on the experimental results. A "c" is used after the run number to indicate the results have been multiplied by a correction factor.

From Figure 3.4.2-2 the optimum condition appears to be a broad plateau which is bounded on the left and at the top by a physical inability to stabilize the high temperature reaction zone in the reactor. Generally speaking the  $O_2/C$  ratio has a greater effect on the moles of  $H_{2(out)}/O_{2(in)}$  than the  $S/C$  ratio.

***Methane reforming results at 28 and 50 bar pressure.*** Fourteen ATR runs were conducted at 28 bar, and twelve runs were conducted at 50 bar using both bottled  $O_2$  and  $H_2O_2$  as oxidizer. The results are presented in Tables 3.4.2-5 and 3.4.2-6, respectively. Additional graphical summaries of test conditions run at 28 bar and 50 bar are shown in Figures 3.4.2-3 and 3.4.2-4, respectively. Correction factors have again been added to account for day to day variance. The layout and symbols used are the same as those used in Figure 3.4.2-2.

The optimum condition at 28 bar shifted to a higher  $O_2/C$  ratio compared to the 6 bar optimum, and therefore required additional  $O_2$  input. Additionally, the maximum yield of  $H_{2(out)}/O_{2(in)}$  decreased from approximately 4.16 moles to approximately 3.43 moles. This is a decrease of 17.5%. Since lower pressures favor the steam reforming reactions, a decrease in the  $H_{2(out)}/O_{2(in)}$  yield was expected with increased pressure.

The optimum condition at 50 bar is in the same region as the optimum for 28 bar. The maximum yield of  $H_{2(out)}/O_{2(in)}$  decreased from approximately 3.43 moles to approximately 2.87 moles. This is a decrease of 16.3%. Since lower pressures favor the steam reforming reactions, a decrease in the  $H_{2(out)}/O_{2(in)}$  yield was expected with increased pressure.

***Equilibrium Model Results.*** For comparison with experimental results, Figures 3.4.2-5 to 3.4.2-7, show the  $H_2$  yield (moles  $H_2$  produced per mole of  $O_2$  fed into the reactor) predicted by thermochemical equilibrium at 6, 28, and 50 bar, respectively. These results are based on ATR with  $O_2$  as the oxidizer. The initial temperature of the reactants was set to 270 °C to match the preheated reactants delivered to the experimental reformer.

Table 3.4.2-5. Summary of autothermal reforming test results at 28 bar.

Variables				Moles per mole of CH <sub>4</sub> (In)												Total
Run	S/C	O <sub>2</sub> /C	Trials <sup>a</sup>	H <sub>2</sub> /O <sub>2</sub>	σ %	[H <sub>2</sub> ] %	σ %	H <sub>2</sub>	σ %	CO	σ %	CH <sub>4</sub>	σ %	CO <sub>2</sub>	σ %	I min <sup>-1</sup>
1	3.00	0.48	5	3.12	0.4	60.68	0.0	1.49	0.4	0.10	0.2	0.37	0.2	0.51	0.3	6.63
2	2.25	0.54	5	2.82	1.5	61.04	0.8	1.52	2.1	0.16	3.1	0.32	1.5	0.51	1.5	6.71
3	2.25	0.42	6	2.87	1.0	55.17	0.7	1.21	1.4	0.09	4.3	0.46	1.1	0.43	0.7	5.93
4	3.75	0.54	6	3.07	0.8	63.01	0.5	1.66	1.2	0.11	4.1	0.31	1.5	0.60	0.7	7.14
5	3.75	0.42	BT <sup>b</sup>													
6	2.25	0.54	5	2.63	3.4	58.86	2.1	1.42	4.8	0.16	7.5	0.36	4.6	0.49	1.6	6.49
7	3.00	0.48	5	3.47	0.2	62.45	0.1	1.67	0.2	0.13	2.0	0.36	0.6	0.54	0.3	7.26
8	3.00	0.48	6 <sup>c</sup>	3.82	1.2	64.50	0.5	1.83	1.5	0.15	4.3	0.31	1.9	0.59	1.9	7.72
9	3.75	0.54	5	3.35	0.7	64.12	0.5	1.80	0.4	0.12	0.4	0.32	0.8	0.61	0.6	7.63
10	3.75	0.54	5 <sup>c</sup>	3.52	0.9	64.90	0.2	1.89	1.0	0.14	0.9	0.28	1.2	0.64	1.2	7.90
11	3.75	0.42	BT <sup>b</sup>													
12	3.75	0.42	BT <sup>b,c</sup>													
13	3.00	0.54	4	3.38	0.7	65.44	0.3	1.82	0.7	0.14	0.8	0.27	2.0	0.59	0.3	7.50
14	3.00	0.48	3	3.39	1.0	62.37	0.5	1.62	1.3	0.11	2.6	0.35	1.0	0.54	0.6	6.99

<sup>a</sup>trials are the number of repetitions at each run condition

<sup>b</sup>indicates break through of high temperature reaction zone

<sup>c</sup>indicates H<sub>2</sub>O<sub>2</sub> was used

Table 3.4.2-6. Summary of autothermal reforming test results at 50 bar.

Variables				Moles per mole of CH <sub>4</sub> (In)										Total		
Run	S/C	O <sub>2</sub> /C	Trials <sup>a</sup>	H <sub>2</sub> /O <sub>2</sub>	σ %	[H <sub>2</sub> ] <sup>b</sup> %	σ %	H <sub>2</sub>	σ %	CO	σ %	CH <sub>4</sub>	σ %	CO <sub>2</sub>	σ %	I min <sup>-1</sup>
1	3.00	0.48	5	2.75	1.0	56.67	0.0	1.31	0.4	0.08	1.0	0.43	2.2	0.50	0.8	6.24
2	3.75	0.54	5	2.77	1.2	60.05	0.9	1.49	2.2	0.09	3.3	0.36	2.2	0.56	1.1	6.70
3	2.25	0.54	4	2.21	0.9	54.48	0.6	1.19	0.6	0.10	4.9	0.41	3.1	0.48	1.2	5.90
4	2.25	0.42	3	1.89	4.0	44.70	3.6	0.80	5.4	0.06	7.7	0.53	3.3	0.37	2.0	4.85
5	3.75	0.42	BT <sup>b</sup>	2.73	1.5	53.84	0.9	1.15	2.0	0.06	22.9	0.47	1.8	0.45	1.6	5.78
6	3.00	0.47	4	2.93	1.5	58.94	1.4	1.38	1.4	0.09	1.7	0.39	5.4	0.50	0.9	6.43
7	3.68	0.49	6	2.81	0.6	58.41	0.3	1.36	0.7	0.08	1.2	0.39	0.4	0.51	0.3	6.40
8	3.75	0.53	5	2.71	0.7	59.69	0.2	1.43	0.9	0.09	1.2	0.35	0.6	0.54	0.8	6.56
9	3.00	0.48	4	2.87	0.7	58.43	0.3	1.38	0.9	0.08	0.9	0.40	0.6	0.50	0.9	6.44
10	3.00	0.48	4 <sup>c</sup>	3.08	2.2	59.77	0.7	1.48	1.9	0.10	1.0	0.37	4.6	0.54	2.2	6.76
11	3.75	0.54	4	2.70	0.8	59.98	0.4	1.46	1.0	0.08	1.6	0.35	0.8	0.54	0.6	6.65
12	3.75	0.54	5 <sup>c</sup>	2.94	0.8	62.02	0.2	1.59	0.9	0.11	0.7	0.30	0.6	0.58	0.8	6.99

<sup>a</sup>trials are the number of repetitions at each run condition

<sup>b</sup>indicates break through of high temperature reaction zone

<sup>c</sup>indicates H<sub>2</sub>O<sub>2</sub> was used





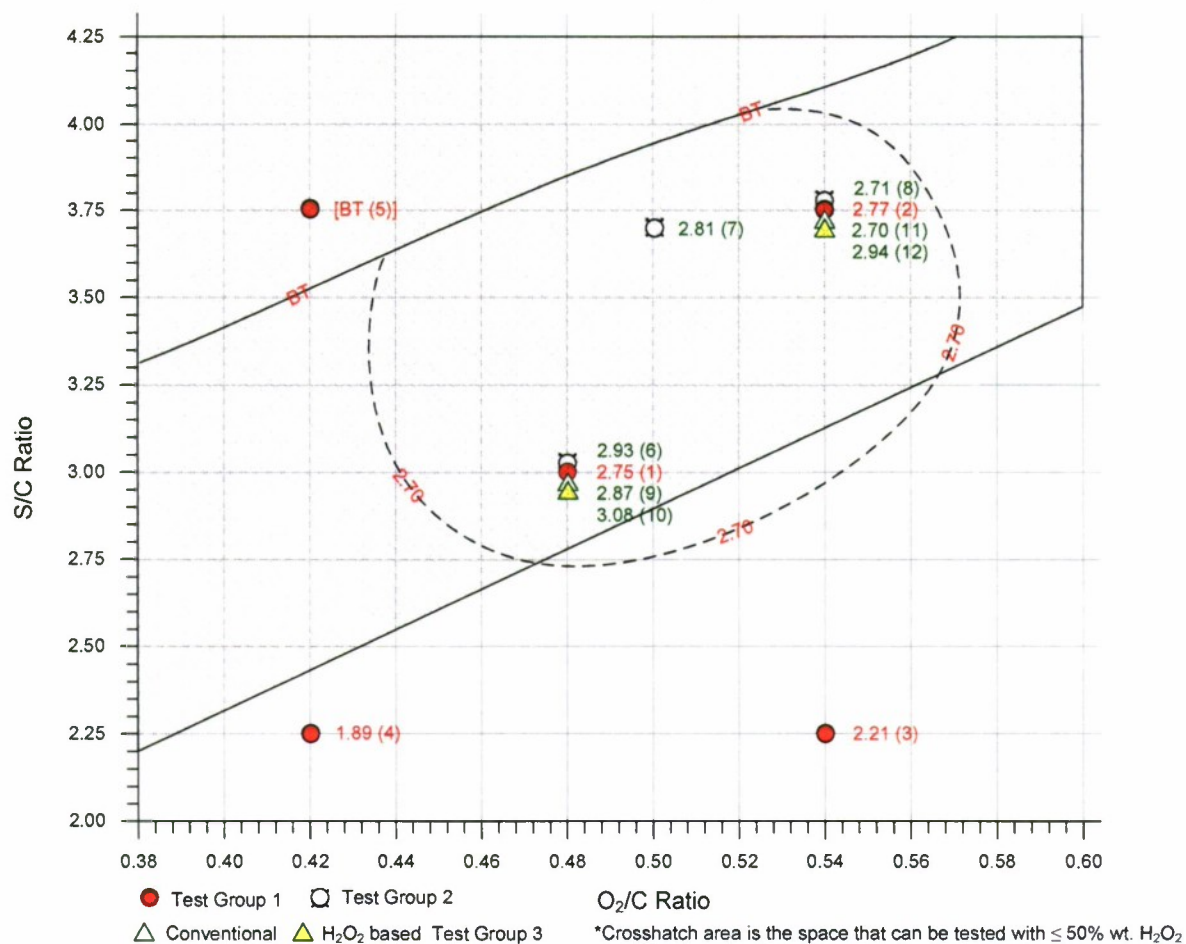


**Figure 3.4.2-4. Yield (moles H<sub>2</sub> per mole O<sub>2</sub>) surface response of autothermal reforming as a function of S/C and O<sub>2</sub>/C ratios based on corrected results at 50 bar operating pressure.**

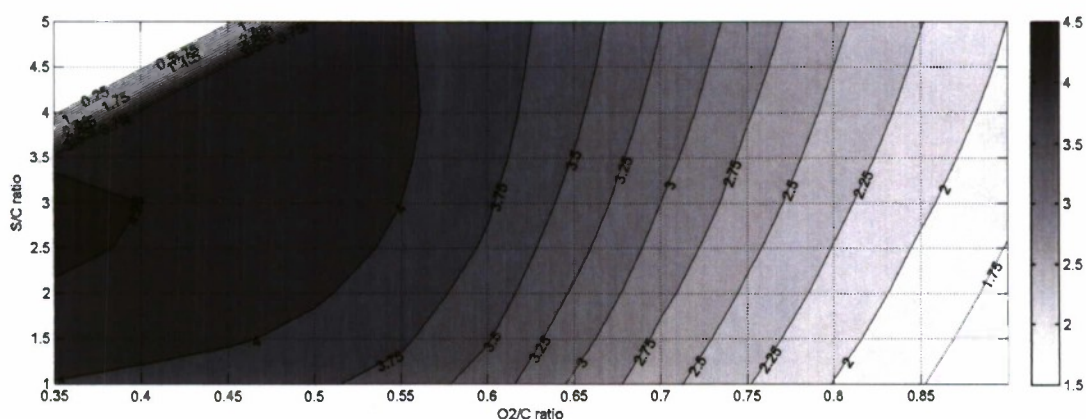


**Figure 3.4.2-5. Yield (moles H<sub>2</sub> per mole O<sub>2</sub>) surface response of autothermal reforming as a function of S/C and O<sub>2</sub>/C ratios based on thermochemical equilibrium results at 6 bar operating pressure and no system heat loss.**

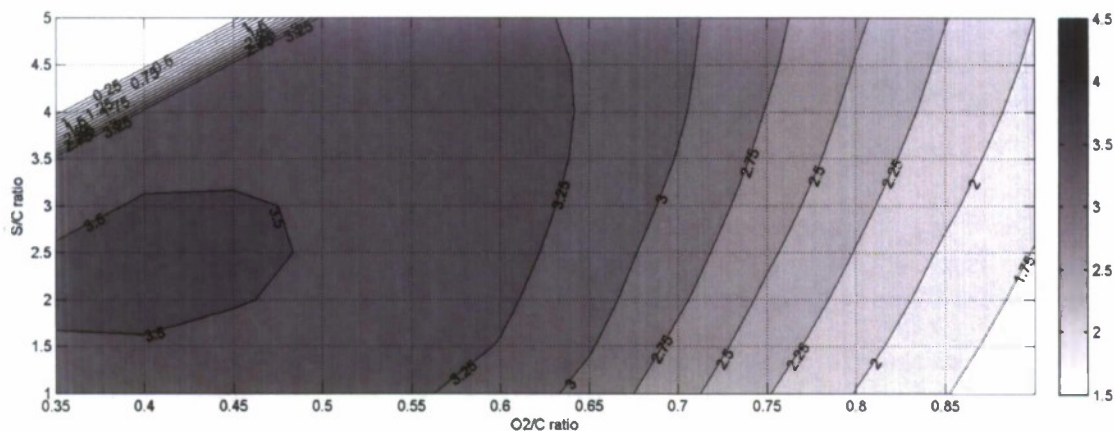


**Figure 3.4.2-6. Yield (moles H<sub>2</sub> per mole O<sub>2</sub>) surface response of autothermal reforming as a function of S/C and O<sub>2</sub>/C ratios based on thermochemical equilibrium results at 28 bar operating pressure and no system heat loss.**

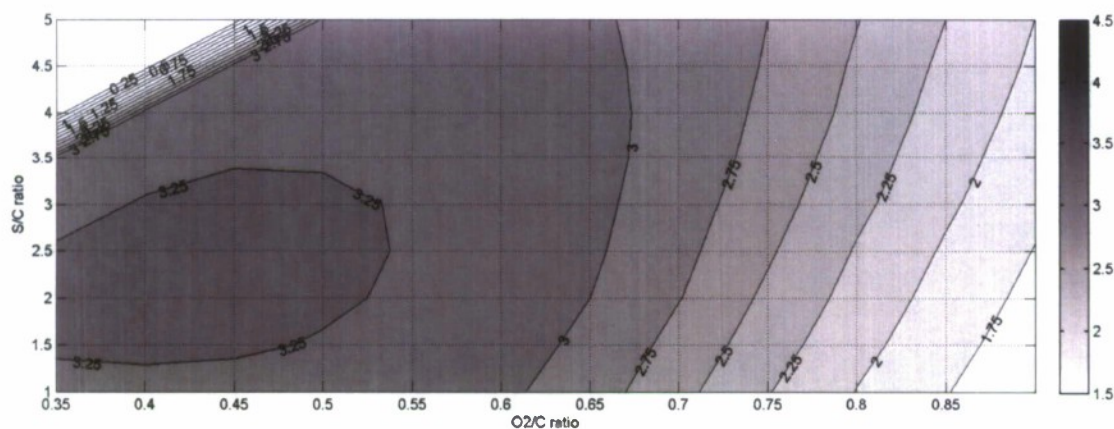


**Figure 3.4.2-7. Yield (moles H<sub>2</sub> per mole O<sub>2</sub>) surface response of autothermal reforming as a function of S/C and O<sub>2</sub>/C ratios based on thermochemical equilibrium results at 50 bar operating pressure and no system heat loss.**

The white area at the upper left of the charts indicates a region where equilibrium does not predict H<sub>2</sub> in the products. This phenomenon was also observed experimentally although the exact location of the boundary of the region where H<sub>2</sub> is present in the products differs as explained later. The darker shaded areas indicate a broad plateau where H<sub>2</sub>/O<sub>2</sub> ratios are high. The white area and the high yielding areas are separated by a steep gradient in H<sub>2(out)</sub>/O<sub>2(in)</sub> productivity.

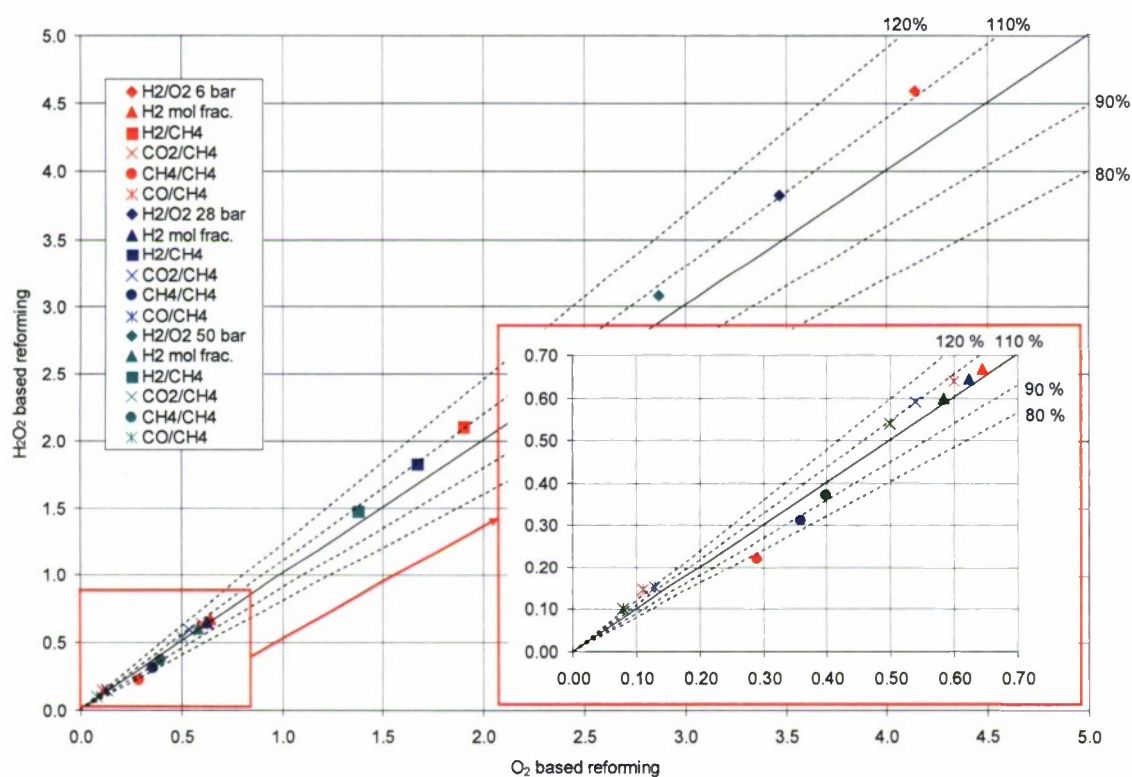
Comparing the equilibrium results at 6 bar (Figure 3.4.2-5) to 28 bar (Figure 3.4.2-6), the following observations were made: (1) the maximum H<sub>2(out)</sub>/O<sub>2(in)</sub> value dropped 16% from 4.35 to 3.64; (2) the optimum condition changed from a S/C ratio of 3.00 and an O<sub>2</sub>/C ratio of 0.35 at 6 bar to a lower S/C ratio of 2.5 and a higher O<sub>2</sub>/C ratio of 0.4 at 28 bar; and (3) both pressures



exhibit a large plateau of insensitive  $H_{2(out)}/O_{2(in)}$  yield in response to changes in the S/C and  $O_2/C$  operating parameters near the maximum value.

Comparing the equilibrium results at 28 bar (Figure 3.4.2-6) to the results at 50 bar (Figure 3.4.2-7), the following observations were made: (1) the maximum moles of  $H_{2(out)}/O_{2(in)}$  dropped 8% from 3.64 to 3.36; (2) the optimum shifted slightly from S/C ratio of 2.5 and an  $O_2/C$  of 0.40 at 28 bar to the same S/C ratio with an increased  $O_2/C$  ratio of 0.45 at 50 bar; (3) the large plateau of insensitive  $H_{2(out)}/O_{2(in)}$  yield in response to changes in the S/C and  $O_2/C$  operating parameters near the maximum is present at both pressures; and (4) the  $H_{2(out)}/O_{2(in)}$  results away from the optimum condition vary little with increased pressure.

**Experimental results comparison.**  $O_2$  vs.  $H_2O_2$  based ATR (Figure 3.4.2-8) shows a parity plot comparing ATR results from experiments using  $O_2$  and  $H_2O_2$  as oxidizer at 6, 28, and 50 bar. Note that the results correspond to the optimal condition identified using  $O_2$  as oxidizer. The  $H_2/O_2$  in the legend refers to the moles of  $H_{2(out)}/O_{2(in)}$  while the  $H_2/CH_4$ ,  $CO_2/CH_4$ ,  $CH_4/CH_4$  and  $CO/CH_4$  refer to moles of each species in the reformat per mole of  $CH_{4(in)}$ . Each pressure level shown is also color coordinated; red representing 6 bar, blue representing 28 bar, and green representing 50 bar.



**Figure 3.4.2-8.** Comparison of ATR experimental results from tests using  $O_2$  and  $H_2O_2$  as oxidizer/reactant at optimal conditions for 6 bar (red points), 28 bar (blue points), and 50 bar (green points). All ratios are (moles of product) / (mole of reactant). Mol frac. = mole fraction.

When H<sub>2</sub>O<sub>2</sub> was injected into the reformer as oxidizer, the moles of H<sub>2(out)</sub> and CO<sub>2(out)</sub> increased an average of 10 %, the moles of CO<sub>(out)</sub> increased 10 - 25 %, and the moles of CH<sub>4(out)</sub> decreased 9 - 25 %. The mole fraction of H<sub>2</sub> in the reformat increased by 4 % or less. Decomposition of H<sub>2</sub>O<sub>2</sub> resulted in higher reactor temperatures which led to higher steam reforming rates but also pushed the water gas shift equilibrium slightly to the left (see equation 4).

The decomposition of H<sub>2</sub>O<sub>2</sub> began before it was injected into the reactor. An increased temperature in the reactant transfer lines and a reduced duty cycle of the controller for the heating elements on the reactant transfer lines served as indicators of the heat release from H<sub>2</sub>O<sub>2</sub> decomposition reactions. Table 7 compares a set of test conditions conducted with O<sub>2</sub> (runs #16) and with H<sub>2</sub>O<sub>2</sub> (run #17) at 6 bar. T<sub>in</sub> and T<sub>out</sub> are the temperatures at the inlet and outlet of the reactor catalyst bed, respectively. The heater duty cycle is the percentage of time that the pre-heater on the reactant transfer lines was energized. The heater output is calculated by multiplying the power consumed in the resistance wire heating element by the duty cycle of the heater.

**Table 3.4.2-7. Comparison of O<sub>2</sub> and H<sub>2</sub>O<sub>2</sub>-based ATR reforming.**

Variables				T <sub>in</sub>	T <sub>out</sub>	Heater	Mol	Mol
Run	S/C	O <sub>2</sub> /C	Trials <sup>a</sup>	(°C)	(°C)	output (W)	H <sub>2</sub> /O <sub>2</sub>	CH <sub>4(out)</sub>
16	3.35	0.44	6	271	527	54	4.14	0.83
17	3.35	0.44	4 <sup>b</sup>	276	550	46	4.59	0.63

<sup>a</sup>trials are the number of repetitions at each run condition

<sup>b</sup>indicates H<sub>2</sub>O<sub>2</sub> was used

The complete decomposition of H<sub>2</sub>O<sub>2</sub> according to Equation 5 would provide an additional input of 163 W of thermal energy to the system for run #17 compared to run #16. The decrease in pre-heater output, 614 W (run #16) to 529 W (run #17), accounts for 85 W. Using the gas flow rate, specific heats (c<sub>p</sub>) of the gas components, and recorded temperatures, the change in the reactant temperature from 271 °C to 276 °C accounts for only 2 W. The increase in temperature of the outlet gas from 527 °C to 550 °C accounts for approximately 8 W. The flow rate of unconverted methane, CH<sub>4(out)</sub>, was 0.20 lpm less in run #17 than in run #16. While several reaction pathways can account for this difference in CH<sub>4</sub> levels, the most likely explanation is an increase in endothermic steam reforming. The exothermic water gas shift reaction does not account for this difference in CH<sub>4</sub> concentration as the outlet temperature increased in run #17 and a temperature increase serves to reduce the WGS reaction. Therefore, based on the steam reforming equation shown in Equation (2), approximately 30 W is calculated to be required to convert the 0.20 lpm CH<sub>4</sub>.

Using this analysis, and summing up the 85 W + 2 W + 8 W + 30 W accounted for earlier and dividing by the total of 163 W provided by the decomposition of H<sub>2</sub>O<sub>2</sub>, 77 % of the additional chemical energy entering the system as H<sub>2</sub>O<sub>2</sub> can be accounted for. This leaves 23% or 38 W unaccounted for and this may be attributed to additional heat loss from the system.



**Conventional experimental results vs. equilibrium calculations.** Figure 3.4.2-9 is a parity plot comparing equilibrium values with experimental ATR using  $O_2$  as oxidizer at the optimal conditions for 6, 28 and 50 bar.

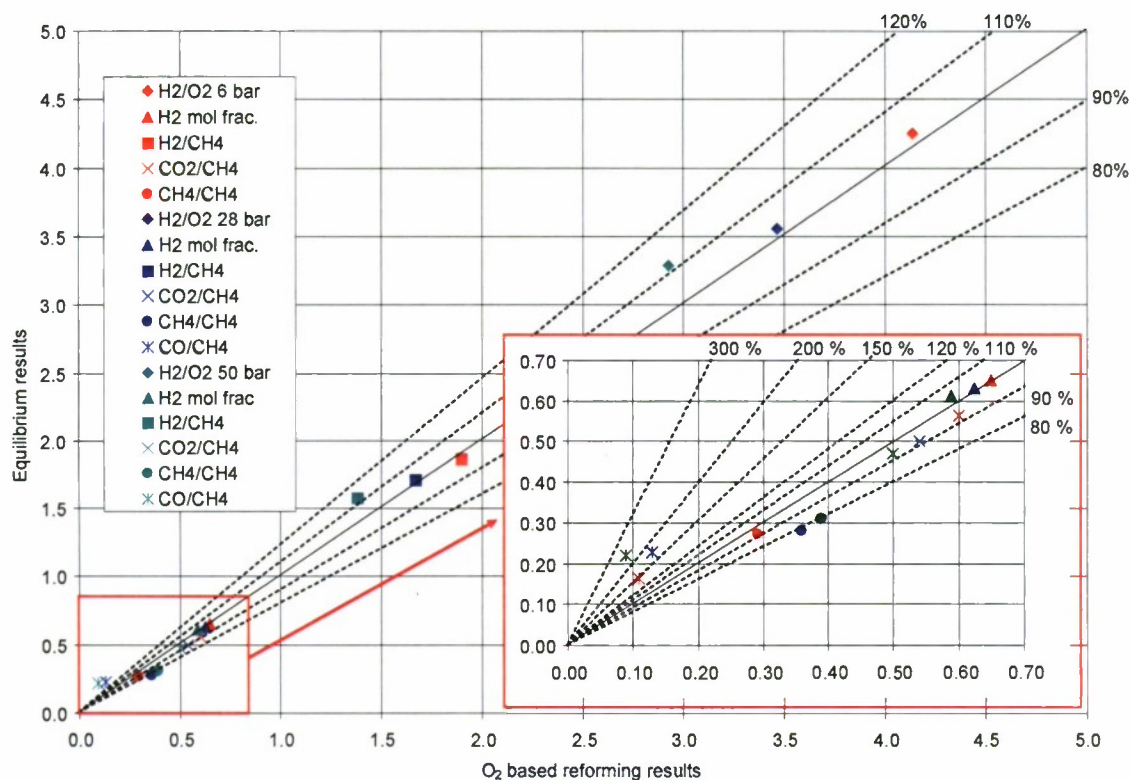


**Figure 3.4.2-9. Comparison of ATR experimental results from tests using  $O_2$  as oxidizer/reactant and thermochemical equilibrium calculations at optimal conditions for 6, 28 and 50 bar.**

At 6 bar the predicted moles of  $H_{2(out)}$  was only 3 % greater than experimentally observed. The predicted moles of  $CH_{4(out)}$  and  $CO_{2(out)}$  differed by 7% or less from the experimental results. The moles of  $CO_{(out)}$  however, were 49% greater. The equilibrium model predicted the temperature of product gas to be 640 °C compared to 512 °C for the experimental results. Overall the equilibrium model showed close agreement with the experimental results at 6 bar.

At 28 bar the predicted moles of  $H_{2(out)}$  was again only 3% greater than the experimental yield. The predicted moles of  $H_{2(out)}$  and  $CO_{2(out)}$  were in close agreement with the experimental results, differing by 8% or less. The predicted value for moles of  $CH_{4(out)}$  was 20% less than experimental while the predicted value for moles of  $CO_{(out)}$  was nearly 200% of the experimental value. The equilibrium model predicted the temperature of product gas to be 743 °C; 229 °C higher than recorded experimentally.

At 50 bar, as observed at lower pressures, the predicted moles of  $H_{2(out)}$  and  $CO_{2(out)}$  per mole of  $CH_{4(in)}$  differed by 14% or less from experimentally observed. The predicted value for moles of  $CH_{4(out)}$  was again 20% less than experimental, while the predicted value for moles of  $CO_{(out)}$  was 240% of the experimental value. The equilibrium model predicted the temperature of product gas to be 774 °C, 202 °C higher than was observed experimentally.



Differences between experimental and equilibrium results can be summarized as: (1) observed moles of  $\text{H}_{2(\text{out})}$  were 97% of predicted values at 6 and 28 bar and 90% of the predicted value at 50 bar, (2) observed moles of  $\text{CH}_{4(\text{out})}$  were 10 % of predicted value at 6 bar and 125% of the predicted value at 28 and 50 bar, (3) observed moles of  $\text{CO}_{2(\text{out})}$  were approximately 8% less than predicted over all pressures, (4) observed moles of  $\text{CO}_{(\text{out})}$  were 67% to 40% of equilibrium values and decreased with increasing pressure, and (5) the experimental outlet gas temperature was on average 186 °C lower than the temperature of products predicted by the equilibrium model. Disagreements indicate that the experimental results did not attain equilibrium and this may be due to non-idealities inherent in the experimental conditions, e.g., the equilibrium calculation does not include the effects of heat loss experienced by the experimental system.

To understand the differences, the temperature profile within the reactor can provide additional insight. The temperature profile in the reactor shown in Figure 3.4.2-10 was captured by a thermocouple located in a stainless sheath at the backend of the catalyst bed as reaction zone slowly blew out of the reactor. As such, the maximum temperature shown would be lower than the maximum gas temperature and the peak shown would be significantly broader than the actual peak. Zone 1 primarily covers the heating of reactants from the oxidation of  $\text{CH}_4$ . Heating largely occurs by conduction through the catalyst bed from the very narrow high temperature region in Zone 2. Zone 2 is characterized by both oxidation and steam reforming reactions. By some point in Zone 2, all of the  $\text{O}_2$  and approximately 25% of the  $\text{CH}_4$  is consumed ( $\text{O}_2/\text{C}$  ratio ~ 0.5) according to Reaction (1). After the peak temperature is reached the steam reforming reactions (Reactions (2) and (3)) consume more heat than is produced and the temperature drops rapidly. This high temperature zone is relatively narrow and conversion in this zone may be limited by catalyst deactivation due to the high peak temperature. Deactivation of the catalyst in this region could be tolerated if the high temperature region is stabilized and provides the necessary heat to the surrounding, active catalyst bed. Further studies should be completed to determine if catalyst performance can be maintained for an extended duration at the observed peak temperatures.

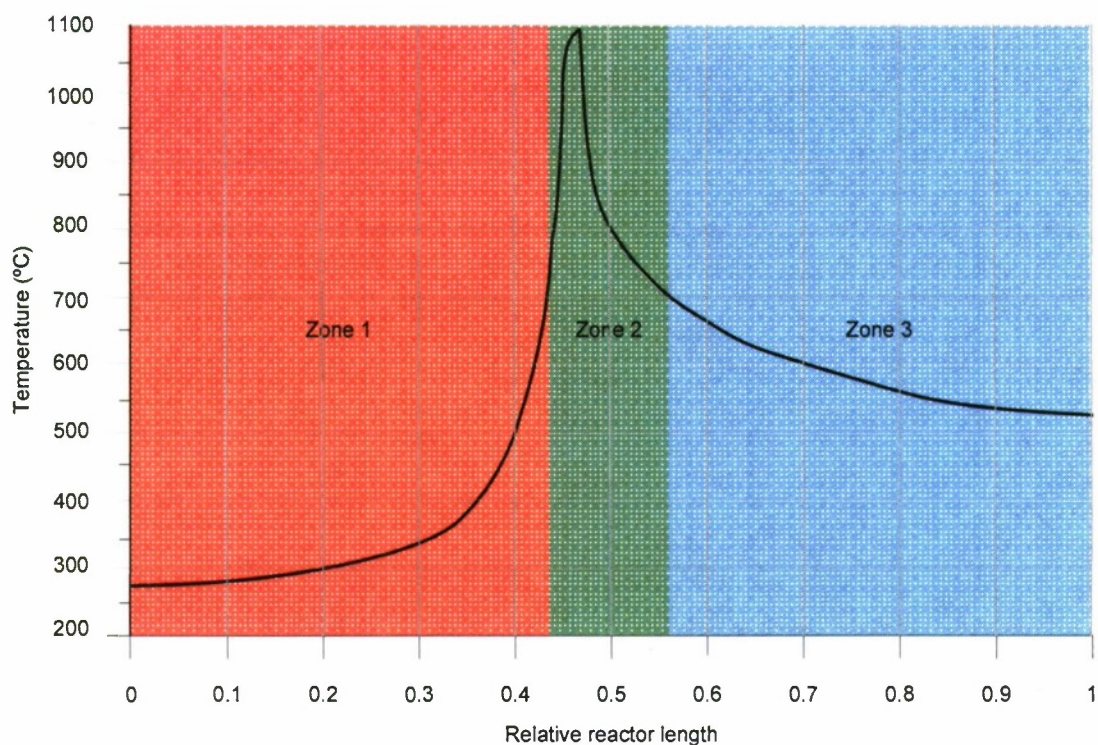


Figure 3.4.2-10. Example experimental ATR temperature profile.

**Comparison to relevant work.** The most complete data set of experimental results in the literature was presented by Hoang *et al.* [24] and figures from this publication were analyzed to produce the comparative data shown in Figure 3.4.2-11 for methane reforming at a pressure of 1 bar. Hoang *et al.* [24] stated that steam was introduced into the reactor, but no further detail on reactant temperature was provided.

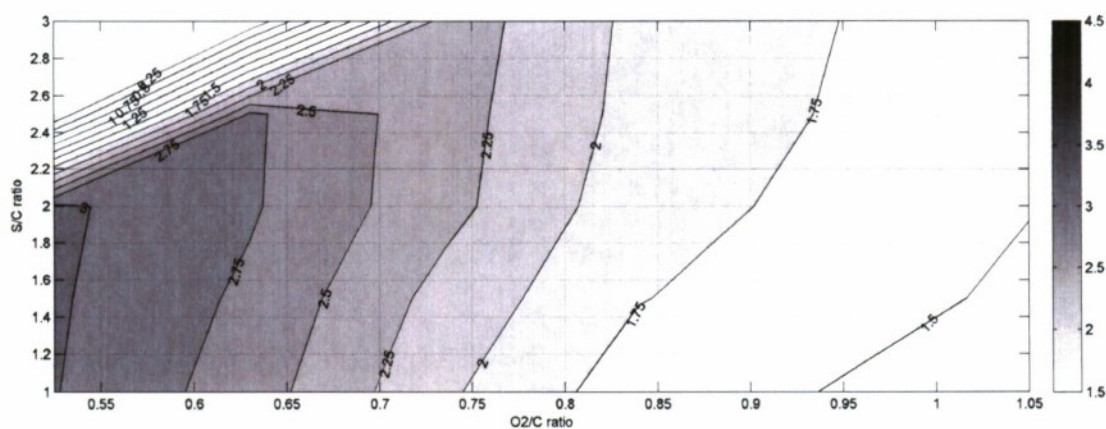


Figure 3.4.2-11. Yield (moles  $H_2$  per mole  $O_2$ ) surface response of autothermal reforming as a function of S/C and  $O_2/C$  ratios based on results at 1 bar operating pressure from Hoang *et al.* [24].



From Hoang's results, the maximum yield of  $H_{2(out)}/O_{2(in)}$  was 3.0 and occurred at an S/C ratio = 1.8 and an  $O_2/C = 0.50$ . This is a marked difference from the present experimental and modeling results and it would appear that Hoang's reactant inlet temperature was significantly lower than the 270 °C inlet conditions in the present study. This would explain why the lower  $O_2/C$  and higher S/C ratios did not produce stable reaction conditions and also why the maximum value of  $H_{2(out)}/O_{2(in)}$  yield occurred at a much higher  $O_2/C$  ratio. While the  $H_{2(out)}/O_{2(in)}$  yield is significantly lower, the trends shown in Figure 3.4.2-11 are very similar to the experimental results from the present study.

**Different optimization criteria.** Reforming experiments are often conducted to optimize the moles of  $H_{2(out)}/CH_{4(in)}$ . From the equilibrium calculations shown in Figure 3.4.2-12, it is clear the optimum yield of  $H_{2(out)}/CH_{4(in)}$  lies in a different region than the optimum yield for  $H_{2(out)}/O_{2(in)}$ . Within the limitations of the operating space, the optimum result is 2.36 moles of  $H_{2(out)}/CH_{4(in)}$  at an S/C ratio = 5 and an  $O_2/C$  ratio = 0.65.

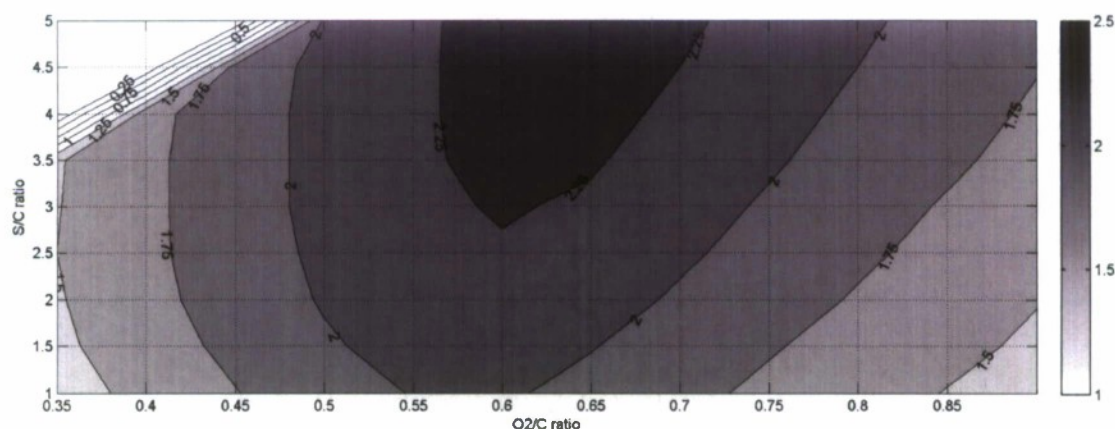


Figure 3.4.2-12. Yield of moles of  $H_2$  produced / mole of  $CH_4$  fed into reactor (equilibrium values, 6 bar, no heat loss).

### 3.4.2.4 References

1. Farrauto, R.J., *Introduction to solid polymer membrane fuel cells and reforming natural gas for production of hydrogen*. Applied Catalysis, B: Environmental, 2005. **56**(1-2): p. 3-7.
2. Larminie, J. and A. Dicks, *Fuel Cell Systems Explained*. 2005. **2nd Edition**.
3. Ersoz, A., H. Olgun, and S. Ozdogan, *Reforming options for hydrogen production from fossil fuels for PEM fuel cells*. Journal of Power Sources, 2006. **154**(1): p. 67-73.
4. Chan, S.H., D.L. Hoang, and O.L. Ding, *Transient performance of an autothermal reformer-A 2-D modeling approach*. International Journal of Heat and Mass Transfer, 2005. **48**(19-20): p. 4205-4214.
5. Ahmed, S. and M. Krumpelt, *Hydrogen from hydrocarbon fuels for fuel cells*. International Journal of Hydrogen Energy, 2001. **26**(4): p. 291-301.



6. Xu, Z., Z. Qi, and A. Kaufman, *Effect of oxygen storage materials on the performance of proton-exchange membrane fuel cells*. Journal of Power Sources, 2003. **115**(1): p. 40-43.
7. Choudhury, N.A., et al., *An alkaline direct borohydride fuel cell with hydrogen peroxide as oxidant*. Journal of Power Sources, 2005. **143**(1-2): p. 1-8.
8. Lyubovsky, M. and D. Walsh, *Reforming system for co-generation of hydrogen and mechanical work*. Journal of Power Sources, 2006. **157**(1): p. 430-437.
9. Faur Ghenciu, A., *Review of fuel processing catalysts for hydrogen production in PEM fuel cell systems*. Current Opinion in Solid State & Materials Science, 2002. **6**(5): p. 389-399.
10. Chan, S.H. and H.M. Wang, *Thermodynamic analysis of natural-gas fuel processing for fuel cell applications*. International Journal of Hydrogen Energy, 2000. **25**(5): p. 441-449.
11. Takeguchi, T., et al., *Autothermal reforming of methane over Ni catalysts supported over CaO-CeO<sub>2</sub>-ZrO<sub>2</sub> solid solution*. Applied Catalysis, A: General, 2003. **240**(1-2): p. 223-233.
12. Hovland, M., A.G. Judd, and R.A. Burke, Jr., *The global flux of methane from shallow submarine sediments*. Chemosphere, 1993. **26**(1-4): p. 559-78.
13. Hornafius, J.S., D. Quigley, and B.P. Luyendyk, *The world's most spectacular marine hydrocarbon seeps (Coal Oil Point, Santa Barbara channel, California): quantification of emissions*. Journal of Geophysical Research, [Oceans], 1999. **104**(C9): p. 20703-20711.
14. Clark, J.F., et al., *Dissolved hydrocarbon flux from natural marine seeps to the southern California Bight*. Journal of Geophysical Research, [Oceans], 2000. **105**(C5): p. 11509-11522.
15. Collier, R.W. and M.D. Lilley, *Composition of shelf methane seeps on the Cascadia Continental Margin*. Geophysical Research Letters, 2005. **32**(6): p. L06609/1-L06609/4.
16. Clark, J.F., et al., *Compositional changes in natural gas bubble plumes: observations from the Coal Oil Point marine hydrocarbon seep field*. Geo-Marine Letters, 2003. **23**(3-4): p. 187-193.
17. Milkov, A.V. and R. Sassen, *Estimate of gas hydrate resource, northwestern Gulf of Mexico continental slope*. Marine Geology, 2001. **179**(1-2): p. 71-83.
18. Kvenvolden, K.A., *Potential effects of gas hydrate on human welfare*. Proceedings of the National Academy of Sciences of the United States of America, 1999. **96**(7): p. 3420-3426.
19. Kvenvolden, K.A., G.D. Ginsburg, and V.A. Soloviev, *Worldwide distribution of subaquatic gas hydrates*. Geo-Marine Letters, 1993. **V13**(1): p. 32-40.
20. Dillon, W. and K.A. Kvenvolden, *Gas (Methane) Hydrates -- A New Frontier*. 1992, U.S. Geological Survey Marine and Coastal Geology Program.
21. *Hawaii Ocean Time-series Data Organization & Graphical System*, <http://hahana.soest.hawaii.edu/hot/hot-dogs/interface.html>.
22. Xiao, T., *Catalytic reaction between methanol and hydrogen peroxide to produce hydrogen, in PCT Int. Appl.* 2005, (Isis Innovation Limited, UK). Wo. p. 24 pp.

23. Box, G.E.P., W.G. Hunter, and J.S. Hunter, *Statistic for Experimenters*. 1 ed. 1978: John Wiley and Sons. 653.
24. Hoang, D.L., S.H. Chan, and O.L. Ding, *Hydrogen production for fuel cells by autothermal reforming of methane over sulfide nickel catalyst on a gamma alumina support*. Journal of Power Sources, 2006. **159**(2): p. 1248-1257.

#### **3.4.2.5 Paper Resulting from this Effort**

Reese, M., S.Q. Turn, and H. Cui. 2009. High pressure autothermal reforming in low oxygen environments. Journal of Power Sources. 187(2) pp. 544-554.





### **Subtask 3.4.3: Plasma Reforming of Methane**

This subtask investigates reforming of methane with plasma. The desired outcomes for this phase are listed below:

1. Design and construct a plasma reactor.
2. Initiate plasma reforming tests.

#### **3.4.3.1 Scope of Work and Approach**

Hydrogen can come from a variety of sources such as natural gas reforming, coal and biomass gasification, and electrolysis. In the near term, large-scale industrial processes utilizing natural gas and coal reforming are expected to play the largest roles in the production of the world's hydrogen [1]. Industrial reforming of hydrocarbons traditionally uses catalytic processes [2]. Downsides of the current catalytic methods include a necessity for large-scale plants, high costs, size, weight, limitations on rapid response, and limitations on the reformation of heavy hydrocarbons [3]. The most detrimental setback, however, is the deterioration of catalysts through the formation of solid carbon on the active sites [4].

Around the turn of the century, gliding arc plasmas started to see use in the production of nitrogen-based fertilizers but soon died out in popularity. Gliding arcs resurged in popularity during the early 90's largely due to Czernichowski who demonstrated their application in a number of processes [5]. He found energy can process any matter without creating a supplementary pollution effect. In addition to the environmental benefits, plasma technology boasted increased reaction rates allowing for smaller reformers, increased speed of response as well as increased fuel flexibility [2]. However, hydrogen conversion can be affected by a host of different variables within the plasma reformers. These include the type of plasma, additive gases, the plasma power generator, the utilization of a catalyst, water vapor injection, as well as the geometry of the reformer [4].

Essentially there are three different types of plasma: thermal plasma (equilibrium plasma), non-thermal (non-equilibrium plasma), and transitional plasma [5]. Depending on system parameters, different arc regimes can be obtained.

Thermal plasma is a high-power, high-temperature plasma. It can deliver more than 50 MW at temperatures from 5,000 to 50,000 °C [6]. At these high temperatures, gases are partially ionized, becoming conductive. The excessive power consumption, however, makes the plasma very inefficient at reforming fuels [7].

Non-thermal plasmas are characterized by low gas temperature, high electron temperature, and direct ionization from electron impact. Cold plasmas such as corona, dielectric barrier discharge (DBD), and glow discharge are very cheap and easy to handle. They typically have an electron temperature from 3,000 to 100,000 °C yet the gas being treated can remain at room temperature [8]. However, they have very low plasma densities, which make it hard to have high flow rates in the reactor. The operating pressures and power levels of the discharges are normally limited, which severely restricts the production rates for large scale industrial processing [9].

Lastly, transitional plasmas exist in a transition regime between the thermal and non-thermal plasma regimes. The most prominent transitional plasma is the gliding plasma arc [7, 9, 10]. This phase contains both the equilibrium and non-equilibrium phases in a given arc and can exist

at atmospheric pressure [10]. This transitional regime has very specific equilibrium and non-equilibrium phases in a given arc and the transitions are smoothly supported by high electric fields. It is believed that the transitional gliding arc discharges have the largest potential [5] as high power levels are maintained with non-equilibrium characteristics.

This work covers the design, construction and initial testing of two plasma reformers. The first reactor design, the traditional gliding arc between two diverging electrodes, was selected as a test set up to gain experience working with a plasma reformer using a relatively simplistic design. Once the system was operational, initial test results were obtained. It was clear that the system was less than ideal and another design was pursued. Previous publications show that reverse vortex flow (RVF) plasma reactors significantly increase the efficiency and fuel reforming abilities of gliding arc plasma [6]. Thus, the second reactor was a RVF reformer which is still under development. A prototype system has been constructed and limited testing has been completed. Preliminary tests involve reforming methane at low flow rates (3.5 l/min or less total gas flow).

### 3.4.3.2 Experimental

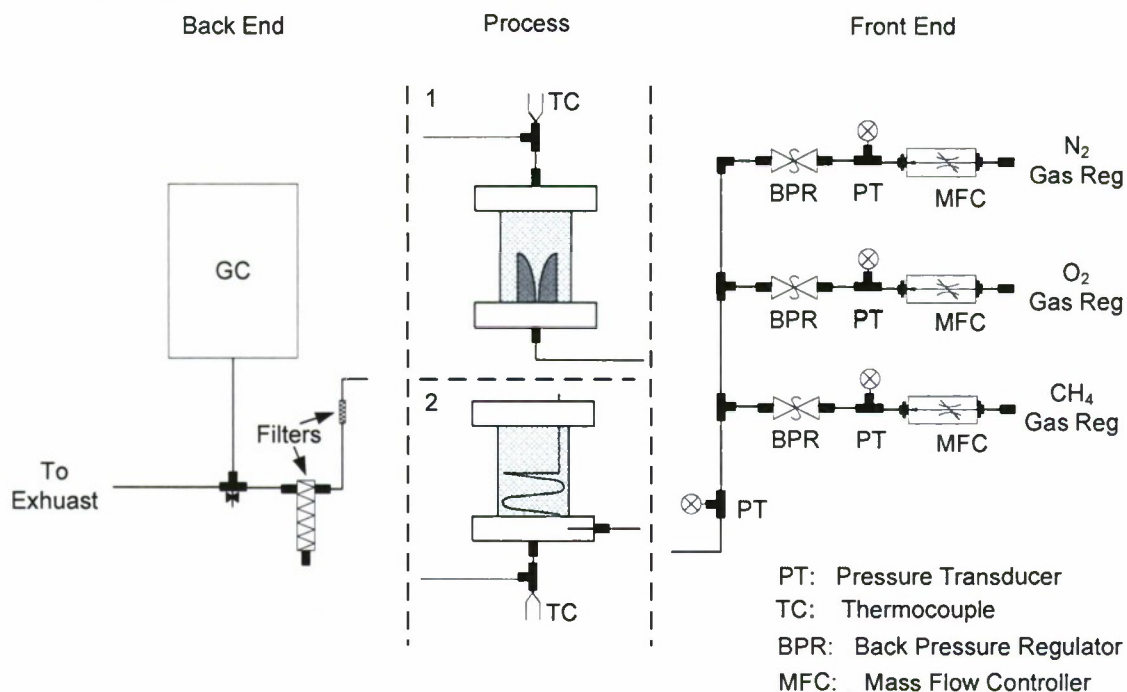


Figure 3.4.3-9. Schematic layout of the plasma reforming system v.1.

The schematic layout of the test facility is shown above in Figure 3.4.3-9. Methane (Grade 4), oxygen, and nitrogen from gas bottles were metered to the reactor using mass flow controllers (MFC) (Brooks 5850 Series E). Flow rates were controlled and recorded along with temperatures and pressures using LabVIEW® (National Instruments, Austin, TX) running on a laptop computer. The temperature at the reactor outlet was measured with a thermocouple. To start the plasma reformer, nitrogen was set to a specified flow rate and the plasma arc was ignited. The arc was initially generated by a 9.0 kV, 145 W neon sign generator (Lecip 4B09N3-

CB, Addison, TX) which was later replaced by a 15 kV, 250 W neon sign generator (Lecip 4B15N3-CB). When the arc was established, oxygen was added to approximate, after mixing with the nitrogen, the composition of air. When the system outlet temperature reached a steady state, methane was added and the plasma reforming began. Downstream of the reactor, the reformat gas passed through a sintered metal 7  $\mu\text{m}$  filter (Swagelok SS-4F-7) and then through a coalescing filter (Balston Model 31G). The dry, effluent, gas was analyzed with a gas chromatograph (GC) (Shimadzu 14A, Columbia, MD) equipped with a Carboxen<sup>TM</sup> 1000 column (SUPELCO 45/60) and thermal conductivity detector (TCD). The schematic layout shows both the gliding arc reformer (1) and the reverse vortex flow (2). The design and operating principals of the two reactor types are described in sections 3.4.3.2.1 and 3.4.3.2.2.

### 3.4.3.2.1 Gliding Arc Reformer

The gliding arc reformer shown in Figure 3.4.3-10 is comprised of a mixing chamber, quartz reactor, electrode mount and two electrode plates. Reactant gases flow into the mixing chamber at the bottom of the gliding arc reformer, pass through an injection port, an axial hole drilled through the middle plate and electrode mount, into the reaction chamber between the electrodes.

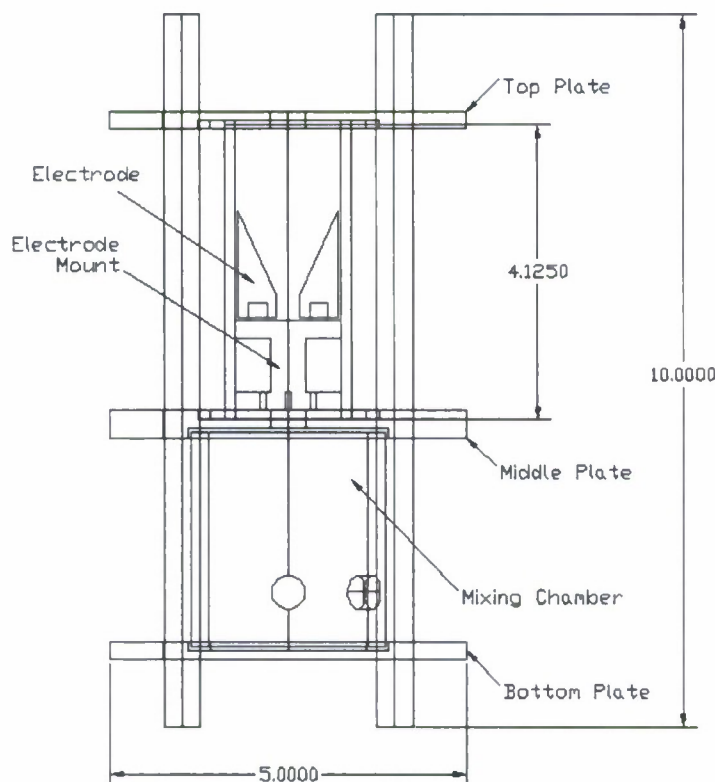


Figure 3.4.3-10. Schematic of gliding arc reformer; units are in inches.

The mixing chamber is sealed to both the bottom and middle plate via a n-buna rubber gasket. All of the Swagelok fittings are welded to the mixing chamber. A gasket between the electrode mount and the middle plate allows for the passage of the electrical connections to the electrodes.



The electrode mount bolted to the middle plate insures gasket compression forcing gases into the reaction chamber through the plasma.

Based on the gas flow rates and injection port diameter, reactant gas enters the reaction chamber at a nominal velocity of 7 m/s and pushes the arc up between the diverging electrodes. As the arc propagates along the electrodes it increases in length and transitions from a thermal arc at the base of the electrodes, to a non-thermal arc. Up to 15 percent of the gas comes in direct contact with the plasma [9]. During the non-thermal phase of the plasma the gas is heated to near 2100 °C but readily cools after exiting the plasma. However the electrons of the treated gas rise to a temperature of near 11,000 °C [7]. These excited electrons break down the methane via direct electron impact ionization [6].

#### 3.4.3.2.2 Reverse Vortex Flow Reformer

The RVF reformer shown in Figures 3.4.3-11 and 3.4.3-12 consists of an inlet/outlet plate, quartz reactor, washer electrode, spiral electrode, and top plate. Premixed reactant gas is introduced tangentially into the bottom of reactor, via the gas inlets in the inlet/outlet plate (Figure 3.4.3-12). The gas flows tangentially and up the wall of the quartz tube (Figure 3.4.3-11). Upon reaching the top plate, the flow continues to spiral and flows axially down the centerline of the reactor inside the outer tornado of gases. This mechanism is referred to as a reverse vortex flow or reverse tornado flow and can be seen in our flow visualization. The axial exit in the inlet/outlet plate has a significantly smaller diameter than the diameter of the quartz tube, which is responsible for the reverse vortex flow [11].

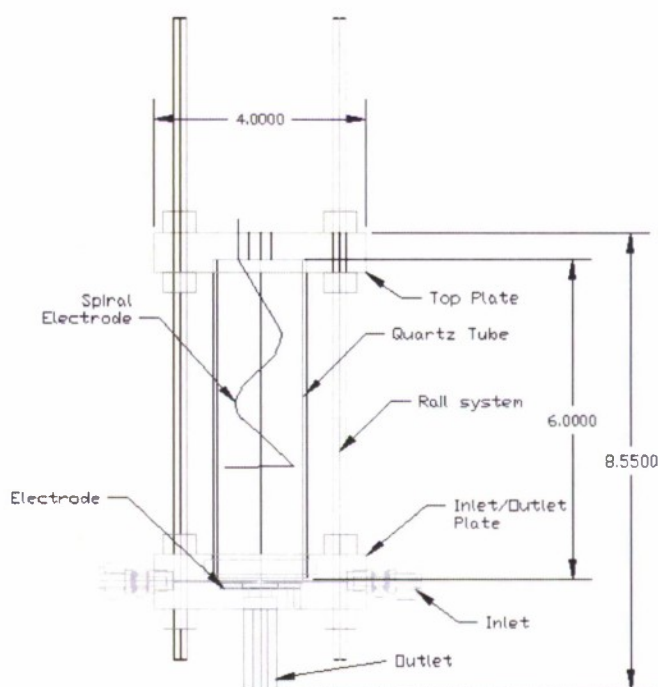
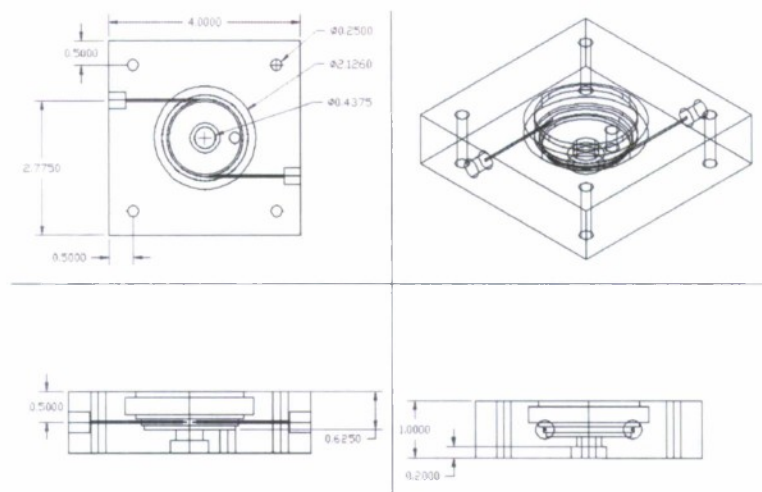


Figure 3.4.3-11. Schematic of the reverse vortex flow reformer; units are inches.



**Figure 3.4.3-12. Reverse vortex inlet and outlet plates; units are inches.**

As the gas enters the reaction chamber it pushes the plasma arc, which is developed between the lower flat disk electrode and the upper spiral electrode, along the spiral electrode causing the length of the arc to increase. Again as the arc length increases the plasma transitions from a thermal to a non-thermal arc. The reactant gas transitions from tangential to axial flow at the top of the reactor and flows down the middle of the quartz tube and recontacts the plasma before exiting through the outlet.

Seals between the quartz tube and the inlet/outlet plate (Macor, Corning Inc.) and the top plate (Macor) are accomplished using high-temperature silicone o-rings. All other parts have been sealed with a zirconium adhesive and high-temperature sealant.

### 3.4.3.3 Technical Accomplishments

Initial testing of the experimental set up has been completed. This section will report preliminary results for the experiments that have been conducted to date.

The reactant ratio of oxygen to carbon ( $O_2/C$ ) present as methane is one of the independent variables that influences reactor performance. An  $O_2/C$  ratio of 0.50 or lower is typical of partial oxidation conditions. Tests were conducted to find a safe range of operating conditions that did not result in soot formation. Initial tests were performed with the gliding arc system using flow rates of 1.04–1.12 l/min  $N_2$ , 0.30–0.32 l/min  $O_2$  and 0.57–0.65 l/min  $CH_4$ . These flow rates produced  $O_2/C$  values of 0.46–0.56 in the reactor.

At an  $O_2/C$  ratio of 0.46, large amounts of carbon quickly deposited on the quartz tube and electrodes. Also, carbon soot could be seen in the gas flow as sparks. Similar results occurred at an  $O_2/C$  ratio of 0.5; however, this took much longer. After one hour of running, visual inspection of the 7  $\mu m$  sintered metal filter showed trapped carbon, and the quartz tube and electrodes had carbon deposition on them as well. At an  $O_2/C$  ratio of 0.56, favorable results were obtained. After an hour of run time, visual inspection of the particulate filter did not show trapped carbon and there was only very trace amounts of carbon deposited on the quartz tube.

Initial test results of the gliding arc reactor are presented in Figure 3.4.3-13. The reformate gas composition by % vol. was as follows:  $H_2$ : 11.6%,  $CO$ : 7.8%,  $CH_4$ : 18.2%,  $CO_2$ : 0.4%, with the

balance  $N_2$ . It is also important to note water could be seen condensing in the tubing and coalescing filter downstream of the reactor. Although  $O_2$  was not measured directly, it is possible that  $O_2$  was passing through the system unreacted, since the entire reactant flow was not acted upon by the plasma. An improved design would ensure a greater percentage of the reactant gas would come into direct contact with the plasma.

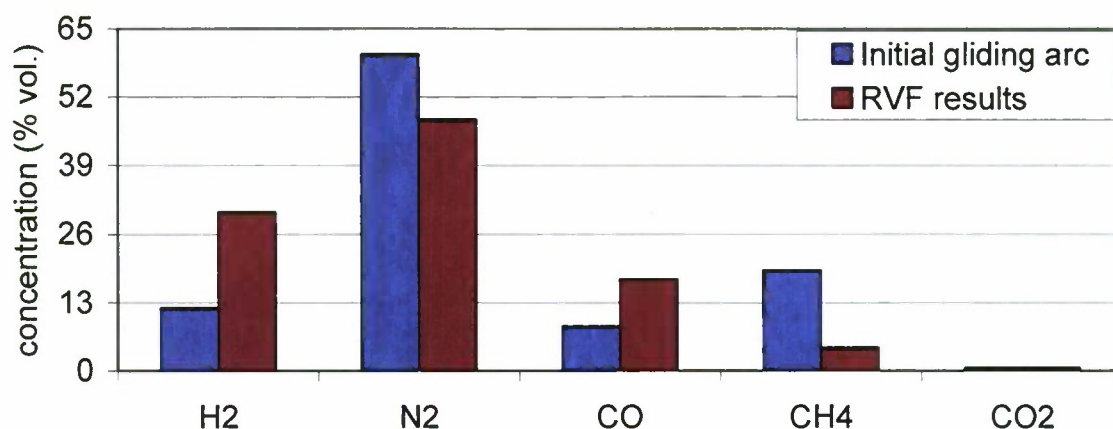


**Figure 3.4.3-13. Comparison of reactor results (initial gliding arc vs. RVF).**

According to the literature, the three dimensional arc in the reverse vortex flow is able to treat significantly more gas than the two dimensional gliding arc. The second system with the reverse vortex was designed and tested. Tests of the two systems with the same gas flow rates, electrical power input, and arc length that would allow direct comparisons were not made as that was not the scope of the project. The gliding arc system was to provide experience and initial data to serve as a starting point. In that aspect the gliding arc reactor was a success.

Once the RVF reactor was designed and built, a series of tests were conducted in order to see the affect of electrical power input on  $H_2$  production. The results of the test are shown in Figure 3.4.3-14. Extrapolating the line fitted to the data indicates that approximately 220 W of power would be required to fully react the  $CH_4$ . A 250 W power supply was purchased and can be used in parallel with additional power supplies to provide 500 W or 750 W.



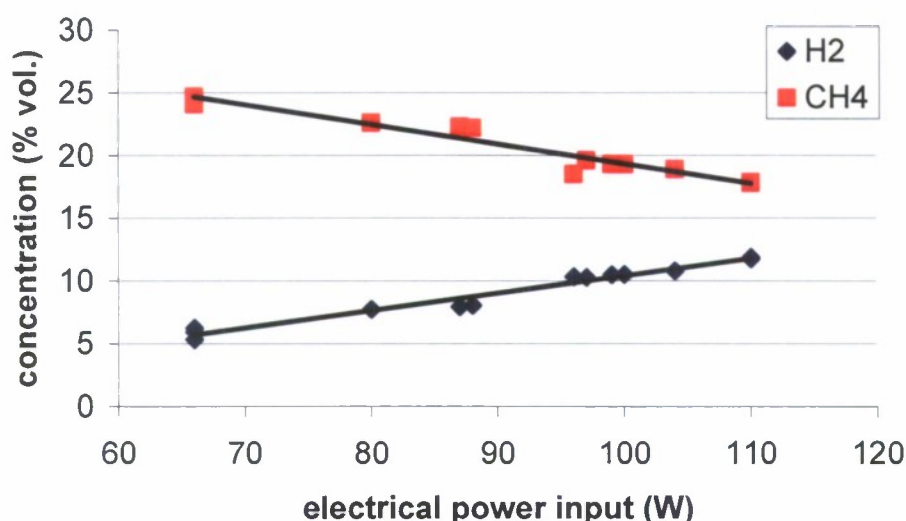


Figure 3.4.3-14. Electrical power in vs. outlet gas composition.

Figure 3.4.3-13 presents results obtained with the RVF with the follow conditions: N<sub>2</sub>: 2.0 l/min, O<sub>2</sub>: 0.5 l/min, CH<sub>4</sub>: 1.0 l/min, and electrical power in: 250 W. Improving the power supply allowed a larger plasma arc to develop, decreased the residual methane from 18.2% to 4.3%, and increased the hydrogen production from 11.6% to 30%.

#### 3.4.3.4 References

1. Mueller-Langer, F., *et al.*, *Techno-economic assessment of hydrogen production processes for the hydrogen economy for the short and medium term*. International Journal of Hydrogen Energy, 2007. 32(16): p. 3797-3810.
2. Czernichowski, A., *GlidArc assisted preparation of the synthesis gas from natural and waste hydrocarbons gases*. Oil & Gas Science and Technology, 2001. 56(2): p. 181-198.
3. Bromberg, L., *et al.*, *System optimization and cost analysis of plasma catalytic reforming of natural gas*. International Journal of Hydrogen Energy, 2000. 25(12): p. 1157-1161.
4. Indarto, A., *et al.*, *Effect of additive gases on methane conversion by using gliding arc discharge*. Energy, 2006. 31(14): p. 2986-2995.
5. Mutař-Yardimci, O., *et al.*, *Thermal and nonthermal regimes of gliding arc discharge in air flow*. Journal of Applied Physics, 2000. 87(4): p. 1632-1641.
6. Kalra, C.S., A.F. Gutsol, and A.A. Fridman, *Gliding arc discharges as a source of intermediate plasma for methane partial oxidation*. IEEE Transactions on Plasma Science, 2005. 33(1, Pt. 1): p. 32-41.
7. Fridman, A., *et al.*, *Gliding arc gas discharge*. Progress in Energy and Combustion Science, 1999. 25(2): p. 211-231.
8. Petitpas, G., *et al.*, *A comparative study of non-thermal plasma assisted reforming technologies*. International Journal of Hydrogen Energy, 2007. 32(14): p. 2848-2867.

9. Rusu, I. and J.-M. Cormier, *On a possible mechanism of the methane steam reforming in a gliding arc reactor*. Chemical Engineering Journal, 2003. 91(1): p. 23-31.
10. Kalra, C.S., et al., *Electrical discharges in the Reverse Vortex Flow – Tornado Discharges*. 2003.
11. Kalra, C.S., et al., *Gliding arc in tornado using a reverse vortex flow*. Review of Scientific Instruments, 2005. 76(2): p. 025110/1-025110/7.

## **3.5 Novel Fuel Cell and Component Development**

The effort to develop novel fuel cell components included two major activities: 1) biocarbons for use in fuel cells, and 2) enzymatic bio-fuel cells. Each of these topics is addressed in the following paragraphs.

### **3.5.1 Biocarbons for use in fuel cells**

#### **3.5.1.1 Objectives**

During 2008, the primary objective of this work was the preparation of biocarbons with widely varied properties for testing by SRI International in their DARPA-sponsored, direct carbon fuel cell research project. A secondary objective was to determine the suitability of sewage sludge for carbonization. Sewage sludge biocarbons were also supplied to SRI for evaluation.

#### **3.5.1.2 Scope of Work and Approach**

Because the USA has the largest reserves of coal in the world, and because biomass can be converted into biocarbons quickly and efficiently, there is growing interest in the efficient use of solid carbon fuels. Also, sewage sludge and battlefield refuse can be quickly and efficiently converted into carbon.

A recent Electric Power Research Institute (EPRI) study indicates that “direct” carbon fuel cells have the potential to convert coal or charcoal into electrical power at a system-level efficiency of about 60%, which is over 20% higher than the efficiencies realized by current state-of-the-art integrated gasification combined cycle (IGCC) or advanced pulverized coal power generation systems.

The following companies are engaged in the commercial development of direct carbon fuel cells: SRI International, SARA, Contained Energy Corp. (representing the Lawrence Livermore National Laboratory -- LLNL), Direct Carbon Technologies LLC (representing Stanford University), and CellTech Power. The most promising direct carbon fuel cell results (published by LLNL) were obtained using a biocarbon (charcoal) fuel. The SRI research also emphasizes biocarbon (charcoal) fuel. Much of this work has been supported by DARPA or the U.S. Department of Defense (DoD).

HNEI has developed and patented a quick and efficient (“Flash Carbonization™”) process for the conversion of biomass and wastes into biocarbons. The patents have been licensed to the Kingsford Products Co. and Carbon Diversion Inc. In addition to the production of biocarbons, with ONR support, HNEI has been a leader in characterizing the properties of biocarbons (see section 3.5.1.4 below). Because of this activity, during 2007 EPRI requested HNEI to supply corn cob biocarbons to two direct carbon fuel cell research projects (SRI International and CellTech Power) for testing. Also, HNEI supplied biocarbons to Contained Energy Corp. (representing the LLNL) for testing. The SRI research is supported by DARPA, and the Contained Energy Corp. research is supported by DoD. During the past year HNEI continued to supply biocarbons to SRI International for testing. These biocarbons were sourced from a variety of feedstocks, including corn cobs, macadamia nutshells, oak and mahogany woods, jatropha, and sewage sludge. HNEI also evaluated the suitability of sewage sludge for carbonization.



### 3.5.1.3 Technical Accomplishments

As mentioned above, during the past year we assisted SRI International with its development of direct carbon fuel cells. The SRI effort is sponsored by DARPA. Corroborating the previous findings of LLNL, SRI has shown that the properties of the carbon fuel influence the performance of its direct carbon fuel cells. But it is not known which properties lead to improved performance. To help SRI identify the desirable properties, HNEI prepared biocarbons with various well-specified properties from a wide variety of biomass feedstocks (e.g., corncobs, macadamia nutshells, oak and mahogany woods, jatropha, and sewage sludge). Biocarbons with low vs. high fixed-carbon contents, low vs. high ash contents, and low vs. high porosities were shipped to SRI for testing and evaluation. The outcome of the tests is confidential to SRI.

We also evaluated the suitability of sewage sludge as a feedstock for biocarbon production. Air-dry sewage sludge is easily carbonized. The properties of its biocarbon resemble those of a lignite coal, but sewage sludge charcoal has very little mercury and sulfur. The details of this work were presented at the recent 2008 American Institute of Chemical Engineers (AIChE) Annual Meeting in Philadelphia and the PowerPoint presentation is available to the public. Currently we are having the heavy metal content of the sewage sludge biocarbon analyzed in preparation for the publication of an archival journal article on sewage sludge biocarbons.

A project sponsored by The Consortium on Plant Biotechnology Research within HNEI, entitled "Flash-Carbonization<sup>™</sup> Catalytic Afterburner Development," has enabled us to make considerable progress towards the operation of a smoke-free, commercial-scale biomass carbonizer on the UH campus. We anticipate successful smoke-free operation of the carbonizer during 2009, and its subsequent use to produce larger quantities of biocarbon fuels for testing and use in DARPA- and DoD-sponsored biofuel research.

### 3.5.1.4 Papers and Presentations Resulting from Efforts

#### PAPERS

Antal, Jr., M.J., Nihous, G.C. "Thermodynamics of an aqueous-alkaline/carbonate carbon fuel cell" *Ind. Eng. Chem. Res.*, Vol. 47, 2008, 2442-2448.

Nunoura, T., Dowaki, K., Fushimi, C., Allen, S., Meszaros, E., and M.J. Antal, Jr. "Performance of a First-Generation, Aqueous-Alkaline Biocarbon Fuel Cell. *Ind. Eng. Chem. Res.* Vol. 46, 2007, pp. 734-744.

Antal, Jr., M.J., Bourke, J., Manley-Harris, M., Fushimi, C., Dowaki, K., and Nunoura, T. "A Model of the Chemical Structure of Carbonized Charcoal" *Ind. Eng. Chem. Res.*, Vol. 46, 2007, pp. 5954-5967.

Antal, Jr., M.J., Meszaros, E., Varhegyi, G., Jakab, E.; Bourke, J., Manley-Harris, M.; and Nunoura, T. "Do all carbonized charcoals have the same chemical structure? Implications of TG-MS measurements." *Ind. Eng. Chem. Res.*, Vol. 46, 2007, pp. 5943-5953.

Antal, Jr., M.J., Varhegyi, G., Meszaros, E., Bourke, J., and Jakab, E. "Combustion Kinetics of Corncob Charcoal and Partially Demineralized Corncob Charcoal in the Kinetic Regime." *Ind. Eng. Chem. Res.*, Vol. 45, 2006, pp. 4962-4970.

Antal, Jr., M.J., Wade, S.R., and Nunoura, T. "Studies of the Flash Carbonization Process. 2. Violent Ignition Behavior of Pressurized Packed Beds of Biomass: A Factorial Study." *Ind. Eng. Chem. Res.*, Vol. 45, 2006, pp. 3512-3519.

PRESENTATIONS by Michael J. Antal, Jr.

Organized and chaired two topical sessions concerning chemical engineering for biomass conversion and novel fuel cell applications during the *AIChE Annual Meeting* in Philadelphia from 16 – 21 November, 2008.

Organized and chaired two topical sessions concerning chemical engineering for novel fuel cell applications and biomass conversion during the *AIChE Annual Meeting* in Salt Lake City from 4 – 9 November, 2007.

Presented invited seminars on the carbon fuel cell at Eindhoven University (7 February 2006), the University of Missouri at Columbia (10 November 2006), the University of Massachusetts at Boston (16 February 2007), the University of Hawaii at Manoa (25 September 2007), and the Hungarian Academy of Sciences (25 October, 2007).

Organized and chaired three topical sessions concerning chemical engineering for novel fuel cell applications and biomass conversion during the *AIChE Annual Meeting* in San Francisco from 13 – 17 November, 2006. Presented two talks: “Optimization of Flash Carbonization<sup>TM</sup> Conditions for Charcoal Production from Sunflower Shells,” and “Performance of a First-Generation Aqueous-Alkaline Biocarbon Fuel Cell” in these sessions.

On 28, 29 August 2006, attended a “by-invitation-only” meeting at EPRI Headquarters in Palo Alto and delivered a lecture entitled: “Performance of a First-Generation Aqueous-Alkaline Biocarbon Fuel Cell.”





## 3.5.2 Enzymatic Bio-Fuel Cells

### 3.5.2.1 Objectives

As stated in our previous reports, enzymatic bio-fuel cells (EBFCs) are fuel cells that use enzymatic biocatalysts to convert chemical energy directly to electricity as power sources. They are promising alternatives to complement conventional fuel cell technologies that rely on transitional metal oxides or noble metals as catalysts for conversion of chemical energy, typically stored in hydrogen, to useful electrical energy. An EBFC exhibits some promising technical merits as follows:

- Selectivity – Enzyme catalysts are fuel specific and capable of handling complex fuels in the liquid phase, which can simplify fuel logistics and cell design;
- Abundance in supply – Unlike conventional Pt-based catalysts, enzymatic catalysts can be produced via biological or chemical methods, thus promising a potentially low-cost mass production and unlimited supply;
- Wider range of operation – Due to their selectivity, enzymes are generally more adaptive to extreme conditions and tolerant to contaminants;
- Reformulation – If the gene coding for the enzyme is obtained, a suite of directed evolution techniques exists to create mutants that are more effective in catalysis; and
- Self-assembly – Unique in biological systems, to simplify fabrication processes for micro-devices *in situ*.

The continuation of support shall enable us to focus on fundamental studies to elucidate charge transfer limitations in enzyme-catalytic electrodes, so we can transfer this knowledge into improved engineering designs of practical *bio-fuel cells*. The following long-term objectives have been pursued under this program:

- Establish an array of quantitative *in situ* characterization techniques, test cells, and modeling capabilities to determine limitations to bioelectrocatalysis [1-4], and to construct a test bed that will allow us to refine such techniques in microbial- or enzyme-based bioelectrocatalysis operation [5]; and
- To develop a technology base with know-how to improve performance (e.g., catalyst lifetime, current density) with respect to important process variables such as choice of catalyst, choice of mediators, immobilization matrix, and mode of immobilization (e.g., covalent attachment versus physical entrapment of enzyme).

### 3.5.2.2 Scope of Work and Approach

Over the course of this project, three major tasks in the EBFC work have emerged:

- 1) Develop platform fabrication technology to control the resulting multidirectional pore structure of three-dimensional electrodes;
- 2) Develop qualitative and quantitative fluorescence as a characterization technique for enzyme fuel cells; and
- 3) Develop *in situ* interface characterization techniques utilizing imaging ellipsometry with quartz crystal microbalance and electrochemical techniques to facilitate fabrication and testing of full bio-fuel cells

For this specific funding period, we were funded to pursue the following:

- 1) Develop platform technology to make multidirectional and multidimensional chitosan scaffolds for use as three-dimensional immobilization matrices for electrode fabrication;
- 2) Continue to develop PQQ-dependent enzymatic systems for bio-anode application<sup>1</sup>; and
- 3) Develop characterization techniques to assess the practicality of using self-assembled monolayers (SAM) for enzyme immobilization.

### 3.5.2.3 Technical Accomplishments

*Summary of work from previous project periods.* In past reports, we have presented several prototype cells constructed to deliver gas (e.g., hydrogen) fuels. A final working hydrogenase enzymatic bio-fuel cell was constructed and tested (Figure 3.5-1). The design considerations and test applications were described in the June 2005 Final Technical Report. Complete details on this work have been published [1]. From this work we determined, and reported previously, that the use of gaseous fuels is limited by the solubility of the gaseous fuel in the aqueous buffer that is required to maintain enzyme activity.

In past reports we have also commented on the development of a suite of characterization techniques, including potentiostatic DC polarization, dynamic potentiometry, and electrochemical impedance spectroscopy (EIS) combined with spectrophotometric detection of enzyme activity, in order to characterize electrode performance, and to differentiate between the relative contributions towards charge transfer efficiency. Among the results of our efforts, in particular, we believe we were one of the first groups to report charge transfer efficiency for bound enzyme [1] and to report a mass transport modeling effort that can be combined with DC-polarization data to yield information valuable for future electrode development [2]. A detailed description of the technique application, data and results can be found in the literature. A summary can also be found in a book chapter that was published in 2007 [6].

To characterize the distribution of enzymes within the polymer films used to immobilize the enzymes, we have applied the technique of fluorescence. Electrode fabrication methodologies using the immobilization process with polymer films inherently assume that the immobilized enzymes are homogeneously distributed. Our work, which has tagged ethanol-oxidizing enzymes with various fluorescent probes, has used laser-scanning confocal microscopy to image the spatial distribution of the enzyme within the film. Our results, which have been published [3] (see Figure 3.5-2), have clearly demonstrated that this is not

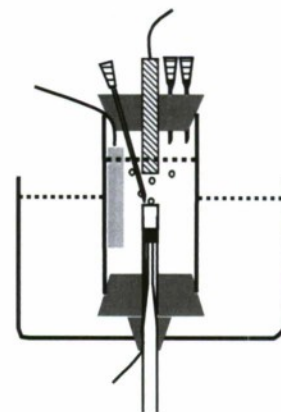


**Figure 3.5-1.**  
Hydrogenase enzyme  
fuel cell.

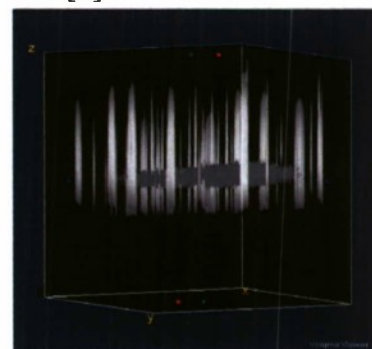


**Figure 3.5-2. 3D  
distribution of tagged  
enzyme within polymer.**

<sup>1</sup> These enzymes can be bound to either chitosan-CNT or conductive polymers, such as polypyrrole, as novel immobilization approaches that can realize direct electron transfer.



necessarily the case, and that the tagged enzymes may not be homogeneously distributed within polymer films. To investigate how the charge-charge interaction between the enzyme and the polymer affect the immobilization process, we have also studied the steady-state and dynamic polarization of fluorescent probes when placed in solution with charged polymers. This work has shown that the enzymes are retained in the micelles of the hydrophobically-modified polymer as it dries, but are not entrapped within those polymers while mixed in free solution [4].

To evaluate film thickness during electrochemical deposition of electrode immobilization matrix or mediator film on electrode surface, we have combined the technique of imaging ellipsometry with the cyclic voltammetric deposition technique to track the thickness of the deposited film with cycle number. This very valuable technique has contributed new information regarding the fundamental reaction kinetics and mechanisms underlying the electrochemical deposition of conductive films onto electrode surfaces (see Figure 3.5-3). The initial work has been published [5]. More, a unique imaging ellipsometric technique in combination with quartz crystal microbalance (QCM) and electrochemical cyclic voltammetric techniques for surface film deposition and characterization has been developed through this effort. Imaging ellipsometry is capable of measuring surface morphology and film thickness in nanometer scale, providing us a powerful surface characterization technique that is *in situ* and non-invasive. We were able to control the polymer film formation with accurate thickness and morphology control during deposition. This technique also helped us understand the stepwise underlying mechanism in the deposition and provided unprecedented details in the film formation process involving redox reactions. We are currently using this technique to study the redox kinetics involved in the NADH oxidation.

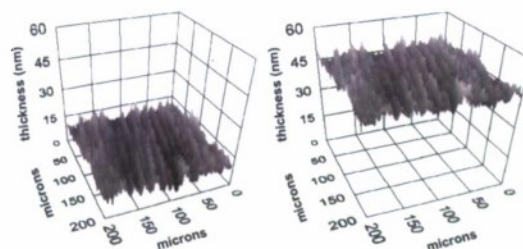


**Figure 3.5-3. Film thickness of poly(methylene green films.**

During this period, these outcomes were also used to leverage two extramurally funded projects. The first one is a grant from the Director of the Central Intelligence Postdoctoral Fellow Research Program to support development of bio-fuel cells for micro-power source applications (B.Y. Liaw, PI). The second is a sub-award from the AFOSR Multi-disciplinary University Research Initiative (MURI) program (M.J. Cooney, PI), awarded to the lead institution, the University of New Mexico (P. Atanasov, PI). Both awards have lent national recognition of this EBFC program.

During this period, these outcomes were also used to leverage two extramurally funded projects. The first one is a grant from the Director of the Central Intelligence Postdoctoral Fellow Research Program to support development of bio-fuel cells for micro-power source applications (B.Y. Liaw, PI). The second is a sub-award from the AFOSR Multi-disciplinary University Research Initiative (MURI) program (M.J. Cooney, PI), awarded to the lead institution, the University of New Mexico (P. Atanasov, PI). Both awards have lent national recognition of this EBFC program.

In collaboration with these partner programs, we have explored chitosan and chitosan-composite scaffolds as a material for the fabrication of macroporous electrodes that can support both mediator-based and direct electron transfer. Work accomplished has included the development of protocols for the fabrication of hydrophobically-modified chitosan scaffolds immobilizing NADH-dependent glucose oxidase, and chitosan/CNT composites for attachment of PQQ-enzymes. With respect to the fabrication of hydrophobically-modified chitosan scaffolds, we have demonstrated proof-of-principle data that shows that the power density can be significantly



increased for mediator-based systems (Figure 3.5-4). This work has been published in the Journal of Materials Chemistry [6]. We have also fabricated three-dimensional chitosan/CNT scaffolds that provide a basis for enzymes that are capable of direct electron transport. The chitosan essentially acts as a binder of the carbon nanotubes and one is left with scaffold structures similar to that presented in Figure 3.5-4, but with carbon nanotubes lining the surface. These scaffolds are highly conductive and represent a new methodology to create multidirectional and multidimensional 3D structures of electrochemically-active carbon nanotube surfaces [7].

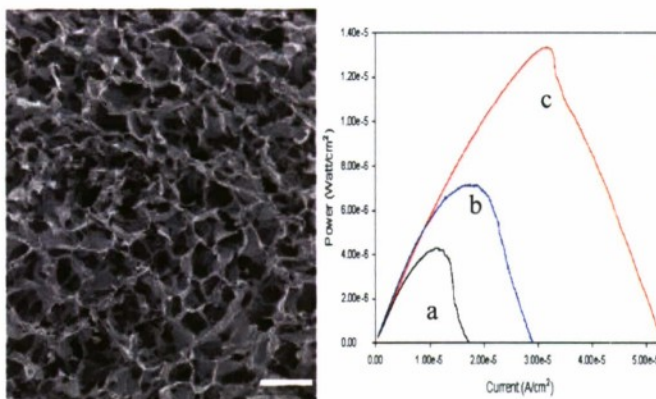


**Figure 3.5-4. SEM image of chitosan scaffold (Left) and power curves from chitosan film (a) and scaffolds (b, c).**

We have also developed a liquid-phase prototype Bio-fuel Test Cell (Figure 3.5-5). This prototype, which we term the modular stack cell, was designed as a characterization tool. For example, we sent duplicate models of the modular stack cell to three cooperating laboratories in the U.S. that also specialize in enzyme fuel cell development. Each laboratory (Dr. Shelley Minter at St. Louis University, Dr. Plamen Atanassov at the University of New Mexico, and Dr. Scott Barton at Michigan State University) was given the same protocol to execute (i.e., to develop a poly[methylene green] electrode film that oxidizes NADH), and the electrochemical data from all laboratories were consolidated and statistically analyzed for reproducibility. The results demonstrated that the modular stack cell provides a framework for comparative analysis of systems. The results have been published in the Journal of Electroanalysis [8]. With this confidence, we have fabricated a full ethanol-based bio-fuel cell based on this design (Figure 3.5-6). Although we have achieved full operation (see power curves in Figure 3.5-6) with an air-breathing cathode, this work is still in development [9].

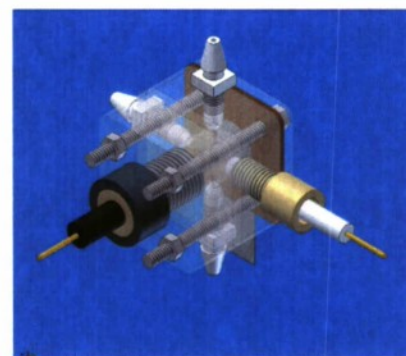


**Figure 3.5-5. The modular stack cell.**

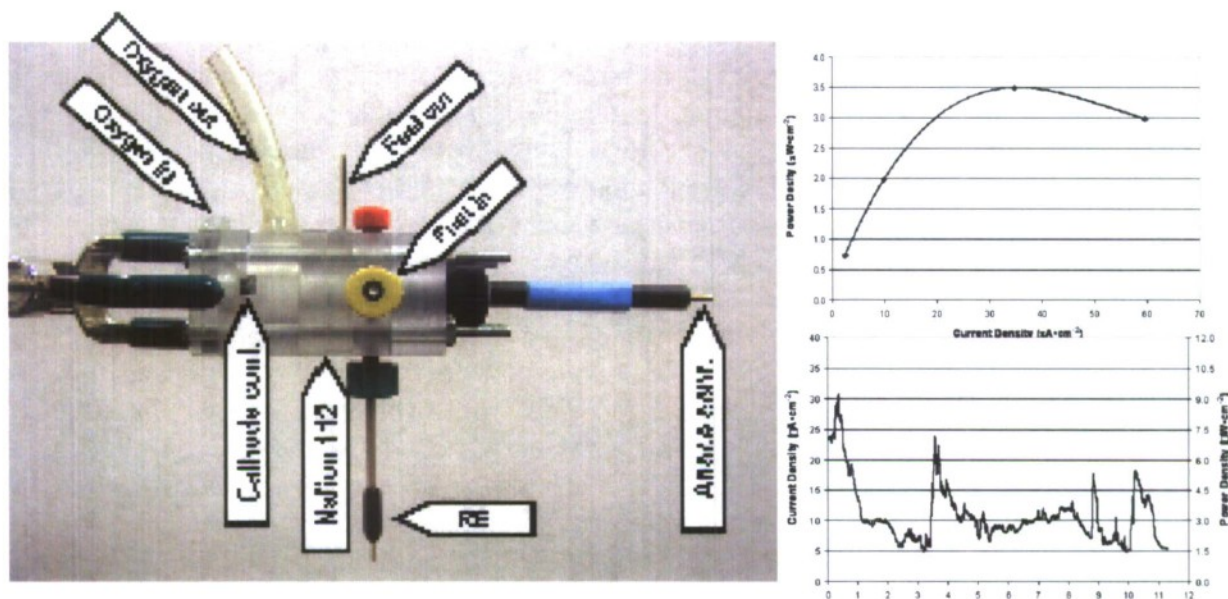


Figure 3.5-6. Operational biofuel cell, based on modular stack cell design.

In addition to these accomplishments, we have also initiated an enzyme immobilization effort to establish a common platform for apo-enzyme reconstitution. The prosthetic group pyrroloquinoline quinine (PQQ) and PQQ-dependent glucose dehydrogenase (PQQ-GDH) has been chemically bound to CHIT-CNT films in the presence of EDC (acronym for 1-ethyl-3-[3-dimethylaminopropyl] carbodiimide hydrochloride), respectively. The immobilized PQQ-GDH in our system displays a quasi-reversible electron transfer with a formal potential  $E^{\circ'}$  of  $-0.110$  V, which was found to be independent of the scan rate. The bioactivity of the immobilized PQQ-GDH was retained. Additionally, the enzyme-free bound PQQ exhibits a more facile electron transfer with a glassy carbon electrode (GCE) compared to the immobilized PQQ-GDH, suggesting that PQQ-bound CHIT-CNT films hold promise as a platform for the reconstitution of PQQ-dependent apo-enzymes, with potential application in biosensors and bio-fuel cells. Evidence of electron transfer between bound PQQ-GDH and the GCE has been observed when the PQQ-GDH has been coupled with EDC to a CNT-functionalized CHIT film. The experimental results suggest that the presence of CNT in the CHIT film promotes the electron transfer of bound PQQ-GDH to the GC electrode. A quasi-reversible electrochemical reaction, as revealed by a pair of well-defined redox peaks, was also observed by cyclic voltammetry, and additional experimental results suggest that the bioactivity of PQQ-GDH was retained in PQQ-GDH-bound CHIT-CNT/GCE, which permits its use as a platform catalyst combination for a mediated bio-fuel cell anode or amperometric biosensor electrode for glucose detection. It should be noted that PQQ bound to CHIT-CNT film also exhibited an effective charge transfer with GCE, suggesting that it can be used as a promising platform for reconstitution of various PQQ-dependent apo-enzymes. A summary of this work has been published [10].

#### *Summary of additional work accomplished during this period.*

Of special interest for an enzymatic power generation from ethanol as biofuel are NAD-dependent dehydrogenases, like alcohol dehydrogenase (ADH) or malate dehydrogenase (MDH), which lie within the Krebs's cycle. This fundamental metabolic pathway involves eight



enzymes for energy production through aerobic respiration. In order to exploit the entire cycle on a bioanode, and within the context of increased power generation, a polymer system that can immobilize and stabilize all eight enzymes in a three-dimensional matrix is needed. In support of developing macroporous chitosan and chitosan-derivate scaffolds as advanced materials for fabrication of biofuel cell electrodes, as specified in 1), we have immobilized MDH within modified chitosan-polymer scaffolds placed upon a poly(methylene green) modified glassy carbon electrode. The current and power density for this MDH bioanode have been tested in half cell mode (Figure 3.5-7) and are currently being tested in a full biofuel cell. The half cell mode results represent a significant advance in the development of flow-through electrodes and confirms the application of an enzyme immobilized in a modified chitosan polymer. We have also used fluorescence to track the spatial distribution of enzyme immobilized in the hydrophobically-modified polymer (Figure 3.5-8). This work, which has been published [11], clearly demonstrated that the distribution of a fluorescently-tagged enzyme (the pink in Figure 3.5-8) distributes quite differently in various forms of the hydrophobically-modified chitosan polymer (i.e., native, butyl-modified, and ALA-modified).

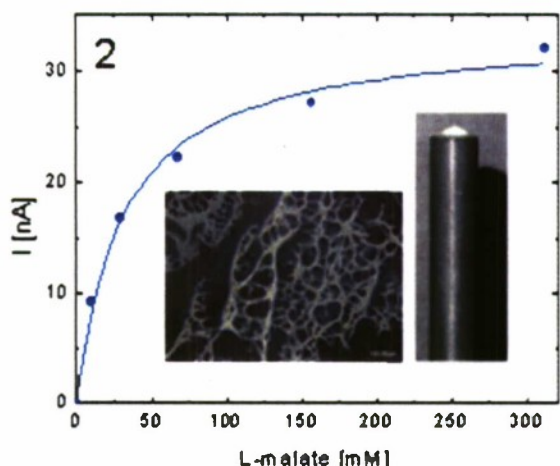


**Figure 3.5.7. Electrical results for MDH bioanode.**

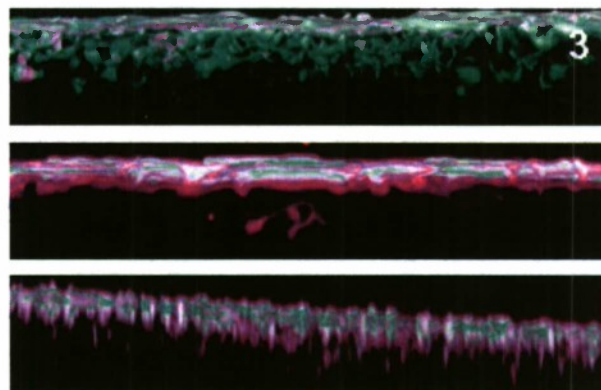


**Figure 3.5.8. Enzyme spacial distribution.**

The poly(methylene green) mediator has been considered one of the best mediators for  $\text{NAD}^+$ -dependent biocatalytic process and thus of great interest to the enzymatic bio-fuel cell operation. However, the interfacial property of this mediator polymer film on biocatalytic electrodes is not well understood to date. We have used electrochemical microgravimetric imaging ellipsometry (EmIE) to study the interfacial property of this mediator compound on Pt or glassy carbon electrode surfaces. The EmIE technique allows us to correlate changes of mass, charge, and ellipsometric measurements in a synchronized and transient manner to derive information on chemical and electrochemical behavior of this polymer mediator film (Figure 3.5-9).



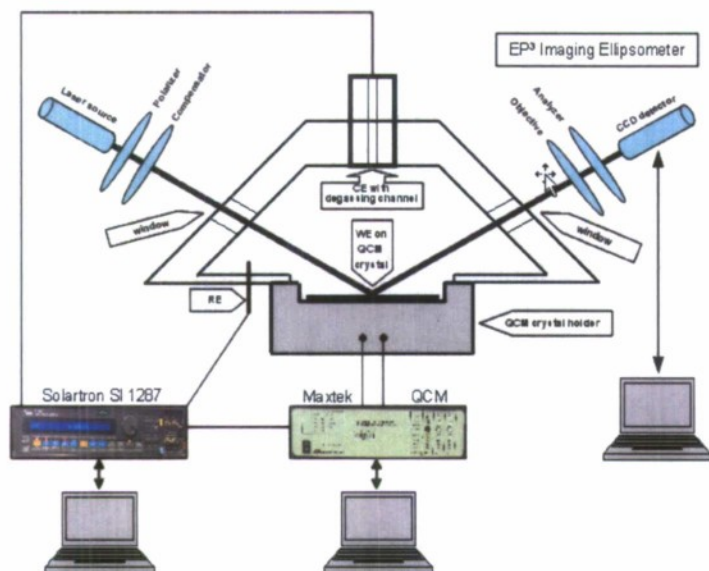


Figure 3.5-9. EmIE measurement set-up.

film thickness is also measurable by the ellipsometric method. The electrochemical redox reaction, on the other hand, occurs at a different time scale and the corresponding current change is also in sync with the ellipsometric angle change in  $\Psi$ , which has a split peak: one corresponds to the mass (thus film thickness) change and the other to the chemical change in the redox process. It is therefore interesting to observe this transient behavior of the film development, where the mass change is related to adsorption, while the redox reaction does not have a direct correlation with mass measured.

We also showed that with proper estimates of the parameters in the optical model, we can simulate the film thickness changes with deposition conditions (Figure 3.5-11). This is a powerful tool to allow real-time *in situ* observation with quantitative characterization.

As a result of such studies, we have produced some interesting results based on the EmIE approach in the study of poly(methylene green) mediator. Highlights are as follows:

Figure 3.5-10 shows that the transient change of mass and current do not coincide in the synchronized measurements. However, the ellipsometric measurements show that the ellipsometric angle  $\Delta$  is in sync with transient mass changes at all times, indicating that the mass change is actually detectable and the corresponding change in such a surface

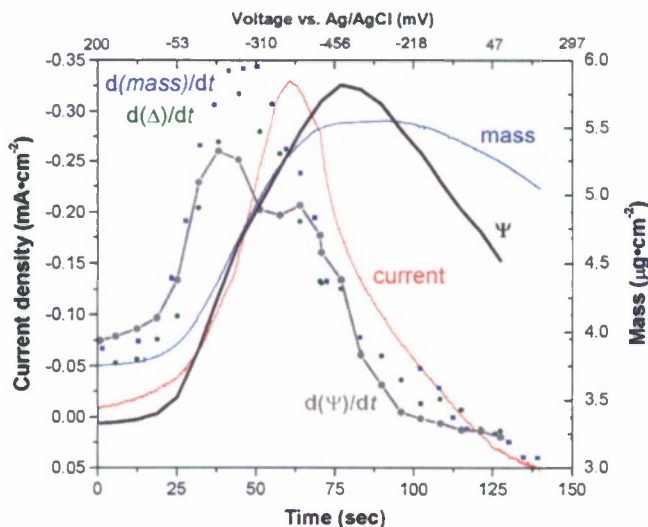


Figure 3.5-10. Current and mass variations.

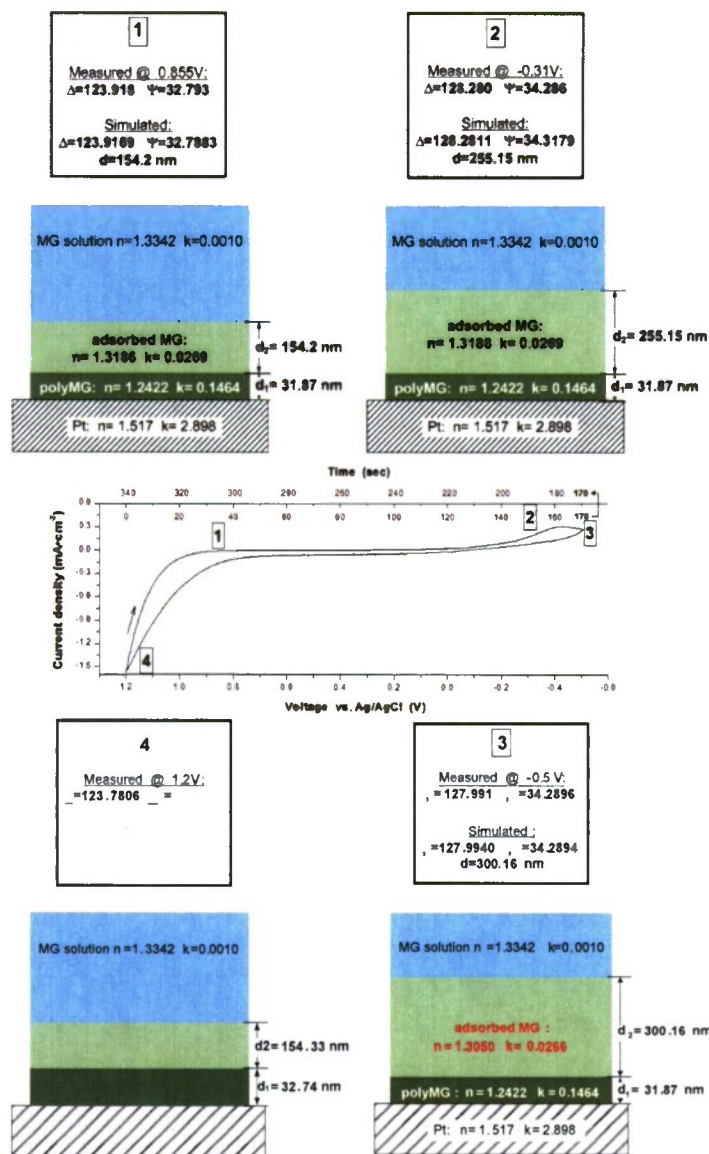


Figure 3.5-11. Simulation of film thickness changes with deposition conditions.

### 3.5.2.4 References

1. Johnston, W., Cooney, M.J., Liaw, B.Y., Sapra, R., and Adams, M.W.W., *Design and characterization of redox enzyme electrodes: new perspectives on established techniques with application to an extremophilic hydrogenase*. Enzyme and Microbial Technology, **2005**. **36**: p. 540-549.
2. Johnston, W., Maynard, N., Liaw, B., and Cooney, M.J., *In situ measurement of activity and mass transfer effects in enzyme immobilized electrodes*. Enzyme and Microbial Technology, **2006**. **39**: p. 131-140.

3. Konash, S., Cooney, M.J., Liaw, B.Y., and Jameson, D., *Characterization of Polymer-Enzyme Interactions using Fluorescence*. Journal of Materials Chemistry, **2006**. **42**, p. 4107-4109.
4. Martin, G. L., Ross, J. A., Minter, S. D., Jameson<sup>☒</sup>, D. M., and M. J. Cooney<sup>☒</sup>. *Fluorescence characterization of polymer chemical microenvironments*. Carbohydrate Polymers. doi:10.1016/j.carbpol.2009.02.021.
5. Svoboda, V., Cooney, M.J., Rippolz, C., and Liaw, B.Y., *In-Situ Characterization of Electrochemically Polymerized Methylene Green Films on Platinum and Glassy Carbon Electrodes*. Journal of the Electrochemical Society, **2006**. **154**(3): p. D113-116.
6. Cooney<sup>☒</sup>, M. J., Windmesier, M, Lau, C., Liaw, B. Y., Klotzbach, T. and S. Minter<sup>☒</sup>. *Design of Chitosan Gel Pore Structure: Towards Enzyme Catalyzed Flow-Through Electrodes*. Journal of Materials Chemistry, **2008**. **18**, 667-674.
7. Lau, C., Cooney<sup>☒</sup>, M. J., and P. Atanassov. *Conductive macroporous composite chitosan-carbon nanotube scaffolds*. Langmuir. **2008**. **24**, 7004-7010.
8. Svoboda, V., Cooney<sup>☒</sup>, M. J., Liaw, B. Y., Minter, S., Piles, E., , Lehnert, D. Barton, S. C., Dmitri Ivnikski, D., and P. Atanassov. *Standardization of a common platform for bioelectrocatalysis characterizations*. Electroanalysis, **2008**. **20**(10):1099 – 1109.
9. Svoboda, V., Cooney, M.J., Rippolz, C., and B.Y. Liaw. *In situ Characterization of an Enzyme Catalyzed Bio-Fuel Cell. In Preparation*.
10. Sun, D., Cooney, M. J., and B. Y. Liaw. *PQQ-glucose dehydrogenase immobilized in chitosan / carbon nanotubes composite films*. Electrochemical Solid State Letters. **2008**. **11**(6) B101-B104.
11. Martin, G., Minter, S. D., and M. J. Cooney<sup>☒</sup>. *Spatial distribution of malate dehydrogenase in chitosan scaffolds*. Applied Materials & Interfaces, 2009. **1**(2):367–372.

### 3.5.2.5 Papers and Presentations Resulting from Efforts

#### PAPERS

- 2009** Martin, G. L., Ross, J. A., Minter, S. D., Jameson<sup>☒</sup>, D. M., and M. J. Cooney<sup>☒</sup>. *Fluorescence characterization of polymer chemical microenvironments*. Carbohydrate Polymers. doi:10.1016/j.carbpol.2009.02.021.
- 2009** Martin, G., Minter, S. D., and M. J. Cooney<sup>☒</sup>. *Spatial distribution of malate dehydrogenase in chitosan scaffolds*. Applied Materials & Interfaces. **1**(2):367–372
- 2009** Cooney<sup>☒</sup>, M. J., Petermann, J., Lau, C., and S. D. Minter<sup>☒</sup>. *Fabrication and Characterization of Hydrophobically Modified Chitosan Scaffolds*. Carbohydrate Polymers, **75**(3):428-435.
- 2009** V. Svoboda and B.Y. Liaw, “In-situ transient study of polymer nano-film growth via simultaneous correlation of charge, mass, and ellipsometric measurements” *Pure Applied Chem.*, **80** (2008) 2439–2449
- 2008** Cooney, M. J., Lau, C., Martin, G., Svoboda, V., and S. D. Minter<sup>☒</sup>, *Biofuel Cells*. Energy and Environmental Science. Energy & Environmental Science, **1**:320 - 337.



- 2008 Lau, C., Cooney<sup>✉</sup>, M. J., and P. Atanassov. *Conductive macroporous composite chitosan-carbon nanotube scaffolds*. Langmuir. 24, 7004-7010.
- 2008 Scott, D., Cooney, M. J., Liaw, B. Y. *Sustainable current generation from the ammonia-polypyrrole interaction*. Journal of Materials Chemistry. (27),3216-3222.
- 2008 Sun, D., Cooney, M. J., and B. Y. Liaw. *PQQ-glucose dehydrogenase immobilized in chitosan / carbon nanotubes composite films*. Electrochemical Solid State Letters. 11(6) B101-B104.
- 2008 Svoboda, V., Cooney<sup>✉</sup>, M. J., Liaw, B. Y., Minter, S., Piles, E., , Lehnert, D. Barton, S. C., Dmitri Ivitski, D., and P. Atanassov. *Standardization of a common platform for bioelectrocatalysis characterizations*. Electroanalysis, 20(10):1099 – 1109.
- 2008 Cooney<sup>✉</sup>, M. J., Windmesier, M, Lau, C., Liaw, B. Y., Klotzbach, T. and S. Minter<sup>✉</sup>. *Design of Chitosan Gel Pore Structure: Towards Enzyme Catalyzed Flow-Through Electrodes*. Journal of Materials Chemistry. 18, 667 – 674.
- 2008 Cooney<sup>✉</sup>, M.J., and B. Y. Liaw<sup>✉</sup>. *In situ characterization techniques for design and evaluation of micro and nano enzyme-catalyzed power sources*. In ( P.S Wang and J. B. Kim Editors) Biomolecular Catalysis: Nanoscale Science and Technology. ACS Symposium Series 986, Oxford University Press.
- 2007 Atanassov, P., Apblett, C., Banta, S., Brozik, S., Barton, S. C., Cooney, M. J., Liaw, B. Y., Mukerjee, S. and S. Minter. *Enzymatic Biofuel Cells*. The Electrochemical Society Interface.
- 2007 Svoboda, V., Rippolz, C., Cooney<sup>✉</sup>, M. J., and Bor Yann Liaw<sup>✉</sup> *Characterization of electrochemically polymerized methylene green films on platinum and vitreous carbon supports*. The Journal of Electrochemical Society. 154(3): D113 – D116.
- 2006 Konash, A., Cooney<sup>✉</sup>, M. J., Liaw<sup>✉</sup>, B. Y., Bor Yann Liaw, and D. M. Jameson. *Characterization of enzyme-polymer interactions using fluorescence*. Journal of Materials Chemistry, (42), 4107-4109.
- 2006 Johnston, W. J, Cooney<sup>✉</sup>, M. J., and B. Y. Liaw<sup>✉</sup>. *In situ measurement of effective diffusion coefficients in enzyme immobilized electrodes*. Enzyme and Microbial Technology. 39:131 – 140.
- 2005 Johnston, W. J., Liaw, B. Y., Sapra, R., Adams, M. W. W., and M. J. Cooney<sup>✉</sup>. *Design and characterization of redox enzyme electrodes: new perspectives on established techniques with application to an extremeophilic hydrogenase*. Journal of Enzyme and Microbial Technology. 36(4): 540 – 549.

## PRESENTATIONS

- 2008 Lau, C., Minter, S. D., and M. J Cooney. *Three dimensional chitosan scaffolds for biofuel cell application*. 214<sup>th</sup> ECS Meeting, October 12-17, Honolulu HI.
- 2008 Martin, G. L., Ross, J. A., Jameson, D. M., and M. J. Cooney. *Fluorescence characterization of chitosan-fluorophore/enzyme interactions*. 7th International Weber Symposium, June 6-12, Kauai, Hawaii.
- 2008 Lau, C., Cooney, M.J., Atannassov, P. *Three dimensional chitosan carbon nanotube composite material for biofuel cell application*. 213<sup>th</sup> ECS meeting, May 18-23, Phoenix Arizona.

- 2008 Cooney, M. J. *Microporous chitosan scaffolds as a material for fabrication of enzyme catalyzed flow through electrodes*. 213<sup>th</sup> ECS meeting, May 18-23, Phoenix Arizona.
- 2008 Svoboda, V., Liaw, B. Y., Cooney, M.J., Minteer, S., Atannassov, P. *Structure and Morphology of Electrochemically Grown Poly-Methylene Green Films*. 213<sup>th</sup> ECS meeting, May 18-23, Phoenix Arizona.
- Minteer, S. D., Klotzbach, T, Cooney, M. J., and Liaw, B.Y. *Nanopore Engineering of Chitosan Polymer for Enzyme Immobilization and Stabilization*. November 4 -9, 2007. Salt Lake City, Utah.
- Cooney, M. J., Liaw, B.Y., Lau, C., and S. D. Minteer. *Application of Mesopore Engineered Chitosan Polymer for Fabrication of Multi-Dimensional and Multi-Directional Enzyme Catalyzed Electrodes*. November 4 -9, 2007. Salt Lake City, Utah.
- Scott, D. Liaw, B.Y., and Cooney, M.J. *Improved Current Sustainability from the Ammonia, PPy Interaction with H<sub>2</sub>O<sub>2</sub> - One Step Closer to a Urine Fuel Cell*. The 212th ECS Meeting, October 7-12, 2007.
- Liaw, B.Y., Cooney, M.J., Svoboda, V., Konash, A., Jameson, D.M. *In situ characterization of polymer matrices for bio-electrode applications*. 17th International Symposium on Fine Chemistry and Functional Polymers (FCFP-XVII) & 3rd IUPAC International Symposium on Novel materials and their Synthesis (NMS-III), Shanghai, China, October 18th-20th, 2007.
- Svoboda, V., Liaw, B.Y., and Cooney, M.J. *In-situ transient characterization of electrochemical polymerization of methylene green with analysis of stepwise reaction mechanism*. 211<sup>th</sup> ECS Meeting, Chicago Illinois. May 6-11<sup>th</sup>, 2007.
- Liaw, B. Y, Svoboda, V., Cooney, M. J., and Minteer, S. *Fabrication of an effective biocatalytic electrode with in situ characterization of electrode and its materials*. 211<sup>th</sup> ECS Meeting, Chicago Illinois. May 6-11<sup>th</sup>, 2007.
- Cooney, M. J., Windmeisser, M., Liaw, B.Y., and Minteer, S. *Design of chitosan gel pore structure: towards enzyme catalyzed electrodes*. 211<sup>th</sup> ECS Meeting, Chicago Illinois. May 6-11<sup>th</sup>, 2007.
- Konash, A., Cooney, M.J., Liaw, B.Y, and Jameson, D. *Enzyme-polymer interaction study using fluorescence probes*. Symposium on Nano-scale Science and Technology in Biomolecular Catalysis. 232<sup>nd</sup> ACS National Meeting, San Francisco CA, Sept 10 – 14, 2006.
- Svoboda, V., Cooney, M.J., Rippolz, C., and Liaw, B.Y. *Development of an Enzymatic Ethanol Bio-Fuel Cell for Micro-Power Generation*. Fuel Cell Seminar, Honolulu HI, November 13 – 17, 2006.
- Cooney, M.J., Svoboda, V., Rippolz, C., and Liaw, B.Y. *Design considerations and characterization of enzymatic ethanol fuel cells*. 209th ECS Meeting, May 7-12, 2006, Denver, CO.
- Svoboda, V., Cooney, M.J., Rippolz, C. and Liaw, B.Y. *Design Consideration and In-situ Characterization of Bio-Anode for Enzymatic Ethanol Fuel Cell Application*. IBA –HBC 2006, Waikoloa, Hawaii, 9-12 January 2006.
- Cooney, M.J., Svoboda, V., Rippolz, C., and Liaw, B.Y. *Design considerations and characterization of enzymatic ethanol fuel cells*. 209th ECS Meeting, May 7-12, 2006, Denver, CO.

- Liaw, B.Y., Quinlan, F., Cooney, M.J. *Polypyrrole Deposition in Aqueous Solutions: Film Characteristic Dependence on Deposition Conditions*. 208th Meeting of the Electrochemical Society. Los Angeles, California. Oct. 16-21, 2005.
- Liaw, B.Y., Svoboda, V., Cooney, M.J. *Morphological Study of Conducting Polymer via Electrochemical Deposition Using Imaging Ellipsometry and RQCM Technique*. 208th Meeting of the Electrochemical Society. Los Angeles, California. Oct. 16-21, 2005.
- Cooney, M.J., Johnston, W. and Liaw, B.Y. *Modeling the relative contribution of mass transfer limitation on performance in enzyme fuel cells*. 207th Meeting of the Electrochemical Society, Quebec City, Canada. May 15 - May 20, 2005.
- Quinlan, F., Cooney, M.J. and Liaw, B.Y. *Investigation of polypyrrole morphology with different deposition conditions*. 207th Meeting of the Electrochemical Society, Quebec City, Canada. May 15 - May 20.
- Liaw, B.Y., Cooney, M.J., Quinlan, F., Svoboda, V. and Maynard, N. *Engineering Effective Bioelectrocatalysis Electrodes for Power Generation*. Second International Conference on Polymer Batteries and Fuel Cells (Fuel Cells). Las Vegas, Nevada from June 12 - June 17, 2005.
- Johnston, W.A., Cooney, M.J., and Liaw, B.Y. *Evaluating adsorption and charge transfer of redox enzymes bound to carbon support*. The 204<sup>th</sup> Meeting of the Electrochemical Society, Inc. July, 2003, Orlando, Florida.



## 4. Methane Hydrates

### 4.1 Objectives

Methane hydrates in ocean sediments constitute an enormous energy reservoir that is estimated to exceed the energy content of all known coal, oil, and conventional natural gas resources. Located on continental margins throughout the world, methane hydrates offer unique opportunities as onsite sources of fuel for various marine applications and are believed to play a major role in seafloor stability and global climate.

National R&D programs on methane hydrates were initiated in Japan and India in the mid-1990s with the goal of commercial gas production within a 20 year time horizon. The U.S. established its own program in May 2000. The Methane Hydrate Research and Development Act of 2000 (Public Law 106-193) included seven technical areas of focus: (1) identification, exploration, assessment, and development of methane hydrate as a source of energy; (2) technology development for efficient and environmentally sound recovery of methane from hydrates; (3) transport and storage of methane produced from methane hydrates; (4) education and training related to methane hydrate resource R&D; (5) assessment and mitigation of environmental impacts of natural and purposeful hydrate degassing; (6) development of technologies to reduce the risks of drilling through methane hydrates; and (7) support of exploratory drilling projects. The objectives of the Methane Hydrates Task of the Hawaii Energy & Environmental Technology (HEET) initiative, which was initiated in 2001, reflect most of the priorities of P.L. 106-193, but emphasize those areas of particular relevance to the Office of Naval Research (ONR) and which are consistent to the overall goals of HEET. Specifically, the development of hydrates and other sources of seafloor methane as logistical fuels for naval applications and related marine environmental issues, have been the principal areas of interest; exploratory drilling projects and seafloor stability/safety have received limited attention. Work also has recently been initiated to explore engineering applications of hydrates such as desalination or gas purification. Task objectives were devised to fully leverage hydrate R&D expertise and infrastructure that have been developed at HNEI during previous research programs on CO<sub>2</sub> ocean sequestration and deep oil spills.

During the present reporting period (09/06-12/08), the goals of the HEET Methane Hydrates Task were:

- Pursue development of methods to recover methane gas from hydrates.
- Explore the use of seafloor methane sources for subsea power generation.
- Investigate the microbial processes in sediment that generate and modulate methane levels.
- Investigate the fate of methane leaking into the water column from the seafloor.
- Investigate engineering applications of hydrates.
- In cooperation with the Naval Research Laboratory (NRL) and ONR Global (previously ONR-IFO), promote international collaborative research on methane hydrates.

Specific technical objectives that were pursued to attain the above goals included:

- Conduct laboratory experiments with the Raman calorimeter on hydrate destabilization using chemical inhibitors.

- Develop a model of hydrate destabilization by chemical inhibitors.
- Explore the technical feasibility of subsea power generation systems using seafloor methane.
- Develop computer models of the production, consumption, and transport of methane in the ocean.
- Characterize the microbial assemblage that modulates methane leakage into the water column, in samples of deep ocean sediment overlying hydrates.
- Correlate molecular biological analyses of the sediment microbial assemblage with NRL geochemical data on pore water methane concentrations and other chemical species.
- Participate in collaborative field studies of offshore hydrate biogeochemistry with NRL.
- Initiate exploratory laboratory experiments of engineering applications of hydrates such as gas or water purification.
- Organize workshops to promote international collaboration on methane hydrate R&D.

## **4.2 Scope of Work and Approach**

Pursuant to the goals and technical objectives identified in the preceding section, work on the Methane Hydrates Task during the present reporting period focused on four primary areas which are described below.

### **4.2.1 Hydrate Thermochemistry and Kinetics**

The major priority of this subtask was to elucidate the fundamental mechanism of methane hydrate destabilization by chemical reagents. This was undertaken by a combination of laboratory experiments and modeling. The experiments utilized the novel Raman calorimeter developed previously as part of the HEET initiative. Chemical reagents, such as alcohols, have been proposed as a means of methane gas production from hydrates and are used extensively to prevent or resolve hydrate blockages in natural gas pipelines.

A secondary area of interest was to review the technical feasibility of generating electrical power on the seafloor (for underwater instrumentation, monitoring, recharging of AUVs, etc.) using methane gas seeps or hydrates. This activity is a continuation of a one-year conceptual design study conducted for DARPA.

### **4.2.2 Environmental Impacts of Methane Release from Seafloor Hydrates**

This subtask is a continuation of activities pursued in previous years to: (1) assess the consequences of inadvertent or purposeful releases of methane from seafloor hydrates via the development of a model of methane transport through the ocean water column to the atmosphere; and (2) elucidate the mechanisms by which sediment microbes control free methane gas levels in, and methane leakage from, the seafloor sediment and arctic permafrost.

Following up on our earlier study of hydrothermal vents as a natural analog of hydrate outgassing from the seafloor, additional modeling studies were performed to examine the validity of laboratory claims regarding microbial carbon isotope fractionation, as well as large-scale oceanic transport mechanisms. These studies are necessary components of our long-term goal of developing a full 3D numerical model of CH<sub>4</sub> in the ocean.



Microbial studies during the present reporting period focused on completing the molecular biological analyses of core samples collected during a 2006 oceanographic research cruise on the Hikurangi Margin offshore of the North Island of New Zealand. These microbiological assays were correlated with geochemical data on corresponding profiles of dissolved methane and geophysical records collected by NRL.

HNEI also participated in a research cruise with NRL in the Gulf of Mexico in July-August 2007. Additional porewater and sediment samples were collected during this expedition and are being cultured to investigate methane consumption by resident methanotrophs.

#### **4.2.3 Hydrate Engineering Applications**

The major priority of this subtask was to develop appropriate experimental systems and to initiate exploratory studies of the use of gas hydrates for separation and purification of mixtures of gases. The long-term goal is to determine whether it is technically and economical feasible to employ hydrates for practical application such as the removal of fuel cell catalyst poisons from syngas mixtures.

#### **4.2.4 International Collaborative R&D**

To promote international R&D cooperation on methane hydrates, HNEI helped organize and sponsor the 6<sup>th</sup> International Fiery Ice Workshop that was held in Bergen, Norway in May 2008.

### **4.3 Technical Accomplishments**

The principal technical accomplishments of the HEET Methane Hydrates Task for each of the components identified above are described in the following sections.

#### **4.3.1 Methane Hydrate Destabilization**

During the present reporting period, the primary accomplishments of this subtask were: (1) completed a series of laboratory experiments of hydrate destabilization by injection of three common alcohols and a diol; and (2) posited and tested a new mechanism for the effect of this class of chemical inhibitors on hydrate stability based on mobile order thermodynamics. These studies constituted the M.S. thesis research of a Mechanical Engineering student at the University of Hawaii. In addition, work continued on developing a system to generate modest amounts of electrical power with alkaline fuel cells using seafloor methane. While limited testing of small alkaline fuels cells under deep ocean conditions originally was proposed, this was deferred in order to apply the available resources to extend and complete the reagent destabilization studies. Work on subsea power generation instead focused on experimental system design and an investigation of high pressure thermochemical methane reforming using  $H_2O_2$ , which is described in a different section of this report.

##### *Reagent Destabilization of Methane Hydrates*

Three methods have been proposed to destabilize and extract fuel gas from hydrates: heating, depressurization, and chemical reagents. Chemical reagents, notably alcohols and other antifreeze compounds, also have been employed for decades to avoid hydrate blockages in natural gas pipelines and, as a result, are often referred to as thermodynamic inhibitors. While there is a substantial amount of information in the literature regarding hydrate decomposition using thermodynamic inhibitors, most studies have been limited to determining the pressure-temperature stability curve of hydrates in the presence of these inhibitors. The mechanism by



which they decompose hydrates remains elusive. Knowledge about the fundamental mechanism could help identify more environmentally-benign and cost-effective alternatives (for, say, methane recovery from hydrates in seafloor sediment or permafrost where the injection of large quantities of methanol or ethylene glycol is not acceptable).

Since the driving force for hydrate dissociation in the presence of thermodynamic inhibitors is not known, models have been developed based, for example, on a change in partial pressure (Masoudi and Tohidi, 2005) or a change in the activity of water (Javanmardi *et al.*, 2001). There are deficiencies in these approaches which underscore the need to identify the driving force.

### Experiments

During the present reporting period, a series of laboratory experiments were conducted to quantify the effectiveness of four common thermodynamic hydrate inhibitors and correlate these results with the structure of the molecules to elucidate the mechanism by which they induce destabilization. The four inhibitors that were studied included three alcohols and one diol: 1) methanol ( $\text{CH}_3\text{OH}$ ); 2) ethanol ( $\text{C}_2\text{H}_5\text{OH}$ ); 3) 2-propanol (isopropyl alcohol,  $\text{C}_3\text{H}_7\text{OH}$ ); and 4) ethylene glycol ( $\text{C}_2\text{H}_34(\text{OH})_2$ ). The alcohols are characterized by a single hydroxyl (OH) group, while the diol has two.

Methane hydrate samples in a modified high-pressure gas circulation cell in a Calvet-Tien calorimeter were decomposed by injection of a fixed amount of an inhibitor at constant temperature and pressure. The amount of hydrate that decomposed per mole of inhibitor was inferred from the calorimeter thermograms by comparing the amount of heat absorbed with the heat of formation of the hydrate. Differences in the molecular structure of the inhibitors were then considered to explain the results.

Based on our previous work, it was posited that thermodynamic inhibitors work by tying up liquid water at the hydrate surface and hence, by disrupting the dynamic equilibrium between hydrate decomposition and formation. The effectiveness of a reagent is believed to depend on the number of hydrogen bonding sites and the other structural characteristics such as the size of its alkyl group. The experiments and modeling reported below was used to test this hypothesis. Additional details are available in the M.S. thesis of Kinoshita (2008).

### Facilities and Procedures

Figure 4-1 presents a schematic diagram of the setup employed in these experiments. Hydrate samples are formed in a Setaram model BT2.15 II Calvet-Tien calorimeter. Custom top closures for the high pressure calorimeter sample cells were fabricated with a penetration connected to a 6.35 mm (0.25 inch) o.d., 5.0 mm (0.194 inch) i.d. stainless steel tube. This tube encloses a 3.18 mm (0.125 inch) o.d. fiberoptic probe which was described in an earlier HEET report and is used to obtain Raman spectra of the samples. A 0.79 mm (0.03125 inch) o.d. PEEK tube also is enclosed within the 6.35 mm tube and is employed to inject liquid hydrate inhibitors into the cell.

The liquid inhibitor is stored in a closed flask and circulated through a counter-flow heat exchanger using an Eldex High Pressure Liquid Metering Pump before being routed into the sample cell. The heat exchanger was employed to match the temperature of the inhibitor to that of the hydrate sample in order to avoid hydrate decomposition driven by thermal effects.

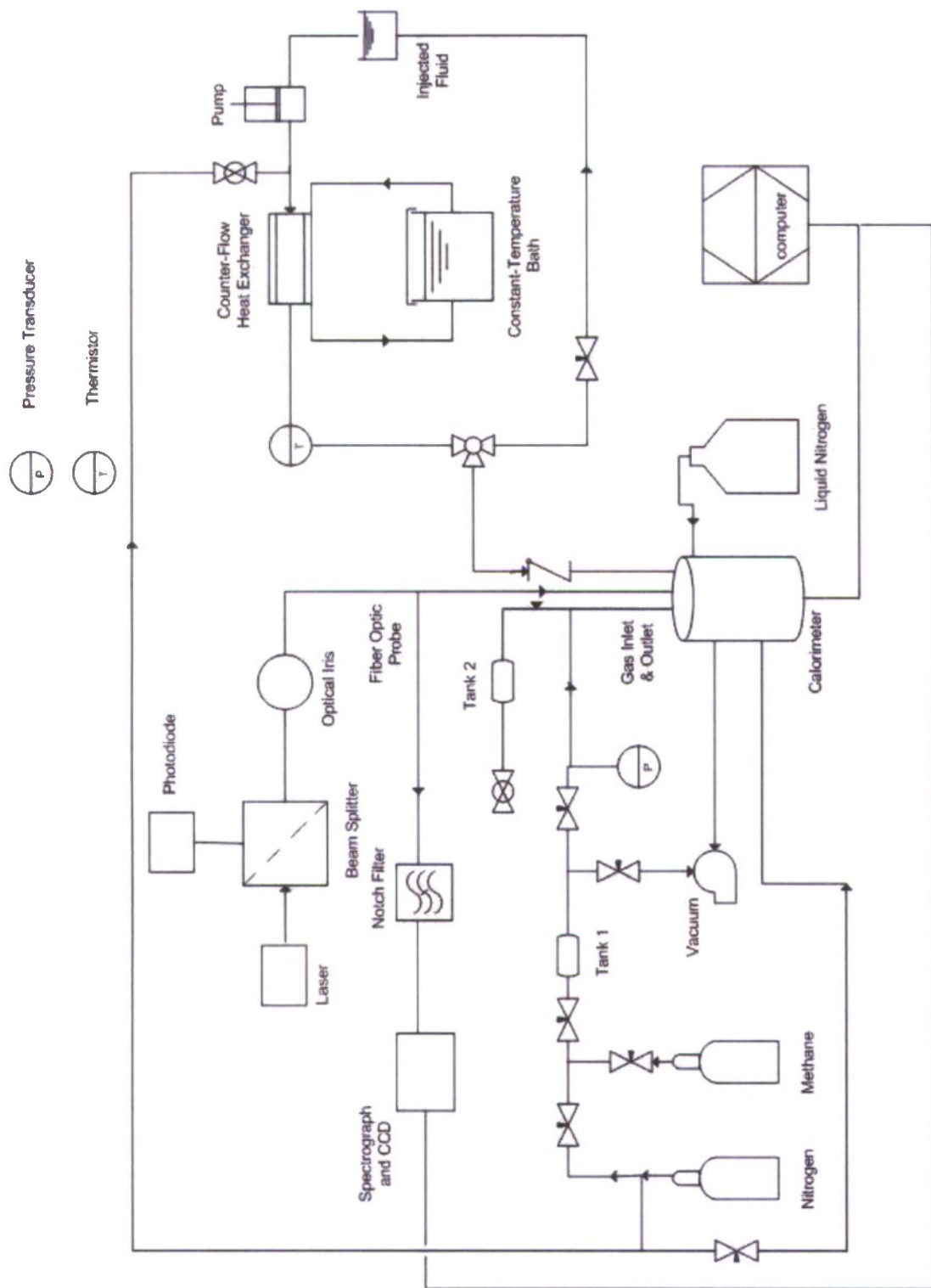


Figure 4-1. Schematic diagram of experimental setup to investigate hydrate destabilization using thermodynamic inhibitors.



Hydrate samples in the calorimeter cells are maintained under an atmosphere comprising high pressure methane gas (99.99% purity). Injection of the liquid inhibitor displaces and compresses the gas. In order to prevent any significant changes in pressure which may affect hydrate stability, the calorimeter gas supply system was equipped with two buffer tanks that increase total system volume to the extent that the small amount of liquid inhibitor added results in minimal compression. A transducer interfaced to our data acquisition system continuously monitors pressure in the sample cell. Maximum pressure perturbations were  $< 1\%$ . The  $N_2$  cylinder (99.99%) and vacuum pump in the schematic are used to purge the system between experiments.

Raman spectroscopy measurements of the hydrate sample were performed with a diode-pumped, solid-state, frequency-doubled Nd:YAG laser (ALPHALAS GmbH Model MONOLAS-532-100-SM). The laser has a maximum power output of 101 mW and operates at a wavelength of 532.05 nm. The laser beam is directed onto a pellicle beamsplitter, which reflects a small portion of the beam onto a photodiode to provide a continuous record (via calibration) of the laser power transmitted into the sample cell. This is necessary since this power must be subtracted from the recorded thermograms. The portion of the laser beam that is transmitted through the beamsplitter is coupled to the fiberoptic probe, which brings it into the pressurized sample cell. The fiberoptic probe consists of seven 200  $\mu\text{m}$  core UV silica fibers encased within a 3.2 mm (0.125 inch) o.d. stainless steel sleeve. The center fiber brings radiation from the laser into the cell, while the six surrounding fibers are used to collect the Raman-shifted light and transmit it to the spectrometer (Princeton Instruments SpectraPro-2558i), where it is diffracted onto a PIXIS 2K CCD detector.

During experiments, the calorimeter is purged of atmospheric air using a vacuum pump and dry nitrogen gas. After purging, it is cooled using liquid  $N_2$ . Following the protocol for methane hydrate synthesis developed previously and described in earlier HEET reports, distilled deionized water was sprayed into a liquid  $N_2$  bath to generate fine ice crystals. Crystals smaller than about 200  $\mu\text{m}$  were collected, weighed, and loaded into a sample cell. The assembled cell was then inserted into the cold calorimeter test well, purged with  $N_2$ , and pressurized slowly with methane.

When the pressure in the cell reached 7.0 MPa (1000 psig), the temperature of the calorimeter was increased from  $-15\text{ }^\circ\text{C}$  to  $-5\text{ }^\circ\text{C}$  and allowed to equilibrate. Once the calorimeter reached steady-state, the sample temperature was increased from  $-5\text{ }^\circ\text{C}$  to  $4\text{ }^\circ\text{C}$  at a rate of  $0.1\text{ }^\circ\text{C}/\text{min}$ . The calorimeter was then held for 12 hours at  $4\text{ }^\circ\text{C}$ , which is above the melting point of ice but below the freezing point of methane hydrate. Once Raman spectra confirmed that methane hydrate existed, the calorimeter was cooled to  $-10\text{ }^\circ\text{C}$ . This forced any remaining liquid water, which did not form hydrate, to freeze back to ice. With the calorimeter at  $-10\text{ }^\circ\text{C}$ , the pressure of the system was adjusted to 6.89 MPa (985 psig) and another Raman measurement was performed. Finally, the calorimeter temperature was raised back to  $-5\text{ }^\circ\text{C}$ .

As the temperature of the calorimeter was slowly raised to  $-5\text{ }^\circ\text{C}$ , the liquid inhibitor being investigated was circulated through the counter-flow heat exchanger. The pump flow rate was set at 1 mL/min and the temperature of the constant-temperature bath was adjusted to a value determined by calibration that would closely match inhibitor temperature at the point of injection in the cell to that of the hydrate sample. Note that a trial-and-error calibration of the injection system was necessary to identify optimal operating conditions due to the complicated heat



transfer processes that occur between the exit of the heat exchanger and the point of injection in the sample cell. Although the lines leading from the heat exchanger to the calorimeter are well insulated, there is some heat pick-up from the environment. Thereafter, as the liquid inhibitor flows down the calorimeter well through the PEEK tubing enclosed within the stainless steel tube connected to the sample cell closure, it passes through a section of the calorimeter where the temperature is unregulated and extremely low ( $<-150\text{ }^{\circ}\text{C}$ ) due to the liquid  $\text{N}_2$  jacket. It then enters the calorimetric block where temperature is maintained at a programmed setpoint by electric heaters. Thermal calibration of the system was performed by substituting a thermistor probe for the fiberoptic probe. The bath temperature was varied for each of the tested reagents, until the measured temperature of the injected inhibitor matched the set point temperature in the sample cell for the fixed 1 mL/min flowrate. Thermograms recorded during these calibration runs were also examined to ensure that no significant heat flows resulted from the injections.

Following another Raman measurement, the inhibitor circulating through the heat exchanger was routed into the sample cell for a predetermined period of time. All tests were conducted at a sample temperature of  $-5\text{ }^{\circ}\text{C}$  and pressure at 6.89 MPa (985 psig). After the inhibitor became inactive and hydrate decomposition ceased (indicated by zero heat flow into the sample cell), Raman data were again collected to determine if any hydrate remained. This measurement was important to confirm that disassociation had stopped as a result of the inhibitor becoming ineffective rather than being due to the consumption of the entire methane hydrate sample. If all the hydrate disappeared, then the inhibitor effectiveness, in terms of hydrate dissociated per unit of inhibitor, could not be determined.

At the end of each test, the spectrograph was calibrated using both a neon lamp and cyclohexane, and all the liquid lines were purged with deionized water and then dried with nitrogen gas. Identical experiments were performed three times for each of the four different inhibitors to check repeatability.

#### Results and Discussion (Experiments)

Figure 4-2 presents a typical calorimetric record comprising a thermogram (energy rejected or absorbed by the sample vs. time) and a temperature time history for the entire test cycle. Important features of the experiment, indicated by the labels in Figure 4-2, are:

1. Ice crystals melting (Endothermic);
2. Hydrate formation (Exothermic);
3. Laser turned on and Raman spectra obtained (Exothermic);
4. Liquid water transforms to ice/hydrate (Exothermic); and
5. Hydrate dissociated by thermodynamic inhibitor injection (Endothermic).

# **Methane Hydrate Formation and Decomposition Using Methanol as an Inhibitor #2**

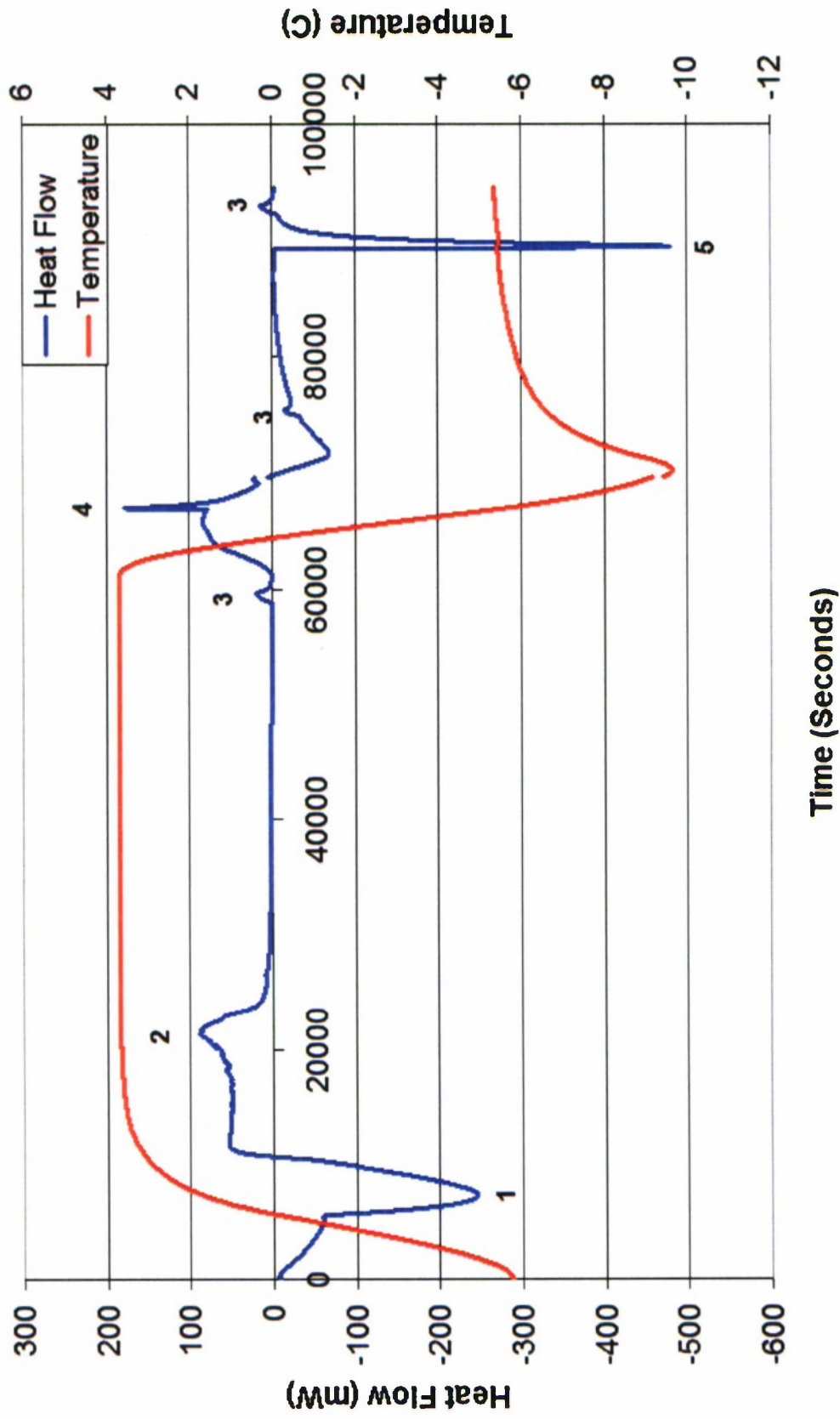


Figure 4-2. Typical calorimeter record during formation and destabilization of methane hydrate with thermodynamic inhibitors.

Raman spectra of the hydrate sample obtained *in situ* with the fiberoptic probe are shown in Figure 4-3. The Raman shift at  $2904.8\text{ cm}^{-1}$  corresponds to  $\text{CH}_4$  engaged in the cavities of pure sl methane hydrate (Subramanian & Sloan, Jr., 1999). Also apparent is the peak associated with methane gas at  $2917\text{ cm}^{-1}$  (Subramanian and Sloan, Jr., 1999).

In order to determine the quantity of hydrate decomposed and the final concentration of the inhibitor-water mixture at the endpoint of the disassociation reaction, the amount of energy absorbed by the hydrate during decomposition had to be calculated. The total energy absorbed by the sample consisted of several components:

1. Energy transferred from the calorimetric block to the sample cell; this is measured and recorded by the calorimeter;
2. Thermal energy of the liquid inhibitor injected into the cell; this is minimized by matching the inhibitor temperature with the sample temperature;
3. Energy added to the sample by the laser during the Raman measurements; this can be estimated via calibration from the photodiode data; and
4. Energy associated with molecular interactions between the water molecules released by the dissolving hydrate and the inhibitor molecules; this is estimated using heat of mixing data found in the literature and confirmed by separate mixing tests conducted with our calorimeter.

Item 1 was determined by integration of the calorimeter thermograms sampled during the hydrate dissociation step. After correcting for items 2, 3, and 4, the calculated energy was divided by the heat of dissociation of methane hydrate to estimate the amount of hydrate that decomposed. Handa (1986) reported that the heat of dissociation of methane hydrate is around  $54.19\text{ kJ/mol}$  of hydrate while the heat of fusion of ice is around  $6.009\text{ kJ/mol}$  of water. Since one mole of sl methane hydrate contains approximately six moles of water (Handa, 1986), the heat of dissociation of methane hydrate is approximately  $9.032\text{ kJ/mol}$  of water produced.

Figure 4-4 presents the amount of hydrate decomposed per mole of inhibitor at  $-5\text{ }^\circ\text{C}$  and  $6.9\text{ MPa}$ . The endpoint (final) concentration of the inhibitor in water that occurs when hydrate dissociation ceases is given in Table 4-1. Raman spectra were used to confirm that hydrate still existed in the sample cell at the end of the dissociation process, so that this endpoint could be unambiguously attributed to the inhibitor losing effectiveness, rather than the consumption of all hydrate. As seen in Figure 4-4, ethylene glycol decomposes the largest quantity of hydrate whereas 2-propanol decomposes the smallest quantity of hydrate. As a result, ethylene glycol releases the largest quantity of water from the hydrate phase and has the most diluted final inhibitor concentration.

Results shown in Table 4.1 and Figure 4-4 were correlated with the structure of the inhibitor molecules. This showed that the effectiveness of an inhibitor is influenced by the number of available hydrogen bonding sites available, as well as the size of the alkyl group. The data indicate that, as the number of hydroxyl groups increases, an inhibitor becomes more effective at decomposing hydrates. For example, ethylene glycol ( $\text{C}_2\text{H}_34(\text{OH})_2$ ), with two hydroxyl groups, is more effective at decomposing hydrates than ethanol ( $\text{C}_2\text{H}_5\text{OH}$ ). As the size of the alkyl group increases, however, the inhibitor appears to become less effective at decomposing hydrates, possibly due to steric effects. Since the alkyl group is non-polar, it will have a tendency to repulse polar water molecules. While all three alcohols tested have a single hydroxyl group (i.e., hydrogen bonding site), methanol has the smallest alkyl group followed, in



order, by ethanol and 2-propanol. The experimental results suggest a clear correlation between increasing alkyl group size and a decreased ability to decompose hydrates.

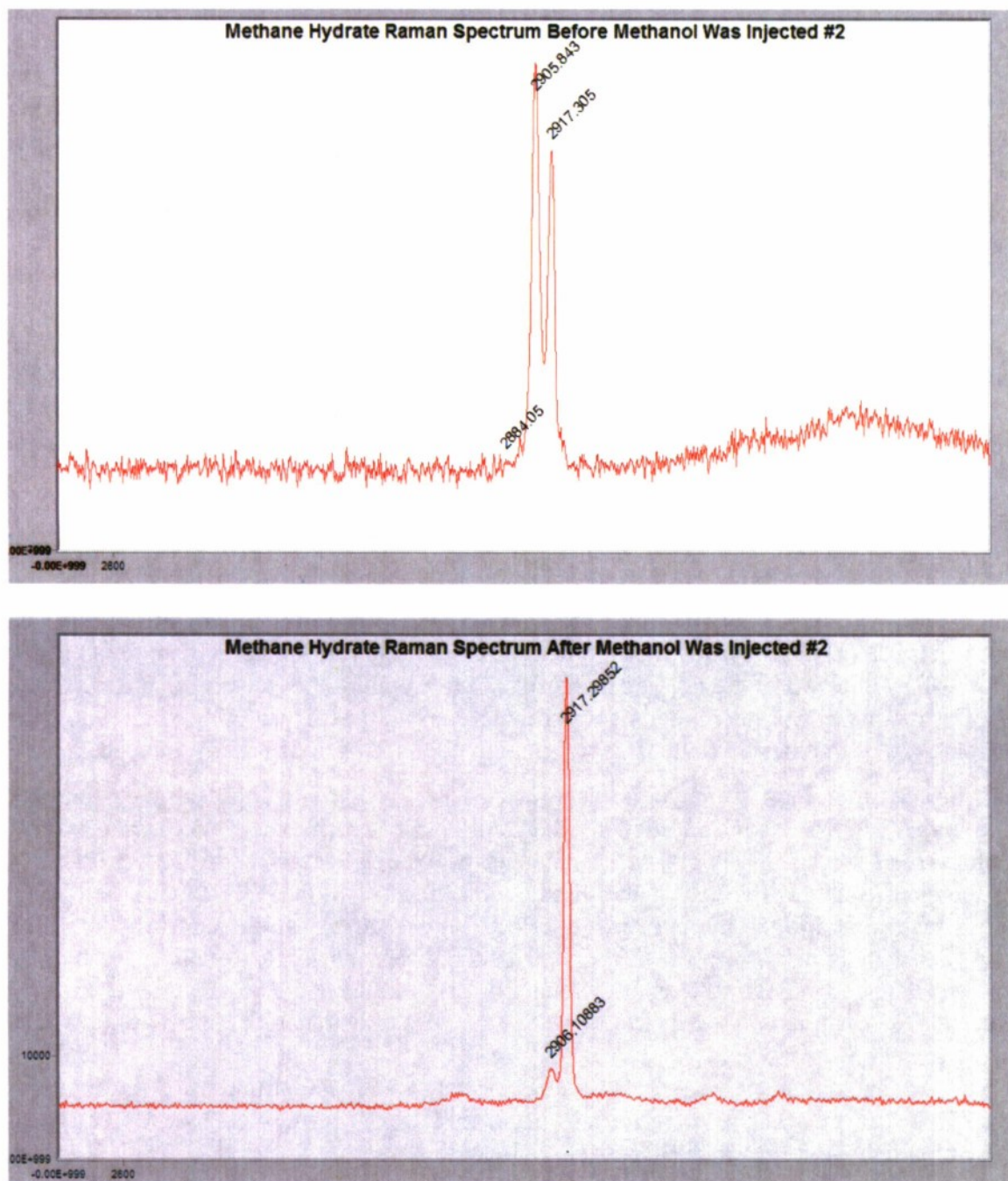


Figure 4-3. Raman spectra taken before and after methanol injection into the sample cell. The peak at  $2917.3 \text{ cm}^{-1}$  corresponds to methane gas; the peak at around  $2906 \text{ cm}^{-1}$  to methane hydrate.

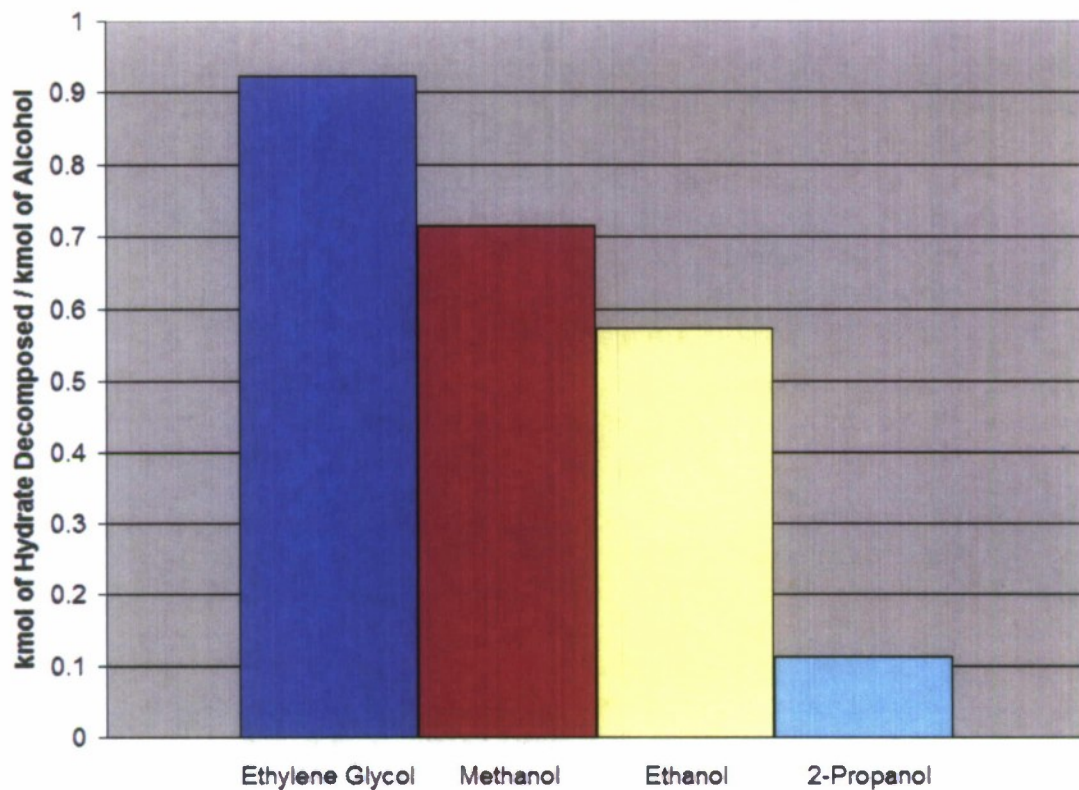


Figure 4-4. Amount of hydrate decomposed per mole of inhibitor.

Table 4-1. Inhibitor concentration at the end of dissociation.

Inhibitor	Final Inhibitor Concentration (mol% Inhibitor)
Ethylene Glycol	0.1547
	0.1498
	0.1543
Methanol	0.1875
	0.1913
	0.1876
Ethanol	0.2080
	0.2217
	0.2459
2-Propanol	0.5826
	0.6267
	0.5798



### Experimental Summary

We have hypothesized that an inhibitor decomposes hydrates by binding up released water molecules in the quasi-liquid layer on the hydrate surface, preventing re-crystallization. The experimental results for four common reagents indicate that the effectiveness of an inhibitor to dissociate hydrate increases with the number of its hydroxyl groups and decreases with the size of its alkyl group. This is consistent with our hypothesis since the hydroxyl group provides a bonding site for water and, through steric effects, a larger alkyl group reduces the hydrogen bonding capability of an inhibitor and the strength of the hydrogen bonds formed with water molecules. A theoretical analysis based on mobile order thermodynamics was undertaken to assess these concepts and is described in the following section.

As a sidenote, this study demonstrated the value of the Raman calorimeter we developed. It has proven to be a reliable and robust instrument to perform unique thermochemical measurements.

### Theory

Since alcohols probably are the best known thermodynamic inhibitors of the formation of gas hydrates, the pressure-temperature phase boundary of hydrates in the presence of various alcohols has been thoroughly investigated (e.g., Hammerschmidt, 1939; Anderson and Prausnitz, 1986; Munck *et al.*, 1988; Masoudi and Tohidi, 2005). The equilibrium thermodynamic models that have been developed express the equality of the chemical potentials of water (and of the guest molecule) in all phases. An important component of equilibrium calculations therefore is the activity of water in the liquid phase. Various methods are available to determine the activity of water in mixtures with alcohols, such as the widely used UNIQUAC equation (Abrams and Prausnitz, 1975). These calculations, however, do not necessarily shed much light on the mechanisms by which one inhibitor may be more effective than another in lowering the activity of water in mixtures. This led to an examination of the problem from the perspective of a different framework specifically developed for the description of hydrogen-bonded liquids and known as mobile order thermodynamics (MOT).

Molecular associations in hydrogen-bonded liquids are non-ergodic since the ensemble fraction of free molecules at any given time is much smaller than the fraction of the time a given molecule is free. The transient nature of open-chain associations thus profoundly differentiates liquids from crystals. On this fundamental basis, Huyskens *et al.* (1988, 1995) developed thermodynamic laws with a revised version of Boltzmann statistics using the fraction of the time a system is in a particular state rather than the static configuration of the system. Ruelle and Kesselring (1996, 1998) and Ruelle (1999) broadened these concepts into a coherent theory of mobile order thermodynamics that allowed them to elucidate the molecular origins of the solvophobic effect and to predict the aqueous solubility of many aliphatic alcohols and hydrocarbons. The interpretative reach of MOT was extended in our study to include several completely miscible hydrogen-bonded liquids.

The chemical potential of water,  $\mu_w$  classically is expressed as the sum of the pure water value  $\mu_w^0$  (implicitly at given temperature and pressure) and of a term involving the activity of water in solution. Alternatively, the excess behavior (relatively to pure water) embodied in the definition of activity may be represented by two components in MOT: one originates from the entropy of mixing distinct substances and the other from a rearrangement of hydrogen bonds. Therefore, we have the following identities:



$$\mu_W = \mu_W^0 + RT \text{Log} a_W = \mu_W^0 + \mu_W^{\text{mixing}} + \mu_W^{\text{H-bonding}} \quad (4.1)$$

$\mu_W^{\text{mixing}}$  has been previously derived from the entropy of mixing, which was shown to reflect a change in molecular mobile domains as well as the possibility of molecular interchange (Ruelle and Kesselring, 1998; Ruelle, 1999). It can be written as follows:

$$\mu_W^{\text{mixing}} = \frac{RT}{2} \left[ \ln(x_W \phi_W) + 1 - \frac{\phi_W}{x_W} \right] \quad (4.2)$$

where  $\phi_W$  and  $x_W$  are the volume and mole fractions of water, respectively.

The central concept in the MOT treatment of hydrogen bonds in liquids is the fraction of the time,  $\gamma$ , a molecule is free. Both water and alcohol molecules are capable of forming hydrogen bonds, and the contribution of such bonds to the excess Gibbs free energy of a system of  $n_W$  moles of water and  $n_A$  moles of alcohol is expressed as:

$$G^{\text{H-bonding}} = RT(n_W \text{Log} \frac{\gamma_W}{\gamma_W^0} + n_A \text{Log} \frac{\gamma_A}{\gamma_A^0}) \quad (4.3)$$

where the superscript 0 refers to pure fluids. Equation (4.3) is a generalization of Equation (16) given in Ruelle and Kesselring (1998) for a mixture containing a single hydrogen-bonded substance. It follows that:

$$\mu_W^{\text{H-bonding}} = \left( \frac{\partial G^{\text{H-bonding}}}{\partial n_W} \right)_{n_A} = RT \left( \text{Log} \frac{\gamma_W}{\gamma_W^0} + A_W + A_A \right) \quad (4.4)$$

where, by definition,  $A_W = \frac{n_W}{\gamma_W} \frac{\partial \gamma_W}{\partial n_W}$  and  $A_A = \frac{n_A}{\gamma_A} \frac{\partial \gamma_A}{\partial n_W}$ . Ruelle and Kesselring (1996, 1998) give  $\gamma_W^0$  as:

$$\gamma_W^0 = \frac{1}{1 + K_{W1} F_W^0 + K_{W1} K_{W2} (F_W^0)^2} \quad (4.5)$$

In Equation (4.5), the two insertion constants  $K_{W1}$  and  $K_{W2}$  are 8 and 0.2 L/mol at 25 °C, respectively (Nelis *et al.*, 1995). The formal concentration of water  $F_W^0$  as a pure substance is 55.55 mol/L. If an inert substance were added to water, then Equation (4.5) could be used to define  $\gamma_w$  as well, simply by removing the superscript 0; in this case, the formal concentration of water would decrease, and water molecules would be free for a greater fraction of the time.

Adding a substance that can interact with water molecules, however, does not systematically reduce the availability of potential bonding sites. Instead, Ruelle and Kesselring (1996) proposed an expression where the sum of concentrations ( $F_W + F_A$ ) is involved:

$$\gamma_W = \frac{1}{1 + K_{W1} (F_W + F_A) + K_{W1} K_{W2} (1 + b V_W F_A) (F_W + F_A)^2} \quad (4.6)$$

The factor  $(1 + b V_W F_A)$  in the denominator reflects modifications of the second insertion constant of water in the mixture, as reported by Nelis *et al.* (1995);  $b$  is a constant depending on the degree of branching of the alcohol, and equal to 1.2 for primary alcohols, 2.0 for secondary alcohols, and 2.9 for tertiary alcohols. Following algebraic manipulations, Equation (4.6) allows the derivation of the auxiliary variable  $A_W$  in Equation (4.4):

$$A_W = \frac{K_{W1} F_W F_A \{b K_{W2} V_W^2 (F_W + F_A)^2 + (V_W - V_A)[1 + 2K_{W2}(1 + b V_W F_A)(F_W + F_A)]\}}{1 + K_{W1}(F_W + F_A) + K_{W1} K_{W2}(1 + b V_W F_A)(F_W + F_A)^2} \quad (4.7)$$

In the case of simple alcohols with only one hydroxyl group, the analog of Equation (4.6) is (Ruelle and Kesseling, 1996):

$$\gamma_A = \frac{1}{1 + K_A(F_A + F_W)} \quad (4.8)$$

$K_A$  is the self-association constant equal to 5 L/mol at 25 °C. Hence, the auxiliary variable  $A_A$  in Equation (4.4) can be obtained:

$$A_A = \frac{K_A (V_W - V_A) F_A^2}{1 + K_A (F_W + F_A)} \quad (4.9)$$

MOT analyses of diols such as ethylene glycol, i.e., of alcohols with two hydroxyl groups, could not be found in the technical literature. Since these species have two insertion sites like water, it appears reasonable to treat them in a similar way. Accordingly, the following form equivalent to Equation (4.6) is proposed for the fraction of the time ethylene glycol molecules are free from hydrogen bonds in mixtures with water:

$$\gamma_{EG} = \frac{1}{1 + K_{A1}(F_W + F_{EG}) + K_{A1} K_{A2}(1 + b' V_{EG} F_W)(F_W + F_{EG})^2} \quad (4.10)$$

Huyskens *et al.* (1995) invoked the presence of two hydrogen atoms per water molecule to explain the approximate factor-of-two difference between the first insertion constant of water and that of simple alcohols; hence,  $K_{A1}$  is assumed to be equal to  $K_{W1}$  in the case of diols. For lack of better knowledge, a value of  $K_{A2} \approx K_{W2} = 0.2 \text{ L/m}^3$  is selected and the functional dependence of the second insertion coefficient on water concentration is expressed as  $(1 + b' V_{EG} F_W)$  by analogy to Equation (4.6); for a small molecule like water, the constant  $b'$  is assumed to be of order unity. Equation (4.10) then allows the determination of the auxiliary variable  $A_A$  in Equation (4.4) in the case of ethylene glycol (written with the index A replaced by EG):

$$A_{EG} = \frac{K_{A1} F_{EG}^2 \{-b' K_{A2} V_{EG}^2 (F_W + F_{EG})^2 + (V_W - V_{EG})[1 + 2K_{A2}(1 + b' V_{EG} F_W)(F_W + F_{EG})]\}}{1 + K_{A1}(F_W + F_{EG}) + K_{A1} K_{A2}(1 + b' V_{EG} F_W)(F_W + F_{EG})^2} \quad (4.11)$$

Equations (4.1), (4.2), (4.4)-(4.7), (4.9), and (4.11) are sufficient to evaluate the activity of water in mixtures with simple alcohols or with a diol like ethylene glycol.

### Results and Discussion (Theory)

In implementing the algorithm developed above, the four inhibitors which were used in the dissociation experiments were initially considered: methanol ( $V = 40.46 \text{ cm}^3/\text{mol}$ ;  $b = 1.2$ ),

ethanol ( $V = 58.38 \text{ cm}^3/\text{mol}$ ;  $b = 1.2$ ), 2-propanol ( $V = 76.46 \text{ cm}^3/\text{mol}$ ;  $b = 2.0$ ), and ethylene glycol ( $V = 55.76 \text{ cm}^3/\text{mol}$ ;  $b = 1.2$ ). Figure 4-5 displays the results, as well as calculations based on the widely used UNIQUAC equation (Abrams and Prausnitz, 1975). There is a broad agreement between predictions from mobile order thermodynamics and UNIQUAC. It should be emphasized that UNIQUAC is a correlative model with two binary energy-of-interaction parameters that are estimated from a fit (regression) to some data, most typically from vapor-liquid equilibrium (VLE). Different choices of data sets and mixing rules often yield different values of the parameters (e.g., Orbey and Sandler, 1996). A critical discussion of the UNIQUAC method *per se* was not the object of this work, however; credible (UNIQUAC) benchmarks simply were sought to assess the soundness of mobile order thermodynamics as an alternative paradigm to estimate the activity of water in mixtures with alcohols. In the case of methanol and ethanol, the *ab initio* estimates of Sum and Sandler (1999) based on quantum mechanics methods were used. For 2-propanol, the recent work of Kaewsichan and Numuang (2005) was considered and the predictions in Figure 4-5 correspond to a pressure of 100 kPa (the authors also provided UNIQUAC parameters at 30 kPa and 60 kPa, but these were found to yield very close results). With ethylene glycol/water mixtures, the published parameters of Nath and Bender (1983) were selected for the lowest temperature among their isothermal data sets (65 °C). The fact that MOT and UNIQUAC calculations are as close as shown in Figure 4-5 lends credibility to mobile order thermodynamics, which, perhaps, should be the preferred method to determine activities in hydrogen-bonded liquids.



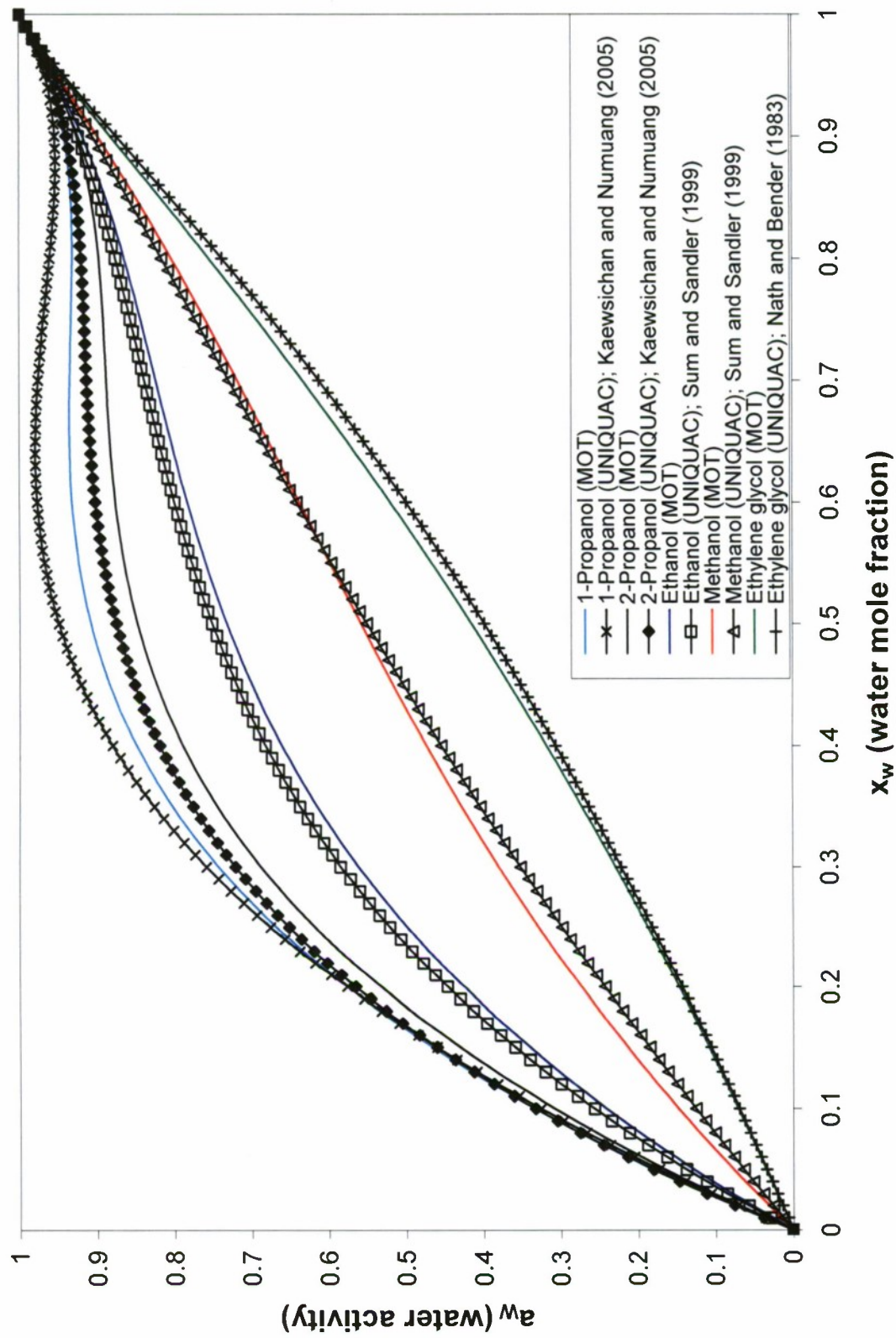


Figure 4-5. Activity of water in binary mixtures with alcohols: Mobile Order Thermodynamics (MOT) and UNIQUAC equation.

Figure 4-5 also reveals definite trends about the ability of alcohols to depress the activity of water. Since ethanol and ethylene glycol have similar molar volumes, the much greater effect of ethylene glycol stems from the availability of two hydrogen bonding sites (hydroxyl groups) per molecule. In other words, water molecules find themselves relatively more restricted in mixtures with a diol. In addition, a comparison between the three simple alcohols shows the occurrence of steric effects, with the larger alkyl group of 2-propanol providing water molecules an expanded environment where hydrogen bonding is relatively less frequent; this effect is less pronounced for ethanol and methanol, and decreases as the size of the alkyl group decreases. In order to assess the effect of alcohol branching, calculations also were performed for 1-propanol-water mixtures ( $V = 74.80 \text{ cm}^3/\text{mol}$ ;  $b = 1.2$ ). Results were compared to the UNIQUAC predictions of Kaewsichan and Numuang (2005). In both MOT and UNIQUAC approaches, the activity of water with the primary alcohol (1-propanol) is slightly higher than with the secondary alcohol (2-propanol) over much of the concentration range. Such ways in which the molecular size and branching of otherwise comparable alcohols in aqueous solutions affect the activity of water agree with the findings of Prucksunand (2000) from a study of several glycols.

How alcohols impact the activity of water in binary mixtures has a direct relevance to their effectiveness as thermodynamic inhibitors in the formation of gas hydrates. Hydrate equilibrium is determined, partly, by expressing an equality of the chemical potentials of water in the hydrate and liquid phases (the equality of the chemical potentials of the hydrate forming substance in all phases also holds). Solving the resulting equation, e.g., Equation (9) in Munck *et al.* (1988) yields the hydrate pressure-temperature phase boundaries. At constant pressure (with little loss of generality) and for hydrate-forming agents of very low solubility, a formally simple relationship can be obtained:

$$\text{Log} a_w = - \int_{T_x}^{T_0} \frac{\Delta H_{fus}}{RT^2} dT \quad (4.12)$$

where  $T_0$  and  $T_x$  are hydrate equilibrium temperatures for pure water and the aqueous mixture, respectively, and  $\Delta H_{fus}$  the enthalpy of fusion of the hydrate per mole of water. The addition of any substance (alcohols, electrolytes, etc.) to the liquid phase proves to have a destabilizing effect on hydrate equilibrium by lowering  $a_w$ ; in other words, lower temperatures and/or higher pressures would be required to maintain a given hydrate phase. At the molecular level, the hydrate lattice is maintained by a balanced interchange of water molecules between the crystal itself and the adjoining quasi-liquid layer; when the activity of water drops in the liquid phase, it becomes more difficult for water molecules to leave the liquid phase to re-crystallize and the hydrate lattice consequently becomes unstable. These general remarks highlight the key role of the activity of water in the determination of hydrate stability and the present work clearly demonstrates how MOT can be used to calculate the activity of water mixed with other liquids.

It should be noted that much simpler formulae than Equation (4.12) are commonly used in the engineering community. Nielsen and Bucklin (1983) treat the solution as ideal ( $a_w = x_w$ ) and  $\Delta H_{fus}$  as constant over the temperature excursion  $T_0 - T_x$ , assumed to be small; in a popular relationship by Hammerschmidt (1939), the logarithm is replaced with  $(1 - 1/x_w)$  as  $x_w$  tends to one. These simplified approaches are limited to low alcohol concentrations and do not differentiate among alcohols (the alcohol molecular weight in the standard form of the Hammerschmidt equation is an artifact of using mass fractions instead of mole fractions). *Ad hoc* adjustments of the basic Hammerschmidt constant for alcohols with markedly stronger



hydrate-inhibition properties have been recommended, for example, in the cases of ethylene glycol, diethylene glycol (DEG) and triethylene glycol (TEG) (e.g., Bai and Bai, 2005). More recent correlations quantifying the inhibition effects of alcohols and electrolytes still consist of curvefits over selected data sets (e.g., Østergaard *et al.*, 2005). This highlights the importance of developing consistent methods of calculating the activity of water. In the case of alcohols in aqueous solutions, MOT offers an alternative to current approaches like UNIQUAC with possibly reduced requirements for parametric determination. Yet, a comprehensive MOT treatment of more general water-alcohol mixtures will necessitate further developments. For example, DEG and TEG are known to be better hydrate inhibitors than ethylene glycol, with TEG surpassing DEG (Bai and Bai, 2005; Østergaard *et al.*, 2005). The basic formalism proposed here would lead to the opposite conclusion for these primary diols of greater molecular sizes; in such cases, it is likely that the oxygen atoms linking ethylene groups through polar covalent bonds play a key role in increasing the H-bonding effectiveness of DEG and TEG molecules.

### Summary of Theoretical Analysis

A novel method based on the non-ergodic theory of mobile order thermodynamics (MOT) was proposed to estimate the activity of water in binary mixtures with ethylene glycol and several common alcohols. Calculations were shown to be in good agreement with those obtained with the widely used UNIQUAC equation, thereby establishing the soundness of the alternative MOT framework for hydrogen-bonded liquids. Consistent with the behavior observed in the dissociation experiments we conducted, results of this analysis suggest that alcohol molecules with a smaller alkyl group or a greater number of hydroxyl groups lower the activity of water more effectively. Primary alcohol isomers (e.g., 1-propanol) seem to affect the activity of water slightly less than secondary alcohol isomers (e.g., 2-propanol). In the case of alcohols with more complex molecular structures, like DEG and TEG, it was shown that the present MOT formalism requires further development to properly describe hydrogen-bonding behavior. Since hydrate stability is determined by an equilibrium condition of equal chemical potentials for water in the hydrate and liquid phases, this analysis is relevant to better understand how alcohols inhibit the formation of gas hydrates and, in general, supports and offers an explanation of the results of our experiments.

### Notation

$a$	activity
$A$	auxiliary variable
$b$	constant
$b'$	constant
$F$	formal concentration (mol/L)
$G^{H-bonding}$	excess Gibbs free energy from hydrogen bonding (J)
$K_A$	insertion constant of alcohol (L/mol)
$K_{A1}$	first insertion constant of diol (L/mol)
$K_{A2}$	second insertion constant of diol (L/mol)
$K_{W1}$	first insertion constant of water (L/mol)
$K_{W2}$	second insertion constant of water (L/mol)
$n$	mole number (mol)
$R$	gas constant (J/mol-K)
$T$	temperature (K)



$T_0$	hydrate equilibrium temperature for pure water at a given pressure (K)
$T_x$	hydrate equilibrium temperature for aqueous mixture at a given pressure (K)
$V$	molar volume (L/mol)
$x$	mole fraction

#### *Greek letters*

$\Delta H_{fus}$	molar enthalpy of fusion of the hydrate at a given pressure (J·mol <sup>-1</sup> )
$\gamma$	fraction of time a molecule is not hydrogen-bonded to neighbors
$\mu$	chemical potential (J/mol)
$\mu^{mixing}$	excess chemical potential from mixing (J/mol)
$\mu^{H-bonding}$	excess chemical potential from hydrogen bonding (J/mol)
$\phi$	volume fraction

#### *Subscripts*

A	alcohol
EG	ethylene glycol
W	water

#### *Superscript*

0	pure substance
---	----------------

### **4.3.2 Subsea Power Generation**

The deep ocean is a region of great tactical, commercial, and scientific significance. A principal hurdle to deep subsea operations is the availability of energy. For example, there are thousands of instruments deployed on the ocean floor for monitoring, surveillance, and navigation that are powered by battery packs with finite lifetimes and capacities. After these batteries are exhausted, typically in less than a year, the device must either be recovered or abandoned. Deep submersibles also run on batteries or are tethered to the surface by a power umbilical. Autonomous Underwater Vehicles (AUVs) that are driven by fuel cells using onboard stores of hydrogen and oxygen are under development, but they have limited range and will need to surface periodically for refueling. Seafloor power cables have also been employed to bring electricity from shore to the ocean depths, but they cannot be deployed at all locales to all depths and, like umbilicals, are vulnerable to natural and human hazards.

The widespread abundance of accessible methane on the seafloor, in the form of free gas seeps or hydrate deposits, offers the possibility for development as an *in situ* energy resource. Toward this end, HNEI received a grant from DARPA (Grant No. HR0011-05-1-0039) in 2005 to conduct a one-year study to evaluate the technical feasibility of generating electrical power in the deep ocean from seafloor methane and to initiate the design of a first prototype system for field deployment. That investigation concluded that it would be possible to produce net power of the order of 100 W employing existing technologies. The lifetime of such a system was unclear; however, values of 1 – 5 years appear to be reasonable, and probably could be extended, through additional R&D, careful design, and component redundancy.

The recommended configuration would thermochemically reform methane fuel gas from seeps or hydrates to H<sub>2</sub>, which would be converted to electricity in a low temperature fuel cell. Although the long-reaching goal is for self-sufficient systems, i.e., devices that run entirely on ambient fuel and oxidizer resources, it was concluded that some stored oxidizer brought from the

surface will be required, since the current level of technology to extract dissolved  $O_2$  from sea water is not adequate to provide the concentrations needed to reform methane. On the other hand, dissolved oxygen (DO) extraction does appear to be a viable option to supply the fuel cell cathode.

Seafloor methane and DO resources were assessed. It was concluded that the energy density of sediment porewater methane and methane dissolved in sea water was too low to sustain operation of a nominal 100 W system. Gas seeps on the seafloor were ranked as the best option to fuel this system, followed by hydrate outcroppings. Although the DO resource is extensive, ambient concentrations limit the maximum partial pressures of  $O_2$  that can be recovered in a mass exchanger to about 8 kPa. Based on our resource assessment, two candidate sites were identified to deploy a first prototype for field testing: a shallow site in the Santa Barbara Channel where there are strong and persistent hydrocarbon gas seeps that have been extensively characterized, and a deep water site in the Gulf of Mexico (GOM) where hydrate outcroppings (and gas seeps) have been observed.

Models of the methane reforming process, PEM and alkaline fuel cells, and direct mass exchangers and membrane contactors to extract DO were developed and associated laboratory experiments were performed. Preliminary case studies based on these models have indicated that one viable configuration would comprise an alkaline fuel cell utilizing a membrane contactor to extract DO to supply the cathode. Stored  $H_2O_2$  would be needed to thermochemically reform collected  $CH_4$  to  $H_2$ .

The DARPA study concluded that the necessary next steps were to test and characterize major components (i.e., reformer; fuel cell; membrane contactor), first on the benchtop, then in pressure chambers at simulated underwater conditions, and finally offshore.

Experiments to investigate high-pressure reforming of methane using  $H_2O_2$  were concluded successfully and are reported in a separate section of this Final Report. During the present reporting period we also proposed to initiate testing of candidate fuel cells under simulated deep ocean conditions. This activity was pursued on a time-available basis, since it was a secondary priority of this subtask relative to the chemical hydrate destabilization study described in the previous sections. Accomplishments were limited to designing a facility to test single cell alkaline fuel cells from Astris Energi Inc. (LABCELL LC50-1) at elevated ambient pressures and temperatures encountered in the deep ocean. These cells produce about 3.75 W when operated with pure  $H_2$  and air, and have an active area of  $50\text{ cm}^2$ . Experiments, which will be pursued in subsequent phases of the HEET initiative, plan to utilize the nominal 12" and 6" stainless steel pressure chambers shown in the photo in Figure 4-6.



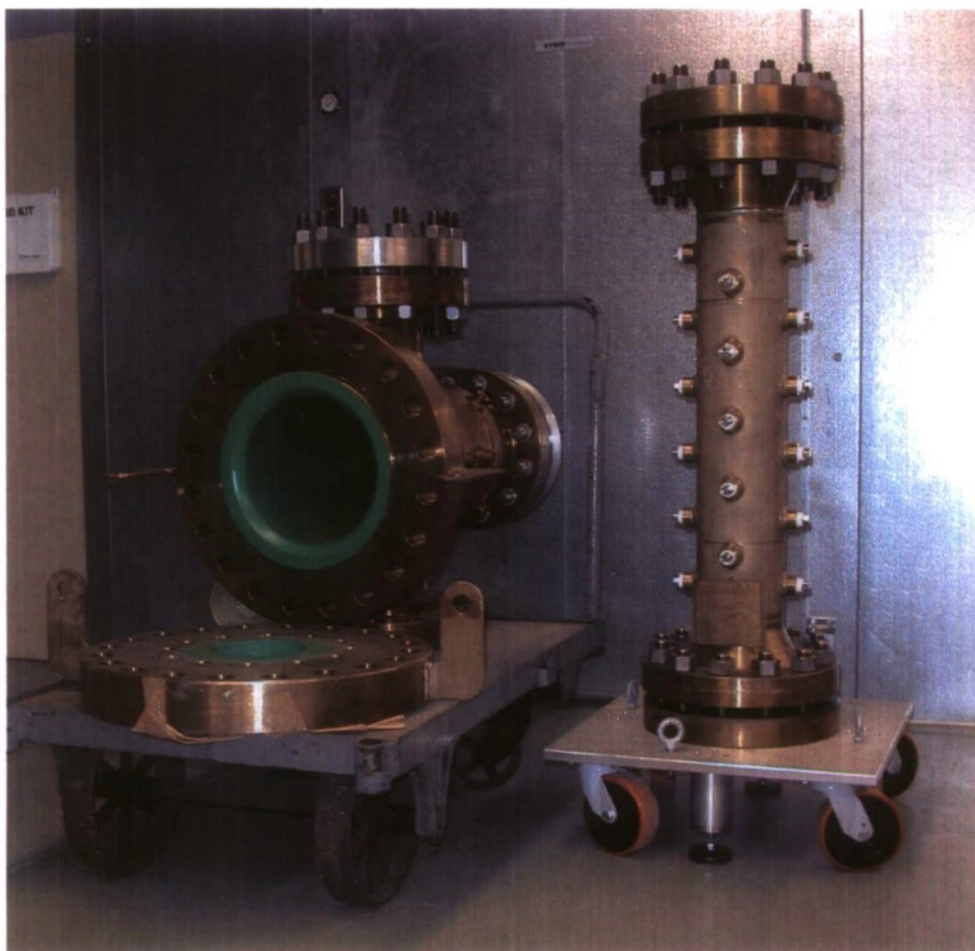


**Figure 4-6. Photo of pressure vessels that will be employed in upcoming experiments to characterize fuel cell operation under simulated deep ocean conditions.**

#### **4.3.3 Environmental Impacts of Methane Release from Seafloor Hydrates**

The long-term goal of this subtask is to develop a robust three-dimensional numerical model of methane in the ocean. Methane is a potent greenhouse gas with a significantly higher Global Warming Potential than CO<sub>2</sub>, but much lower levels of emissions into the atmosphere. Whereas the oceans currently are a net sink for atmospheric CO<sub>2</sub>, they represent a net source of CH<sub>4</sub>. Moreover, the historical record contains evidence of massive methane outgassing from marine and permafrost hydrate reservoirs that may have greatly exacerbated earlier episodes of global warming.

The target model will need to consider the production, oxidation, and transport of CH<sub>4</sub>, and will require an understanding of processes that affect the exchange of methane between the atmosphere, ocean, and seafloor sediment. During the present reporting period, work continued on the development of components of the 3D model and experimental investigations of the role of microbes in methane production and consumption.

##### *Modeling*

A recently published model of methane released from seafloor hydrothermal vents (Nihous and Masutani, 2007) highlighted: a) the importance of isotope fractionation by aerobic



methanotrophs as a modeling diagnostic, and b) the need to adequately represent buoyant seafloor sources in simple parametric ways since they likely would not be resolved in coarser far-field models. This led to a couple of very specific studies. The first one addressed the reliability of claims made from the results of laboratory incubation experiments that methanotrophs seem to relax their preferential uptake of  $^{12}\text{CH}_4$  as bacterial population grows (Templeton *et al.*, 2006). The second consisted of a numerical investigation of the analysis of mixing layers over distributed sources of buoyancy performed by Epstein and Burelbach (2001).

### Carbon Isotope Fractionation by Aerobic $\text{CH}_4$ -oxidizing Bacteria

A laboratory setup to determine carbon isotope fractionation by  $\text{CH}_4$ -oxidizing bacteria typically consists of a volume of liquid culture with a substrate-rich gas phase; this gas phase may simply be a headspace initially rich in methane and oxygen, or it may also include a bubbling mechanism. Substrate may be supplied on a continuous basis or not as methanotrophs grow; in the case of chemostats, liquid also is continuously replenished. With little loss of generality, systems for which the liquid volume is constant were examined. Of particular interest is whether isotope discrimination by methanotrophs changes in the course of a given experiment, i.e., whether bacteria relax their preferential uptake of  $^{12}\text{CH}_4$  as their population grows. Coleman *et al.* (1981) performed experiments that largely support Rayleigh distillation (constant kinetic isotope fractionation factor); the possible exception when this factor seemed to change occurred when a given culture was restarted, i.e., a case with a relatively higher initial cell density; the experimenters interpreted this as a possible change in the methane-oxidation pathway. Barker and Fritz (1981) reported the results of a suite of experiments where isotopic separation ( $\delta^{13}\text{CH}_4 - \delta^{13}\text{CO}_2$ ) varied between 5‰ and 29.6‰; for each individual experiment, a downward trend as a function of incubation time could be discerned. The recent and detailed work of Templeton *et al.* (2006) clearly showed a decrease in fractionation as cell density increased to several decigrams per liter. The authors offered a heuristic interpretation based on the relative strengths of the biomass methane sink and other fluxes (e.g., from bubble dissolution and volatilization across the gas-liquid interface). Their insight suggests that extrinsic phenomena typical of the experimental setup (gas-liquid phase partition) may affect the measurement of intrinsic fractionation at the bacterial level. A simple quantitative model was developed further to clarify the respective effects of experimental protocol and bacterial methane oxidation pathway on measured isotope fractionation.

### Mathematical Model

Experiments of Templeton *et al.* (2006), that studied pure cultures of methanotrophs, considered a gas headspace of volume  $V_g$  over a liquid of volume  $V_c$ . In these experiments, a gas mixture of known composition is bubbled through the liquid at a volumetric rate  $v_{in}$ ; gas withdrawal from the headspace also is performed at a volumetric rate  $v_{out}$ . Chemical species involved in the methane oxidation reaction, i.e., methane, oxygen and carbon dioxide, as well as the inert species nitrogen are analyzed in both phases. While the experiments of Templeton *et al.* (2006) were performed at room temperature  $T$  (isothermal), the additional assumption that the total pressure  $P$  was constant is made here with little loss of generality. As a result, the total moles of gas in the headspace is equal to  $PV_g/(RT)$ , where  $R$  is the gas constant. To ensure the integrity of the model, it suffices to continuously adjust the withdrawal rate  $v_{out}$ . In what follows,  $s$ ,  $x$ ,  $y$ ,  $z$  and  $w$  are the respective concentrations of biomass-bound carbon, methane, carbon dioxide, oxygen and nitrogen in the culture solution.  $X$ ,  $Y$ ,  $Z$  and  $W$  are the respective number of gas moles of methane, carbon dioxide, oxygen and nitrogen in the headspace. Three additional concentrations

$^{13}\text{s}$ ,  $^{13}\text{x}$ , and  $^{13}\text{y}$  and two additional gas mole numbers  $^{13}\text{X}$  and  $^{13}\text{Y}$  are necessary to track the stable isotope  $^{13}\text{C}$ .

The global stoichiometry of the methane oxidation reaction may be written as:



where  $\alpha$  is the biomass carbon assimilation ratio. The reaction can be broken down into two steps with methane initially being converted to formaldehyde by methane monooxygenase (MMO) enzymes found in methanotrophs. The rate of methane consumption (molar per second per molar of biomass carbon) is represented here by the Michaelis-Menten form  $q = q_m x / (K_m + x)$ . An order-of-magnitude for the half-saturation constant  $K_m$  is 1  $\mu\text{M}$  (Dunfield *et al.*, 1999). For culture experiments with methane-rich atmospheres, i.e., with partial pressures exceeding 0.1 atm (Coleman *et al.*, 1981; Templeton *et al.*, 2006),  $x \gg K_m$  since the solubility of methane  $k_x$  is about  $1.4 \times 10^{-3} \text{ M/atm}$  (Wilhelm *et al.*, 1977); such cases essentially correspond to a zero<sup>th</sup> order reaction with respect to  $x$  and  $q \approx q_m$ . In many natural environments, however, such as the ocean,  $x$  is found at nanomolar levels and methane oxidation typically proceeds as a first order reaction with respect to  $x$ .

The abundance of  $^{13}\text{CH}_4$  is low and the overall concentration of methane closely represents that of  $^{12}\text{CH}_4$ . The rate of  $^{13}\text{CH}_4$  consumption (molar per second per molar of biomass carbon) therefore can be expressed as  $q^{13}\text{x}/(x\alpha_{\text{MMO}})$  where  $\alpha_{\text{MMO}}$  is the kinetic isotope fractionation ratio corresponding to the formaldehyde branch point. The subsequent assimilatory step from formaldehyde into biomass, for example via the ribulose monophosphate (RuMP) pathway for Type I methanotrophs, entails further isotope fractionation with a kinetic ratio  $\alpha_{\text{Bio}}$ . These considerations lead to the following system of 14 first-order ordinary differential equations for the 14 functions of time,  $t$ :

$$ds/dt = \alpha qs \quad (4.14)$$

$$dx/dt = -qs + (D_x - F_x)/V_c \quad (4.15)$$

$$dy/dt = (1 - \alpha)qs + (D_y - F_y)/V_c \quad (4.16)$$

$$dz/dt = -2qs + (D_z - F_z)/V_c \quad (4.17)$$

$$dw/dt = (D_w - F_w)/V_c \quad (4.18)$$

$$d^{13}\text{s}/dt = \alpha qs^{13}\text{x}/(x\alpha_{\text{MMO}}\alpha_{\text{Bio}}) \quad (4.19)$$

$$d^{13}\text{x}/dt = -qs^{13}\text{x}/(x\alpha_{\text{MMO}}) + (^{13}\text{D}_x - ^{13}\text{F}_x)/V_c \quad (4.20)$$

$$d^{13}\text{y}/dt = (1 - \alpha/\alpha_{\text{Bio}})qs^{13}\text{x}/(x\alpha_{\text{MMO}}) + (^{13}\text{D}_y - ^{13}\text{F}_y)/V_c \quad (4.21)$$

$$dX/dt = D_x^{\text{in}} - D_x + F_x - v_{\text{out}}X/V_g \quad (4.22)$$

$$dY/dt = D_y^{\text{in}} - D_y + F_y - v_{\text{out}}Y/V_g \quad (4.23)$$

$$dZ/dt = D_z^{\text{in}} - D_z + F_z - v_{\text{out}}Z/V_g \quad (4.24)$$

$$dW/dt = D_w^{\text{in}} - D_w + F_w - v_{\text{out}}W/V_g \quad (4.25)$$

$$d^{13}\text{X}/dt = ^{13}\text{D}_x^{\text{in}} - ^{13}\text{D}_x + ^{13}\text{F}_x - v_{\text{out}}^{13}\text{X}/V_g \quad (4.26)$$

$$d^{13}\text{Y}/dt = ^{13}\text{D}_y^{\text{in}} - ^{13}\text{D}_y + ^{13}\text{F}_y - v_{\text{out}}^{13}\text{Y}/V_g \quad (4.27)$$



$F_x$  represents the molar flux of methane from the liquid phase into the gas headspace across the free surface. It is defined as:

$$F_x = v \{x - RTk_x X/V_g\} \quad (4.28)$$

$F_y$ ,  $F_z$ ,  $F_w$ ,  $^{13}F_x$  and  $^{13}F_y$  are defined likewise for other chemical and isotopic species. The carbon dioxide, oxygen and nitrogen solubilities are, respectively,  $k_y = 3.5 \times 10^{-2}$  M/atm (Edwards *et al.*, 1978),  $k_z = 1.3 \times 10^{-3}$  M/atm (Wilhelm *et al.*, 1977) and  $k_w = 6.5 \times 10^{-4}$  M/atm (Wilhelm *et al.*, 1977).  $v$  is a volume flux, which is the product of a mass transfer coefficient and the transfer area; it is assumed to be independent of species since mass transfer coefficients weakly depend on liquid-side diffusivities and that the diffusivities of CH<sub>4</sub>, CO<sub>2</sub>, O<sub>2</sub> and N<sub>2</sub> are within 20% of one another. Kinetic and thermodynamic isotopic fractionation that could affect the mass transfer coefficient and solubility of  $^{13}\text{C}$  species across the liquid-gas interface is deemed negligible as well (Knox *et al.*, 1992; Zhang *et al.*, 1995). For lack of better knowledge,  $v$  can be viewed as a modeling parameter that has to be tuned.  $D_x^{\text{in}}$  is the input molar flux of methane bubbled through the liquid culture and  $D_x$  represents the amount thereof that goes into solution. It is expressed as:

$$D_x = \min \{ D_x^{\text{in}}, \beta(k_x p_x^{\text{in}} - x) \} \quad (4.29)$$

where  $p_x^{\text{in}} = RT D_x^{\text{in}}/v_{\text{in}}$  is the partial pressure of methane in the incoming bubble stream. As physically expected,  $D_x^{\text{in}}$  is the maximum amount of methane that can be dissolved. Otherwise, Equation (4.29) is formally similar to Equation (4.28), with the volume flux  $\beta$  expressing mass transfer kinetics; the fixed partial pressure inside the bubbles is a simplification since the description of detailed bubble evolution phenomena are beyond the scope of this modeling effort.  $D_y$ ,  $D_z$ ,  $D_w$ ,  $^{13}D_x$  and  $^{13}D_y$  are defined likewise. Methane oxidation reactants (CH<sub>4</sub> and O<sub>2</sub>) bubbled through the culture should partially dissolve ( $D_x$  and  $D_z$  positive), but some carbon dioxide is expected to be stripped instead ( $D_y$  negative). The  $^{13}\text{C}$  terms are defined differently whether dissolution or stripping occurs: in the former case, e.g., for  $D_x > 0$ ,  $^{13}D_x = (^{13}D_x^{\text{in}}/D_x^{\text{in}}) D_x$ ; in the latter case, e.g. for  $D_y < 0$ ,  $^{13}D_y = (^{13}y/y) D_y$ . In this formalism, the modeling parameter  $\beta$  must be tuned. To complete the definition of Equations (4.14) through (4.27), the isobaric condition  $d(X+Y+Z+W)/dt = 0$  can be enforced to yield:

$$v_{\text{out}} = v_{\text{in}} - RT \sum_{i=x,y,z,w} (D_i - F_i)/P \quad (4.30)$$

### Results and Discussion

The mathematical model developed in the previous section was numerically implemented to simulate the pure culture experiments of Templeton *et al.* (2006) with *Methylomonas methanica* (with copper). The assimilatory pathway (RuMP) for this Type I methanotroph is simpler and the equations were derived accordingly. Choosing a particular data set results in little loss of generality given the focus of this study on the importance of gas-liquid mass transfer phenomena in this type of experiments.

Table 4-2 lists the parameters used in the calculations. Initial conditions for aqueous concentrations and headspace mole numbers not shown in Table 4-2 were assumed to correspond to equilibrium with the influent gas composition. Calling  $\rho$  the isotopic ratio  $^{13}\text{C}/^{12}\text{C}$  of a species,  $\delta^{13}\text{C} = 1000 (\rho/\rho_{\text{PDB}} - 1)$  is used to express its isotopic composition per mil (‰) based



on the PDB standard (Craig, 1957). The maximum bacterial growth rate  $q_m$  was estimated from the results of chemostat experiments performed by Templeton *et al.* (2006) with mixed cultures of  $\text{CH}_4$ -oxidizing bacteria. It can be inferred from Table 4-2 that the steady-state chemostat aqueous methane concentration in equilibrium with a methane gas partial pressure of about 0.095 atm ( $1.33 \times 10^{-4}$  M) far exceeds  $K_m$ . It follows that at steady-state,  $q_m \approx q$ , i.e., the ratio of the chemostat liquid turnover rate (0.2 per day) over the biomass carbon assimilation ratio (which approaches 20% here). It is also the ratio of the methane consumed by the bacteria (in M/s) over the biomass-bound carbon concentration. An average value  $\alpha \approx 0.185$  corresponds to an estimated  $q_m = 1.25 \times 10^{-5} \text{ s}^{-1}$  (a little over one per day). A time step of 1 s was selected. Even though such a small value of  $dt$  is not physically significant for the relatively slow phenomena being considered, it allows a simple Euler forward scheme to solve the system of first-order differential Equations (4.14) through (4.27) without jeopardizing solution accuracy. Figure 4-7 shows the predicted isotopic composition of effluent methane gas, effluent carbon dioxide gas and biomass as a function of cell density in  $\text{g-L}^{-1}$ , which is taken as 24 times  $s$  (with an approximate 50% cell carbon content per Sundh *et al.*, 2005). Values of  $\delta^{13}\text{CO}_2$  were corrected to remove the effect of the influent value (-18‰) as in Templeton *et al.* (2006); this correction only matters at very low cell densities.

Table 4-2. Input for numerical calculations.

Parameter	Comments
$K_m$	$10^{-6}$ M typical <sup>a</sup>
$k_x$	$1.4 \times 10^{-3}$ M/atm ref. <sup>b</sup>
$k_y$	$3.5 \times 10^{-2}$ M/atm ref. <sup>c</sup>
$k_z$	$1.3 \times 10^{-3}$ M/atm ref. <sup>b</sup>
$k_w$	$6.5 \times 10^{-4}$ M/atm ref. <sup>b</sup>
$P$	1 atm assumed
$P_x^{in}$	0.14 atm ref. <sup>d</sup> , $P = 1$ atm
$P_y^{in}$	$4 \times 10^{-4}$ atm ref. <sup>d</sup> , $P = 1$ atm
$P_z^{in}$	0.20 atm ref. <sup>d</sup> , $P = 1$ atm
$q_m$	$1.25 \times 10^{-5}$ s <sup>-1</sup> see text
$T$	296.15 K 23°C average <sup>d</sup>
$v_{in}$	$8.33 \times 10^{-5}$ L-s <sup>-1</sup> 5 mL/min <sup>d</sup>
$V_c$	0.2 L ref. <sup>d</sup>
$V_g$	0.3 L ref. <sup>d</sup>
$\alpha$	0.40 average <sup>e</sup>
$\alpha_{MMO}$	1.035 estimate <sup>f</sup>
$\alpha_{Bio}$	0.994 estimate <sup>f</sup>
$\beta$	$10^{-3}$ L-s <sup>-1</sup> baseline
$\nu$	$4 \times 10^{-5}$ L-s <sup>-1</sup> baseline
<i>Selected initial values</i>	
$s$	$1.25 \times 10^{-3}$ M 0.03 g-L <sup>-1dg</sup>
$\delta^{13}CH_4$	-20.2‰ influent, ref. <sup>h</sup>
$\delta^{13}CO_2$	-18‰ influent, ref. <sup>i</sup>
$\delta^{13}C_{cell}$	-30‰ best guess <sup>j</sup>

(a) Dunfield *et al.* (1999)

(b) Wilhelm *et al.* (1977)

(c) Edwards *et al.* (1978)

(d) Templeton *et al.* (2006), p. 1741

(e) Templeton *et al.* (2006), p. 1745

(f) Templeton *et al.* (2006), Figure 3C

(g) 50% cell carbon content (Sundh *et al.*, 2005)

(h) Templeton *et al.* (2006), Table 3

(i) Templeton *et al.* (2006), p. 1743

(j) Templeton *et al.* (2006), Tables 2 and 3

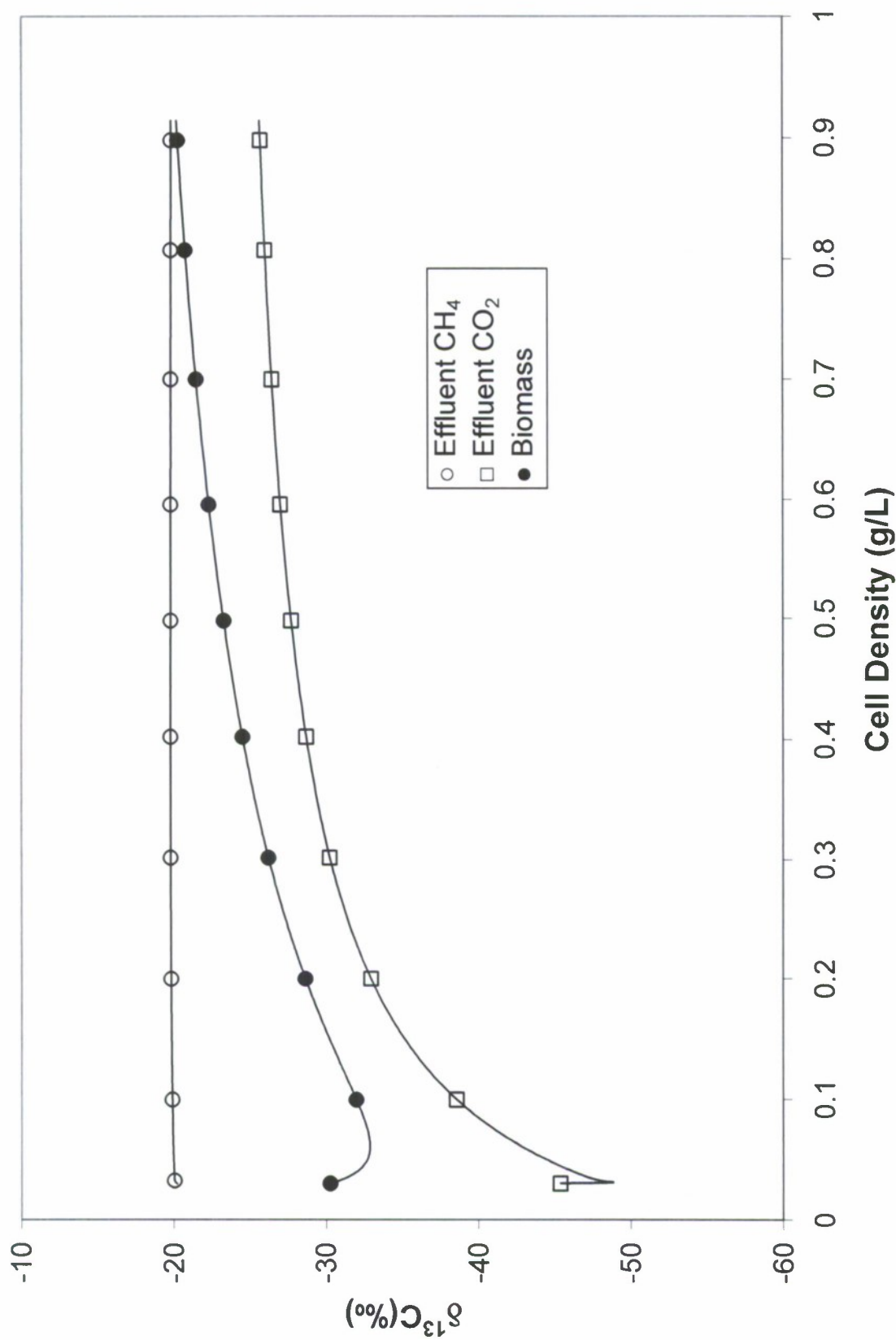


Figure 4-7. Predicted  $\delta^{13}\text{C}$  versus cell density ( $\text{g}\cdot\text{L}^{-1}$ ): baseline case.



Figure 4-7 is remarkably similar to *Figure 3C* in Templeton *et al.* (2006). Even though  $\alpha_{\text{MMO}}$  is a constant in the model, results show a substantial decrease in the isotopic separation between effluent methane and carbon dioxide, from nearly 30‰ at low cell densities to about 6‰ at  $0.90 \text{ g-L}^{-1}$ . Biomass is isotopically heavier than effluent  $\text{CO}_2$  by about 6‰. With the baseline values of the mass-transfer model parameters  $\beta$  and  $\nu$ , it took a little less than 8 days (190 hours) to reach a predicted cell density of  $0.9 \text{ g-L}^{-1}$ , at which time the effluent gas contained 1.7%  $\text{CO}_2$  and 12.1%  $\text{CH}_4$ . This effluent composition is in good agreement with the data.  $\nu_{\text{out}}$  was only slightly less than  $\nu_{\text{in}}$  (93%) and methane transfer from bubble dissolution,  $D_x$  over  $D_x^{\text{in}}$ , was 14%. The specific methane consumption rate  $q$  remained very close to the maximum value  $q_m$ . Varying the bubble mass transfer parameter  $\beta$  indicated that, for values smaller by at least an order of magnitude than the baseline choice, bacteria took much longer to grow to a given cell density, but more importantly, the effluent gas  $\text{CO}_2$  content remained far too low when compared to data; in this case,  $q$  was shown to be substantially less than  $q_m$ . When  $\beta$  was increased by a factor of 10 instead, little change occurred with respect to the baseline case, with  $\text{CH}_4$  transfer from bubbles not exceeding 20% at a cell density of  $0.9 \text{ g-L}^{-1}$ ; larger values of  $\beta$  were essentially compensated by an increase in aqueous methane concentration  $x$  and therefore, a reduction of  $(k_x P_x^{\text{in}} - x)$  in Equation (4.29); at the same time, no significant additional methane consumption by the bacteria occurred since the condition  $q \approx q_m$  was unchanged. This suggests that incomplete dissolution of the bubbles may not be responsible for the sharp drop in  $(\delta^{13}\text{CH}_4 - \delta^{13}\text{CO}_2)$  shown at high cell densities in Figure 4-7 and in the data of Templeton *et al.* (2006).

Next, the effect of  $\nu$  was investigated and a 100-fold increase in the baseline value was considered. While global results (cell density, effluent gas composition) showed virtually no change, isotopic compositions were dramatically altered as shown in Figure 4-8. For sufficiently high mass transfer across the gas-liquid free surface, the isotopic separation  $(\delta^{13}\text{CH}_4 - \delta^{13}\text{CO}_2)$  in the effluent gas stream remained essentially constant and accurately reflected the intrinsic isotope fractionation occurring during the methane oxidation process (35‰). These results highlight the importance of mass transfer across the gas-liquid interface when interpreting isotope fractionation in this type of experiments. Dewulf *et al.* (1998) measured some exchange coefficients  $(\nu/V_c)$  for a standard stirred reactor. Dividing the baseline value  $\nu = 4 \times 10^{-5} \text{ L-s}^{-1}$  by  $V_c = 0.2 \text{ L}$ , one would obtain an exchange coefficient of 17.3 per day corresponding to a stirring Reynolds number,  $Re$ , of the order of 25000. More accurately, however, the exchange coefficient is the ratio of mass transfer coefficient over average liquid height; the latter was considerably greater (19 cm) for the reactor of Dewulf *et al.* (1998) than for the pure culture experiments of Templeton *et al.* (2006) performed in a 500 ml KIMAX flask. Taking this into account leads to an estimated exchange coefficient of 2.6 per day that is lower than the range tested by Dewulf *et al.* (1998) for  $Re > 5600$ . Although magnetic stir bars were used by Templeton *et al.* (2006), it is not clear how effective stirring was in promoting mass transfer across the gas-liquid interface.

Templeton *et al.* (2006) used a somewhat heuristic argument to explain the decrease in apparent isotope fractionation  $(\delta^{13}\text{CH}_4 - \delta^{13}\text{CO}_2)$  in the course of their experiments. They adapted a formula derived by O'Leary and Osmond (1981) for the fractionation occurring in the assimilation of  $\text{CO}_2$  by certain plants. Their main conclusion was that the shift was due to the progressive increase of methane consumption relative to the rate of methane transfer across the

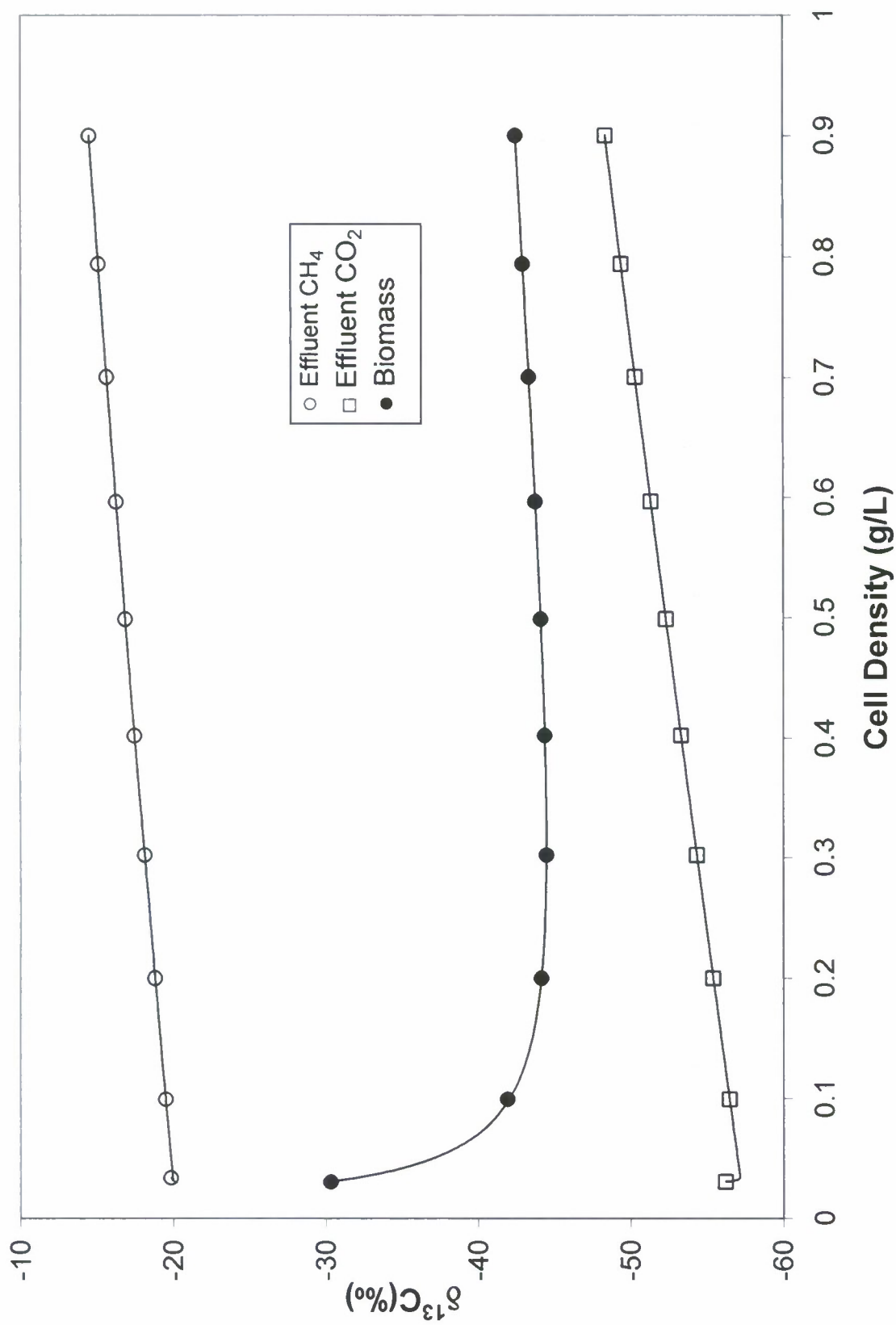


Figure 4-8. Predicted  $\delta^{13}\text{C}$  versus cell density (g-L<sup>-1</sup>):  $\mu = 0.004 \text{ L}\cdot\text{s}^{-1}$ .



gas-water interface is validated by the calculations shown in Figure 4-7. The formula of O'Leary and Osmond (1981) was derived in a simpler context where three elementary reactions are proportional to biomass concentration (per cell, or per molar of biomass-bound carbon basis). The intermediate product ( $\text{CO}_2$  concentration inside the plant's intercellular air space) also was assumed to have reached steady-state; this approach has often been adopted, e.g., in phytoplankton studies (Laws *et al.*, 1995; Rau, 1997). Templeton *et al.* (2006) modified the formula by assuming that two of the three elementary reactions were independent of biomass concentration. Their success in the qualitative interpretation of their data may indicate good intuition but a generalization of these results warrants caution. The predictions displayed in Figure 4-8 demonstrate that unless mass transfer rates across the gas-water interface are quantified for a specific suite of experiments, a strong correlation between the decrease in apparent isotope fractionation ( $\delta^{13}\text{CH}_4 - \delta^{13}\text{CO}_2$ ) and cell density is not justified.

In a system such as Equations (4.14) through (4.27), intrinsic terms are those proportional to  $s$  while others describe the overall physical context (experimental apparatus, microcosm, natural environment with open boundaries, etc.). It is often difficult to separate the respective effects of intrinsic and extrinsic terms since quantitative modeling often cannot be done. In the open ocean, for example, one way to reduce the impact of extrinsic terms arising from generally complex mixing phenomena is to scale substrate (methane) concentrations with those of a passive tracer (e.g., temperature anomaly in Cowen *et al.*, 2002). If only the  $s$ -proportional terms are retained in Equations (4.15) and (4.20), direct integration straightforwardly yields:

$$\alpha_{\text{MMO}} = \text{Log}(x/x_0)/\text{Log}({}^{13}\text{x}/{}^{13}\text{x}_0) \quad (4.31)$$

This result is independent of the biomass-specific methane oxidation rate  $q$  (although it generally is derived by assuming  $q$  to be first-order with respect to methane concentration as in Coleman *et al.*, 1981). An experimental system that should behave as predicted by Equation (4.31) would be an isolated liquid culture of  $\text{CH}_4$ -oxidizing bacteria with high initial methane and oxygen concentrations and no free surface. Chemostat equations when only liquid turnover is allowed (i.e., with no substrate turnover in a gas phase) show that bacterial growth would be exceedingly slow. Instead, bacterial growth could be promoted as a first step in a chemostat where substrate is provided in a gas phase, as in Templeton *et al.* (2006); the second step to measure isotope fractionation would be done by isolating a large liquid volume from the chemostat and measuring the evolution of the aqueous concentrations  $x$  and  ${}^{13}\text{x}$ .

Finally, the above quantitative analysis was tentatively applied to the experimental results of Coleman *et al.* (1981). In order to do this, all terms corresponding to gas input and output in Equations (4.14) through (4.27) were set to zero (sparse gas sampling from the large headspace  $V_g = 11.5$  L negligibly affected gas composition):  $v_{\text{in}} = v_{\text{out}} = 0$ ;  $D_i^{\text{in}} = 0$  for  $i = x, y, z, w$ ;  ${}^{13}D_i^{\text{in}} = 0$  for  $i = x, y$ ;  $D_i = 0$  for  $i = x, y, z, w$ ; and  ${}^{13}D_i = 0$  for  $i = x, y$ . Table 4-3 lists the input parameters needed for the numerical simulation of the growth of the bacterial culture labeled A at 26 °C, except for the constants  $K_m$ ,  $k_i$  ( $i = x, y, z, w$ ),  $q_m$ ,  $\alpha$ ,  $\alpha_{\text{Bio}}$ , as well as the initial conditions for  $\delta^{13}\text{CO}_2$  and  $\delta^{13}\text{C}_{\text{cell}}$  that were all kept unchanged (cf., Table 4-2). Total and partial pressures are now variables since the system is isolated. Initial conditions for aqueous concentrations were assumed to correspond to equilibrium with the initial headspace gas mixture. The nitrogen evolution given by Equations (4.18) and (4.25) are then unnecessary



**Table 4-3. Input for numerical calculations (experiments of Coleman *et al.*, 1981<sup>a</sup>).**

Parameter	Comments
T	299.15 K
V <sub>c</sub>	0.5 L
V <sub>g</sub>	11.5 L
α <sub>MMO</sub>	1.030 estimate <sup>b</sup>
υ	0.02 L·s <sup>-1</sup> baseline
<i>Selected initial values</i>	
P	1 atm assumed
P <sub>x</sub>	0.2 atm typical in range <sup>a</sup>
P <sub>y</sub>	3 × 10 <sup>-4</sup> atm assumed
P <sub>z</sub>	0.50 atm high value <sup>c</sup>
s	8.33 × 10 <sup>-5</sup> M 2 × 10 <sup>-3</sup> g·L <sup>-1</sup> de
δ <sup>13</sup> CH <sub>4</sub>	-40‰ Figure 1 <sup>a</sup>

(a) Coleman *et al.* (1981), culture A at 26 °C.

(b) value slightly higher than upper bound in ref.

(c) high value to prevent O<sub>2</sub> starvation; oxygen addition through experiments is reported in ref.

(d) value yields a CH<sub>4</sub> depletion of 50% in 2 weeks quoted in ref. (with q<sub>m</sub> = 1.25 × 10<sup>-5</sup> s<sup>-1</sup>).

(e) 50% cell carbon content (Sundh *et al.*, 2005).

(nitrogen equilibrium is always maintained). With q<sub>m</sub> = 1.25 × 10<sup>-5</sup> s<sup>-1</sup>, the initial condition for s yields a methane depletion of 50% in 2 weeks, as reported by Coleman *et al.* (1981).

The numerical simulation of the growth of the bacterial culture labeled B at 11.5 °C (T = 284.65 K) was also performed. In this case, the average fractionation ratios given in the reference were adopted, i.e., α<sub>MMO</sub> = 1.013. For this cold culture, the baseline value of q<sub>m</sub> was reduced to a twelfth (q<sub>m</sub> = 9.9 × 10<sup>-7</sup> s<sup>-1</sup>) since a 50% methane depletion took 6 months. According to the Rosso model described for example in Kevbrina *et al.* (2001), the same mesophilic methanotrophs could exhibit such a change in specific growth rate q<sub>m</sub> with temperature; they would grow between 9 °C and 37 °C only, and optimally at 26 °C. Figure 4-9 displays predicted results as symbols and the best linear fits of Coleman *et al.* (1981) to their data (not shown) as lines. A high model value of the gas-liquid transfer parameter (υ = 0.02 L·s<sup>-1</sup>) ensures that predictions remain relatively linear on these semi-log plots (one can always pick υ large enough to achieve linearity). δ<sup>13</sup>CH<sub>4</sub> predictions for Culture A at 26 °C seem to bend slightly at low values of X/X<sub>0</sub> whereas the data of Coleman *et al.* (1981) do not. As expected, this tendency is far less pronounced for the slow growth case (Culture B at 11.5 °C). Unfortunately, it is not possible to assess whether experiments were performed with υ at least as large as 0.02 L·s<sup>-1</sup>; on the basis of free-surface area alone, the setups of Coleman *et al.* (1981), i.e., 0.5 L of solution

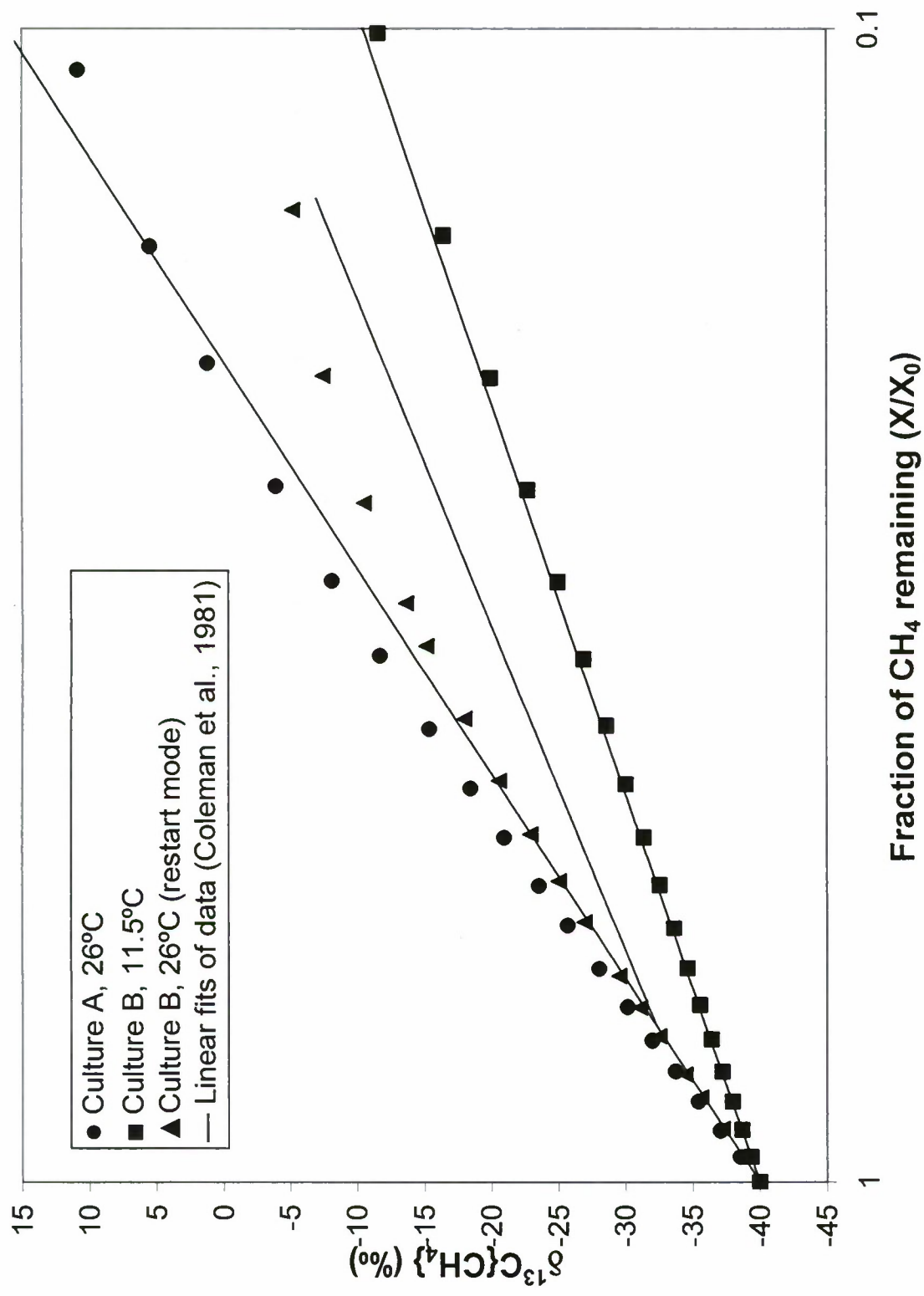


Figure 4-9. Predicted  $\delta^{13}\text{C}$  versus fraction of methane in the gas phase (experiments of Coleman et al., 1981).

in a 12 L round bottom flask, and of Templeton *et al.* (2006) only differ by a factor of about 4. A last numerical experiment consisted in simulating the warm growth of Culture B following its incubation at the lower temperature (restart mode). Accordingly, the concentrations of all liquid species were initialized to values corresponding to cold culture predictions when  $X/X_0 \approx 0.15$ ; the mole numbers of all gaseous species were initialized as before (flushing of the headspace). Model parameters are those given in Table 4-3. A significant difference here is that the initial value of  $s$  corresponds to a high cell density of  $1.6 \text{ g-L}^{-1}$ . As a result, the non-linearity of the predictions as methane depletion increases is more pronounced, as shown in Figure 4-9. Coleman *et al.* (1981) did observe a difference as well but limited their interpretation to a change of slope (at  $X/X_0 \approx 0.73$ ) that would reflect a change in methane oxidation pathway (i.e., a different value of the intrinsic fractionation ratio  $\alpha_{\text{MMO}}$ ). A definitive interpretation is not available, the present modeling effort suggests that the observed differences in Cultures A and B at  $26^\circ\text{C}$  could have been partially caused by a growing imbalance between methane consumption and gas-liquid transfer.

#### Carbon Isotope Fractionation Summary

The main issue considered in this study is whether carbon isotope fractionation data measured in laboratory experiments or collected in natural environments can be interpreted (and utilized for modeling purposes) accurately. Even though the very high bacterial cell densities causing an apparent isotope fractionation reduction in the experiments of Templeton *et al.* (2006) are unlikely to be found in natural environments, it remains conceptually incorrect to attribute an intrinsic reality to this measured fractionation shift, as if it could be extrapolated to other contexts. The possible occurrence of very high cell densities with data that would support constant isotope fractionation has been shown in simulations, and the preference expressed by methanotrophs for  $^{12}\text{CH}_4$  may not depend on bacterial cell density after all. Carbon isotope fractionation factors are not measured or estimated just for their own sake. They provide a key component toward understanding carbon cycling and often allow researchers to determine or constrain other parameters; the fractionation data of Cowen *et al.* (2002), for example, was incorporated in a simple model of waters in the vicinity of deep seafloor geothermal vents, where methanotroph growth rate and carbon content could be estimated (Nihous and Masutani, 2007).

#### Numerical Simulation of a Mixing Layer over a Distributed Source of Buoyancy

Epstein and Burelbach (2001) developed a theoretical steady-state boundary-layer analysis describing the upward injection of a buoyant fluid at a velocity  $V_0$  over a circular area of radius  $R_0$  into another fluid of constant properties (subscript  $\infty$ ). Their primary motivation was the assessment of flammability hazards (by analogy) when light fuel gas is released into quiescent air-filled storage containers. The experimental setup consisted of a tank filled with brine and a porous circular disk placed on the tank bottom through which freshwater could be injected. A schematic diagram of the physical problem under investigation is shown in Figure 4-10. It should be noted that such a configuration could be useful in describing diffuse hydrothermal vents on the ocean floor as well (Lupton *et al.*, 1985; Bemis *et al.*, 2002), and is therefore relevant to our modeling activity. Both data and theory successfully showed the existence of a mixing boundary layer above the buoyancy source as ambient fluid is drawn radially inward until conditions for the existence of a rising plume are met, at a transition radius  $r = R_p$ . Perhaps the most compelling results were that the shape of the boundary layer as well as the transition radius



normalized with  $R_0$  appear to be independent of source size ( $R_0$ ), freshwater injection rate ( $V_0$ ) and background solute concentration ( $Y_\infty$ ).

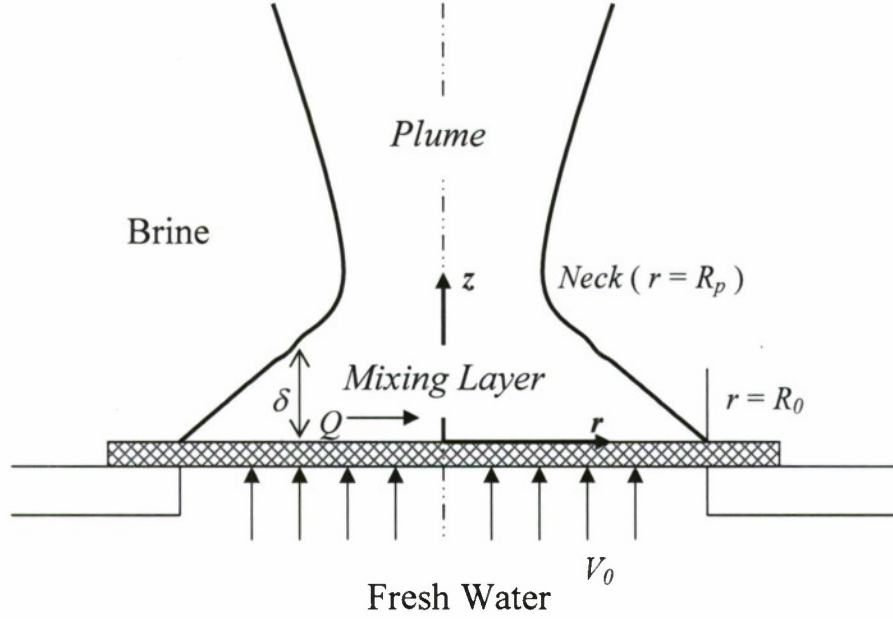


**Figure 4-10. Schematic diagram and selected notation for the experimental setup of Epstein and Burelbach (2001); remote tank boundaries are not shown.**

The theoretical approach followed by Epstein and Burelbach (2001) is based on a number of scaling assumptions and similitude arguments. It also applies to low densimetric Froude numbers  $F = V_0 \{g R_0 (\rho_\infty - \rho_0) / \rho_\infty\}^{-1/2}$  for the distributed source. A recent examination of the mixing layer equations showed that the low Froude number assumption could mathematically be relaxed and that closed-form equations could still be derived (Nihous, 2009). Omitting details, the mixing layer thickness  $\delta$  and average salt mass fraction in the mixing layer  $\bar{Y}$  were obtained as:

$$\delta = R_0 [3F^{2/3} (\frac{1-\eta^2}{\eta})^{2/3} + 6^{3/2} \beta^2 (\frac{1-\eta^2}{\eta})] \quad (4.32)$$

$$Y_\infty - \bar{Y} = \frac{Y_\infty}{3 + \frac{6^{3/2} \beta^2}{F^{2/3}} (\frac{1-\eta^2}{\eta})^{1/3}} \quad (4.33)$$

It can be verified that in the limit  $F \rightarrow 0$ , the published results are recovered, except that the apparent singularity for  $\bar{Y}$  at  $r = R_0$  ( $\eta = 1$ ) is now lifted and replaced with the anticipated finite value  $2Y_\infty/3$  corresponding to  $Y(R_0, 0) = 0$  (freshwater).

At this juncture, a puzzling question arose given that the Froude numbers for the experiments are not small enough for Equation (4.32) to match the experimental data (cf. Table 4-4); the range for  $F$  is also too wide to simply redefine the constant  $\beta$  estimated by Epstein and Burelbach (2001) to be 0.14. In other words, a relaxation of one model assumption (i.e., a more exact boundary condition) led to a mismatch between theory and experiment. There is no obvious explanation why the low-Froude-number limit apparently performs better than a more complete solution at moderate values of  $F$ . To further investigate this issue, numerical simulations of the experiments were undertaken. The approach adopted is to use sufficiently fine finite-element grids to resolve the buoyancy-driven production of kinetic energy (and the associated ‘large’ eddies). Turbulence then can be represented by the relatively simple Smagorinsky model based on a balance between shear-driven production and dissipation of subgrid-scale kinetic energy. Large eddy simulation (LES) has become a widespread method for numerical investigations of turbulent fluid flows, especially since computers have become more powerful (Lesieur and Metais, 1996; Alendal and Drange, 2001; Pesteanu and Schwerdtfeger, 2003; Felten *et al.*, 2004).

**Table 4-4. Experimental and simulation parameters.**

Experiment #	1	2	3	4	5	6
$R_0$ (m)	0.0572	0.0572	0.114	0.114	0.114	0.178
$V_0$ (m s <sup>-1</sup> )	0.0200	0.0270	0.0021	0.0054	0.0084	0.0066
$Y_\infty$	0.087	0.141	0.169	0.146	0.122	0.136
$F$	0.113	0.120	0.006	0.017	0.028	0.017
$Y$ at transition ( $\pm 0.001$ )	0.083	0.135	0.162	0.140	0.117	0.130
Simulation time (s)	10	7	12	12	11	16
Snapshot range in Figure 2 (every second)	5-10	6-7	9-12	6-12	5-11	8-13

To make calculations practical on a single-processor computer, the fluid domain under consideration and the velocity and salt concentration fields were assumed to be axisymmetric about the vertical axis through the center of the buoyancy source. Accordingly, the tangential velocity  $u_\theta$  and partial derivatives  $\partial/\partial\theta$  are identically set to zero henceforth. This choice is consistent with the circular geometry of the buoyancy source, but not with the rectangular footprint of the tank used in the experiments. The overall horizontal area of the tank ( $0.66 \text{ m}^2$ ), however, was deemed large enough ( $\gg \pi R_0^2$ ) to preclude side-wall effects so that the precise shape of the outer boundaries should not be important. The assumption of axisymmetric flow and concentrations seems reasonable, in an average sense at least, for this particular problem, but it can be questioned in principle since turbulence is inherently asymmetric at a given time. Axisymmetric problems have been considered before as computationally efficient shortcuts for full three-dimensional configurations (Mahalingam *et al.*, 1990; Mell *et al.*, 1996). More recently, axisymmetric turbulence alone has been used in otherwise three-dimensional formulations (Jacques *et al.*, 2002; Randriamampianina *et al.*, 2004). Within the axisymmetric

fluid domain of radius 0.45 m and height 0.75 m closely representative of the experimental tank, the following coupled partial differential equations are solved:

$$\nabla \cdot \vec{u} = 0 \quad (4.34)$$

$$\rho \frac{\partial \vec{u}}{\partial t} + \rho(\vec{u} \cdot \nabla) \vec{u} = \nabla \cdot (-P[I] + \mu[\nabla \vec{u} + (\nabla \vec{u})^T]) + \vec{F} \quad (4.35)$$

$$\frac{\partial Y}{\partial t} + \vec{u} \cdot \nabla Y = \nabla \cdot (D \nabla Y) \quad (4.36)$$

The first two are the incompressible Navier-Stokes equations, and the third the advection-diffusion equation for salt.  $[I]$  is the identity tensor and  $\nabla$  the Nabla operator. The fluid velocity vector  $\vec{u}$  has two components  $u_r$  and  $u_z$  in the radial and vertical directions. To further simplify the analysis, water density  $\rho$  is taken as a constant ( $\rho_0 = 1000 \text{ kg/m}^3$ ) except in the body force  $\vec{F}$  (Boussinesq approximation);  $\vec{F}$  has no radial component, but its vertical component is equal to  $\rho_0 g k(Y_\infty - Y)$ . In this simplified formulation, hydrostatic pressure and background weight cancel out so that  $P$  is interpreted as the remaining dynamic pressure.  $\mu$  is the dynamic viscosity and is the sum of a molecular term and of a turbulent (subgrid) expression discussed further below; this formalism is representative of first-order turbulence closure schemes where Reynolds stresses are parameterized.

Initial conditions at  $t = 0$  are  $\vec{u} = \vec{0}$ ,  $P = 0$  and  $Y = Y_\infty$ . Boundary conditions for the Navier-Stokes equations are  $\vec{u} = \vec{0}$  along the outer wall and on the bottom for  $r > R_0$  (no slip), and  $\vec{u} = (0, V_0)$  on the bottom for  $r \leq R_0$  (water injection); the upper free surface is simplified as a rigid lid subject to the slip condition  $u_z = 0$ , and outflow is allowed to occur at  $P = 0$  along the upper 5 cm of the outer vertical wall. All boundaries are insulated as far as salt transfer is concerned, except for the small outflow segment where a convective flux (zero gradient) is enforced. The kinematic viscosity  $\nu = \mu/\rho \approx \mu/\rho_0$  is the sum of a molecular term  $\nu_0 = \mu_0/\rho_0$ , of the order of  $10^{-6} \text{ m}^2 \text{ s}^{-1}$ , and of a turbulent term  $\nu_{SM}$  defined as follows for this axisymmetric problem:

$$\nu_{SM} = (c_{SM} h)^2 \sqrt{2[(\frac{\partial u_r}{\partial r})^2 + (\frac{\partial u_z}{\partial z})^2 + (\frac{u_r}{r})^2] + (\frac{\partial u_r}{\partial z} + \frac{\partial u_z}{\partial r})^2} \quad (4.37)$$

$h$  is interpreted as an average finite-element mesh size, and  $c_{SM}$  is the Smagorinsky constant which can be related to the Kolmogorov constant  $c_K$  as  $(3c_K/2)^{-3/4}/\pi$  (Lesieur and Metais, 1996).  $c_{SM}$  is selected here as 0.1; this value is consistent with choices in the technical literature (Lesieur and Metais, 1996; Alendal and Drange, 2001; Pesteanu and Schwerdtfeger, 2003) and corresponds to a Kolmogorov constant when anisotropy and acceleration fluctuations significantly contribute to the energy budget (Heinz, 2002). Following a parameterization based on renormalization group theory, the overall diffusivity  $D$  can then be obtained by solving an implicit equation for the ratio  $D/\nu$  (Yakhot and Orszag, 1986). A close explicit approximation was derived instead, to avoid the numerical burden of an implicit equation:

$$D = \nu [1.3929 - (1.3929 - \frac{\alpha}{\nu_0})(\frac{\nu_0}{\nu})^{1.78}] \quad (4.38)$$



Without turbulence,  $\nu = \nu_0$  and  $D$  would be equal to the molecular diffusivity  $\alpha$  (about  $1.5 \times 10^{-9} \text{ m}^2 \text{ s}^{-1}$  for salt); in very turbulent areas ( $\nu \gg \nu_0$ ),  $D \approx 1.3929\nu$ .

The six physical experiments conducted by Epstein and Burelbach (2001) were numerically simulated. A commercial finite-element package (FEMLAB<sup>®</sup> 3, Version 3.1, 2003) was used to solve Equations (4.34) through (4.38) subject to the initial and boundary conditions discussed earlier. No artificial diffusion was added and the software's general solution form was selected. Default settings and options were adopted as much as possible, including the direct linear solver UMFPACK (based on the unsymmetric-pattern multifrontal method and direct LU factorization). The parameters  $R_0$ ,  $V_0$  and  $Y_\infty$  defining each experiment are listed in Table 4-4. Numerical grids of about 25,000 elements corresponding to an average mesh size  $h$  of the order of 5.7 mm were used; element quality was higher than 0.5. Results obtained at such spatial resolution were found to be insensitive to further grid refinement. Simulation times varied between 7 and 16 s depending on the convergence rate (cf., Table 4-4); this corresponded to computer runtimes of several hours (1.86 GHz processor with 2 GB RAM). In all cases, turbulent viscosity was activated after a simulation time of 0.1 s. A quasi steady-state for the mixing boundary layer seemed to be reached rapidly ( $t$  of the order of 4 to 6 s); because of highly turbulent conditions, this was estimated visually from 1-second solution snapshots of the salt mass fraction. Figure 4-11 shows sample calculated values of the salt mass fraction for Experiment No. 6 at  $t = 12$  s, with arrows representing the velocity field.

For each set of numerical simulations, points where  $Y$  was within 0.001 of a salinity threshold approximately equal to  $0.96 Y_\infty$  (cf., Table 4-4) were used to track the edge of the mixing boundary layer at low vertical coordinates. Figure 4-12 shows 32 snapshots of those 'boundary points' from all simulations (every second in the time intervals listed in Table 4-4). Time intervals for the data in Figure 4-12 were selected without the first few seconds (transient phase), and in the case of Experiment No. 6, without the period between 13 and 16 s where eddies detached from the rising plume somewhat obscured the edge of the mixing boundary layer below. Also shown as thick lines are the fundamental results from Epstein and Burelbach (2001): the normalized boundary-layer thickness from Equation (4.32) with  $F = 0$  and  $\beta = 0.14$ ; and a vertical line (of arbitrary height) marking the plume transition at  $R_p = 0.43 R_0$ . Given the highly turbulent nature of the flows and the absence of any time averaging in constructing Figure 4-12, the agreement between numerical simulations and the low-Froude-number analysis is remarkable. Figure 4-13 is a plot of the time-averages of the salt mass fraction for Experiment No. 6 between 6 and 16 s when they fall below 0.130. As expected, time averaging strongly smoothes the highly irregular solution.

#### Mixing Layer Simulation Summary

This study performed a critical evaluation of a published theoretical and experimental investigation of vertical mixing above a circular source of buoyancy. Normalized data showing the existence of a mixing boundary layer that is independent of several experimental parameters could be reproduced well with axisymmetric large-eddy numerical simulations. This lent additional credibility to the theoretical boundary-layer analysis of Epstein and Burelbach (2001), even though relaxing some of their model's assumptions failed to preserve a good agreement between theory and experiments given the range of Froude numbers under consideration.

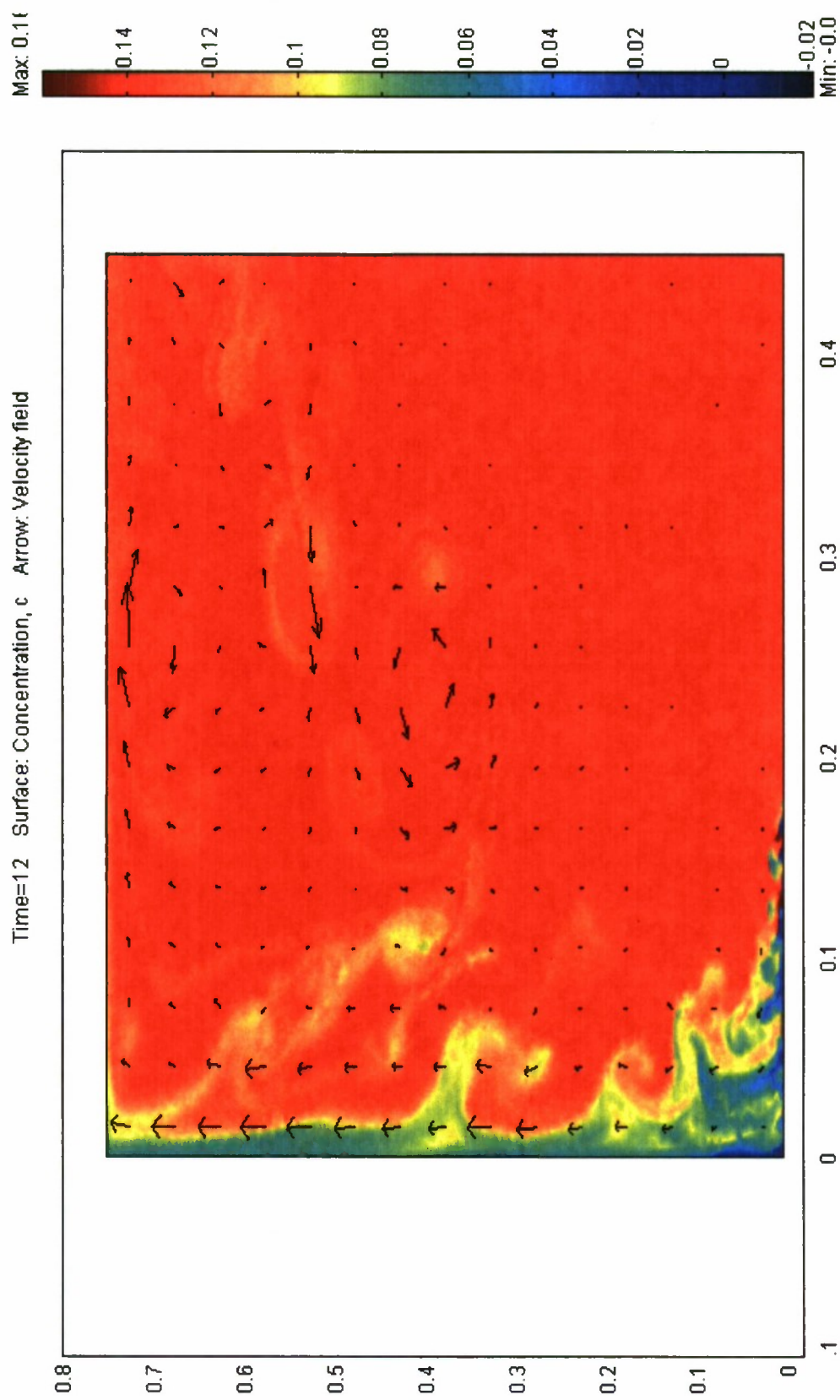


Figure 4-11. Snapshot of LES calculations of salt mass fraction for Experiment # 6 at  $t = 12$  s (axis dimensions in meters).

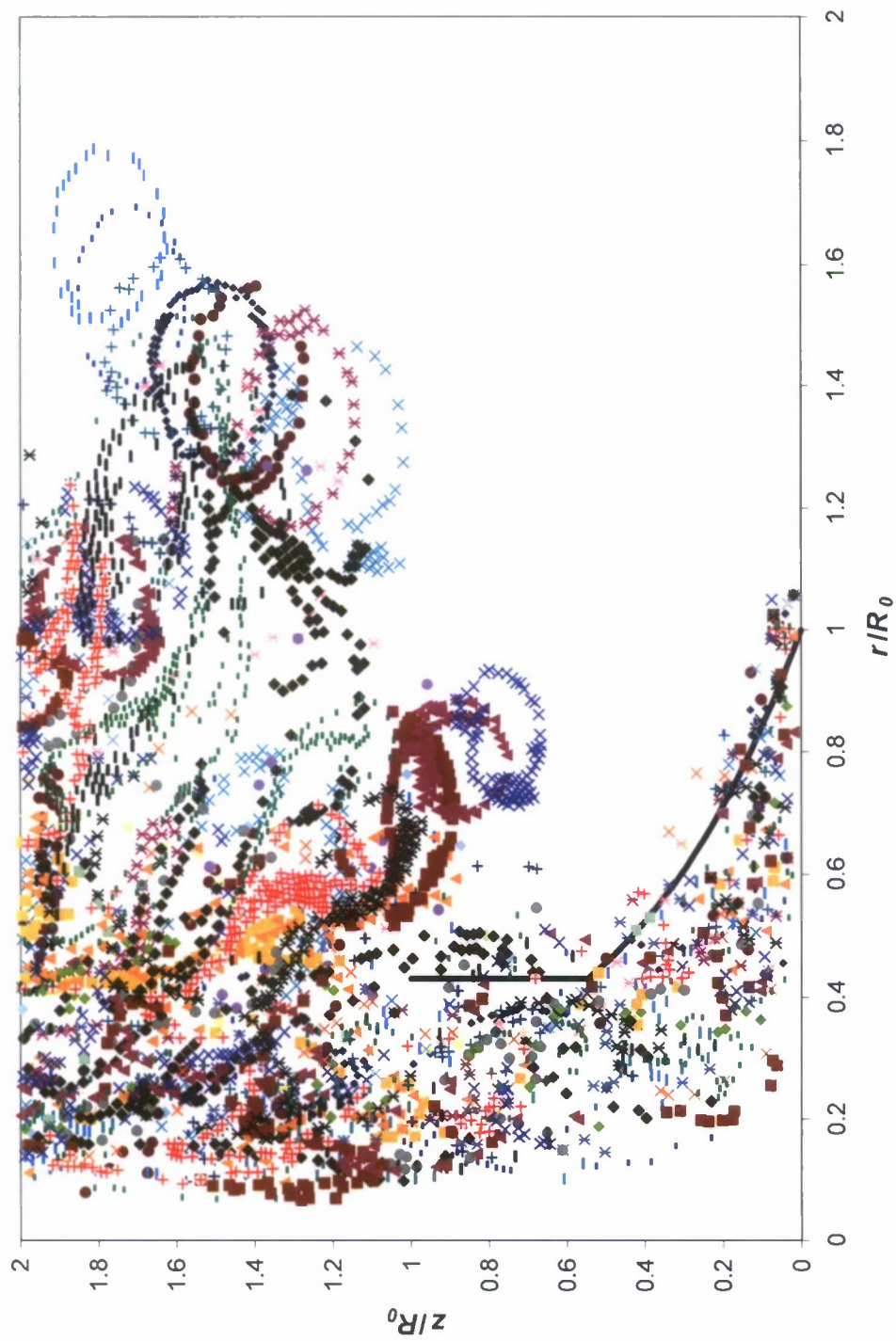


Figure 4-12. Selected snapshots of calculated salt-mass-fraction transitions for all simulated experiments (cf., Table 4-4).



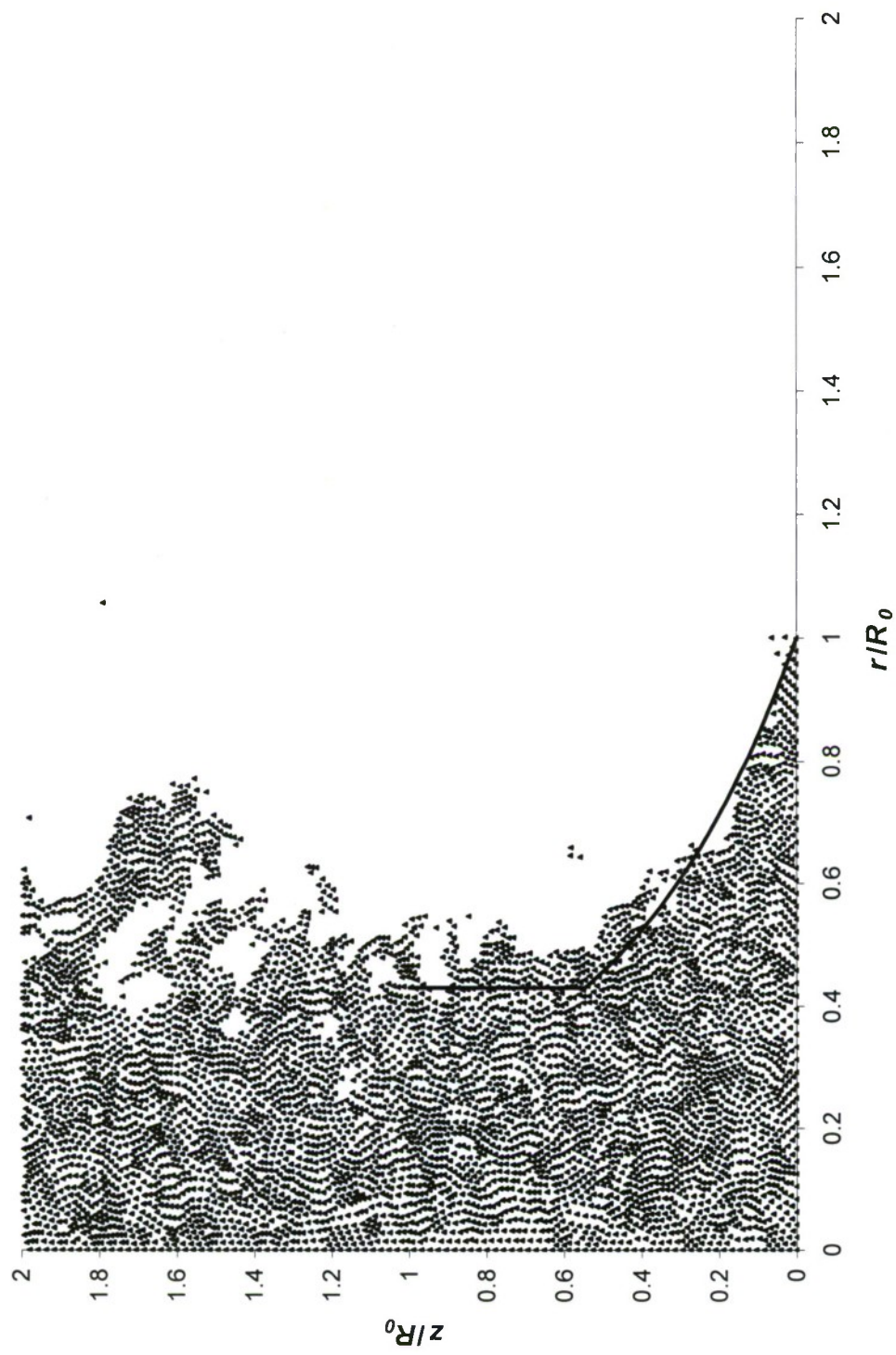


Figure 4-13. Time averages (from 6 s to 16 s) of calculated salt mass fractions for Experiment No. 6: values below 0.130.

## Notation

$C_K$	Kolmogorov constant
$C_{SM}$	Smagorinsky constant (0.1)
$D$	turbulent diffusivity ( $\text{m}^2 \text{s}^{-1}$ )
$E$	dispersion coefficient for vertical mixing ( $\text{m}^2 \text{s}^{-1}$ )
$E_0$	entrainment coefficient for plume (0.12)
$F$	densimetric Froude number; $V_0\{gR_0(\rho_\infty-\rho_0)/\rho_\infty\}^{-1/2}$
$g$	gravitational acceleration ( $\text{m s}^{-2}$ )
$h$	finite-element grid size (m)
$k$	constant of proportionality between water density and salt concentration (0.64)
$l$	characteristic mixing length for turbulent diffusion (m)
$P$	pressure (Pa)
$Q$	inward volume flux within mixing layer ( $\text{m}^3 \text{s}^{-1}$ ); $2\pi r \delta \bar{u}$
$Q_p$	volume flux from mixing layer into rising plume ( $\text{m}^3 \text{s}^{-1}$ )
$r$	radial coordinate (m)
$R_0$	radius of source of buoyant fluid (m)
$\vec{u}$	velocity vector ( $\text{m s}^{-1}$ )
$\bar{u}$	average radial inward velocity in mixing boundary layer ( $\text{m s}^{-1}$ )
$V_0$	upward velocity of injected fluid (m)
$Y$	salt mass fraction
$Y_p$	average salt mass fraction at plume neck
$\bar{Y}$	average salt mass fraction in mixing boundary layer
$z$	vertical coordinate (m)

## Greek letters

$\alpha$	molecular salt diffusivity ( $\text{m}^2 \text{s}^{-1}$ )
$\beta$	mixing-length thickness proportionality coefficient (0.14)
$\delta$	vertical thickness of mixing boundary layer (m)
$\eta$	non-dimensional radial coordinate
$\mu$	dynamic viscosity ( $\text{kg m}^{-1} \text{s}^{-1}$ )
$\mu_0$	molecular dynamic viscosity ( $\text{kg m}^{-1} \text{s}^{-1}$ )
$\nu$	kinematic viscosity ( $\text{m}^2 \text{s}^{-1}$ ); $\nu_0 + \nu_{SM}$
$\nu_0$	molecular kinematic viscosity ( $\text{m}^2 \text{s}^{-1}$ )
$\nu_{SM}$	turbulent kinematic viscosity ( $\text{m}^2 \text{s}^{-1}$ )
$\rho$	water density ( $\text{kg m}^{-3}$ )
$\rho_0$	freshwater density ( $\text{kg m}^{-3}$ )

## Subscript

p	properties at transition from mixing boundary layer to buoyant plume
r	radial direction
z	vertical direction
$\theta$	tangential direction
$\infty$	ambient water

### Hydrate Microbiology

The Hikurangi Margin, offshore New Zealand's North Island east coast is predicted to contain large quantities of gas hydrates, based on the observation of wide-spread bottom simulating reflections (BSRs) (Pecher and Henrys 2003). The Hikurangi Plateau, a large igneous province populated by seamounts, is being subducted at this Margin.

Seafloor sediment cores from regions on the Hikurangi Margin with hydrate accumulations were collected during an international joint oceanographic research cruise between 20 June and 3 July 2006. During this reporting period, molecular investigations of the microbial assemblages in these cores were conducted. Two cores, identified as Nos. 11 and 14, were selected based on their geochemical profiles that exhibited common sulfate and methane distributions and a pronounced sulfate methane interface (SMI). Figures 4-14 and 4-15 present the methane, sulfate, sulfide, and DIC (dissolved inorganic carbon) profiles in these cores. The cores were profiled using a DNA extraction method developed by Corinaldesi *et al.* (2005) and qualitatively PCR amplified for the presence and distribution of specific groups of microorganisms (Table 4-5). Positive PCR amplification was observed by gel electrophoresis for both intracellular and extracellular fractions, as indicated in Tables 4-6 and 4-7.

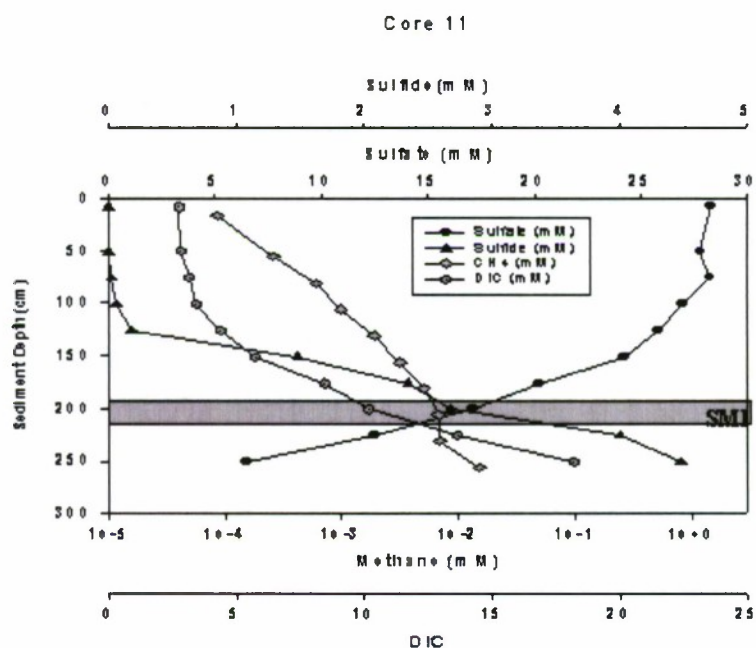


Figure 4-14. Geochemical profiles for New Zealand Hikurangi Margin core No. 11. The grey box identifies the SMI.



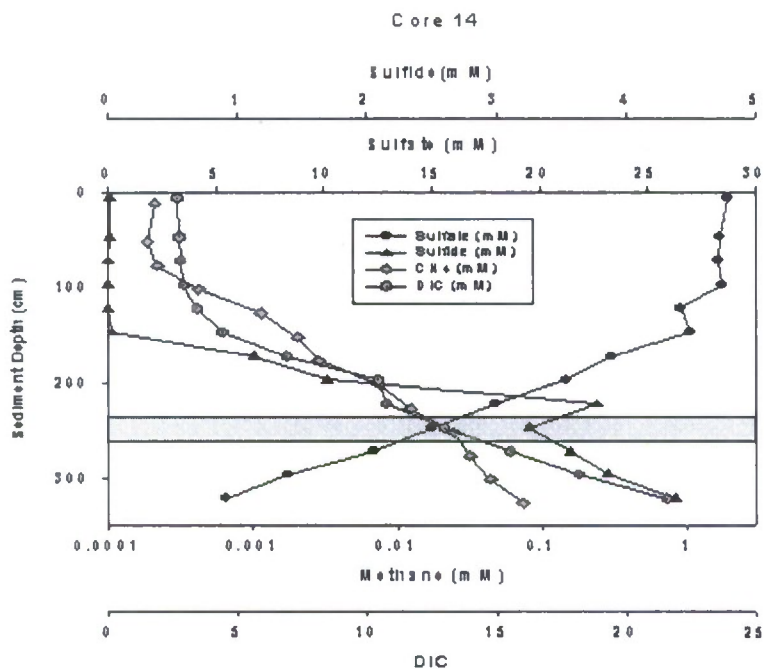


Figure 4-15. Geochemical profiles for New Zealand Hikurangi Margin core No. 14. The grey box identifies the SMI.

Table 4-5. PCR primers for specific microbial groups associated with methane hydrates.

Primer list	Forward	Reverse
Bacteria (Lane <i>et.al.</i> 1991)	27F	1492R
Archaea (DeLong, 1992)	21F	958R
Sulfate Reducing Bacteria (Wagner <i>et.al.</i> 1998)	Dsr1F	Dsr4R
Methanogen (Marchesi <i>et.al.</i> 2001)	146F	1324R
Methanotroph I (Wise <i>et.al.</i> 1999)	MethT1dF	MethT1bR
Methanotroph II (Wise <i>et.al.</i> 1999)	27F	MetT2R

Table 4-6. PCR amplification results for 7 different sections of core No. 11.

Core section DNA extracts from cellular fraction (c)  
and extracellular fraction (ex)

Primer specificity	50c/ex	80c/ex	105c/ex	155c/ex	180c/ex	205c/ex	260c/ex
<i>Bacteria</i>	X / X	X / X	X / X	X / X	X / X	X / X	X / X
<i>Archaea</i>	O / X	O / X	O / O	O / X	O / O	X / O	O / X
Methanogen	O / O	O / X	O / X	O / X	O / X	O / X	O / X
Sulfate Reducing Bacteria	O / O	O / X	O / X	O / X	O / X	O / X	O / X
Methanotroph Type I	O / X	O / X	O / X	O / X	O / X	O / X	O / X

Notes: Positive amplification (X); negative amplification (O).

**Table 4-7. PCR amplification results for 8 different sections of core No. 14.****Core section DNA extracts from cellular fraction (c)  
and extracellular fraction (ex)**

Primer specificity	50c/ex	75c/ex	100c/ex	125c/ex	150c/ex	200c/ex	225c/ex	260c/ex
<i>Bacteria</i>	X / X	X / X	X / X	X / X	X / X	X / X	X / X	X / X
<i>Archaea</i>	O / O	O / O	O / O	O / O	O / O	O / X	O / X	O / X
Methanogen	O / O	O / O	O / O	O / O	O / X	O / X	O / X	O / X
Sulfate Reducing Bacteria	O / O	O / O	O / O	O / O	O / O	O / X	O / X	O / X
Methanotroph Type I	O / O	O / O	O / O	O / O	O / O	O / X	O / X	O / X

Notes: Positive amplification (X); negative amplification (O).

DNA was amplified using published PCR primer sets targeting 16S rDNA, methanogenic, methanotrophic, and the sulfate-reducing communities. Positive PCR amplification was observed by gel electrophoresis for all of the core sections when using the general 16SrDNA primers for both intracellular and extracellular fractions. The intracellular DNA could not be amplified using any of the other specific primer sets. The amplification of the methanotrophic and sulfate-reducing bacteria DNA was not unusual and appear to correlate with the individual core geochemical profiles. Higher levels of methane existed throughout core No. 11 and methanogens were detected in all sections with the exception of the uppermost section. Sulfide production becomes geochemically apparent between 80-100 cmbsf and sulfate-reducing bacteria appear to be present in this region. Core No. 14 displayed a similar trend where methanogen and sulfate reducer presence can be explained by methane and sulfide concentrations. The amplification of specific targets only in the extracellular fraction suggests either that concentrations of these targets are too low or that the preservation techniques employed were not adequate given the time elapsed from sample collection to DNA extraction. Furthermore, observed preservation of DNA in sediments does raise concerns about the accuracy of current molecular DNA profiling methods for sediments. Extracellular DNA may be responsible for the generation of incorrect community profiles. This phenomenon needs to be investigated further.

The positive PCR amplification of methanotrophic targets in anoxic sediment slices for both cores was interesting. While the amplification was rather weak and difficult to reproduce – with nonspecific banding occurring – bands with the appropriate target size were nevertheless obtained. Ten core sections showed successful methanotroph amplification. The PCR products were cleaned by gel excision using a Qiaquick gel extraction kit from Qiagen. The PCR product was then used for DNA cloning using a TOPO TA cloning kit from Promega with ampicillin. The cloning reaction produced sufficient colonies for selection and approximately ten from each of the reactions were sampled (90 clones total). Plasmid extraction was performed using a Qiaprep spin miniprep kit from Qiagen. Plasmid isolates were re-amplified using the methanotroph-specific primers and visualized by gel electrophoresis prior to DNA sequencing. Re-amplified clone DNA samples from each of the ten sediment samples were sent out for DNA sequencing. The first five core samples produced sequences with sufficient quality for database comparison using Entrez Pubmed BLAST. It initially was believed that the positive PCR amplifications could be a result of DNA preservation in the extracellular environment and

sediment deposition, or the presence of a closely related species of bacteria with anaerobic methanotrophic ability. Unfortunately, disappointing sequencing results were obtained. While the published primers were suitable for amplification of methanotrophic bacteria, our results indicate a non-specificity for a psychropiezophilic bacteria belonging to the Genus *Psychromonas*. The preferable growth conditions of this species of bacteria suggest that it is a resident of the sediment community, but is unlikely to be associated with methane cycling.

Community distributions determined with cloning data from core No. 11 was investigated. DNA extraction was performed using a commercially available kit (MoBio) for each core section and PCR amplified using *Bacteria* and *Archaea* primers (see Table 4-5). PCR products were cloned using a Promega kit and TOP 10F cells. Plasmid extraction was performed using a Qiaprep spin miniprep kit from Qiagen. Plasmid isolates were re-amplified using the specific primers and visualized by gel electrophoresis prior to DNA sequencing. 58 clones were obtained and the results are shown in the phylogenetic trees presented in Figures 4-16 and 4-17. The clone results did not indicate the presence of a clearly defined ecology that would be unique to methane-hydrate-containing sediments.

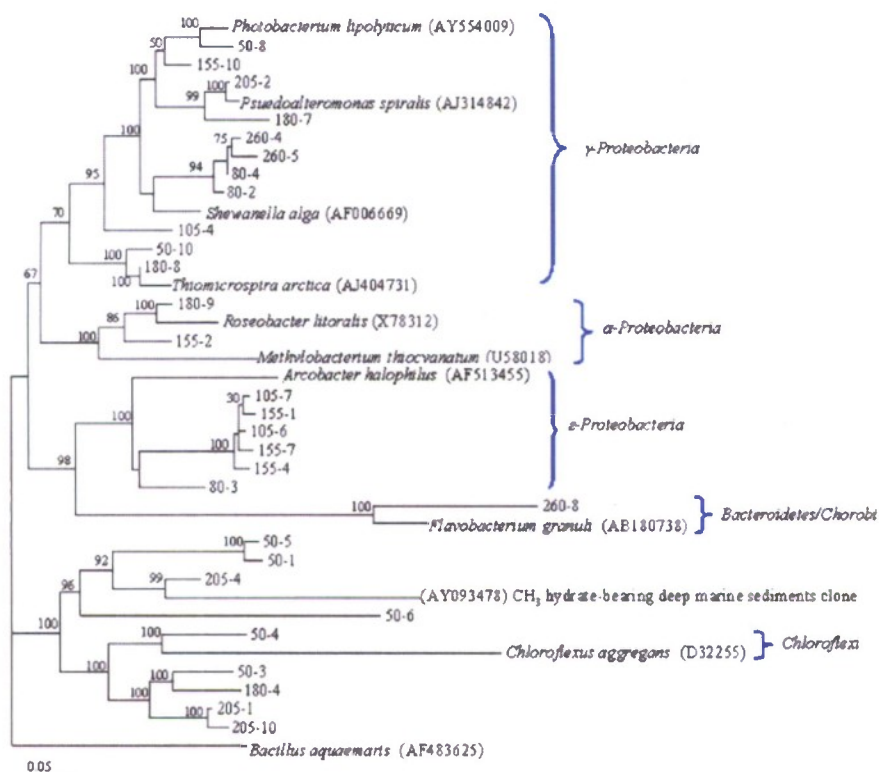
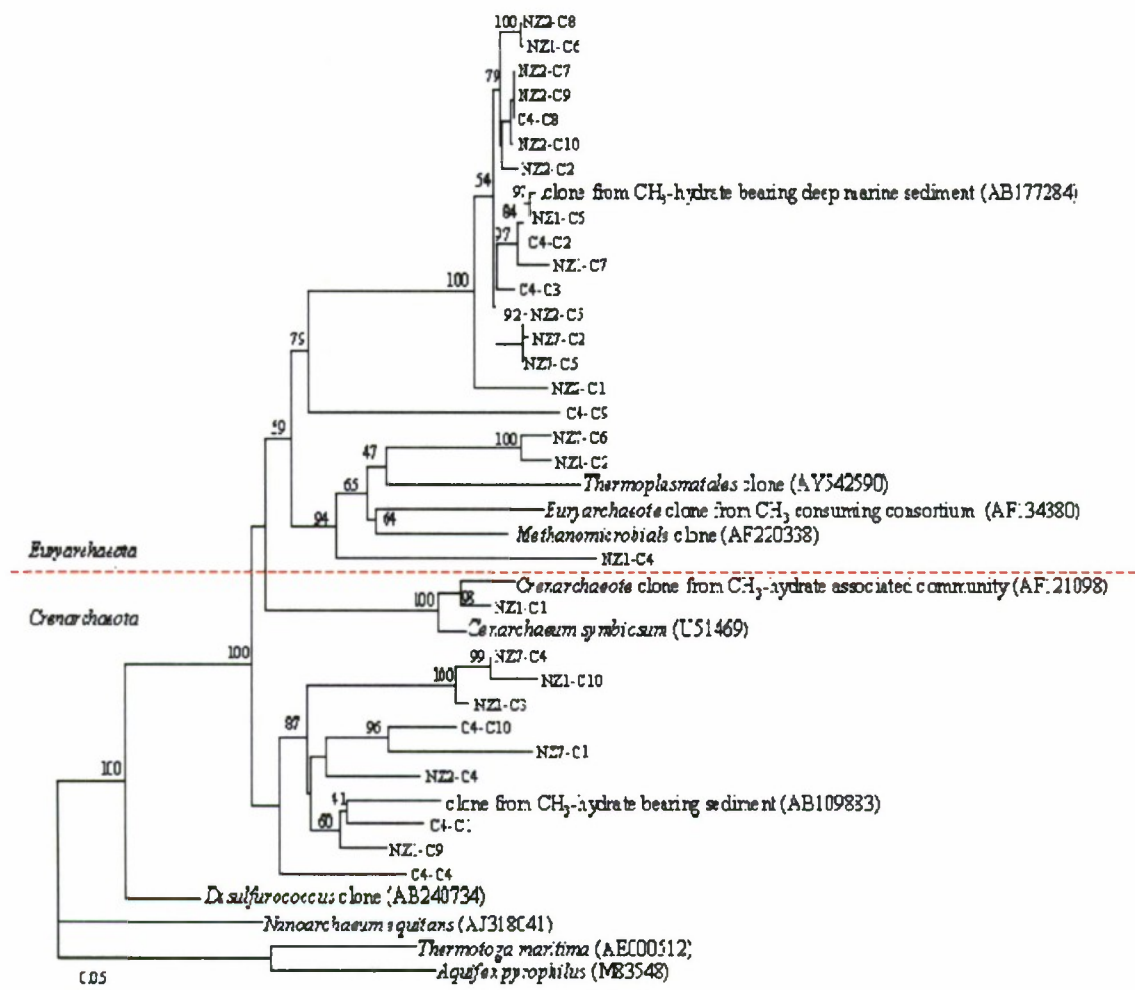


Figure 4-16. A *Bacteria* 16S r DNA phylogenetic tree based on partial sequences obtained from NZ Hikurangi Margin core No. 11 using 27F / 1492R primer pairs. Five distinct clusters are observed. The majority of sequences recovered were Gamma *Proteobacteria* similar to other deep sea sediment environments.





**Figure 4-17. A Archaea 16S r DNA phylogenetic tree based on partial sequences obtained from NZ Hikurangi Margin core No. 11 using 21F/958R primer pairs. The majority of sequences recovered were Euryarchaeota, including Methanosarcinales, Methanobacteriales. Some species of Crenarchaeota, are present, including those that live in high sulfur environments.**

As part of our collaboration with the NRL, a portion of a six-inch push core sampled from a hydrate mound in Barkley Canyon in the Gulf of Mexico was sent frozen to the University of Hawaii for analysis. Barkley Canyon is the site of a cold gas seep with methane hydrate mounds located along an active accretionary margin and sustained by a primary thermogenic gas source. Information on methane and sulfate consumption and production of DIC provided by sediment cores indicate anaerobic oxidation of methane (AOM). A conceptual biogeochemical model for the Barkley Canyon seep system has been proposed based on this information as well data on stable carbon isotopes from dissolved methane hydrate-bound methane, DIC, gas condensate, TOC (total organic carbon), TIC (total inorganic carbon), and authigenic carbonates. Although the primary source of methane is thermogenic, we identified a microbial contribution near the sulfate-methane transition zone (SMT) suggestive of coupled AOM and methanogenesis.

The core sample received from NRL was initially profiled using a DNA extraction method developed by Corinaldesi *et al.* (2005) and qualitatively PCR amplified for the presence and distribution of specific groups of microorganisms (see Tables 4-5 and 4-8). Positive PCR amplification was observed by gel electrophoresis. The *Archaea* community analysis was performed for this core.

**Table 4-8. PCR amplification results for 6 different sections of Barkley Canyon push core.**

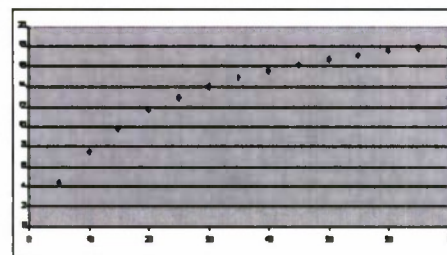
Core section DNA extracts from cellular fraction (c) and extracellular fraction (ex)						
Primer specificity	38c/ex	39c/ex	40c/ex	41c/ex	42c/ex	43c/ex
<i>Bacteria</i>	X / X	X / X	X / X	X / X	X / X	X / X
Methanogen	X / O	X / X	X / X	X / X	X / X	X / X
Sulfate Reducing Bacteria	O / O	X / X	O / O	O / O	X / O	X / O
Methanotroph Type I	O / O	O / O	X / O	X / O	O / O	O / O
Methanotroph Type II	O / O	O / O	O / O	O / O	O / O	O / O

Notes: Positive amplification (X); negative amplification (O).

*Archaea* participate in both the methane production and AOM in hydrate-containing ocean sediments. *Archaeal* groups were specifically emphasized for analysis due to the unique geochemistry of the Barkley Canyon region. DNA extraction for cloning was performed using commercially available kits (MoBio) for each core section and PCR amplified using *Archaea* specific primers (DeLong, 1992). Cloning was performed with a Promega kit using TOP 10F cells with ampicillin selection. When compared with the NCBI database, the 85 recovered clones are closely related to the 17 accession sequences that are listed there. Rarefaction curves and diversity index analysis for the individual core sections as well as from the total for the core suggest that clones were representative of the sections and total sample, and that there is a significant amount of diversity. As shown in Figure 4-18, a species that is known to exist in hydrate-containing sediments was found with high frequency, and another species specifically associated with AOM was detected. A phylogenetic tree using the actual clone sequences currently is being constructed and a manuscript for publication will be prepared with colleagues from NRL.

Finally, as part of this subtask, HNEI researchers participated in another NRL Gulf of Mexico oceanographic hydrate research cruise in July-August 2007. Sediment and pore water samples collected during that cruise were shipped back to the University of Hawaii and currently are undergoing molecular biological analyses and culturing. Results will be reported in the future.

NCBI Accession #	Clone Description	# of clones
AF419625.1	Uncultured Archaeon GBa1r013	9
AF419624.1	Uncultured Archaeon GBa1r010	7
EU246003.1	Uncultured MAT-CR-P1-d06	3
AF354126.1	Uncultured Archaeon SB17a1A11	4
AY835414.2	Uncultured Archaeon 4E12	4
AY592837.1	Uncultured Archaeon Milano WF2A-12	7
AJ578118.1	Uncultured Archaeon HydBeg22	29
AF419644.1	Uncultured Archaeon C1_R048	4
AB019759.1	Unidentified Archaeon pISA14	4
AY592843.1	Uncultured Archaeon Milano-WF2A-19	3
AF134381.1	Uncultured Archaeon BA1a2	1
AJ578134.1	Uncultured Archaeon BS-S-D7	1
AJ890142.1	Uncultured Archaeon fos0626f11	2
EF484913.1	Uncultured ANME DGGE ANME-40	2
AJ578140.1	Uncultured Archaeon BS-SR-C1-Arch	3
AF134387.1	Uncultured Archaeon TA1a9	1
AJ578084.1	Uncultured Archaeon HydBeg01	1
Total		85



Rarefaction curve of sampled clones using *Archaea* specific primers

Simpson's Diversity Index = 0.145  
Simpson's Index of Diversity = 0.855  
Simpson's Reciprocal Index = 6.89

**Figure 4-18. Cloning results for Barkley Canyon push core No. R696-C1 using *Archaea* primers 21F/958R. Diversity index indicates relatively high species diversity, and rarefaction curves suggest sufficient cloning.**

#### 4.3.4 Hydrate Engineering Applications

As a precursor to studies of hydrate gas purification, work was initiated during the present reporting period to test the performance of the Raman calorimeter and confirm our laboratory protocols in applications involving hydrates formed from gas mixtures. As a first step, we examined a simple mixture of 10% (by volume) ethane (C<sub>2</sub>H<sub>6</sub>) in methane.

Following the general procedures employed to synthesize pure methane hydrate, the calorimeter sample cell was loaded with approximately 3 g of fine ice crystals (< 212 μm). The cell was closed and inserted into the calorimeter well cooled to -15 °C. It was then purged twice using the vacuum pump and dry N<sub>2</sub> gas. A Raman spectrum of the ice sample in the cell under 0.035 MPa (5 psig) of N<sub>2</sub> is shown in Figure 4-19.

The sample cell was then pressurized to 7.0 MPa (1000 psig) using the 10% ethane-90% methane gas mixture and another Raman measurement was performed. Figure 4-20 presents the spectrum in which the ethane gas peaks at 2900 cm<sup>-1</sup> and 2955 cm<sup>-1</sup> (Subramanian *et al.*, 2000) are visible along with the methane peak at 2917 cm<sup>-1</sup> (Subramanian & Sloan, Jr., 1999). As expected, the intensities of the ethane peaks are low due to the smaller concentration of that gas.



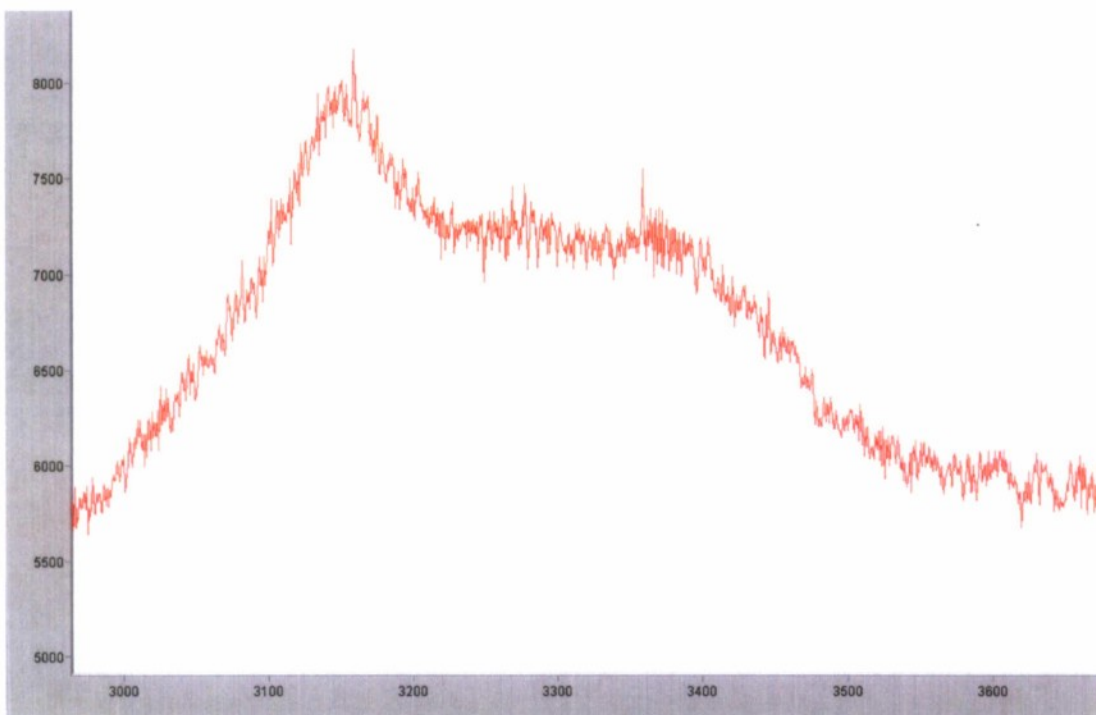


Figure 4-19. Raman spectrum of ice sample under nitrogen gas at 0.035 MPa (5 psig) and -15 °C.

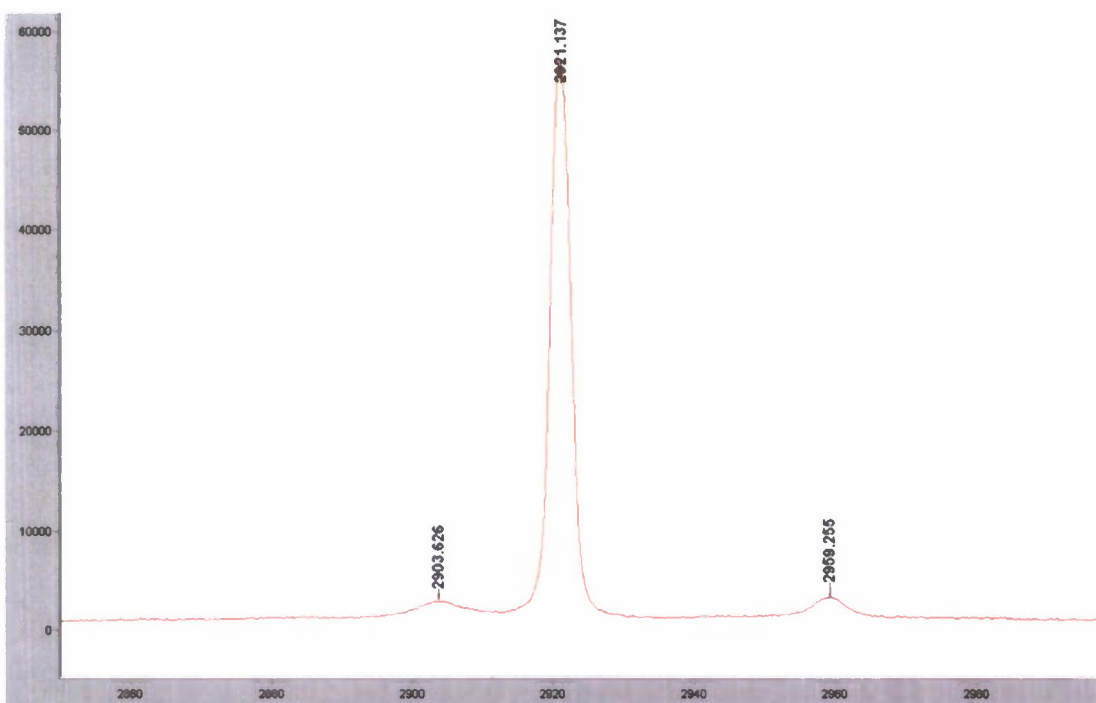
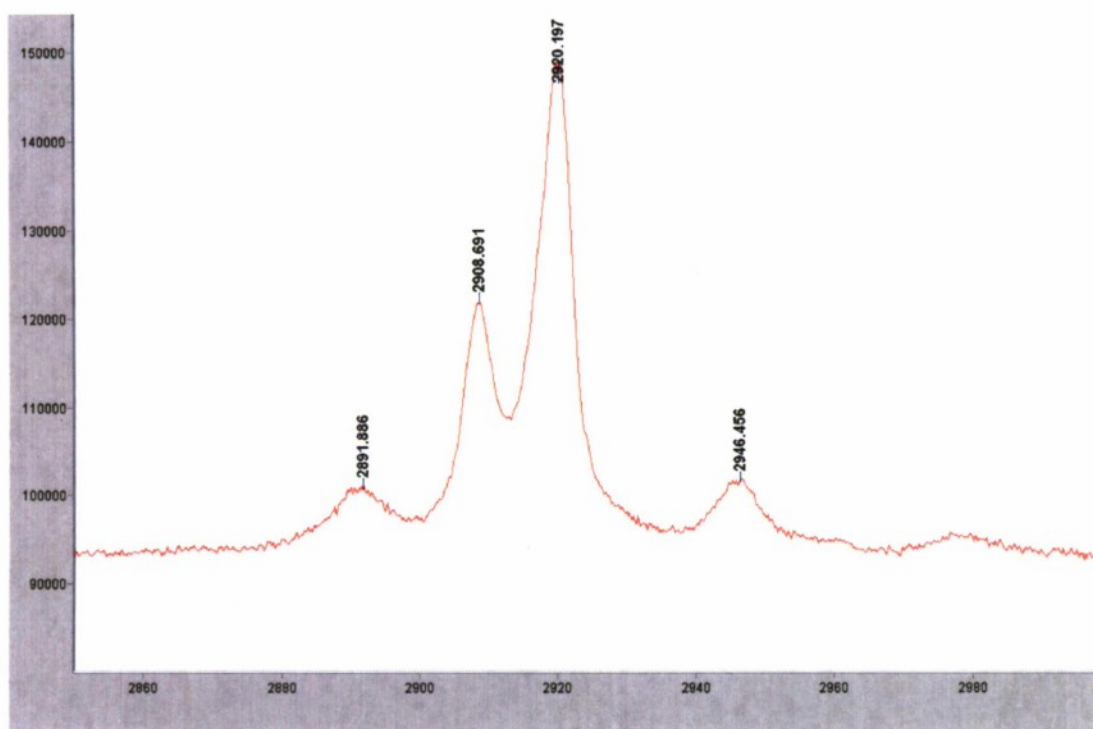


Figure 4-20. Raman spectrum at -15 °C and 7.0 MPa (1000 psig). The peak at 2921  $\text{cm}^{-1}$  corresponds to  $\text{CH}_4$ ; the peaks at 2959  $\text{cm}^{-1}$  and 2903  $\text{cm}^{-1}$  correspond to  $\text{C}_2\text{H}_6$ .

At 7.0 MPa, the temperature of the calorimeter was increased from  $-15^{\circ}\text{C}$  to  $5^{\circ}\text{C}$  at a rate of  $0.1^{\circ}\text{C}/\text{min}$ . The calorimeter was then held at  $5^{\circ}\text{C}$ , which is above the melting point of ice but below the freezing point of methane-ethane hydrate, for about 12 hours. After 12 hours, Raman data were collected to determine if methane-ethane hydrate had formed. As seen in Figure 4-21, the measured spectrum exhibits four distinct peaks. Subramanian and Sloan, Jr. (1999) observed a Raman shift of  $2904.8\text{ cm}^{-1}$  by methane encaged in the cavities of pure sl methane hydrate. Subramanian *et al.* (2000) observed a Raman shift of  $2891\text{ cm}^{-1}$  and  $2946\text{ cm}^{-1}$  by ethane encaged in the cavities of pure sl ethane hydrate. Ohno *et al.* (2009) detected ethane hydrate peaks at  $2889\text{ cm}^{-1}$  and  $2945\text{ cm}^{-1}$ . These values correspond well to three of the four peaks in Figure 4-21, with the fourth at  $\sim 2920\text{ cm}^{-1}$  arising from residual methane gas. The weak ethane gas peaks overlap with and are obscured by those of the ethane hydrate. The Raman measurements therefore seem to confirm the formation of a mixed gas hydrate.



**Figure 4-21.** Raman spectrum at  $5^{\circ}\text{C}$  and 6.8 MPa (985 psig). The peak at  $2920\text{ cm}^{-1}$  is due to methane gas; the peak at  $2908\text{ cm}^{-1}$  corresponds to methane hydrate; and the peaks at  $2946\text{ cm}^{-1}$  and  $2891\text{ cm}^{-1}$  are due to ethane hydrate.

To dissociate the hydrate, the temperature of the calorimeter was increased from  $5^{\circ}\text{C}$  to  $25^{\circ}\text{C}$  at a rate of  $0.05^{\circ}\text{C}/\text{min}$ . Raman spectra obtained as the hydrate decomposed are shown in Figures 4-22, 4-23, and 4-24. The peaks associated with the methane and ethane hydrate are observed to disappear as the ethane gas peaks re-emerge. The strength of the methane hydrate signal appears to decline much faster than the ethane hydrate peaks. This is not unexpected since, at the same pressure, ethane hydrate is stable at higher temperatures than methane hydrate.

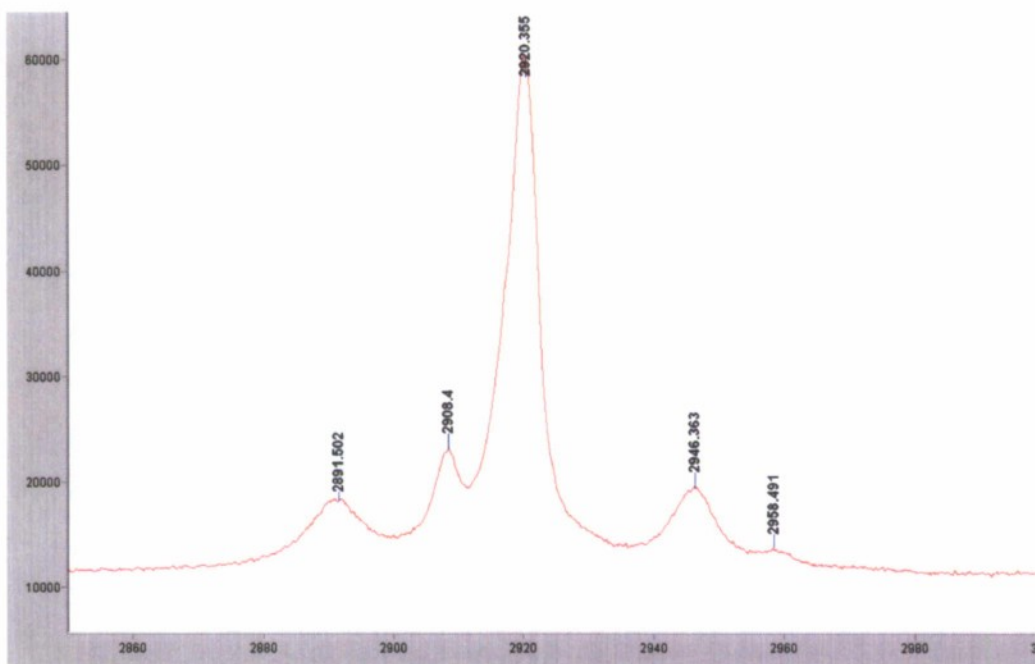


Figure 4-22. Raman spectrum at 16°C and 6.8 MPa (985 psig) showing a reduction of the methane and ethane hydrate peaks at 2908  $\text{cm}^{-1}$ ; and 2891  $\text{cm}^{-1}$  and 2946  $\text{cm}^{-1}$ , respectively. The peak at 2958  $\text{cm}^{-1}$  corresponding to ethane gas has become more visible. The peak at 2920  $\text{cm}^{-1}$  is due to methane gas.

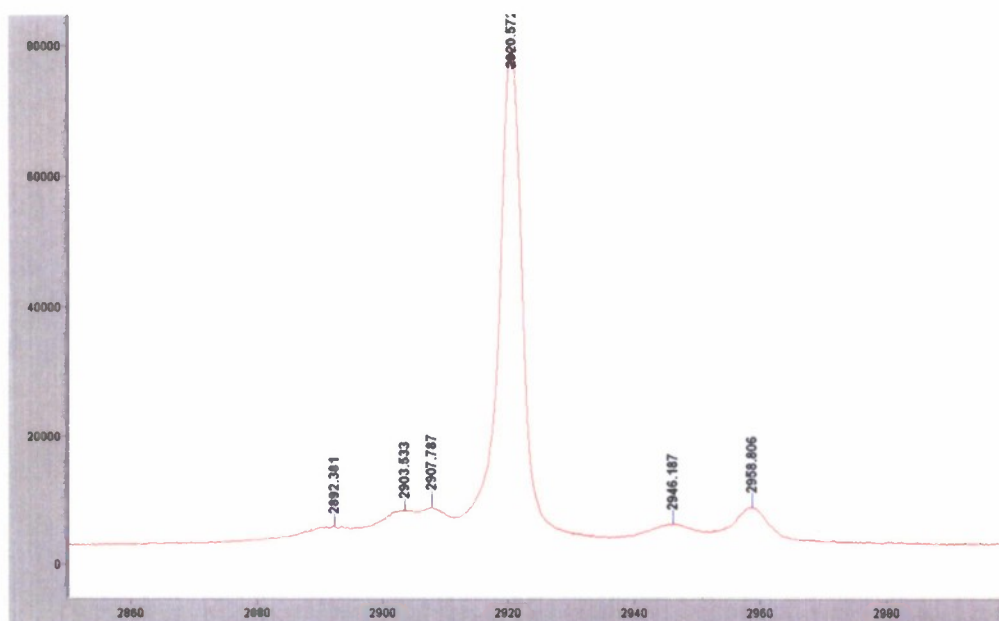
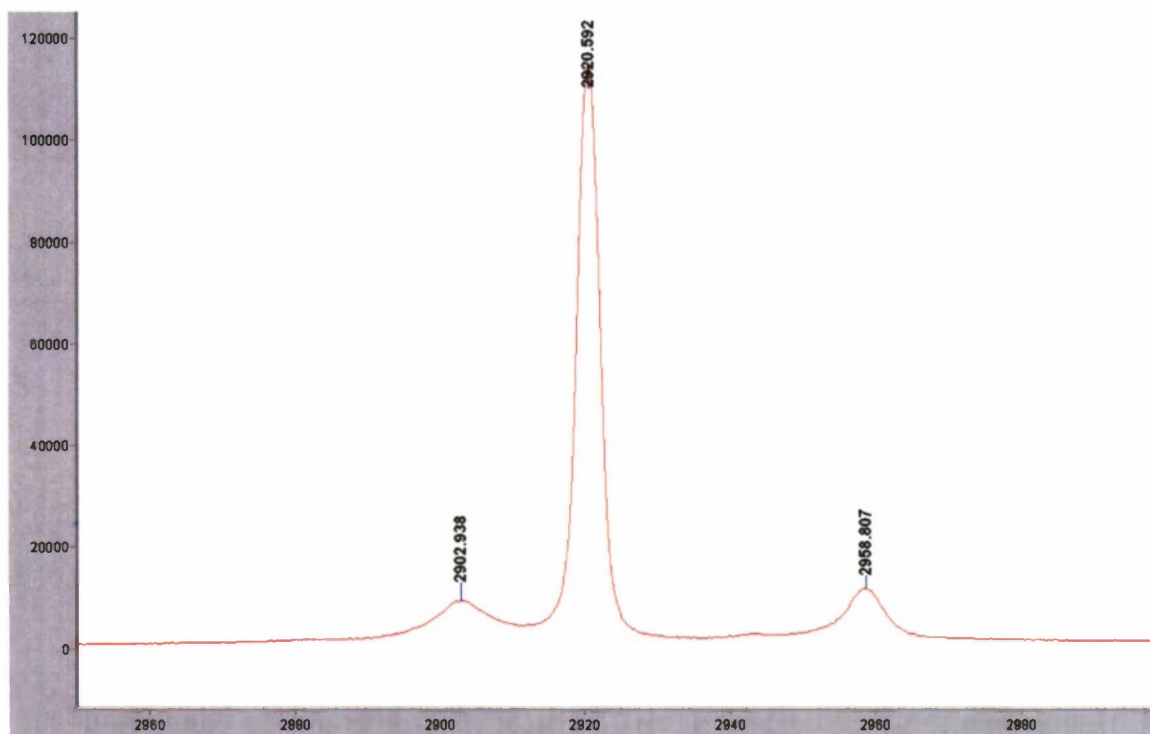


Figure 4-23. Raman spectrum at 19 °C and 6.8 MPa (985 psig). The hydrate peaks continue to disappear while the ethane gas peaks at 2958  $\text{cm}^{-1}$  and 2903  $\text{cm}^{-1}$  become more visible.





**Figure 4-24. Raman spectrum at 21 °C and 6.9 MPa (990 psig). The methane-ethane hydrate has completely decomposed.**

The thermogram and time history of the sample temperature during the hydrate formation and decomposition process are presented in Figure 4-25. Important features of the experiment, indicated by the labels in Figure 4-25, are:

1. Ice crystals melting (endothermic);
2. Hydrate formation (exothermic);
3. Raman spectra acquired (exothermic); and
4. Hydrate decomposition (endothermic).

It is evident from the thermogram that there are two distinct hydrate disassociation peaks. As noted above, the ethane hydrate is thermodynamically stable at higher temperatures than the methane hydrate, so the first decomposition event that occurs between 60,000 and 70,000 s probably is associated with methane escaping from the lattice, and the second event due to melting of the ethane hydrate.

The Raman calorimeter performed well in this first experiment involving mixed gas hydrates and the protocols we have developed to form hydrate appear to be viable. During the next phase of the experiments, the calorimeter gas supply system will be modified to allow extraction and analysis of the gas composition during hydrate formation and decomposition to determine if fractionation of the mixture is occurring.

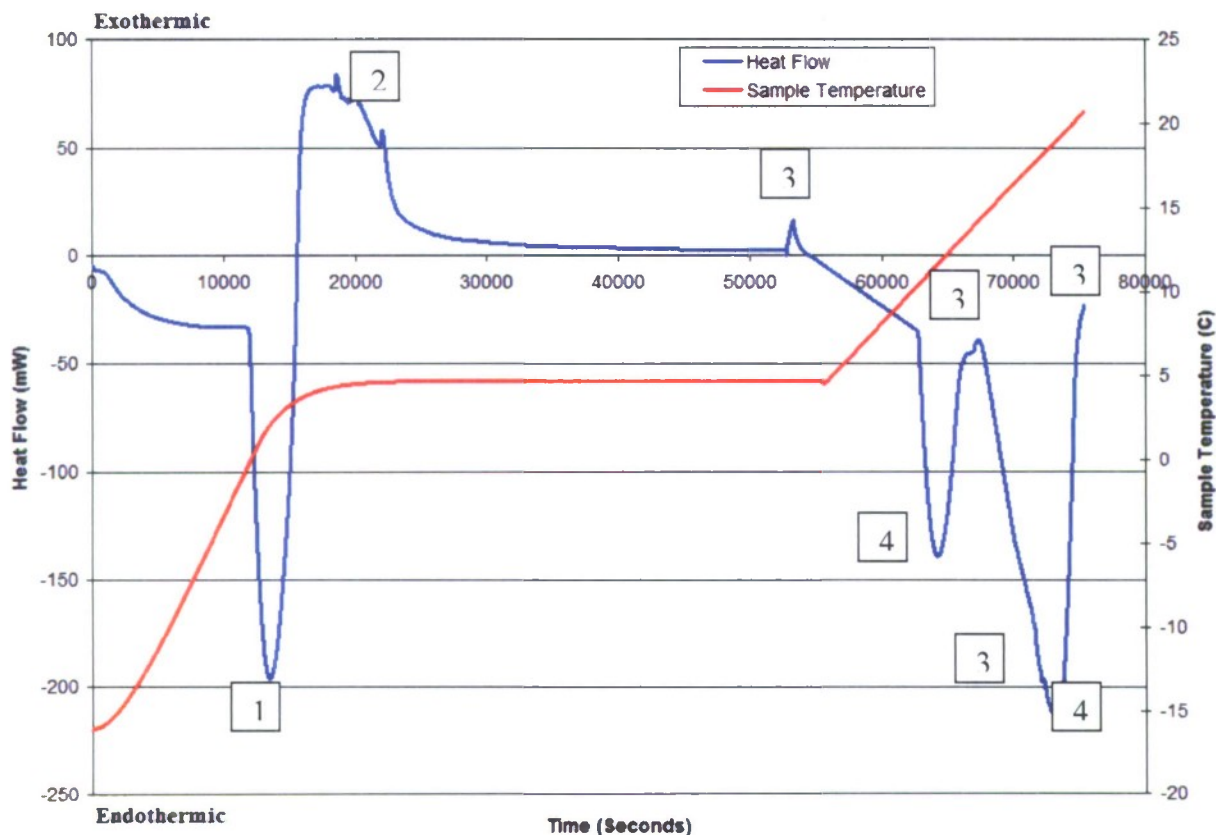


Figure 4-25. Calorimeter thermogram and temperature time history of the formation and dissociation of mixed methane-ethane hydrate.

#### 4.3.5 International Collaborative R&D

The 6<sup>th</sup> international workshop on methane hydrate R&D was held in Bergen, Norway on 13-15 May 2008. This series of meetings was initiated as part of HEET and HNEI has served on the organizing committee and as a sponsor for all of the past workshops. The 6<sup>th</sup> Workshop was attended by 55 scientists, engineers, and other stakeholder from 12 countries. This turnout was a bit smaller than previous workshops, but the quality of presentations, poster, and discussions remained high. A workshop report that includes copies of the presentation slides and posters was issued in July 2008 and is available from the Marine Biogeochemistry Section, Code 6114, of the Naval Research Laboratory.

#### 4.4 Papers Resulting from Efforts

Kinoshita, C.K., "An Experimental Investigation Employing Combined Calorimetry and Raman Spectroscopy of Thermodynamic Inhibitors Used to Decompose Methane Hydrates," M.S. thesis, Mechanical Engineering, University of Hawaii, August 2008.

Nihous, G.C., "A quantitative interpretation of recent experimental results on stable carbon isotope fractionation by aerobic CH<sub>4</sub>-oxidizing bacteria," *Geochimica et Cosmochimica Acta*, **72**, 4469-4475, 2008.

Nihous, G.C., C.K. Kinoshita and S.M. Masutani, "A determination of the activity of water in water-alcohol mixtures using Mobile Order Thermodynamics," accepted for publication in *Chemical Engineering Science*, February 2009.

Nihous, G.C., "Axisymmetric Large Eddy Simulation of a Circular Source of Buoyancy," revised manuscript submitted to the *International Journal of Heat and Fluid Flow*, February 2009.

Yoza B., Harada, R., Li, Q., Masutani, S.M. (2007). Methane hydrate associated microbial communities from the Hikurangi Margin, New Zealand. Presented at PACON 2007, also in PACON International Proceedings. <http://www.hawaii.edu/pacon/P07Abstracts.html>.

#### 4.5 References

Abrams, D. S. and Prausnitz, J. M. (1975). Statistical thermodynamics of liquid mixtures: a new expression for the excess Gibbs energy of partly or completely miscible systems. *AIChE Journal*, **21**, 116-128.

Alendal, G., Drange, H. (2001) Two-phase, near-field modeling of purposefully released CO<sub>2</sub> in the ocean. *J. Geophys. Res.*, **106**, 1085-1096.

Anderson, F. E. and Prausnitz, J. M. (1986). Inhibition of gas hydrates by methanol. *AIChE Journal*, **32**, 1321-1333.

Bai, Y. and Bai, Q. (2005). *Subsea Pipelines and Risers*. 2<sup>nd</sup> edition, Elsevier, Oxford, 812 pp.

Barker J. F., Fritz P. (1981) Carbon isotope fractionation during microbial methane oxidation. *Nature* **293**, 289-291.

Bemis, K.G., Rona, P.A., Jackson, D., Jones, C., Silver, D., Mitsuzawa, K. (2002) A comparison of black smoker hydrothermal plume behavior at Monolith Vent and at Clam Acres Vent Field: Dependence on source configuration. *Marine Geophys. Res.*, **23**, 81-96.

Coleman D., Risatti J. B. (1981) Fractionation of carbon and hydrogen isotopes by methane-oxidizing bacteria. *Geochim. Cosmochim. Acta* **45**, 1033-1037.

Cowen J. P., Wen X., Popp B. N. (2002) Methane in aging hydrothermal plumes. *Geochim. Cosmochim. Acta* **66**, 3563-3571.

Corinaldesi C., Danovaro, R., Dell'Anno, A. (2005). Simultaneous recovery of extracellular and intracellular DNA suitable for molecular studies from marine sediments. *Appl. and Environ. Microbiol.* **71**(1), 46-50.



- Craig H. (1957) Isotopic standards for carbon and oxygen and correction factors for mass-spectrometric analysis of carbon dioxide. *Geochim. Cosmochim. Acta* **12**, 133-149.
- DeLong, E. F. (1992) Archaea in coastal marine environments. *Proc. Natl. Acad. Sci. USA* **89**:5685-5689.
- Dewulf J., Van Langenhove H., Heireman B. (1998) The air/water exchange of volatile organic compounds from waters in the transient and turbulent regime. *Wat. Res.* **32**, 2106-2112.
- Dunfield P. F., Liesack W., Henckel T., Knowles R., Conrad R. (1999) High-affinity methane oxidation by a soil enrichment culture containing a Type II methanotroph. *Appl. Environ. Microbiol.* **65**, 1009-1014.
- Edwards T. J., Maurer G., Newman J., Prausnitz J. M. (1978) Vapor-liquid equilibria in multicomponent aqueous solutions of volatile weak electrolytes. *AIChE J.* **24**, 966-976.
- Epstein, M., Burelbach, J.P. (2001) Vertical mixing above a steady circular source of buoyancy. *Int. J. Heat Mass Trans.*, **44**, 525-536.
- Felten, F., Fautrelle, Y., Du Terrail, Y., Metais, O. (2004) Numerical modeling of electromagnetically-driven turbulent flows using LES methods. *App. Math. Model.*, **28**, 15-27.
- FEMLAB (2003) Multiphysics Modeling, Version 3.1, COMSOL, Inc.
- Hammerschmidt, E.G. (1939). Preventing and removing gas hydrate formations in natural gas pipe lines. *The Oil and Gas Journal*, **37**, 68-72.
- Heinz, S. (2002) On the Kolmogorov constant in stochastic turbulence models. *Phys. Fluids*, **14**, 4095-4098.
- Huyskens, P. L., Haulait-Pirson, M. C., Siegel, G. G., and Kapuku, F. (1988). Gibbs energy of some binary systems containing hydrogen bonds. *Journal of Physical Chemistry*, **92**, 6841-6847.
- Huyskens, P. L., Huyskens, D. P., and Siegel, G. G. (1995). Non-ergodicity of transient open-chain association in liquids. *Journal of Molecular Liquids*, **64**, 283-300.
- Jacques, R., Le Quéré, P., Daube, O. (2002) Axisymmetric numerical simulations of turbulent flows in rotor-stator enclosures. *Int. J. Heat Fluid Flow*, **23**, 381-397.
- Javanmardi, J., M. Moshfeghian and R. Maddox. (2001) An accurate model for prediction of gas hydrate formation conditions in mixtures of aqueous electrolyte solutions and alcohol. *Can. J. Chem. Eng.* 367-373.
- Kaewsichan, L. and Numuang, C. (2005). UNIQUAC activity coefficient model for the systems of 1-propanol + water and 2-propanol + water. *Songklanakarin Journal of Science & Technology*, **27**, 825-838.
- Kevbrina M. V., Okhapkina A. A., Akhlynin D. S., Kravchenko I. K., Nozhevnikova A. N., Gal'chenko V. F. (2001) Growth of mesophilic methanotrophs at low temperatures. *Microbiology*, **70**, 384-391.
- Kinoshita, C.K. (2008). An experimental investigation employing combined calorimetry and Raman spectroscopy of thermodynamic inhibitors used to decompose methane hydrates. M.S. thesis, Mechanical Engineering, University of Hawaii.

- Knox M. P., Quay P. D., Wilbur D. (1992) Kinetic isotope fractionation during air-water gas transfer of O<sub>2</sub>, N<sub>2</sub>, CH<sub>4</sub>, H<sub>2</sub>. *J. Geophys. Res.* **97**, 20335-20343.
- Lane, D. J. (1991). 16S/23S rRNA sequencing. in *Nucleic Acid Techniques in Bacterial Systematics*, pp. 115–175. Edited by E. Stackebrandt & M. Goodfellow. London: Wiley.
- Laws E. A., Popp B. N., Bidigare R. R., Kennicutt M. C., Macko S. A. (1995) Dependence of phytoplankton carbon isotopic composition on growth rate and [CO<sub>2</sub>]<sub>aq</sub>: Theoretical considerations and experimental results. *Geochim. Cosmochim. Acta* **59**, 1131-1138.
- Lesieur, M., Metais, O. (1996) New trends in large-eddy simulations of turbulence. *Annu. Rev. Fluid Mech.*, **28**, 45-82.
- Lupton, J.E., Delaney, J.R., Johnson, H.P., Tivey, M.K. (1985) Entrainment and vertical transport of deep-ocean water by buoyant hydrothermal plumes. *Nature*, **316**, 621-623.
- Mahalingam, S., Cantwell, B.J., Ferziger, J.H. (1990) Full numerical simulation of coflowing, axisymmetric jet diffusion flames. *Phys. Fluids A*, **2**, 720-728.
- Marchesi, J.R., Sato, T., Weightman, A.J., Martin, T.A., Fry, J.C., Hiom, S.J., Dymock, D. & Wade, W.G. (1998) Design and evaluation of useful bacterium-specific PCR primers that amplify genes coding for bacterial 16S rRNA. *Appl Environ Microbiol* **64**, 795–799.
- Masoudi, R. and Tohidi, B. (2005). Estimating the hydrate stability zone in the presence of salts and/or organic inhibitors using water partial pressure. *Journal of Petroleum Science and Engineering*, **46**, 23-36.
- Mell, W.E., McGrattan, K.B., Baum, H.R. (1996) Numerical simulation of combustion in fire plumes. *Proc. 26<sup>th</sup> Int. Symp. Comb.*, 1523-1530.
- Munck, J., Skjold-Jørgensen, S. and Rasmussen, S. (1988). Computations of the formation of gas hydrates. *Chemical Engineering Science*, **43**, 2661-2672.
- Nath A. and Bender, E. (1983). Isothermal vapor-liquid equilibria of binary and ternary mixtures containing alcohol, alkanolamine, and water with a new static device. *Journal of Chemical and Engineering Data*, **28**, 370-375.
- Nelis, K., Van den Berge-Parmentier, L., and Huyskens, F. (1995). The two non-ergodic insertion constants of the water molecule in H-bond chains at 25°C and their influence on the ternary diagrams water-alcohol-alkane. *Journal of Molecular Liquids*, **67**, 157-173.
- Nielsen, R. B. and Bucklin, R. W. (1983). Why not use methanol for hydrate control? *Hydrocarbon Processing*, April 1983, 71-78.
- Nihous G. C., Masutani, S. M. (2007) Notes on the modeling of methane in aging hydrothermal vents. *J. Mar. Res.*, **65**, 789-812.
- Nihous, G.C. (2009) Axisymmetric Large Eddy Simulation of a circular source of buoyancy. Revised manuscript submitted to the *International Journal of Heat and Fluid Flow*, February 2009.
- Ohno, H., Strobel, T.A., Dec, S.F., Sloan, E.D., Jr., Koh, C.A. (2009) Raman studies of methane-ethane hydrate metastability. *The Journal of Physical Chemistry A.*, **113**, 1711-1716.
- O'Leary M., Osmond C. B. (1981) Carbon isotope fractionation in plants. *Phytochemistry* **20**, 553-567.



Orbey, H. and Sandler, S. H. (1996). Analysis of excess free energy based equations of state models. *AIChE Journal*, **42**, 2327-2334.

Østergaard, K. K., Masoudi, R., Tohidi, B., Danesh, A. and Todd, A. C. (2005). A general correlation for predicting the suppression of hydrate dissociation temperature in the presence of thermodynamic inhibitors. *Journal of Petroleum Science and Engineering*, **48**, 70-80.

Pecher, I. A. and S. A. Henrys. (2003) Potential gas reserves in gas hydrate sweet spots on the Hikurangi Margin, New Zealand, Science Report, Institute of Geological and Nuclear Sciences, Lower Hutt, 32 pp.

Peşteanu, O., Schwerdtfeger, K. (2003) Contribution to the large eddy simulation of flows in electromagnetic stirrers for continuous casting. *ISIJ Int.*, **43**, 1556-1561.

Prucksunand, P. (2000). Effect of molecular size on the activity coefficient of glycols in aqueous solution. Master of Engineering Thesis, Chulalongkorn University, Thailand. ISBN 9741310293, <http://cuir.car.chula.ac.th/handle/123456789/5963>

Randriamampianina, A., Schiestel, R., Wilson, M. (2004) The turbulent flow in an enclosed corotating disk pair: axisymmetric numerical simulation and Reynolds stress modeling. *Int. J. Heat Fluid Flow*, **25**, 897-914.

Rau G. H. (1997) CO<sub>2aq</sub>-dependent photosynthetic <sup>13</sup>C fractionation in the ocean: A model versus measurements. *Global Biogeochem. Cycles* **11**, 267-278.

Ruelle, P. and Kesselring, U. W. (1996). The hydrophobic propensity of water towards amphiprotic solutes: prediction and molecular origin of the aqueous solubility of aliphatic alcohols. *Journal of Pharmaceutical Sciences*, **86**, 179-186.

Ruelle, P. and Kesselring, U. W. (1998). The hydrophobic effect. 1. A consequence of the mobile order in H-bonded liquids. *Journal of Pharmaceutical Sciences*, **87**, 987-997.

Ruelle, P. (1999). Towards a comprehensive non-ergodic treatment of H-bonds and hydrophobicity in real solutions: The mobile order and disorder theory. *Perspectives in Drug Discovery and Design*, **17**, 61-96.

Subramanian, S. and E.D. Sloan Jr. (1999) Molecular measurements of methane hydrate formation. *Fluid Phase Equilibria*, **158-160**, 813-820.

Subramanian, S., Kini, R., Dec, S., Sloan, E.D. (2000) Structural transition studies in methane+ethane hydrates using Raman and NMR. in *Gas Hydrates: Challenges for the Future*. Annals of the New York Academy of Sciences, Vol. 912, Eds. G.D. Holder and P.R. Bishnoi, 873.

Sum, A. K. and Sandler, S. I. (1999). A novel approach to phase equilibria predictions using *ab initio* methods. *Industrial and Engineering Chemistry Research*, **38**, 2849-2855.

Sundh I., Bastviken D., Tranvik L. J. (2005) Abundance, activity, and community structure of pelagic methane-oxidizing bacteria in temperate lakes. *Appl. Environ. Microbiol.*, **71**, 6746-6752.

Templeton A. S., Chu K.-H., Alvarez-Cohen L., Conrad M. E. (2006) Variable carbon isotope fractionation expressed by aerobic CH<sub>4</sub>-oxidizing bacteria. *Geochim Cosmochim. Acta* **70**, 1739-1752.



- Wagner, M.; Roger, A.; Flax, J.; Brusseau, G.; Stahl, D. (1998) Phylogeny of dissimilatory sulfite reductases supports an early origin of sulfate respiration. *J. Bacteriol.* 180:2975–2982.
- Wilhelm E., Battino R., Wilcock R. J. (1977) Low-pressure solubility of gases in liquid water. *Chem. Rev.* 77, 219-262.
- Wise M.G., McAuthur J.V., Shimkets L.J. (1999) Methanotroph diversity in landfill soil: isolation of novel type I and type II methanotrophs whose presence was suggested by culture independent 16S ribosomal DNA analysis. *App. Environ. Microbiol.* 65(11): 4887-4897.
- Zhang J., Quay P. D., Wilbur D. O. (1995) Carbon isotope fractionation during gas-water exchange and dissolution of CO<sub>2</sub>. *Geochim. Cosmochim. Acta* 59, 107-114.
- Yakhot, V., Orszag, S.A. (1986) Renormalization group analysis of turbulence I. Basic theory. *J. Sci. Comput.*, 1, 3-51.